Non-Newtonian fluid mixing in agitated vessels in the transitional flow regime

Manuele Romano

Thesis submitted to the School of Chemical Engineering of the

University of Birmingham for the Degree of

Doctor of Engineering (EngD)

School of Chemical Engineering
The University of Birmingham
B15 2TT
May 2022

Abstract

This thesis provides an original contribution to knowledge of fluid mixing in agitated vessels. This flow application has a critical importance in the manufacture of a wide range of intermediates and products in Johnson Matthey. The novelty of the research undertaken is twofold. Firstly, it presents quantitative investigations of the agitation of Newtonian and non-Newtonian fluids under transitional flow conditions. Despite the fact that transitional mixing is very common in industry, particularly for formulated products showing non-Newtonian rheology, most studies in the literature focus on fully laminar or fully turbulent mixing. Secondly, with the development of a methodology for 3D Particle Tracking Velocimetry measurements in laboratory scale vessels, this thesis has taken a step towards more accessible flow visualisation capabilities in industry. Numerical simulations have also been carried out to cross-validate the 3D-PTV data and provide additional information that could not be obtained experimentally.

Experiments and simulations have been conducted for many combinations of fluid rheology and impeller speed and at two vessel sizes. The hydrodynamics of transitional flows have been shown to depend significantly on the Reynolds number and fluid rheological behaviour. Non-Newtonian fluids showed smaller values of shear rate, Lagrangian acceleration and flow numbers, compared to the Newtonian ones. For Newtonian fluids, the local energy dissipation rate scaled differently depending on the position relative to the impeller. Non-Newtonian fluids did not follow the same scaling.

The information obtained in this thesis will help the design, optimisation and scale-up of mixing operations within Johnson Matthey.

Acknowledgements

I would like to thank the EPSRC, the University of Birmingham and Johnson Matthey for funding my EngD and providing me with their research facilities.

This thesis is the result of four years of commitment and hard work. It is my pleasure to acknowledge all the people who have contributed to my achievements.

I would like to express my gratitude to my supervisors for their valuable guidance. It has been an honour to work with them and my esteem for them will outlast this adventure. Li, thank you for helping me steer my research in the right direction day by day. Hugh, thank you for your humour and for always believing in me and in this project. The autonomy you granted me empowered me and made me grow as a researcher. Mark, I have treasured all your constructive feedback and technical suggestions. Your help with my writing and presentations has been invaluable. Fede, thank you for encouraging me to start the EngD and for all the good times spent over a few glasses of wine. Congratulations and good luck in your new job in Bologna.

Richard, I greatly admire your dedication to managing the EngD programme. Bringing young people closer to research is one of the noblest missions of a person of science.

I would like to thank all the wonderful people I met in JM. I will always treasure the skills and work ethics that I have developed during these four years. Rob is a great colleague and a brilliant scientist, always willing to help. Carl is an inexhaustible source of ideas, and some of his suggestions became the milestones of this project. Rebecca helped me on countless occasions and has set very high standards for all other students. I wish her a bright future after the EngD. Ben, Dan and Sid, good luck in your studies and thank you for all our ranting against IT.

Finally, I want to thank my girlfriend, best friend, superShero and travel planner, the light in my darkest hour, Alessia. Even though I had some difficult times over the past two years, I wake up every morning feeling like the luckiest man in the world. I couldn't have made it through this EngD without you. I love you, Nina mia.

Manuele

Table of Contents

List of figures

List of tables

List of acronyms and abbreviations

ACF	Autocorrelation function
CARPT	Computer automated radioactive particle tracking
CCD	Charge-coupled device
CFD	Computational fluid dynamics
CMC	Carboxymethylcellulose
CPU	Central processing unit
CV	Control volume
2D	Two dimensional
3D	Three dimensional
DES	Detached eddy simulations
DNS	Direct numerical simulations
EngD	Engineering doctorate
fps	Frames per second
JM	Johnson Matthey
JMTC	Johnson Matthey Technology Centre
LDA	Laser doppler anemometry

LES	Large eddy simulations
MAD	Mean absolute difference
MALD	Mean absolute logarithmic difference
MSD	Mean Square Displacement
MI	Macro-instability
MRF	Multiple reference frame model
PCC	Pearson’s correlation coefficient
PDF	Probability density function
PEPT	Positron emission particle tracking
PIV	Particle image velocimetry
PLIF	Planar laser induced fluorescence
POD	Proper orthogonal decomposition
PTV	Particle tracking velocimetry
ppp	Particles per pixel
px	Pixel (linear)
RANS	Reynolds-averaged Navier-Stokes equations
RT(-#)	Rushton turbine (with # blades)
RMS	Root mean square

RNG	Renormalization group
rpm	Revolutions per minute (60^{-1} s^{-1})
SGF	Savitzky-Golay filter
SM	Sliding mesh model
SNR	Signal to noise ratio
SST	Shear stress transport
TKE	Turbulent kinetic energy
UW	Upwind
2UW	Second order upwind
v.v.m.	Vessel volumes per minute (specific gas flow rate)

Mathematical notation and symbols

Mathematical expressions are frequently used in this thesis. Whenever possible, a consistent notation is adopted. It is assumed that the reader is familiar with linear algebra, vector calculus and indicial notation.

Scalars are represented in italic font (e.g. D for the impeller diameter). Vectors are indicated with bold lowercase letters (e.g. $\mathbf{u}$ for fluid velocity). Bold uppercase letters (e.g. $\mathbf{R}$) are used for tensors, unless common practice suggests differently (e.g. the stress tensor is typically indicated as $\boldsymbol{\sigma}$). Square brackets are used to represent a matrix (e.g. [A]). Its elements are indicated in italic font, and two subscripts identify, in the order, the row and the column (e.g. A_{12} is the element in the first row and second column).

Some symbols may be used for different quantities (e.g. σ for some turbulence model constants and for the standard deviation of a random variable). When the meaning is not obvious from the context, it will be explicitly explained in the text.

Some recurrent symbols are listed below.

Roman symbols

a	Lagrangian acceleration, magnitude (-)
B	Baffle width (m)
Bi	Bingham number (-)
C	Impeller bottom clearance (m)

D	Impeller diameter (m)
f	Frame acquisition rate (s^{-1})
Fl	Impeller flow number (-)
H	Tank height (m)
K	Fluid consistency index (Pa s^n)
k	Turbulent kinetic energy (m^2 s^{-2})
K_P	Impeller power constant (laminar regime)
k_s	Metzner-Otto constant
N	Impeller rotational speed (rps)
n	Fluid behaviour index (-)
P	Power (W)
p	Mechanical pressure (Pa) or PTV tracking parameter (-)
Po	Impeller power number (-)
r	Radial coordinate (m)
R	Tank radius (m)
Re	Reynolds number (-)
S	Scale-up ratio (-)
T	Tank diameter (m)

t	Time (s)
U	Characteristic velocity, magnitude (m s^{-1})
$\mathbf{u}$	Velocity vector (m s^{-1})
V	Tank volume (m^3)
X	Scale-up index (-)
x, y, z	Cartesian coordinates: width, height and depth (m)

Greek symbols

$\dot{\gamma}$	Shear rate (s^{-1})
ε	Energy dissipation rate (m^2 s^{-3})
η	Kolmogorov length microscales (m)
θ	Azimuthal coordinate (rad)
Λ	Torque (N m)
μ	Fluid dynamic viscosity (Pa s)
ν	Fluid kinematic viscosity (m^2 s)
ν_T	Turbulent eddy (kinematic) viscosity (m^2 s)
ρ	Fluid density (kg m^{-3})
τ_0	Fluid yield stress (Pa)
χ^2	Chi-squared statistic

Chapter I

INTRODUCTION

I.1. Project context and motivations

I.1.1. Industrial background

Fluid mixing is one of the most common unit operations across industrial applications where physical and chemical changes occur (Paul et al., 2003; Aubin et al., 2006). Mixing can be considered as an operation which reduces inhomogeneities, in terms of concentration, temperature or phase, to achieve specific process results (Paul et al., 2003). Adequate mixing is essential to achieve the desired product quality (Verschuren et al., 2001; Stitt, 2002; Zadghaffari et al., 2010).

The enormous variety of industrial mixing equipment designs reflects the myriad fluid properties and process objectives that can be encountered. Mechanically agitated vessels have a key role in the production of chemicals (van der Gulik et al., 2001; Stitt, 2002; Gao et al., 2010; Murasiewicz and Esteban, 2019; Peralta-Reyes et al., 2022), pharmaceuticals (Hörmann et al., 2011, 2012; Nienow, 2014; Ismail et al., 2017), polymers (Cavadas and Pinho, 2004; Zhang et al., 2007; Heidari and Karim Nejadian, 2022), ceramics (Celani et al., 2018; Poernomo et al., 2022), paints (Shah and Kakar, 1972; Antognoli et al., 2019), food (Malcata, 1991; Maingonnat et al., 2008; Mehauden et al., 2009), personal and home care products (Baghli et al., 2018; Story et al., 2018; Jaszczur et al., 2020), pulp and paper (Lin et al., 2011; Kouko et al., 2021), in waste and water treatment (Gargouri et al., 2011; Siddique et al., 2014; Castillo-Hernández et al., 2015; Karthikeyan et al., 2016; Akizuki et al., 2021), mineral

processing (Bakhtiari et al., 2008), cell culture (Guoqiang et al., 1992; Okibe et al., 2003; Dusting et al., 2006; Bulnes-Abundis et al., 2013) and many other applications. They are widely used in the production lines of Johnson Matthey (JM), the industrial sponsor of this project. Finished and intermediate formulated products made by JM often show complex rheology and high apparent viscosity. Thus, to avoid an excessive power consumption at the industrial scale, mixing is frequently conducted in the transitional flow regime, which is still poorly understood (Machado et al., 2013).

The design, optimisation and scale-up of agitated vessels in the transitional regime remain challenging tasks. If carried out inadequately, they can lead to huge costs, due to product yield reduction, delays, process corrections and lost opportunities (Paul et al., 2003). Non-Newtonian fluid rheology brings additional difficulties. General scaling rules for such flows are not available. Most empirical correlations in the literature are only applicable to a specific vessel configuration and within a limited range of conditions (Yoon et al., 2005; Bashiri et al., 2016b). Practitioners often design and scale-up transitional mixing operations based on experience and rules of thumb (Bashiri et al., 2016b), which provide suboptimal solutions. For a reliable and robust process development, decision making should be based upon evidence and strong understanding of the fundamentals. Consequently, case-specific raw data are extremely valuable in the manufacturing industry. Fluid velocity field, impeller flow number, power number, distributions of energy dissipation and shear rate are typical examples of important information regarding the fluid dynamics in stirred vessels, as they directly affect the process objectives such as liquid turnover, power consumption, mass transfer and blending time (Kapic and Heindel, 2006; Kresta et al., 2006; Hörmann et al., 2012; Martinetz et al., 2021). Assessing how those quantities vary with the operational variables and fluid rheology is essential for a deep understanding and knowledge of the mixing phenomena. Accurate data on mixing in

agitated vessels can be obtained through experimental flow visualisation and Computational Fluid Dynamics (CFD).

Experimental research has devoted considerable effort to understanding the fundamentals of mixing. As discussed in detail in **§II.2**, well-established optical measurement techniques, such as Particle Image Velocimetry (PIV), Laser Doppler Anemometry (LDA) and Planar Laser-Induced Fluorescence (PLIF) have contributed significantly to the existing body of knowledge (Kresta and Wood, 1993; Escudié and Liné, 2006; Alberini et al., 2014a). Positron Emission Particle Tracking (PEPT) and Computer Automated Radioactive Particle Tracking (CARPT) are valid alternatives which allow opaque fluids and geometries of industrial relevance to be studied (Rammohan et al., 2001; Fangary et al., 2002; Windows-Yule et al., 2020a, 2020b). However, all these techniques involve complex hardware and require high skills to perform experiments (CORDIS, 2022). Thus, they are typically only available in academia, whilst in-house flow visualisation capabilities within industry are quite rare (Schröder et al., 2009).

The development of modern computers and the reduction of the costs of CPUs and GPUs in the last few decades have popularized the use of CFD in industry (Haddadi et al., 2017; Xiang et al., 2017; Szewc et al., 2018). Numerical simulations of fluid flows are extremely useful in mixing research, as they can provide information that is hard to gather experimentally. However, the computational capabilities of a typical industrial R&D sector today only allow the *modelling* of fluid flows rather than their full resolution on a fine numerical grid. Experience in selecting the correct models and a careful interrogation of the numerical results are essential for obtaining meaningful information. The risk of a poor application of CFD without proper know-how, leading to misleading results, is omnipresent. For this reason, validation against experimental data should always accompany numerical studies. The simulation of transitional stirred tanks remains particularly challenging, as most turbulence models have been shown to

be inadequate for swirling flows and at intermediate Reynolds numbers (Mendoza et al., 2018). The best practices for simulating such systems are not yet clearly identified.

The industrial background behind this EngD project can therefore be summarised as follows. The existing knowledge about transitional mixing in stirred tanks is still incomplete, and both experiments and numerical simulations pose some difficulties. Any step towards greater accessibility and reliability of mixing data would represent a valuable contribution to the industrial value chain. Validated evidence would support decision making in the mixing process design and operations.

I.1.2. Johnson Matthey

Johnson Matthey plc (https://matthey.com) is a leading science and technology company which operates in the market of precious metals and catalysts, process technology, energy storage devices and pharmaceuticals. JM is a FTSE 100 company and has ca. 14,000 employees in more than 30 locations across the world (Johnson Matthey, 2021). In FY 2020/2021, despite the negative effects of the Covid-19 pandemic, it had revenues for £15.7 billion and operating profits of £323 million (Johnson Matthey, 2021). In 2021, JM joined the UN "Race to Zero Campaign" (https://unfccc.int/climate-action/race-to-zero-campaign), committing to achieving net zero carbon emissions by 2040. The company is structured into five main sectors, which are described below.

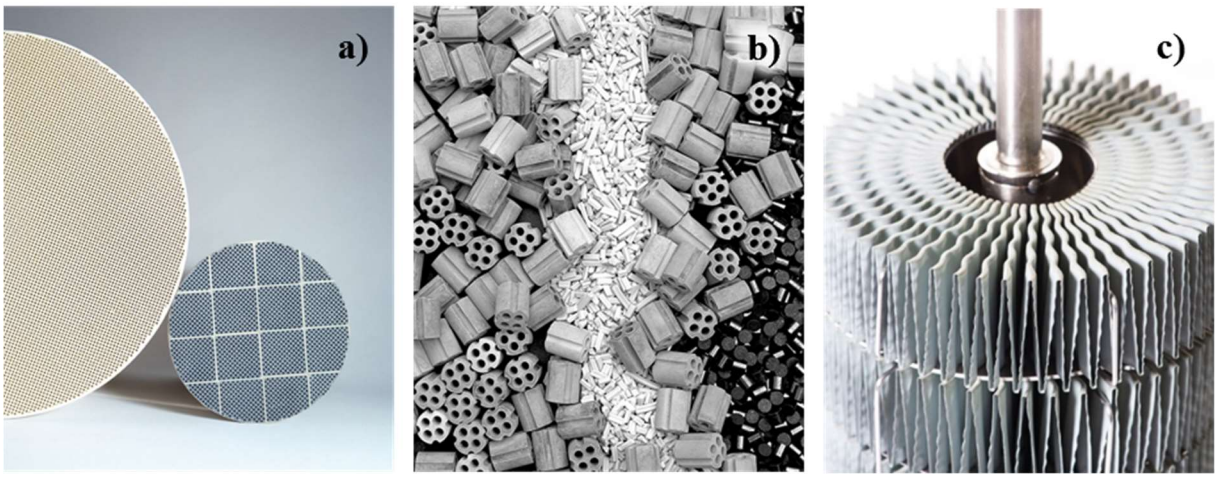

***Figure I-1**: Examples of catalysts manufactured in JM. Vehicle emission control converter (a), pellets used in different chemical processes (b) and foiled catalyst for hydrogen production (c) (https://matthey.com).*

I.1.2.1. Clean Air

Clean Air operates in the business of emission control catalysts for gasoline, diesel and hybrid vehicles and for industrial processes. Today, one third of new cars sold around the world carries a catalytic converter manufactured by JM. Overall, 2.5 million tonnes per year of pollutants are prevented from getting into the atmosphere by these catalysts (Johnson Matthey, 2021). The global catalyst market size was valued at USD 33.9 billion in 2019 and is expected to grow at a compound annual growth rate of +4.4% between 2020 and 2027 (Grand View Research, 2020). This is despite the fact that the Covid-19 pandemic contributed to a decrease in demand for oil, the first instance in a decade. The key drivers for this growth are the environmental regulations across industries and countries and the cost reduction associated to lower emissions.

I.1.2.2. Efficient Natural Resources

This sector aims at developing and applying advanced technologies to help JM's customers achieve greater efficiency and optimal yield in the use of natural resources. The main related activities are described below.

- Catalysts Technologies supplies catalysts and licensed processes to the oil and gas and bulk chemical industries, for instance in hydrogen, ammonia and methanol production plants.

- Platinum Group Metals Services focuses on refining and recycling precious metals and provides related support services.

- Advanced Glass Technologies produces functional and decorative glass-based materials for the automotive industry (e.g. the obscuration enamels used on car windscreens) and for electronics, anti-corrosion and architectural applications.

- Diagnostic Services (also known as Tracerco) provides detection, diagnostic and measurement technologies to the oil and gas industry.

I.1.2.3. Health

The Health sector produces active pharmaceutical ingredients (APIs) used in existing off-patent and in new drugs. It also provides services for drug development and synthesis.

I.1.2.4. New Markets

This sector operates in a wide spectrum of applications which represent appealing market opportunities. Today, JM is a leading supplier of fuel cell catalysts, membrane electrodes and battery cathode materials (Johnson Matthey, 2021). In 2020/2021, JM's battery materials and fuel cell technologies have avoided the release of 211,000 tonnes of CO2 equivalent (Johnson Matthey, 2021). Heavy duty transport is essential for keeping goods and people moving. It is forecasted that about 5% of trucks globally will be powered by fuel cells by 2030, rising to 30% by 2040. The New Markets sector also produces precision components for medical devices, catalysts and fine chemicals for life science applications.

I.1.2.5. Johnson Matthey Technology Centre

JMTC is the company's Research and Development division and provides support and enabling capabilities to the four business sectors. In FY 2020/2021, JM invested £199 million in research, that is about 5.5% of overall sales (Johnson Matthey, 2021). JMTC has provided financial support to this EngD.

I.1.3. Business case

Agitated vessels are widely encountered across Johnson Matthey business units. An important example is the preparation of washcoats for the manufacture of vehicle emission control catalysts. Washcoat is defined by JM as the intermediate fluid, containing the active materials, which is coated onto the catalyst monolith. This is then dried and calcined to make the final product. The fluids involved are typically high solids fraction suspensions (slurries) which possess non-Newtonian rheology. Due to their high viscosity, mixing occurs under transitional flow conditions.

A catalytic converter for emission control consists of a metal or ceramic monolith, coated with support material and active metals, located in the vehicle exhaust train (***Figure I-2***). Metal monoliths have thinner walls and heat up quickly. This is important, because ~75% of harmful emissions are produced within the first minutes from vehicle start-up, when the catalyst is not yet sufficiently warm (Cybulski and Moulijn, 2005). Ceramic monoliths are cheaper and have higher micro-porosity, which facilitates the adhesion of the support material onto the monolith walls and extends the catalyst life (Adegbite, 2010). During the vehicle operation, the exhausts pass through the converter channels. In the case of gasoline-fuelled vehicles, oxidation of carbon monoxide, oxidation of residual hydrocarbons and reduction of nitrogen oxides occur at the active sites of the catalyst surface (Twigg, 2011). Diesel engines work at lower temperatures than gasoline engines and produce leaner exhausts with high oxygen content

(Twigg, 2015). The chemical mechanisms in a converter for diesel vehicles are more complicated, and a filter is additionally employed to trap particulate matter (Twigg, 2015).

***Figure I-2**: Section of a catalytic converter for vehicle emission control (https://matthey.com).*

The manufacturing process involves many steps (***Figure I-3***). First, γ-alumina and zeolite powders are incorporated into demineralised water. The formulation may include other mineral oxides such as zirconia, depending on the application. The solid content in the slurry can reach 50% in weight. The pH of the slurry is controlled through addition of pH modifiers, typically acetic acid and ammonia, to prevent gelation and denaturation of the alumina. These procedures are carried out in large batch stirred vessels, where mechanical agitation ensures both powder incorporation and homogenisation of the slurry properties. The slurry is then milled to reduce the particle size distribution of the solid phase within the desired range. This dramatically impacts the surface area of the catalytic carrier, its adhesion onto the monolith and thus the catalyst performance (Agrafiotis et al., 1999). At this point, the platinum group metals (PGMs) are added, typically platinum, palladium and rhodium in the form of salts. These metals are the active components of the catalyst and represent most of its value. The blending operation is

conducted in large batch vessels. The rheology is carefully adjusted through addition of rheology modifiers, to guarantee good coating properties of the slurry. The liquid obtained from the blending is a thick non-Newtonian fluid. The washcoat is coated onto the monoliths and dried with hot air to remove most of its water content. The final step is the calcination of the monolith, i.e. a thermal treatment in ovens at high temperature to eliminate the residual water and organic compounds, activate the metals and enhance the adhesion between the different materials.

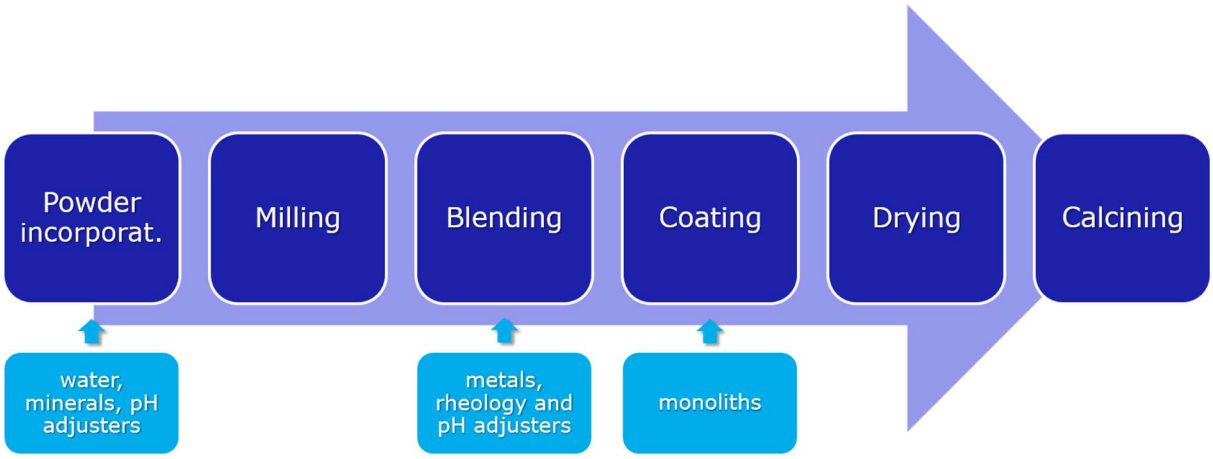

***Figure I-3**: Process steps in the production of a vehicle emission control catalyst.*

The blending of slurries and washcoats are delicate and precise operations, because many variables can affect the quality of the final product. The complex fluid rheology, which changes throughout the production stages, is an important process variable. The high viscosity makes the homogeneous dispersion of the components a difficult task. The spatial distribution of mixing intensity is another critical variable. With non-Newtonian liquids, fluid velocity and shear rate may vary by several orders of magnitude in different zones of the vessel, and the blending time is controlled by the unmixed regions (Greenville, 1992). A better understanding of the role of fluid rheology and mixing intensity in the agitation of non-Newtonian fluids under transitional conditions will help achieve better product quality and batch consistency, while reducing the costs of overmixing.

***Figure I-4**: Monolith used in the production of a catalytic converter for vehicle emission control (https://matthey.com).*

A longstanding collaboration exists between Johnson Matthey and the University of Birmingham, built on numerous EngD and PhD projects. While Particle Image Velocimetry (Adrian et al., 2011) and Positron Emission Particle Tracking (Windows-Yule et al., 2020a) facilities for fluid flow measurements are available at Birmingham, JM invested on a 3D-PTV experimental rig to develop its own flow visualisation capabilities. The applicability of PTV to lab-scale stirred tanks has been tested by researchers from JM and the University of Birmingham (Alberini et al., 2017), who compared PTV velocity measurements against PIV data. The encouraging results led to the research proposal of this EngD project. However, significant work was still necessary to enhance data acquisition, processing and post-processing with the PTV technique. For this reason, the preliminary development of PTV experimental protocols for lab-scale agitated vessels represents a substantial part of the work undertaken.

I.2. About this thesis

I.2.1. Scope

This thesis describes the research work undertaken during a four-year Engineering Doctorate project funded by the EPSRC CDT in Formulation Engineering at the University of Birmingham and JM and based full-time at the Johnson Matthey Technology Centre (JMTC) in Chilton. The project is focused on the mixing of Newtonian and non-Newtonian fluids in agitated vessels in the transitional flow regime. As outlined above, this application has a particular relevance to the manufacturing of automotive catalysts by JM. Throughout the thesis, aspects of laminar and fully turbulent mixing are present only to highlight the peculiar features of mixing under transitional conditions.

The fluid dynamics of transitional flows in stirred vessels has been examined using both experimental (3D-PTV) and numerical methods (CFD) at both the laboratory scale and the pilot scale. A detailed comparison and cross-validation of data obtained from the two techniques has been made.

To date, the large volumes and ranges of velocity involved have limited the use of 3D-PTV for studying mixing in stirred tanks. The development of a reliable methodology for 3D-PTV measurements in agitated vessels is thus a priority for this project. This included algorithmic and operational aspects, data analysis and protocols for investigating large volumes using the current hardware. Most of the high-impact existing literature involving 3D-PTV is limited to small observation volumes and simple flow geometries and aims at quantifying the statistics of turbulence related quantities (Lüthi et al., 2005, 2009; Guala et al., 2005; Holzner et al., 2008; Liberzon et al., 2012). In this thesis, 3D-PTV has not been applied to investigate the turbulence micro-scales. Due to the large observation volumes represented by the vessels, micro-scales

could not be resolved adequately using 3D-PTV. On the other hand, the application of PTV to stirred tank flows represents a pioneering approach of great appeal for JM, because it enables crucial information about the flow dynamics to be obtained with relatively simple hardware.

I.2.2. Objectives

This thesis aims at achieving the following objectives.

I. To develop a methodology for 3D-PTV experiments in agitated vessels at the laboratory scale. This objective is aimed at ensuring good quality measurements and enhancing JM's capabilities in flow measurements through documented good practices.

   a. To assess the effects of the main operational and algorithmic variables on the experimental errors and tracking efficiency, in order to define an adequate operational window based on the flow conditions. These findings will be easily generalisable to other flow applications, and the know how within JM for flow visualisation and measurement will be improved.

   b. To develop procedures of signal-to-noise ratio enhancement and post-processing of the Lagrangian data. This is also relevant to other Lagrangian techniques, such as PEPT.

   c. To address the limitations and rooms for improvement of the current hardware.

II. To measure the flow fields of Newtonian and non-Newtonian fluids in agitated vessels operated in the transitional regime by means of 3D-PTV. This technique will give new insights in the mixing process, as Lagrangian quantities will be extrapolated directly by time-resolved 3D data, while Eulerian quantities will be inferred.

a. To address the effects of fluid rheology on the hydrodynamics occurring in the vessel.

b. To find correlations between measurable quantities (directly and indirectly) valid in the transitional regime and to address whether fluid rheology and Reynolds number influence such relationships. For instance, to investigate the validity of the Metzner-Otto model over a wide range of transitional flow conditions.

III. To assess the capability of the most used CFD models in simulating transitional flows in stirred tanks through cross-validation against experimental measurements. CFD results will provide additional understanding of mixing processes, through quantities that are not easily measurable experimentally, e.g. turbulent kinetic energy and energy dissipation rate.

a. To assess the effects of the turbulence model.

b. To compare experimental and numerical data in terms of mean flow velocities. Unfortunately, PTV and steady RANS data do not allow a direct comparison of the instantaneous velocity, Given the fact that transitional flows are inherently time dependent, this represents a limitation to this thesis work that should be highlighted. Nevertheless, such a comparison has not been reported previously in the scientific literature.

c. To study the effects of fluid rheology and Reynolds number on the spatial distribution of the onset of turbulence and to assess the turbulence level scaling in the transitional regime.

IV. To test the viability of 3D-PTV experiments in agitated vessels at the pilot scale.

V. To develop appropriate scale-up rules for transitional mixing, based on experimental and numerical results. Traditional scale-up approaches for agitated vessels are based on global quantities, such as the power per volume. While these methods have been used extensively for turbulent flows, they have not been proven to work adequately for the transitional regime. Transitional flows in stirred tanks are notoriously heterogeneous, showing turbulent behaviour close to the impeller and laminar behaviour in the bulk (Gabelle et al., 2013).

   a. To address how local flow quantities, evaluated at different positions in the vessel, scale with the impeller diameter and speed.

   b. To address the role of fluid rheology on the scale-up rules. The proportion between the turbulent and laminar regions depends on the fluid properties.

   c. To assess how scale-up affects the cavern extension with yield-stress fluids.

I.2.3. Thesis structure

This thesis consists of seven chapters.

Chapter I is an introduction to the EngD project and to this document.

Chapter II is a critical review of the relevant literature concerning fluid mixing in agitated vessels (**§II.1**), experimental flow measurement techniques (**§II.2**) and numerical simulations of stirred tanks (**§II.3**). The gaps in current knowledge are summarised in **§II.4**.

Chapter III describes the work aimed at developing a PTV methodology for investigations in stirred vessels. The PTV operational variables, namely the camera frame rate and tracer concentration, are optimised based on the tracking efficiency and computational costs. A methodology for enhancing the PTV data signal-to-noise ratio is assessed and optimised.

In **Chapter IV**, the flows of Newtonian and non-Newtonian fluids in a 4.6 L vessel, measured by means of PTV, are described and discussed. The effects of fluid rheology and Reynolds number on the flow dynamics are addressed in terms of impeller flow number, shear rate and Lagrangian acceleration.

In **Chapter V**, the experimental data from the previous chapter are compared against CFD simulations, and the effects of mesh size, turbulence model and discretisation scheme on the numerical predictions are investigated. The CFD data provide further information about the mixing process by giving access to the spatial distributions of the turbulent quantities in the vessel.

In **Chapter VI**, PTV experiments and numerical simulations in a larger scale (21 L) vessel are discussed to identify scaling rules valid under transitional conditions. It is shown how the main flow variables change with the impeller diameter and speed, the position in the vessel and the fluid rheology.

Chapter VII is a conclusive summary of the main findings and recommendations for future research in this topic.

I.3. List of scientific publications and contributions

I.3.1. Journal papers

- **Chapter III** has been published in the *Chemical Engineering Research and Design* journal as

  Romano, M.G., Alberini, F., Liu, L., Simmons, M.J.H. and Stitt, E.H. (2021a) Development and application of 3D-PTV measurements to lab-scale stirred vessel

flows. *Chemical Engineering Research and Design*, 172: 71–83. doi:10.1016/j.cherd.2021.06.001.

- The work described in **Chapter IV** has been published in the *Chemical Engineering Science* journal as

  Romano, M.G., Alberini, F., Liu, L., Simmons, M.J.H. and Stitt, E.H. (2021b) 3D-PTV flow measurements of Newtonian and non-Newtonian fluid blending in a batch reactor in the transitional regime. *Chemical Engineering Science*, 246: 116969. doi:10.1016/j.ces.2021.116969.

- The work discussed in **Chapter V** has been submitted to the *Chemical Engineering Science* journal and, at the time of writing, is under review.

I.3.2. Scientific conferences

- Romano, M.G., Alberini, F., Simmons, M.J.H., Raso, G., Stitt, E.H., Liu, L. (2018) *Assessment of 3D-PTV to measure Lagrangian flow fields in stirred tanks*. Presented at the 16th European Conference on Mixing, Toulouse, France.

- Romano, M.G., Alberini, F., Simmons, M.J.H., Raso, G., Stitt, E.H., Liu, L. (2019a) *Assessment of the accuracy and precision of 3D-PTV*. Presented at the 15th International Conference on Fluid Control, Measurement and Visualization, Naples, Italy.

- Romano, M.G., Alberini, F., Simmons, M.J.H., Stitt, E.H., Liu, L. (2019b) *Assessment of 3D-PTV to measure Lagrangian flow fields in stirred tanks*. Presented at the 2019 AIChE Annual Meeting, Orlando, US.

- Romano, M.G., Alberini, F., Simmons, M.J.H., Stitt, E.H., Liu, L. (2020) *3D-PTV measurements in a stirred tank with Newtonian and non-Newtonian fluids*. Presented at the 2020 Virtual AIChE Annual Meeting, Online.

- Romano, M.G., Alberini, F., Simmons, M.J.H., Stitt, E.H., Liu, L. (2021) *Non-Newtonian fluid mixing in stirred tanks in the transitional flow regime*. Presented at the Johnson Matthey Academic Conference, Online.

Chapter II

LITERATURE SURVEY

The scientific interest in fluid flows is very old. Romans' capability to deliver fresh water via aqueducts remained unmatched for 1,500 years (Smith, 1978). In the 15-th century, Leonardo da Vinci used plant seeds as tracers to observe the flow of blood around the three-cusp aortic valve (Kemp, 2019). The equations of fluid motion were published in 1757 and 1821 by Euler and Navier, respectively (Euler, 1757; Navier, 1821). However, they were considered just a mathematical challenge by academics at that time. For most practical applications, even approximate solutions remained unavailable till the advent of CFD. A neat separation between '*hydrodynamics*', a branch of theoretical physics taught at universities, and '*hydraulics*', an empirical discipline for practitioners, persisted till the beginning of the 20th century (Eckert, 2017). Then, the military industry sponsored a more engineering approach to fluid dynamics and, in turn, stimulated the development of new measurement technologies. For instance, Prandtl's research in Göttingen wind tunnel facility was almost exclusively oriented towards war-related goals, such as the development of airplanes (Eckert, 2017). Modern velocimetry was born in the 1960's with the implementation of the first Laser Doppler Velocimetry rig (Yeh and Cummins, 1964) and enabled fully quantitative characterisation of fluid flows. The first PIV experiment was conducted in the Göttingen wind tunnel in 1984 (Kompenhans and Hinsch, 2009). In those days, images were captured on film, and the tracer displacements were evaluated manually. A few years later, the first automated PTV setup was used (Adamczyk and Rimai, 1988a, 1988b). That hardware only allowed 2 – 3 images per minute to be analysed. The poor quality of camera sensors would limit the application of PTV for more than a decade, until the necessary software and hardware improvements were achieved at the Institute of

Geodesy and Photogrammetry at ETH Zurich. In the 90's, the publication rate in the field of fluid mixing experienced a rapid growth. The spread of charge-couple device (CCD) cameras and digital technology, the increasing affordability of computational power and the popularisation of CFD opened new research possibilities, by reducing the time and costs associated to experiments and simulations and improving the data quality.

In 2011, the North American Mixing Forum voted on the most influential contributions to mixing research (NAMF, 2011). The list encompasses about six decades, from Kolmogorov's turbulence theory (Kolmogorov, 1941a, 1941b) to the experimental investigations on multiphase and non-Newtonian fluid mixing by Prof. Nienow (Chapman et al., 1983; Elson et al., 1986) and the studies on turbulence in stirred tanks by Prof. Kresta (Kresta and Wood, 1991, 1993). None of the works on their list focused specifically on transitional flow conditions or application of PTV.

This chapter provides a critical review of the existing literature concerning fluid mixing in stirred vessels and describes the experimental and numerical techniques used in modern research. ***Figure II-1*** displays the distribution of the year of publication of the main references cited in this thesis. This analysis only includes peer reviewed journal papers, conference contributions and books focusing on fluid mixing, flow visualisation and flow simulation.

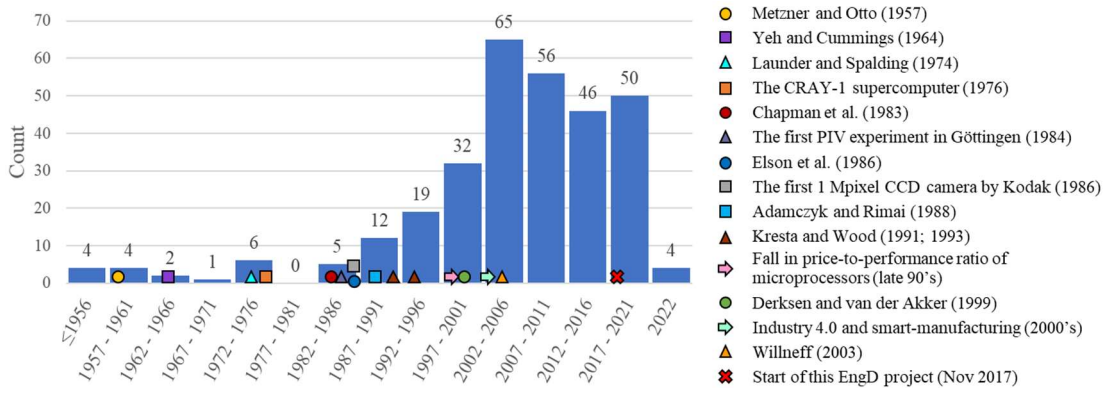

Figure II-1*: Year of publication of the scientific works concerning fluid flows and mixing cited in this thesis. Important publications and events are indicated by symbols.*

II.1. Mixing in mechanically agitated vessels

II.1.1. Equipment elements

A mechanically agitated vessel consists of a tank, a rotating mixer comprised of impeller, shaft and motor, and possibly includes other elements such as baffles, draft tubes, gas spargers and heat exchange surfaces. ***Figure II-2*** represents the standard configuration of a mechanically stirred tank for fluid blending.

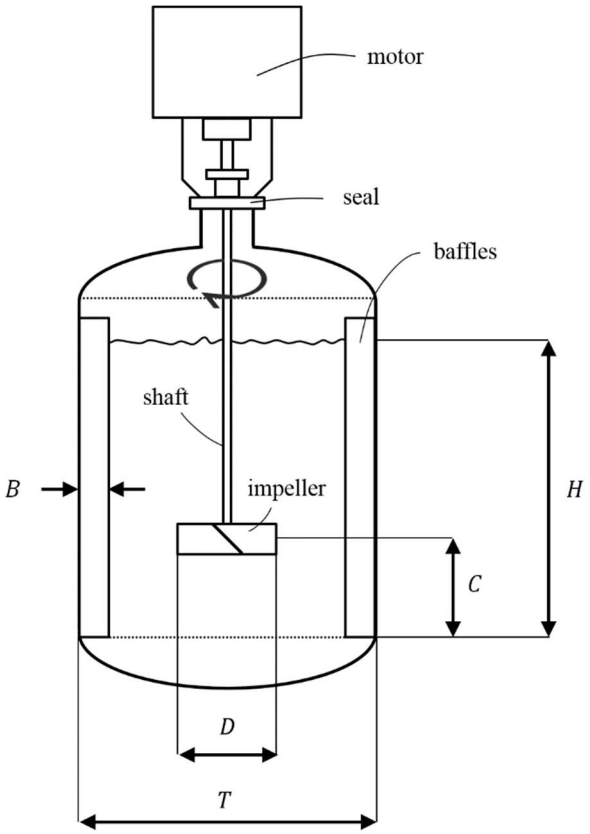

Figure II-2*: Schematic of a mechanically agitated vessel.*

The tank is usually a vertical cylinder and is filled with fluid to a height-to-diameter ratio $H/T = 1$ or more (Hemrajani and Tatterson, 2003). Non-standard geometries include square cross sections (Kresta et al., 2006). The vessel diameter can be as small as $T \sim 0.1$ m in lab scale units (litres) and reach $T \sim 10$ m in large installations (thousands of cubic metres). The base of the tank can be flat, dished or conical. The correct choice depends on the application

and affects the flow patterns below the impeller, hence the mixing efficiency (Hemrajani and Tatterson, 2003). For example, in solid suspensions, solids would tend to accumulate at the corners of a flat base, therefore dished bases are preferred (Hemrajani and Tatterson, 2003). Horizontal tanks are sometimes used for large scale operations (van der Gulik et al., 2001).

Baffles are solid surfaces positioned on the peripheral wall of the vessel and orthogonally to the tangential flow. They are used in transitional and turbulent mixing to limit solid-body swirling and vortex formation (Hemrajani and Tatterson, 2003). The presence of baffles enhances axial recirculation, minimize air entrainment and increases the power input required by the impeller (Ammar et al., 2011). The standard configuration consists of four rectangular plates arranged at 90 degrees from each other.

The mixer includes an impeller, a shaft and a motor unit. In tall vessels with a large height-to-diameter ratio, multiple impellers at different heights are often used. The shaft is typically introduced from the top along the vertical axis of the tank (Hemrajani and Tatterson, 2003). In some cases, the shaft can enter from the bottom to reduce its length and ensure mechanical stability (Doran, 2013). Side entering mixers are common in large inventory blending and in sludge control in oil tanks (Sossa-Echeverria and Taghipour, 2012). Tilted entering and eccentric mixers can be used in small unbaffled vessels or in operations where baffles are undesirable, such as fouling fluids (Wood et al., 2018b). They limit vortex formation by producing asymmetric flows.

The selection of the impeller has a great impact on the flow pattern, pumping versus dispersive capability, distribution of shear rate, power input and mixing efficiency (Kumaresan and Joshi, 2006; Torotwa and Ji, 2018; Jaszczur et al., 2020). There are a multitude of impeller designs, based on the fluid properties and process objectives (***Figure I-3***). Axial flow impellers, such as the marine propeller, are common in solid suspension and powder incorporation. Radial flow

impellers, such as the Rushton turbine (RT) are particularly efficient in gas-in-liquid and liquid-in-liquid dispersion. Mixed flow impellers, like the pitched blade turbine (PBT), produce both axial and radial flow discharge. High-shear impellers are operated at high speeds for phase dispersion, e.g. in pigment dispersion and liquid-liquid emulsions. To compensate for their low pumping capacity, high-shear impellers are often used along with axial impellers. Hydrofoils are specifically designed for high axial pumping with low shear and minimum power consumption. They are used in shear-sensitive applications, such as cell cultures, and in solid suspension. Proximity mixers such as anchors, screws, helical ribbons and similar have an impeller-to-tank diameter ratio close to unity and very small bottom clearance. They are used in laminar blending of highly viscous fluids, such as pastes and polymers. Sometimes proximity impellers are combined with coaxial turbines to enhance mixing (Li et al., 2012; Bao et al., 2015).

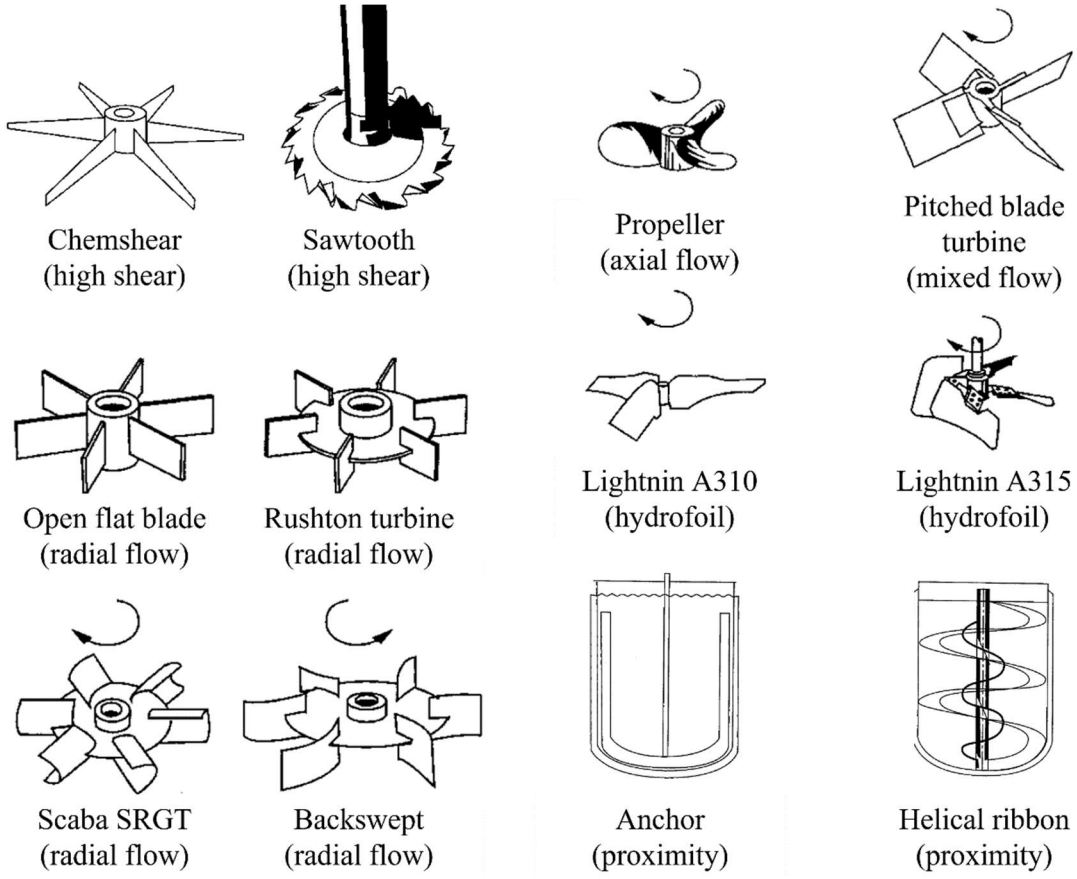

Figure II-3*: Common impeller geometries. Images from Hemrajani and Tatterson (2004).*

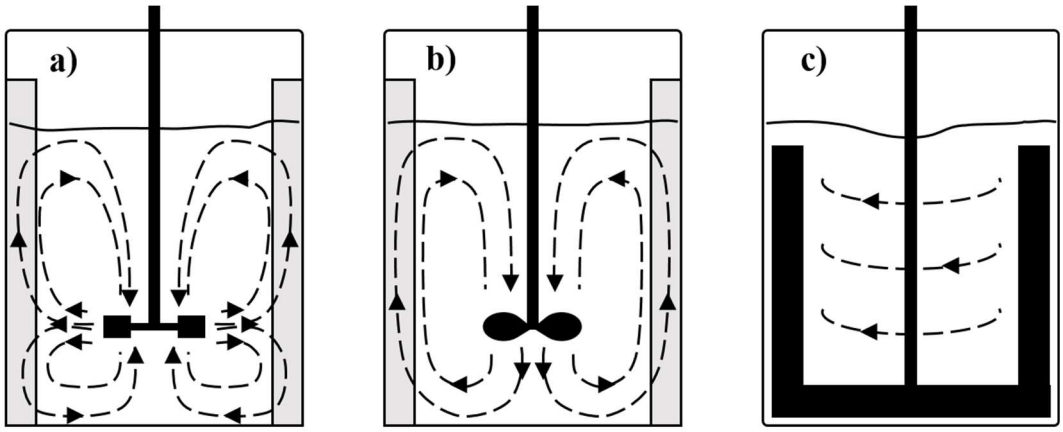

***Figure II-4**: Flow patterns generated by radial (a), axial (b) and proximity (c) impellers.*

In JM mixing processes, proprietary impellers and/or non-standard configurations are typically used. For these geometries, data in the public domain are scarce. On the contrary, the RT is undoubtedly one of the most popular mixing geometries. Its hydrodynamic properties have been extensively investigated on a fundamental level (Nienow and Wisdom, 1974; Yianneskis et al., 1987; Nienow et al., 1995) and flow data are easily available in the public domain. For this reason, experiments and numerical simulations of flows induced by a RT have been conducted in this thesis. Therefore, this geometry will receive particular attention in the remainder of the literature survey.

II.1.2. Reynolds number, power number and flow regimes

Everyday experience shows that there are two opposite ways in which flows occur in nature. Laminar flows are dominated by linear viscous forces, which can damp out disturbances (Kresta and Brodkey, 2003). Consequently, laminar flows tend to be highly ordered and predictable, with the fluid elements moving parallel to each other along smooth streamlines. Turbulent flows are dominated by non-linear inertial forces (Kresta and Brodkey, 2003). Infinitesimal disturbances grow into a myriad of complex interacting structures (Kresta and Brodkey, 2003). Thus, turbulent flows are highly unsteady, with the fluid velocity varying significantly and irregularly in space and time (Pope, 2000). In transitional flows, both viscous

and inertial forces play a role (Kresta and Brodkey, 2003). All flows, whether laminar, transitional, or turbulent, can be fully described by the Navier–Stokes equations (Kresta and Brodkey, 2003). Yet, the flow regime plays a critical role in mixing applications, because of the different prevailing mechanisms of momentum, mass and energy transport. The mechanism of laminar mixing involves reorientation and redistribution of the fluid elements (Hemrajani and Tatterson, 2003). The presence of unsteady and irregular eddies in a broad spectrum of length scales, interacting with each other, makes turbulent flows more effective in mixing (Pope, 2000). Nevertheless, turbulent conditions are often unfeasible for industrial stirred tank operations, e.g. in blending of highly viscous fluids and shear-sensitive products.

The Reynolds number is the ratio between inertial and viscous transport of momentum. It is named after the Irish physicist who first used it to describe the transition of pipe flows from laminar to turbulent (Reynolds, 1883). In stirred vessels, the impeller Reynolds number is

$$Re \equiv \frac{\rho\, D^2\, N}{\mu}, \qquad \textit{Eq. II-1}$$

where ρ is the fluid density (kg m^{-3}), μ the fluid dynamic viscosity (Pa s), D is the impeller diameter (m) and N is the impeller rotational speed (s^{-1}). The kinematic viscosity (m^2 s) is $\nu \equiv \mu/\rho$. The Reynolds number can vary from less than 10^1 in laminar operations to more than 10^4 in turbulent mixing. The flow regime in stirred vessels may be identified by measuring the power input, P, hence the dimensionless power number, that is

$$Po \equiv \frac{P}{\rho\, D^5\, N^3}. \qquad \textit{Eq. II-2}$$

Analogously to the friction factor in a pipe flow, Po is inversely proportional to Re in the laminar regime, i.e. $Po = K_P\, Re^{-1}$, and constant in the turbulent regime, i.e. $Po = Po_T$ (Hemrajani and Tatterson, 2003). For a given geometry, the power number data of any

Newtonian fluid will lie on the same curve (Böhme and Stenger, 1988; Fradette et al., 2007; Cabaret et al., 2008). These plots are commonly used to select the impeller for a certain application and to predict the power consumption (Scargiali et al., 2013). The power curves of common geometries and the extension of flow regimes have been measured by many authors. These studies tacitly assume that the more energy drawn from the impeller, the better the mixing, provided that energy would be dissipated uniformly and effectively (Zalc et al., 2001). A detailed list of references can be found in the paper by Kaiser et al. (2017). For instance, in the case of the RT, $K_P \approx 68$ for $Re \leq 10$ (Cabaret et al., 2008) and $Po_T \approx 5$ (Distelhoff et al., 1995). Compared to pipe flows, the transitional regime extends in a wider range of Reynolds number. In the literature, $Re \geq 2 \times 10^4$ is commonly considered enough to sustain a fully turbulent flow in the vessel (Machado et al., 2013). However, since most of the energy provided by the impeller is dissipated in the impeller discharge stream (Zhou and Kresta, 1996), it is not guaranteed that the whole flow is fully turbulent. Additional requirements are the scaling of the mean velocity and of energy dissipation. Machado et al. (2013) applied LDA to measure the fluid velocity in vessels of different scales and configurations. They found that only a portion of the tank was fully turbulent at $Re = 2 \times 10^4$. Also, they observed that Newtonian fluids of different viscosity mixed at identical values of Reynolds number could present different flow regimes at the same location in the tank. This apparently contradicts the fact that the Navier-Stokes equations provide a unique solution for a given Reynolds number. The inevitable imperfections in the experimental set-up, e.g. in the impeller speed, shaft alignment, impeller position et cetera, were identified as the most probable cause of the observed differences. The situation is even more complicated when non-Newtonian fluids are mixed, as their viscosity changes significantly within the vessel volume.

II.1.3. Non-Newtonian fluid mixing

II.1.3.1. Non-Newtonian rheology

Non-Newtonian rheology is a common characteristic of everyday products, like cosmetics, paints and foods (Dickey, 2015). The constitutive equation of an isotropic, incompressible, time-independent, non-Newtonian fluid reads

$$\boldsymbol{\sigma} + p\mathbf{I} = 2\mu(\mathbf{S})\,\mathbf{S}, \qquad \textit{Eq. II-3}$$

where $\boldsymbol{\sigma}$ is the stress tensor (Pa), p is the pressure (Pa), $\mathbf{I}$ is the identity matrix and $\mathbf{S} \equiv {}^{1}/_{2}\,(\nabla\mathbf{u} + \nabla\mathbf{u}^{T})$ is the strain rate tensor (s^{-1}).

The power-law (*Eq. II-4*) and the Herschel-Bulkley (*Eq. II-5*) equations are two common non-Newtonian time-independent rheological models:

$$\mu = K\,\dot{\gamma}^{n-1}. \qquad \textit{Eq. II-4}$$

$$\mu = K\,\dot{\gamma}^{n-1} + \tau_0\,\dot{\gamma}^{-1}. \qquad \textit{Eq. II-5}$$

Here

$$\dot{\gamma} = \sqrt{2\,\mathbf{S}{:}\,\mathbf{S}}. \qquad \textit{Eq. II-6}$$

is the shear rate (s^{-1}), n is the flow index (dimensionless), K is the consistency index (Pa s^{n}) and τ_0 is the yield stress (Pa). When $n < 1$, which is the most frequent case, the viscosity reduces with shear rate and the fluids are said shear thinning. Fluids that exhibit a yield stress flow only if the applied shear forces are above a critical value, i.e. $\tau > \tau_0$, otherwise they behave like a solid. For $n = 1$ and $\tau_0 = 0$ the two models reduce to a Newtonian fluid with constant viscosity.

When non-Newtonian fluids are mixed in a stirred tank, the viscosity changes greatly in space, because of the different shear conditions. Away from the impeller and near walls and baffles, shear forces are low, and the viscosity can be very high. These zones of the tank control the blending time (Greenville, 1992) and may remain unmixed because of inadequate fluid motion (Dickey, 2015). Yield stress liquids tend to form caverns of moving fluid around the impeller, while the fluid outside remains completely still (***Figure II-5***). Viscous shear thinning liquids may form pseudo-caverns. In this case, the fluid flows throughout the entire vessel, but velocities outside the pseudo-cavern are orders of magnitude smaller than those found within. Cavern and pseudo-cavern formation have detrimental effects on mixing. These phenomena have been investigated in many studies (Arratia et al., 2006; Adams and Barigou, 2007; Cabaret et al., 2008) and a number of models have been proposed to predict the (pseudo-) cavern shape and size, based on the power input, the agitation speed and the fluid rheological parameters (Solomon et al., 1981; Elson et al., 1986; Amanullah et al., 1998; Wilkens et al., 2005a; Hui et al., 2009).

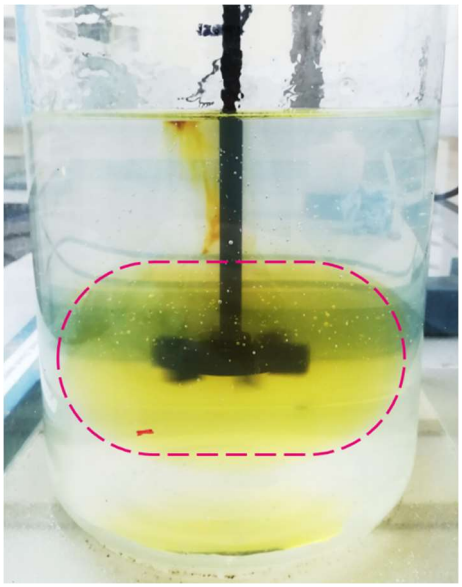

Figure II-5*: Cavern formed during the agitation of a Carbopol-water solution (Herschel-Bulkley fluid) and visualised by injection of a dye.*

II.1.3.2. The Metzner-Otto model

The Metzner-Otto model (Metzner and Otto, 1957) is the most widely used method for estimating the power requirements of non-Newtonian fluids (Márquez-Baños et al., 2019). It assumes that, in laminar flow, the fluid motion in the impeller region is characterized by an effective shear rate, which is proportional to the impeller speed:

$$\dot{\gamma}_e = k_s\, N. \qquad \textit{Eq. II-7}$$

The apparent, or effective, viscosity is calculated at that value of shear rate, according to the fluid rheological model. This allows the effective Reynolds number to be obtained as

$$Re = \frac{\rho\, D^2\, N}{\mu_e}. \qquad \textit{Eq. II-8}$$

The value of k_s is fitted so that the power number curve of any non-Newtonian fluid matches the curve for Newtonian fluids. The Metzner-Otto equation (*Eq. II-7*) was originally developed for flat-blade turbines operated at $2 \leq Re \leq 270$, and the authors reported a value of $k_s = 13$, which appeared to be independent of the fluid rheology, the impeller-to-tank diameter ratio, D/T, and the presence of baffles. However, the authors did not exclude an effect of the flow index, which was not varied widely in their work. They also suggested that, with close-clearance impellers, the effective shear could become dependent on D/T. Subsequent works have tried to determine the dependence of k_s on the fluid rheology and geometrical ratios, with significant discrepancies reported.

***Table II-1**: Some experimental correlations for k_s reported in the literature.*

Source	Geometry	n	k_s
Metzner and Otto (1957)	flat-blade turbines	0.24 – 1	$k_s = 13$
Calderbank and Moo-Young (1959, 1961)	different geometries	0.2 – 0.84	$k_s = f(n)\, g\left({}^{D}/_{T}\right)$

Beckner and Smith (1966)	anchors	0.25 – 0.73	$k_s = f(n)\, g(C/D)$
Nagata et al., (1971)	RT; anchor; ribbon	0.27 – 1	$k_s = 11.8$; $k_s = 25$; $k_s = 30$
Rieger and Novak (1973)	different geometries	0.50 – 0.97	$k_s = f(n)$
Torrez and André (1998)	RT	0.53	$k_s = 12.1$
Márquez-Baños et al. (2019)	PBT	0.36	$k_s = 8.53$

Bertrand et al. (1996) extended the Metzner-Otto concept to yield stress fluids agitated with anchor impellers. They found that k_s was independent of Bi for $Bi \leq 7500$, where

$$Bi = \frac{\tau_0}{K\, N^n}. \qquad \textit{Eq. II-9}$$

is the Bingham number, i.e. the ratio between yield stress and viscous stress (this definition assumes $\dot{\gamma} = N$). On the contrary, Anne-Archard et al. (2006) simulated yield stress fluid flows induced by helical and anchor agitators and observed that k_s changed with Bi in the range $60 \leq Bi \leq 12{,}000$.

In the original Metzner-Otto approach, the shape and size of the impeller region were not specified and thus k_s was intended as a global parameter that could be determined through power measurements. More generally, the ratio between a volume-averaged shear rate and the impeller speed, i.e. $k_s^*(\Omega) = \langle\dot{\gamma}\rangle_\Omega / N$, is a function of the volumetric domain, Ω, and can be evaluated from local velocity data obtained either by experiment or by simulation using CFD. Some authors have tried to determine the correct size and position of the volumetric domain that would lead to $k_s^*(\Omega) = k_s$. For example, Jahangiri et al. (2001) investigated the flow of

four viscoelastic polyacrylamide solutions within a vessel stirred with a RT under transitional conditions and evaluated, by means of LDA, the shear rate from the velocity data at different radial positions. At the impeller tip, k_s^* varied between 10.22 and 10.50. Ramírez-Muñoz et al. (2017) used CFD to simulate the flow induced by a RT and divided the impeller region into many control volumes. In each volume, k_s^* was calculated from the volume-averaged shear rate and a value of $k_s^* = 11.8$ was obtained in the volume swept by the impeller blades. This is very close to the value of $k_s = 11.1$ fitted directly from power measurements and to the typical value of $k_s = 11.5$ reported in the literature. Márquez-Baños et al. (2019) carried out a similar analysis for a PBT, though in that case, a larger volume than that swept by the impeller blades had to be considered to match the volume-based k_s^* with the power-based k_s.

As the Reynolds number increases ($Re > \sim 10^2$), the characteristic shear rate diverges from the Metzner-Otto model (*Eq. II-7*) and becomes proportional to $N^{3/2}$ (Sánchez Pérez et al., 2006) due to the turbulence contribution to shear generation. Nonetheless, due to its simplicity, the Metzner-Otto model is commonly applied outside of laminar flow conditions (Böhme and Stenger, 1988). This can result in severe mispredictions. Kelly and Gigas (2003) simulated the flow of Newtonian and power-law liquids ($0.4 \leq n \leq 0.8$) near axial flow impellers operating in the transitional regime. They found that the shear rate around the impeller surface could be approximated as a linear function of the impeller frequency, but upon closer inspection it also depended on the flow index. This was because the impeller discharge angle changed dramatically with both Re and n. Using Newtonian data from Kelly and Gigas (2003), Sánchez Pérez et al. (2006) observed that a power-law fitting of the impeller shear with $N^{1.4}$ provided a higher coefficient of determination than the linear fitting ($R^2 = 0.99$ instead of $R^2 = 0.95$). However, given the small number of data points, the 4% increase in R^2 is not enough to demonstrate a better fitting. More likely, this was just an effect of the additional degree of freedom introduced by the power law model.

II.1.4. Impeller flow number

The flow number, defined as

$$Fl \equiv \frac{Q}{D^3\, N} \qquad \textit{Eq. II-10}$$

normalizes the flow rate of fluid pumped by the impeller, Q ($m^3\ s^{-1}$). In the case of a Rushton turbine, which pumps the fluid radially, Q can be obtained from velocity data as the flux across a control surface parallel to the impeller blade height (Dyster et al., 1993):

$$Q(s) = 2\pi\left(\frac{D}{2} + s\right)\int_{C-W/2}^{C+W/2} \langle U_r\rangle_\theta \, dy. \qquad \textit{Eq. II-11}$$

In *Eq. II-11*, $\langle U_r\rangle_\theta$ is the azimuthally averaged radial component of the velocity at a radial coordinate $r = D/2 + s$, where s is an arbitrary distance from the impeller tip, C is the vertical coordinate of the impeller plane and W is the vertical size of the impeller blade. Norwood and Metzner (1960) measured the flow rates of Newtonian fluids with RTs. In the range of Re between 36 and $1.7 \cdot 10^4$, the flow rates were

$$Q \propto D^2\, N\, W \left(D^{0.4}\frac{\rho}{\mu}\right)^{0.5} (1 - q^2)^{0.5}. \qquad \textit{Eq. II-12}$$

The term q, representing the difference between the impeller velocity and the fluid velocity at the blade tip, was found to be negligible.

In the laminar and transitional regimes, the flow number depends on Reynolds, then it becomes constant under turbulent conditions. Dyster et al. (1993) measured Fl of the Rushton turbine in a range of Re between 5 and $5 \cdot 10^4$ with Newtonian fluids, based on the mean velocity profiles. They found that Fl was proportional to $Re^{0.5}$ till $Re \leq 500$, and it approached a constant value of ~0.78 for $Re > 500$. The profiles of the rms values of the radial velocity,

normalized by the impeller tip speed, were also independent of Re for $Re > 500$. Koutsakos *et al.* (1990) conducted a similar analysis with shear thinning liquids ($0.37 \leq n \leq 0.58$). The flow number of shear thinning fluids was always smaller than with Newtonian fluids, Re being the same. In particular, Fl was proportional to Re for $Re \leq 60$ and to $Re^{0.2}$ for $Re > 60$, till eventually it reached the constant value of ~0.78. Venneker et al. (2010) measured the velocity profiles of ten liquids ($0.56 \leq n \leq 1$) agitated with a Rushton turbine. The Reynolds number of the experiments varied from the transitional ($Re \sim 10^3$) to the turbulent regime ($Re \sim 10^5$). The flow index was found to have a different impact on the various velocity components (both mean and rms). The shear thinning rheology had a widening effect on the discharge profiles of the radial and tangential velocities, resulting in lower flow numbers compared to the Newtonian liquids. However, the differences were not as pronounced as in Koutsakos et al. (1990).

II.1.5. The transitional regime

In industry, mixing operations in stirred vessels are frequently carried out under transitional flow conditions. However, most experimental and numerical studies reported in the literature focus on fully laminar or fully turbulent flows (Mendoza et al., 2018), where the availability of well-established scaling laws helps with the design of experiments and simulations. The transitional regime is still not well understood (Machado et al., 2013) and the simultaneous presence of viscous and inertial effects makes these flows extremely complex.

In the fully turbulent regime, time-averaged velocity fields in stirred tanks show Reynolds-independence when scaled according to the impeller tip speed, $U_{tip} \sim D\,N$. As already discussed in the previous sections, the same Reynolds-independent behaviour is observed for other dimensionless groups, such us the power number and the flow number. Also, the turbulent energy dissipation rate in the impeller region scales as $\varepsilon \sim D^2 N^3$ (Zhou and Kresta, 1996). In

the transitional regime, Reynolds independence does not occur. Zhang et al. (2017) used PIV to measure the flow induced by a RT in a standard configuration vessel and identified the transitional-to-turbulent flow transition in the range $2{,}600 < Re < 6{,}000$. This was characterised by a loss of Reynolds independence of the scaled mean velocity and velocity fluctuations. At $Re \leq 270$ the random velocity fluctuations were negligible, indicating a laminar flow. Moreover, their CFD simulations (both DNS and RANS with the Transition SST turbulence model) did not reproduce the experimental observations in the transitional regime. It should be pointed out that the Transition SST model, which they describe as specifically designed for transitional flows, was actually developed for turbulent external aerodynamics applications with separation of the boundary layer. Similarly, Mendoza et al. (2018) measured the flows of Newtonian liquids induced by an axial hydrofoil by means of PIV. Self-similarity of the average velocity fields was confirmed at $Re = 3{,}000$, but for $Re = 340$ and $Re = 980$ the flows clearly depended on impeller speed and fluid viscosity. Similar conclusions were drawn from the POD analysis of the instantaneous velocity fields, revealing an increasing variability of the coherent flow structures at low Reynolds number. Instead, transient laminar simulations at $Re = 340$ showed self-similarity of the velocity fields, in contrast to the experimental observations. Ultimately, these works confirmed the difficulty of validating CFD simulations of flows in the transitional regime. Yoon et al. (2005) applied stereo-PIV to two unbaffled vessels of different scales, agitated with a RT, and observed that the mean flow scaled with the tip speed for $Re > \sim 15{,}000$. However, some quantities associated to the impeller jet and the tip vortices did not reach independence until $Re > \sim 10^5$. Furthermore, the two systems showed slight differences in the normalised velocities, suggesting an effect of scale. Gabelle et al. (2013) measured the transitional flows ($100 \leq Re \leq 237$) of a yield stress fluid induced by a RT impeller by means of PIV. The POD decomposition of the velocity fields revealed that, unlike in the fully turbulent regime, the shear rate and viscous kinetic energy dissipation

associated to mean and organised motion were far from negligible compared to the turbulent case. Furthermore, the energy dissipation rate in the impeller region did not scale with D^2N^3. This work also highlighted the difficulty of identifying a representative shear rate in agitated vessels, since this quantity varies significantly in space and is characterised by multi-modal distributions.

Low frequency macro-instabilities (MI) are another important feature of transitional flows in stirred tanks. They consist of pseudo-periodic perturbations of the flow whose size is comparable to the size of the vessel and whose time scale is comparable to the tank turnover time, i.e. two or three orders of magnitude larger than the impeller period. For instance, the MIs generated by the RT are tornado-like vortices which appear above and below the impeller plane and precess around the impeller axis (Ducci et al., 2008).

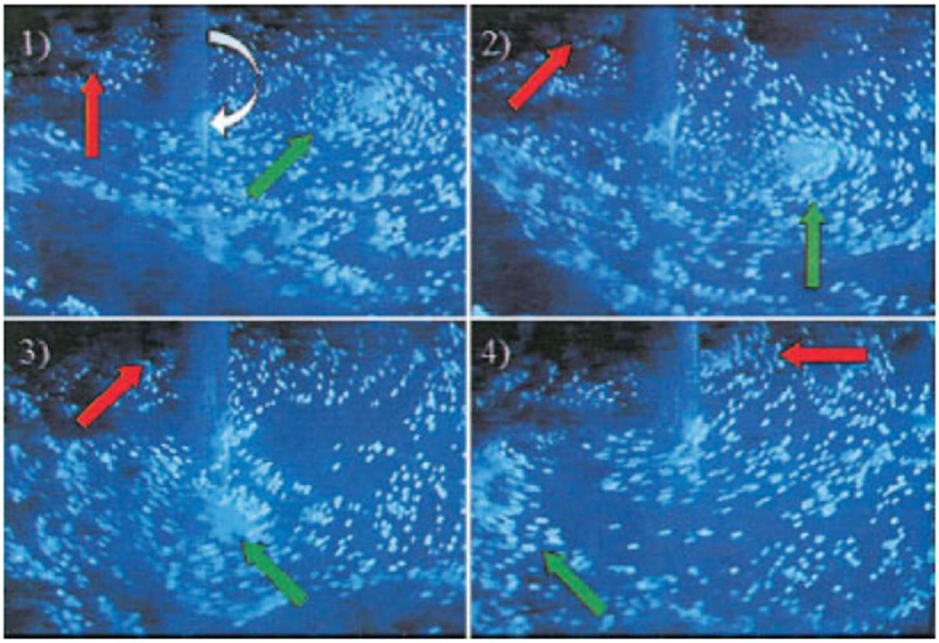

Figure II-6*: Flow visualisation experiment by Galletti et al. (2004a), showing two vortices of different intensity moving around the impeller shaft. The vessel was stirred with a Rushton turbine at Re = 2,000.*

The presence of MIs can be displayed by peaks in the low-frequency region of the power spectra of flow-related experimental data (fluid velocity, pressure, force, etc.). However, in some cases the MI is not associated to a coherent frequency and the power spectrum shows a broad band instead of distinct peaks (Roussinova et al., 2000). MIs can have significant impact on the dynamics of circulation loops (Kresta and Wood, 1993; Montes et al., 1997; Roussinova et al., 2000; Galletti et al., 2003; Brůha et al., 2007), impeller discharge angle (Fan et al., 2004), local heat and mass transfer (Haam et al., 1992), mixing time (Ducci and Yianneskis, 2007), local gas hold-up (Bakker and Van den Akker, 1994) and on the forces acting on the mechanical elements of the vessel (Hasal et al., 2002, 2003, 2004). If the MIs are not accounted for, e.g. in RANS of transitional flows, errors in the rms velocity computation can be large, particularly in the low-turbulence regions (Roussinova et al., 2000). Great efforts have been devoted to characterising the MI properties in relation to the flow regime and mixer geometry (***Table II-2***). In many cases, a linear relationship between the MI frequency and the impeller frequency has been found. However, the proportionality constant $f' \equiv f_{MI}/N$ differed greatly, despite the studies being conducted under similar flow conditions or even with the same vessel configuration (Hasal et al., 2004). Some works have shown that MIs appear less regularly and become hardly identifiable at high Reynolds, i.e. in the turbulent regime, possibly because they are broken down by the small turbulent eddies (Montes et al., 1997; Hasal et al., 2000; Fan et al., 2004). Furthermore, Paglianti et al. (2008) observed that the MI intensity becomes lower than the effect of the impeller blade passage above a critical impeller speed, which depends on geometry. Other authors have ascertained the presence of MIs only above a minimum Reynolds number (Brůha et al., 1996; Galletti et al., 2004a).

***Table II-2**: Research studies on flow macro-instabilities properties.*

Reference	Technique	Re	Impeller	Main findings
Brůha et al. (1996)	force measurements	200 – 67,000	PBT-6	$f' \propto \log Re$ for $200 \leq Re \leq 5{,}000$. $f' = 0.045$ for $Re > 9{,}000$.
Montes et al. (1997)	LDV	300 – 100,000	PBT-6	$f' = 0.09$ at $Re = 1{,}140$. $f' = 0.057$ at $Re = 75{,}000$.
Hasal et al. (2000)	LDV	750 – 75.000	PBT-6	$f' = 0.087$ at $Re = 750$ and $1{,}200$. $f' = 0.057$ at $Re = 75{,}000$.
Roussinova et al. (2000)	LDV	fully turbulent	RT, PBT and other axial impellers	MIs can explain a large share of velocity rms. The MI amplitude decreases with local turbulence intensity, baffles and D/T ratio.
Hasal et al. (2002)	force measurements	16,000 – 83,300	PBT-4 and PBT-6	$f' = 0.074$ regardless of Re, position and impeller geometry.
Galletti et al. (2003)	LDV	15,000 – 35,000	RT, $0.17 \leq C/T \leq 0.20$	The flow changed randomly from single to double circulation loop, with an intermediate state. All three states had a lifetime of a few minutes. During the transition, $f' = 0.12$.
Hasal et al. (2003)	force measurements	6,000 – 60,000	RT, $C/T = 0.35$ and $C/T = 0.50$	$f_1' = 0.026$ and $f_2' = 0.087$ for $c/T = 0.35$. $f_1' = 0.016$ and $f_2' = 0.082$ for $c/T = 0.50$. The slowest MI (f_1') disappears when $Re >$ ~30,000.
Roussinova et al. (2003)	LDV and CFD	3,000 – 500,000	PBT-4	$f' = 0.186$ for $Re > 20{,}000$.
Fan et al. (2004)	PIV	70,000 – 420,000	RT-4	$f' = 0.22$ for $70{,}000 \leq Re \leq 280{,}000$.

Galletti et al. (2004a)	LDV	400 – 54,400	RT, various D/T and C$/T$	RT of $D/T = 1/3$ and various C/T: $f' = 0.106$ for $400 \leq Re < 6{,}300$. $f_1' = 0.015$ and $f_2' = 0.106$ for $6{,}300 \leq Re \leq 13{,}600$. $f' = 0.015$ for $13{,}600 < Re \leq 54{,}400$. The frequencies changed with D/T.
Nikiforaki et al. (2004)	LDV and PIV	5,000 – 56,000	RT (different geometrical ratios) and PBT	$0.01 \leq f' \leq 0.02$. Presence of larger values ($0.04 \leq f' \leq 0.15$) in the transitional regime. Lack of scaling with the geometrical parameters.
Brůha et al. (2007)	image analysis of the primary circulation loop	62,200	PBT-6	$f' = 0.094$.
Paglianti et al. (2008)	pressure measurements	not specified	different geometries, one or more impellers	f' decreases with the number of impellers. The MI intensity decreases with the impeller speed (Re).

II.1.6. Scale-up

Since tests in large scale tanks are time consuming and expensive, design and optimisation studies are usually conducted at the laboratory scale, under equivalent flow conditions. The findings must be then replicated at the production scale. In industry, the scale-down and scale-up of mixing operations are a critical milestone for a rapid product development and for the success of the manufacturing process. The current state of the art regarding the scale-up and

design of stirred tanks is based on empirical correlations, best practices and rules of thumb (Bashiri et al., 2016b). This often results in a time-consuming and expensive series of iterations between laboratory experiments and pilot plant tests (Yoon et al., 2005).

There are many challenges in the migration of a mixing process from laboratory to the production scale.

- In common scale-up strategies, geometrical similarity is typically adopted, that is all the length ratios are kept constant. Ideally, kinematic and dynamic similarities are also desirable, that is maintaining the same velocity ratios and force ratios at corresponding positions in the small and large vessels. However, different quantities, e.g. mean velocities, turbulent fluctuations, power requirement and transport coefficients, change differently with vessel size and impeller speed. Therefore, only the most critical quantities can be kept constant, depending on the process aims (***Table II-3***).

- Non-Newtonian rheology complicates the scaling relationships even further, because the apparent fluid viscosity depends on the flow index and shear conditions.

- The variables characterising the flow are usually assumed to be uniform in the entire volume ('well-mixed' assumption). However, in real systems, such parameters may vary significantly within the vessel (Bashiri et al., 2016b). For instance, a common scale-up strategy for turbulent mixing is to keep the same power per unit volume, hence the same average energy dissipation rate, $\langle \varepsilon \rangle_V = P/\rho V$. However, it is well known that the local energy dissipation in the proximity of the impeller can be over one order of magnitude higher than the average value (Zhou and Kresta, 1996; Ng and Yianneskis, 2000; Baldi and Yianneskis, 2004; Micheletti et al., 2004; Ducci and Yianneskis, 2005;

Gabriele et al., 2009; Delafosse et al., 2011; Soos et al., 2013). The Kolmogorov length microscales, η (m), change accordingly as $\eta \sim \nu^{3/4}\ \varepsilon^{-1/4}$.

- Some physical processes, e.g. heat and mass transfer, may become limiting in large units (Li et al., 2005).

- Finally, the overall flow regime may change from the laboratory to commercial scale, because the Reynolds number increases with the linear dimension of the system (Letellier et al., 2002). This aspect must be considered carefully, as some scale-up criteria might be effective only within a specific range of flow conditions (Montante et al., 2003a).

***Table II-3**: Factors of change in the flow variables when the vessel size is increased by a factor $S = D_l/D_s$, according to some common scale-up criteria.*

$\frac{N_l}{N_s}$	$\frac{U_{tip_l}}{U_{tip_s}}$	$\frac{\dot{\gamma}_l}{\dot{\gamma}_s}$	$\frac{Re_l}{Re_s}$	$\frac{Po_l}{Po_s}$	$\frac{P_l}{P_s}$	$\frac{(P/V)_l}{(P/V)_s}$	$\frac{\Lambda_l}{\Lambda_s}$	$\frac{(\Lambda/V)_l}{(\Lambda/V)_s}$	$\frac{\eta_l}{\eta_s}$	$\frac{Q_l}{Q_s}$	$\frac{Fl_l}{Fl_s}$
Fully laminar regime (Newtonian fluid): $\dot{\gamma} \propto N$; $Po \propto Re^{-1}$; $Fl \propto Re^{1/2}$.											
1	S	**1**	S^2	S^{-2}	S^3	**1**	S^3	1	1	S^4	S
S^{-1}	**1**	S^{-1}	S	S^{-1}	S	S^{-2}	S^2	S^{-1}	$S^{1/2}$	$S^{5/2}$	$S^{1/2}$
S^{-2}	S^{-1}	S^{-2}	**1**	1	S^{-1}	S^{-4}	S	S^{-2}	S	S^2	1
Fully turbulent regime (Newtonian fluid): $\dot{\gamma} \propto N^{3/2}$; $Po = const$; $Fl = const$.											
1	S	**1**	S^2	1	S^5	S^2	S^5	S^2	$S^{-1/2}$	S^3	1
$S^{-2/3}$	$S^{1/3}$	S^{-1}	$S^{4/3}$	1	S^3	**1**	$S^{11/3}$	$S^{2/3}$	1	$S^{7/3}$	1
S^{-1}	**1**	$S^{-3/2}$	S	1	S^2	S^{-1}	S^3	1	$S^{1/4}$	S^2	1
S^{-2}	S^{-1}	S^{-3}	**1**	1	S^{-1}	S^{-4}	S	S^{-2}	S	S	1

Many researchers have proposed or tested a variety of scale-up criteria for agitated vessels, based on different applications and goals (***Table II-4***). These rules are often expressed in the general form

$$(N\,D^X)_l = (N\,D^X)_s. \qquad \textit{Eq. II-13}$$

Here the subscripts l and s indicate the large and small scales, respectively. Although for similar applications the differences in the exponent X may seem small, they can lead to significant variations in power consumption, product selectivity, yield and mixing performance at the large scale (Montante et al., 2003a; Jafari et al., 2012).

***Table II-4**: Some scale-up criteria for stirred vessels reported in the literature.*

Reference	Application	Goal	Technique	Scale-up rule
Montante et al. (2003)	solid suspension	equal solid concentration profiles	optical	$X = 0.93$ (close to equal U_{tip})
Montante et al. (2008)	solid suspension	equal solid concentration profiles	turbulence theory and CFD	$X = 0.96$ (close to equal U_{tip})
Jafari et al. (2012)	solid suspension	equal solid concentration profiles	optical	$X = 0.78$
Zhao et al. (2017)	solid suspension	operate at just-suspended speed ($N = N_{JS}$)	optical	$X = 0.87$
Harrison et al. (2020)	solid suspension	equal homogeneity index	ERT	$X = 0.67$ (equal P/V)
Özcan-Taşkin (2006)	drawdown of floating solids	operate at just-drawdown speed ($N = N_{JD}$)	visual observation	$X = 0.5$ (equal Fr)
Wood et al. (2018a)	powder incorporation	work at just-incorporated speed ($N = N_{JI}$)	visual observation	$X = 0.33$ (equal $Fr \cdot N$)
Bonvillani et al. (2006)	mixing in gas/liquid bioreactors	equal overall volumetric mass transfer	correlations from literature	$X = 1$ (equal U_{tip}) and equal

		coefficient (provided adequate mixing time)	(Hubbard, 1987), pH-metry for mixing time	gas specific flow rate (v.v.m.)
Bashiri et al. (2016)	mixing in gas/liquid bioreactors	equal overall volumetric mass transfer coefficient (provided adequate mixing time)	CFD	$X = 0.67$ (equal P/V) and equal gas superficial velocity
Qiu et al. (2021)	laminar agitation of shear-thinning fluids	equal power per unit volume	torque measurements and CFD	$X = 0$ (equal P/V)
Yavuz and Sandeep (2019)	laminar agitation of shear-thinning fluids with eccentric impellers	equal velocity profiles, suitable power consumption and mixing time	PLIF, torque measurements and CFD	Compared $X = 0.47$ (equal P/V), $X = 1$ (equal U_{tip}), $X \sim 1.25$ (equal Re)
Letellier et al. (2002)	laminar and transitional mixing in unbaffled multi-impeller vessels	equal flow patterns	CFD	$X = 0$ (equal P/V) without geometrical similarity
Li et al. (2005)	turbulent mixing in pharmaceutical and fine chemical industry	equal power number, impeller flow number, secondary circulation	CFD	$X = 2$ (equal Re)

II.2. Experimental flow measurement techniques

II.2.1. Laser Doppler Velocimetry (LDV)

LDV, also called Laser Doppler Anemometry (LDA), is a well-established optical technique that uses the fluctuating light scattered by particles moving in a small observation volume to measure local fluid velocities. The fundamentals are thoroughly described by Brown et al. (2003). Two coherent laser beams of equal intensity are made to cross in an ellipsoidal region of the flow called the probe volume. This is typically in the order of millimetres long. Due to the different angle of the laser beams, their apparent frequencies are slightly different. This generates an interference pattern due to beat frequency, that is a series of parallel planes of high and low light intensity called fringes. The fringe distance depends on the wavelength of the laser light and the angle between the beams and can be measured optically. As tracers travel across the probe volume, they scatter light back to a photo detector. The reflected light intensity is a sinusoid with a Gaussian envelope and is converted to an electric signal to be processed. The velocity component normal to the fringes is proportional to the beat frequency and can be determined. By combining three devices with different wavelengths, all three velocity components in a Cartesian reference frame can be measured simultaneously.

Typically, the laser beams are obtained by splitting a single beam with a Brag cell, in order to ensure coherence between the two. Laser with wavelengths in the visible spectrum, such as He-Ne, Argon ion and laser diode, are commonly used. The tracers can be seeded or naturally present into the fluid and are typically in the order of ~10 μm in size (Brown et al., 2003).

LDV has distinctive strengths and limitations. The technique is non-intrusive and is characterized by a unique linear response to fluid velocity. Therefore, any velocity magnitude is measured with equal accuracy, without drift effects (Brown et al., 2003). This eliminates the

need to calibrate the rig depending on the range of velocities to be measured. As with PIV, phase-resolved velocity observations in agitated vessels can be obtained by means of a shaft encoder, e.g. to investigate the trailing vortices leaving the impeller blades (Derksen et al., 1999; Galletti et al., 2004b) or to separate the turbulent and coherent parts of the kinetic energy (Li et al., 2004). Velocity signals can be analysed in the frequency domain to study macro-instabilities (Montes et al., 1997; Galletti et al., 2004a; Nikiforaki et al., 2004; Ducci and Yianneskis, 2007) and flow pattern transitions (Galletti et al., 2003). Two-point LDA measurements, with small spatial separations and short coincidence windows, enable the direct measurement of the velocity fluctuation gradients, hence the estimation of the energy dissipation rate (Micheletti et al., 2004; Ducci and Yianneskis, 2005).

As any optical technique, LDV can only be applied to transparent fluids and optically accessible systems. The installation costs and the safety concerns associated with laser illumination are major limitations, particularly in the industrial environment. The technique only allows pointwise measurements to be conducted, therefore the study of many locations of the flow is time-consuming (Galletti et al., 2004b). The velocity is measured as the tracers pass through the measurement volume. Due to the randomness of particle arrival, the time between the measurements is non-uniform. Therefore, a preliminary signal interpolation to obtain evenly spaced data is required before standard spectral analysis (Roussinova et al., 2003). Also, the arrival rate is highly correlated to the flow rates passing through the measurement volume, thus to the fluid velocity. Consequently, an arithmetic averaging of the velocity observations would bias the result in favour of high values (Brown et al., 2003) and weighting methods are required.

II.2.2. Particle Image Velocimetry (PIV)

PIV is a correlation-based velocimetry technique and today it is the primary method used in research. The works by Adrian (1984, 1991, 1997) and Adrian et al. (2011) represent excellent sources of information about the principles of PIV and its application to fluid flows. A typical PIV apparatus consists of a laser and its optical arrangement, a CCD camera, and a synchronizer. The flow under investigation is seeded with tracer particles, which follow the flow faithfully if their Stokes number is sufficiently low. Typically, the errors in flow tracing are negligible when $St < \sim 10^{-1}$, (McKeon et al., 2007). The doubled pulsed laser illuminates a section of the fluid, so that particles are visible. A combination of cylindrical and spherical lenses is used to reduce the laser beam into a thin sheet. The CCD camera is synchronised to the laser and takes a pair of images (frames) of the flow. The frames are split into a large number of interrogation areas (IA), typically with partial overlap. At the typical particle concentrations, individual particles can be resolved in an image, but they cannot be tracked individually from the first frame to the second one. Instead, a cross-correlation algorithm is used to calculate the most probable displacement vector in each IA. Then, the velocity vector is calculated in each IA using the physical length of the IA and the time between laser shots. The final output is typically a 2D-2C flow field (two dimensions of the measurement space - two components of the velocity vectors), although more sophisticated setups such as stereo-PIV enable 3D-3C measurements by using multiple cameras (Prasad, 2000). A schematic of the measurements principles is given in ***Figure II-7***.

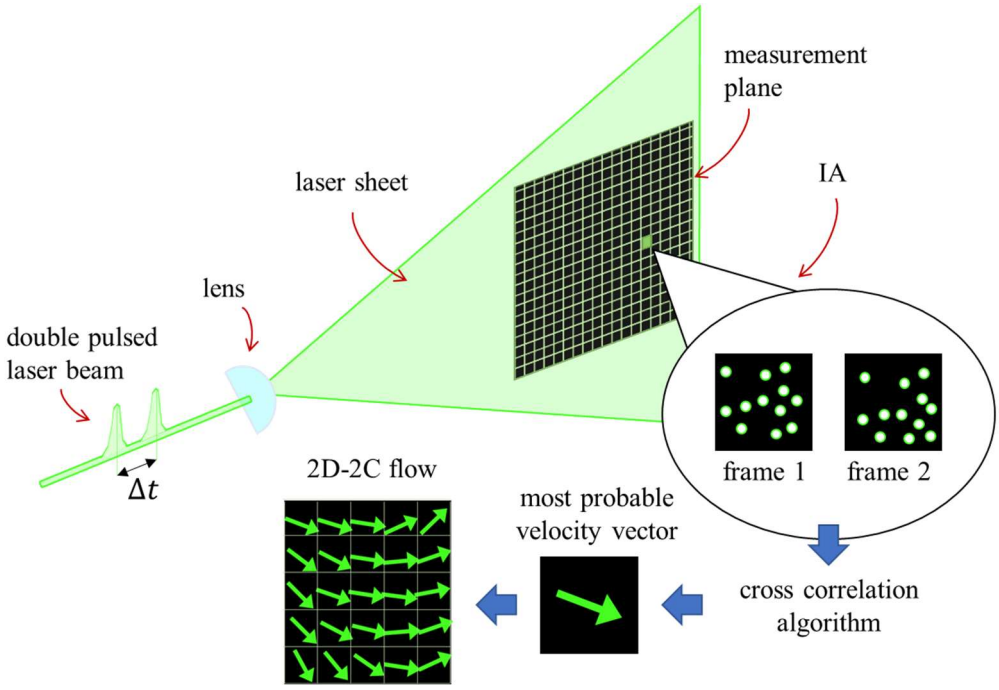

***Figure II-7**: Principles of 2D-PIV.*

Some parameters are critical for the quality of a PIV experiment. The typical tracer diameter ranges from 10 to 100 µm, so that their Stokes number is low. The refractive index of the tracers should be different from the fluid one, so that the light can be reflected by the particles and be scattered towards the camera. Melling (1997) has reviewed a variety of tracer materials that have been used in liquid and in gas PIV experiments. The methods for producing the tracers are also discussed. The size of the IA should be chosen such that between 6 and 10 particles are present in each IA. This is necessary for a reliable cross-correlation analysis and to ensure robustness of the results to noise. The time lag between the laser shots, Δt, must be chosen properly. If too short, it may become difficult to identify any displacement, since the physical length of the pixel represents the limit to the resolution of the technique. On the other side, if the time interval is too long, the ratio of the displacement to time is a poor approximation of the instantaneous velocity. It is common practise to start PIV experiments with a first attempt value given by $\Delta t \approx 25\%\, l_{IA}/U$, where l_{IA} (m) is the physical length of the IA and U (m s^{-1})

is the characteristic velocity of the flow. The camera settings should be adjusted so that the particles are imaged in at least 2×2 px^2.

The main advantage of PIV is that it is a whole field measurement technique and thus velocity information in the entire measurement space is captured simultaneously. The technique is non-intrusive. The resolution limits of digital PIV depend on the camera optical properties, the tracer size and the window-correlation method (Kähler et al., 2012a). Modern hardware can reach measurement resolutions comparable to the average Kolmgorov length scale, if operated with small field of view (Khan et al., 2004). The Eulerian data, in the form of a map of many velocity vectors, can be post-processed in numerous ways to provide different information about fluid mixing in stirred vessels. Typical investigated quantities include the impeller flow number (Khan et al., 2004; Simmons et al., 2007; Chung et al., 2009; Gabriele et al., 2009; Story et al., 2018), the turbulent kinetic energy (Khan et al., 2004, 2006; Chung et al., 2007, 2009; Gabriele et al., 2009, 2011; Driss et al., 2014; Li et al., 2018a, 2018b; Taghavi and Moghaddas, 2019), the energy dissipation rate (Piirto et al., 2000; Saarenrinne and Piirto, 2000; Saarenrinne et al., 2001; Baldi and Yianneskis, 2003, 2004; Tanaka and Eaton, 2007; Gabriele et al., 2009; Delafosse et al., 2011) and vorticity and related invariants for trailing vortices identification (Baldi and Yianneskis, 2003; Escudié et al., 2004; Khan et al., 2004; Chung et al., 2009; Gabriele et al., 2009; Zhao et al., 2011; Chara et al., 2016). Finally, the structure of PIV data is ideal for the application of proper orthogonal decomposition (POD). This method enables the contributions of turbulence and organized motion to be discriminated (Graftieaux et al., 2001; Gabelle et al., 2013).

The main limitation of PIV is that, in its typical 2D arrangement, the velocity component normal to the measurement plane cannot be determined. Since the flow governing equations are inherently 3D, simplifying assumptions must be adopted to work around the unavailability

of the third component. For instance, most of the works cited above used the isotropic assumption to calculate the turbulent kinetic energy as $k \approx {}^{3}/_{4}\left(\overline{u'^2} + \overline{v'^2}\right)$, where u' and v' are the two available velocity fluctuations. 3D-PIV rigs would eliminate the problem, but these are particularly expensive because of the additional hardware required. These costs would add to those associated to laser facilities, which may already be prohibitive for industrial R&D sectors. Also, the velocity is obtained through cross-correlation within the IAs and this introduces a spatial averaging effect. This influences the accuracy of the spatial derivatives, which are often the most interesting output of a PIV experiment. Finally, PIV can only be conducted in transparent fluids.

II.2.3. Planar Laser Induced Fluorescence (PLIF)

PLIF is a non-intrusive, laser-based optical technique, which can be used to obtain the concentration maps of a dye as a function of time. The setup is similar to that of PIV. The fluid under investigation is doped with a fluorescent dye and a section of the flow is illuminated by a laser sheet. The dye is excited by the laser and re-emits photons at a lower frequency. A typical PLIF experiment involves the use of a Nd-YAG laser, which emits at 532 nm wavelength (green), and rhodamine dye, which re-emits at 550 – 560 nm (yellow). A camera positioned perpendicularly to the laser sheet records a sequence of images of the flow. For each image, the concentration distribution of the dye can be determined through image analysis, because a monotonic relationship exists between the pixel levels and the local dye concentration. This enables the visualisation of the flow patterns (Arratia et al., 2006), the study of segregation and mixing effectiveness through the methods of coefficient of variance (CoV) or striation thickness (Kukukova et al., 2011) and the quantification of mixing time (Chung et al., 2007; Simmons et al., 2007). Alberini et al. (2014a) have developed an alternative method, based on the analysis of striations characterised by the same level of mixing, that provides more

consistent measures of mixing performance than either CoV or maximum striation thickness alone. The same group of authors has also proposed a method for evaluating the local mixedness based on the normalised area and perimeter of well-mixed striations (Alberini et al., 2014b). Poor or good mixing conditions correspond to small or large areas and perimeters. This information can be used, for instance, to optimize the fluid sampling point location in mixing devices (Stamatopoulos et al., 2016). Finally, reactive-PLIF is a version of PLIF in which a reagent is employed to oxidise the dye and quench the fluorescent signal. It can be used to investigate the effects of mixing on fast chemical reactions conducted in stirred vessels (Hu et al., 2010, 2012; Taghavi and Moghaddas, 2019).

II.2.4. Positron Emission Particle Tracking (PEPT)

In PEPT, a tracer is labelled with a radioactive nuclide which decays by positive beta decay, whereby a proton is converted to a neutron by the emission of a positron and a neutrino (Parker, 2017). After travelling a short distance, the positron annihilates with a nearby electron. This results in the emission of two back-to-back 511 keV photons, which are collected by gamma detectors (Parker, 2017). Only coincidence events – typically within a few nanoseconds (Windows-Yule et al., 2020b) are recorded, and the line of response (LoR) of the decay is determined (***Figure II-8***). In principle, the triangulation of two lines of response is enough to estimate the 3D position of the tracer. In practice, a larger number of events (typically 50 – 100) at high temporal resolution are used to determine each location (Windows-Yule et al., 2020b). This is because the measurements always contain a fraction of spurious events (Parker, 2017), as schematised in ***Figure II-9***. Tracking rate and precision depends on the tracer activity and the amount of material which the photons have to traverse to reach the detector (Govender et al., 2011). Today, the tracer can be located with a precision of less than 1 mm every millisecond (Windows-Yule et al., 2020a, 2020b). In a well-mixed flow, the time average of

the behaviour of a single tracer moving through a system of identical tracers can be assumed to be representative of the ensemble-averaged behaviour of all tracers within the system, provided that the average is taken over a period long enough to allow the particle to explore the entire system (Windows-Yule et al., 2020b). Such flows are called ergodic. The technique may also be performed with multiple tracers (Rosato and Windows-Yule, 2020).

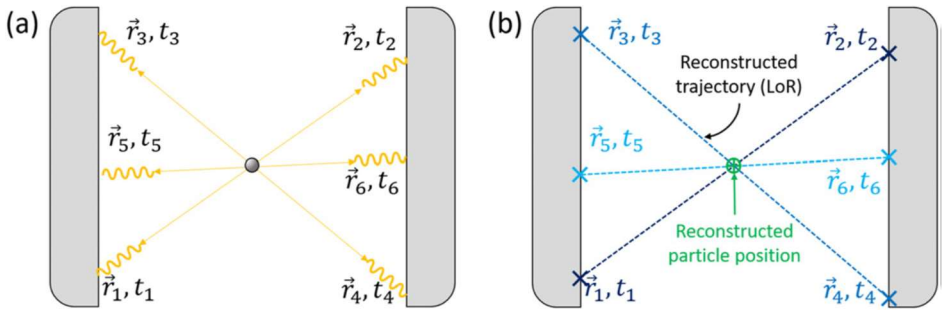

***Figure II-8**: Schematic diagrams illustrating (a) the emission and detection of multiple pairs of photons and (b) the reconstruction of their LoR, from which the particle position may be obtained. Image from Windows-Yule et al. (2022).*

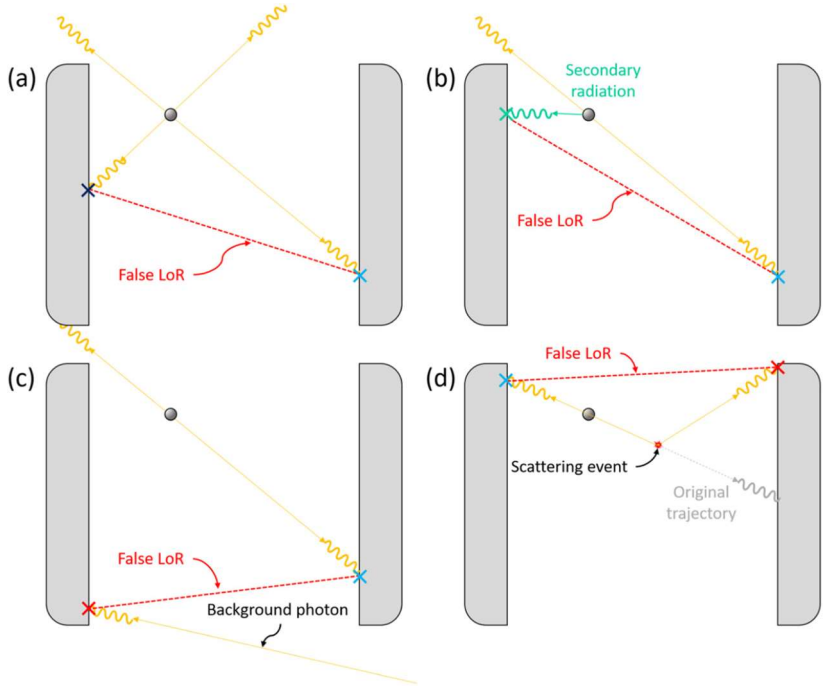

***Figure II-9**: False coincidence events which may occur during PEPT imaging. Image from Windows-Yule et al. (2022).*

II.2.5. Computer Automated Radioactive Particle Tracking (CARPT)

Unlike PEPT, CARPT deploys a strategically-placed array of scintillation detectors to measure the relative intensity of gamma radiation at different points, from which it is possible to determine the tracer's position (Rosato and Windows-Yule, 2020). In the absence of attenuation, the count rate would decrease with the square of the distance (Parker, 2017). In real systems, this relationship must be corrected to account for the attenuation of the materials and the finite size of the detectors (Parker, 2017; Rosato and Windows-Yule, 2020). As a consequence, with every new system to be studied, a laborious trial and error experimental procedure has to be undergone before a good experimental run can be implemented (Roy et al., 2002). Similarly to PEPT, only a limited number of tracers can be traced simultaneously (Rosato and Windows-Yule, 2020).

PEPT and CARPT allow investigations in opaque dense fluids and multiphase systems. Lagrangian data obtained through PEPT and CARP measurements in agitated vessels can be post-processed to provide useful information regarding fluid mixing, such as flow patterns, identification of dead zones in the vessel and residence time distributions. Eulerian information can be also inferred through interpolation or binning of the Lagrangian data, under the assumptions of ergodicity and statistical steadiness of the flow (Fangary et al., 2000, 2002; Rammohan et al., 2001, 2003; Chiti et al., 2011; Govender et al., 2011; Pérez-Mohedano et al., 2015).

II.2.6. 3D Particle Tracking Velocimetry (3D-PTV)

3D-PTV is a whole field technique which enables all three dimensions of the Lagrangian velocity field to be obtained with relatively simple hardware. The technique is based on the visualization of the measurement space from multiple viewing orientations through a

stereoscopic imaging system. The flow is seeded with small tracers, which are tracked individually in 3D space. This requires reliable tracer identification in the images, stereoscopic matching in multiple image planes, 3D coordinate reconstruction and frame-to-frame linking of each tracer (Maas et al., 1993). Particle size can vary in the range from ~10 µm to ~10^3 µm. The choice is a compromise between an adequate response to the variations of the flow and a high signal-to-noise ratio of the scattered light (Melling, 1997; Hadad and Gurka, 2013). LED lights are typically sufficient for the illumination of tracers larger than ~200 µm. This obviates the need for expensive and hazardous laser illumination. Single camera setups with image splitters cut the costs even further, at the expense of a reduction in spatial resolution and accuracy. In the early 90's, image quality was poor because of the technical limits of camera sensors (Kähler et al., 2012a); correlation-based techniques, such as PIV, were preferred because they could tolerate the high noise levels in the images. Today, high-quality images and advances in digital image analysis algorithms allow particle centroids to be calculated with subpixel precision. For all these reasons, 3D-PTV is becoming increasingly attractive, particularly in industrial R&D sectors, where lab-scale experiments with model fluids are routinely carried out before expensive tests at the pilot and production scales.

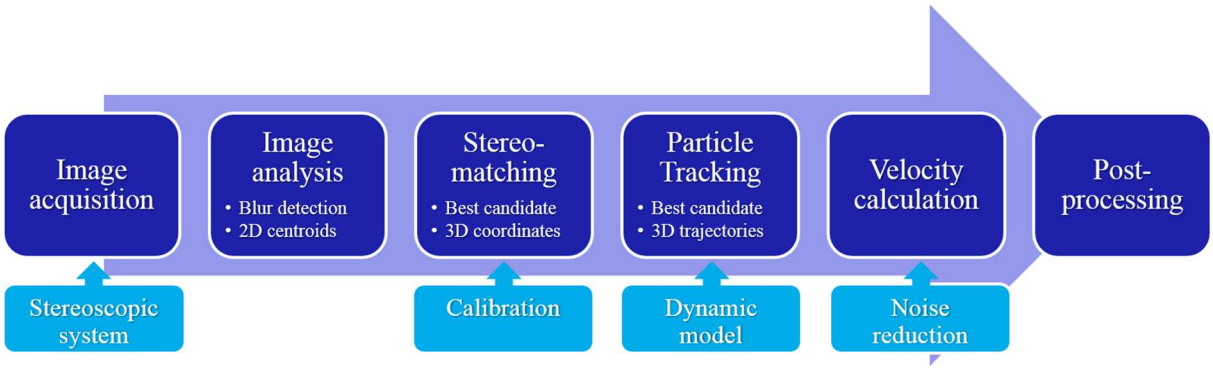

***Figure II-10**: Data flow in PTV measurements.*

The stereo-matching step is the establishment of the correspondences between the same particle in the different image planes. In absence of other characteristic features, the correspondences

are found with the method of the epipolar lines (Maas et al., 1993). The method is explained in **§A.1.3** and requires the spatial calibration of each image plane (Maas et al., 1993). Usually, 3 or 4 viewing orientations are used in 3D-PTV, in order to minimize the ambiguities at the stereo-matching stage (Willneff and Gruen, 2002). Bendicks et al. (2011) have utilized dyes to classify particles based on their colour prior to 3D localization. The effect was to reduce the apparent tracer concentration, hence the ambiguities, while increasing the overall data yield. Aguirre-Pablo et al. (2019) have developed a method for single view 3D-PTV measurements which exploits structured illumination with an intensity profile in space.

The tracers must also be linked between consecutive time steps to reconstruct their trajectories. The principles of frame-to-frame tracking are: (i) to estimate the position of the particle in the next frame via a dynamic model, (ii) to delimit a search volume around the expected location and (iii) to determine the most likely link, in case of multiple candidates, based on a physical criterion. The goal is to reconstruct as many trajectories for as long as possible. The particle spacing displacement ratio (Malik et al., 1993),

$$p = \frac{d}{\Delta l} = \frac{d}{U\,\Delta t}, \qquad \textit{Eq. II-14}$$

is a measure of the tracking difficulty. Here d is the particle spacing, which decreases with the cubic root of the tracer concentration, Δl is the distance moved by the particles between two consecutive time steps, U is the velocity and Δt is the time between two frames. Tracking is relatively easy for $p \gg 1$ and difficult for $p \ll 1$. The nearest neighbour (Malik et al. 1993), the neural network (Labonté, 1999, 2000) and the relaxation (Baek and Lee, 1996) methods are three commonly used tracking algorithms. Pereira et al. (2006) compared these three schemes in terms of recovery ratio (correct links found to actual links) and mismatch ratio (incorrect links to total links found) and found that the relaxation scheme had the best performance. Willneff (2003) has developed a multi-frame matching algorithm which

combines the temporal and spatial information to increase the recovery ratio. Instead of establishing the spatial and temporal correspondences separately, this method exploits the redundant information in time, image and object space to link particle positions even when stereoscopic or temporal ambiguities occur. This allows gaps in the particle trajectories to be bridged and substantially longer trajectories to be obtained.

While the representativeness of a PTV experiment depends on the absolute number of established links, the quality of PTV results decreases rapidly with the tracer concentration (Cierpka et al., 2013), because of the increment in stereoscopic ambiguities, wrong temporal links and overlapping particle images. The number of indistinguishable particles in an image increases approximately with the square of the tracer concentration and linearly with their image size (Maas, 1992). On the other hand, the particle concentration will determine the number of velocity vectors obtained per volume. Therefore, this variable must be chosen carefully.

The 3D velocity vectors are computed through finite differentiation of the particle coordinates varying in time. The frame rate, f (s^{-1}), represents the temporal resolution of the data, meaning that a larger f allows higher velocities and smaller length scales to be described. On the other hand, for a given camera system, the experimental error in the coordinates is amplified by a factor $\Delta t^{-1} = f$ if the velocities are calculated by common finite differentiation schemes, such as the centred differences. This assumes that the error is not autocorrelated between consecutive data points, hence it does not cancel out. Therefore, the frame rate is another critical variable for the measurements quality.

An important limitation of PTV is that, due to sparsity and random location of the velocity vectors, the analysis of the instantaneous velocity field becomes difficult, and interpolation or binning are necessary for the estimation of the spatial derivatives (Kähler et al., 2012b). Flow ergodicity and statistical steadiness must be assumed in order to infer Eulerian information

from Lagrangian data (Alberini et al., 2017). Another difficulty with PTV experiments is that the observation volume that can be effectively investigated is limited by the precision in the tracer identification. The most important factors affecting the precision are the fluid opacity and the camera specifications and settings, e.g. the digital resolution and depth of field. Large differences in the optical path lengths lead to large variations in the tracer image size, due to perspective effects, and in the scattered light intensity, due to attenuation according to the Beer-Lambert law.

In the literature, 3D-PTV measurements have been carried out to study many applications. These include turbulence (Lüthi et al., 2005; Liberzon et al., 2012), impinging jets (Hwang et al., 2007), pipe flows (Oliveira et al., 2015), flows in a lid-driven cavity (Kreizer et al., 2010; Kreizer and Liberzon, 2011), aortic flows (Gülan et al., 2012; Gallo et al., 2014), Couette flows (Krug et al., 2012), gravity currents in tilted tanks (Krug et al., 2014), von Kármán swirling flows (Aguirre-Pablo et al., 2019), flows behind a heated cylinder (Kieft et al., 2002) and flows through porous media (Monica et al., 2009). However, there is a great lack of research studies in which 3D-PTV is applied to fluid mixing in agitated vessels (Alberini et al., 2017), mainly because the large volumes and wide range of velocities involved represent a big challenge.

II.3. Numerical simulations of flows in agitated vessels

Computational Fluid Dynamics (CFD) is a body of knowledge and techniques for simulating fluid flows. The flow governing equations are discretised on a computational grid and solved with a computer, which performs the large amount of calculations in a reasonable time.

CFD was firstly applied in the aerospace and automotive industry, triggered by the development of modern computers. Later, its use spread to many other engineering

applications, including industrial mixing, chemical reactions, process safety etc. Today, computational power is increasing at accelerating pace, roughly one order of magnitude of FLOPS every 5 years (Bartels et al., 2002; Roser and Ritchie, 2013), while becoming less and less expensive. This forecasts an increasingly important role of CFD in engineering research.

CFD modelling of agitated vessels has some significant advantages compared to experimental measurements:

- Accurate measurements of certain quantities, e.g. shear rate, energy dissipation rate and phase dispersion, may be unfeasible or too expensive. Numerical simulations can provide this information at high spatial and temporal resolutions.
- The effects of relevant variables can be isolated easily. For instance, the fluid rheological parameters can be changed one at a time.
- Opaque systems, large industrial installations and hazardous conditions can be studied.

However, numerical simulations always represent a reasonable compromise between accuracy and associated computational cost. Therefore, calibration of the models and validation of the results against experimental data are necessary. In general, published simulations of stirred vessels tend to predict the mean flow reasonably well but under- or over-predict the turbulent effects (Aubin et al., 2004; Gillissen and Van den Akker, 2012; Zhang et al., 2017).

As already stated in **§II.1.5**, simulations of transitional flows is stirred vessels remain challenging, because common turbulence models are designed for high Reynolds numbers (Mendoza et al., 2018) and the resolution of low-frequency macro-instabilities would require unfeasibly long simulated time (Lane, 2017).

II.3.1. Turbulence modelling approach

In stirred tanks, instantaneous quantities can be Reynolds-averaged (Reynolds, 1895) over realisations at the same impeller phase φ, i.e

$$\phi(\mathbf{r},t) = \bar{\phi}\big(\mathbf{r},\varphi(t)\big) + \phi'(\mathbf{r},t) = \langle\phi\rangle(\mathbf{r}) + \phi_{\varphi}\big(\mathbf{r},\varphi(t)\big) + \phi'(\mathbf{r},t). \qquad \textit{Eq. II-15}$$

Here $\mathbf{r}$ is the position vector and t is time, $\bar{\phi}$ is the Reynolds-average and $\langle\phi\rangle$ is its phase-average. The triple decomposition allows the turbulent random fluctuations, ϕ', to be discriminated from the periodic variations, ϕ_{φ}, caused by the impeller passage (*pseudo-turbulence*).

CFD techniques are classified into Direct Numerical Simulation (DNS), Large Eddy Simulation (LES) or Reynolds-Averaged Navier-Stokes (RANS) simulation, according to how the random fluctuations are handled (***Figure II-11***).

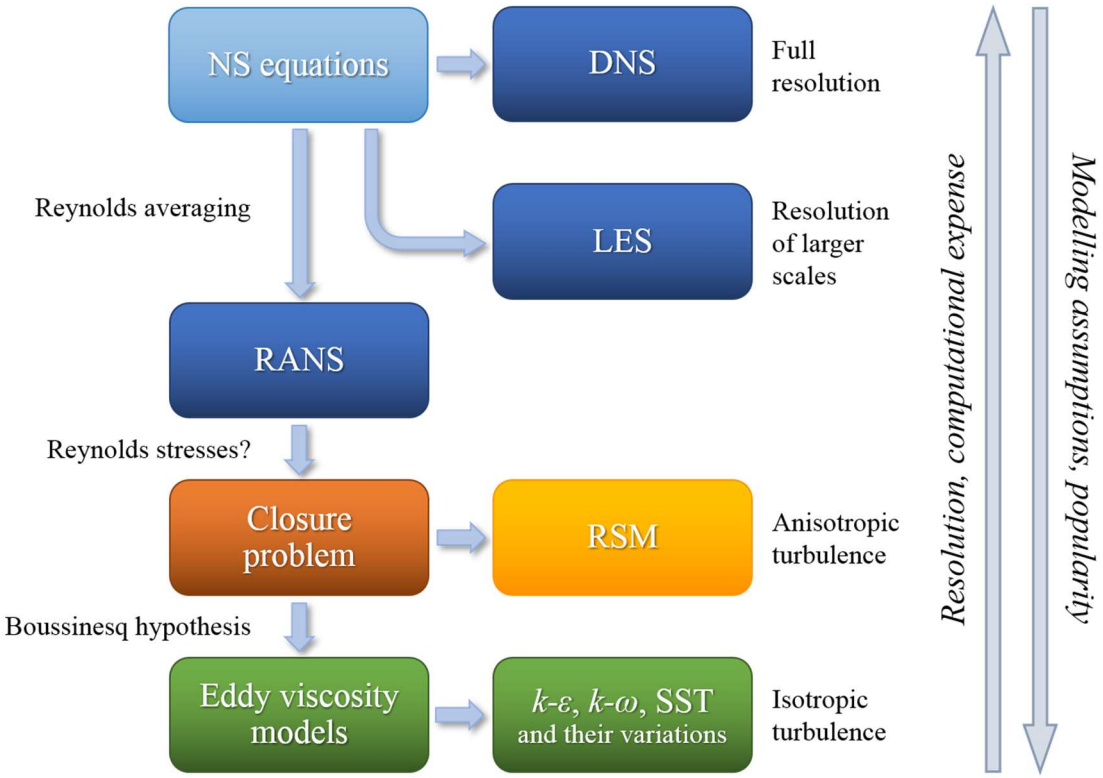

Figure II-11*: Scheme of the turbulence modelling approaches used in CFD.*

II.3.1.1. DNS

DNS solves the conservation of mass and momentum in terms of instantaneous quantities, without the need for a simplifying turbulence model. In an incompressible flow,

$$\nabla \cdot \mathbf{u} = 0, \qquad \textit{Eq. II-16}$$

$$\frac{\partial \mathbf{u}}{\partial t} = \nabla \cdot \left(-\mathbf{u}\mathbf{u} - \frac{p}{\rho}\mathbf{I} + 2\nu\mathbf{S} \right) + \mathbf{g}. \qquad \textit{Eq. II-17}$$

Here $\mathbf{u}$ is the velocity (m s^{-1}) and $\mathbf{g}$ represents the body forces per unit mass (m s^{-2}). In order to resolve the whole spectrum of flow scales, the grid must be smaller than the dissipative scales.

A DNS is initialised by superimposing the mean velocity field and some random noise, which triggers the turbulent evolution of the flow. Even if no perturbations are initialised by the user, truncation and round-off errors in the computed solution act as numerical noise and eventually trigger chaotic behaviour (Tamburini et al., 2018). Boundary conditions also require the fluctuations to be specified. Due to the lack of accurate knowledge of turbulence a priori, the flow becomes independent of initial and boundary conditions only after simulating a long time and outside the development region near the boundary. This represents a significant share of a DNS computational expense. For example, starting from quiescent conditions, a stirred tank flow simulation requires approximately 100 impeller revolutions to develop to a statistically steady state (Gillissen and Van den Akker, 2012). If the DNS are initialised with a LES solution, this transient can be reduced to 20 – 60 impeller revolutions (Verzicco et al., 2004; Gillissen and Van den Akker, 2012; Başbuğ et al., 2017).

DNS is a powerful research tool. Controlled studies can provide useful insights about turbulence statistics and help develop new models (Joshi et al., 2011), while simulations of real-life flows can potentially replace experimental data for RANS and LES validation (Gillissen and Van den Akker, 2012). However, DNS of agitated vessels operated at

industrially relevant conditions has a prohibitive computational cost. Since the ratio of the macroscopic to dissipative length scales increases as $\sim Re^{3/4}$, the required number of grid cells is proportional to $\sim Re^{9/4}$. In addition, the macro-to-micro temporal scale ratio increases as $\sim Re^{1/2}$. Therefore, the cost of a DNS is proportional to $\sim Re^{11/4}$. This limits DNS to low Re operations ($Re \leq \sim 10^3$). To date, only a few authors have run DNS of stirred tanks (Bartels et al., 2002; Sbrizzai et al., 2006; Gillissen and Van den Akker, 2012; Başbuğ et al., 2017; Tamburini et al., 2018).

II.3.1.2. RANS

The RANS approach is the most widespread method for simulating turbulent fluid mixing (Coroneo et al., 2011). The equations for the mean flow are obtained by Reynolds-averaging all terms in the mass and momentum equations:

$$\nabla \cdot \bar{\mathbf{u}} = 0, \qquad \textit{Eq. II-18}$$

$$\frac{\partial \bar{\mathbf{u}}}{\partial t} = \nabla \cdot \left(-\bar{\mathbf{u}}\,\bar{\mathbf{u}} - \frac{\bar{p}}{\rho}\mathbf{I} + 2\nu\bar{\mathbf{S}} + \mathbf{R} \right) + \bar{\mathbf{g}}, \qquad \textit{Eq. II-19}$$

$$\bar{\mathbf{S}} \equiv \frac{1}{2}(\nabla\bar{\mathbf{u}} + \nabla\bar{\mathbf{u}}^T), \qquad \textit{Eq. II-20}$$

$$\mathbf{R} \equiv -\overline{\mathbf{u}\mathbf{u}} + \bar{\mathbf{u}}\,\bar{\mathbf{u}} = -\overline{\mathbf{u}'\mathbf{u}'}. \qquad \textit{Eq. II-21}$$

RANS equations keep the same mathematical form of the original equations, except for the additional term **R**, called the Reynolds stress tensor. This represents the effects of turbulence on the mean flow and introduces six new unknowns. Therefore, the Reynolds stresses must be modelled to obtain a complete set of equations. Many RANS closure models have been developed, each one with intrinsic benefits and limitations. Only those widely used in stirred tank simulations are described below.

The family of eddy viscosity models assumes that the deviatoric part of the Reynolds stress tensor is proportional to the average strain rate $\bar{\mathbf{S}}$ (*Boussinesq's hypothesis*):

$$\mathbf{B} \equiv \mathbf{R} + \frac{2}{3}k\mathbf{I} = 2\nu_T\bar{\mathbf{S}}, \qquad \textit{Eq. II-22}$$

$$k \equiv \frac{1}{2}\overline{u_i'u_i'}. \qquad \textit{Eq. II-23}$$

With this approach, the Reynolds tensor is defined up to two new unknowns. The first is called the eddy viscosity, ν_T ($m^2\ s^{-1}$), by analogy with the fluid constitutive equation. The second is the turbulent kinetic energy, k (energy per unit mass, $m^2\ s^{-2}$). Boussinesq's hypothesis has two major consequences. Firstly, the assumption of scalar ν_T means that the ratio between the Reynolds stresses and the mean deformation rates is uniform in all directions, hence $\mathbf{B}$ and $\bar{\mathbf{S}}$ are aligned. Gillissen and Van den Akker, (2012) averaged DNS data of a stirred tank flow and found that this assumption was acceptable in the impeller discharge stream, but questionable in the bulk. Secondly, only the isotropic contribution of turbulence (k) will appear in the momentum equation, while any information about turbulence anisotropy ($\mathbf{B}$) is modelled in terms of the mean flow and is lost. Experimental evidence and numerical studies indicate that turbulence in agitated vessels is anisotropic (Derksen et al., 1999; Galletti et al., 2004b; Yeoh et al., 2004; Ducci and Yianneskis, 2005; Escudié and Liné, 2006; Haque et al., 2011; Zamiri and Chung, 2018).

The standard k-ε model (Launder and Spalding, 1974) is the most established closure model for engineering applications. It has been widely used for modelling high Reynolds flows in stirred tanks (Deglon and Meyer, 2006). The eddy viscosity is calculated as

$$\nu_T = C_\mu \frac{k^2}{\varepsilon}, \qquad \textit{Eq. II-24}$$

where

$$\varepsilon \equiv 2\nu\,\overline{\mathbf{S}':\mathbf{S}'} = \nu\,\overline{\left(\frac{\partial u_i'}{\partial x_j}+\frac{\partial u_j'}{\partial x_i}\right)\frac{\partial u_i'}{\partial x_j}} \qquad \textit{Eq. II-25}$$

is the turbulent energy dissipation rate (power per unit mass, $m^2\,s^{-3}$). Both k and ε are evaluated through dedicated transport equations:

$$\frac{\partial k}{\partial t} = \nabla\cdot\left(-k\bar{\mathbf{u}}+\left(\nu+\frac{\nu_T}{\sigma_k}\right)\nabla k\right)+2\nu_T\bar{\mathbf{S}}:\bar{\mathbf{S}}-\varepsilon; \qquad \textit{Eq. II-26}$$

$$\frac{\partial \varepsilon}{\partial t} = \nabla\cdot\left(-\varepsilon\bar{\mathbf{u}}+\left(\nu+\frac{\nu_T}{\sigma_\varepsilon}\right)\nabla\varepsilon\right)+2C_{\varepsilon1}\nu_T\bar{\mathbf{S}}:\bar{\mathbf{S}}-C_{\varepsilon2}\frac{\varepsilon^2}{k}. \qquad \textit{Eq. II-27}$$

The constants are determined experimentally, depending on the flow. The default values are $C_\mu = 0.09$, $\sigma_k = 1.0$, $\sigma_\varepsilon = 1.3$, $C_{\varepsilon1} = 1.44$ and $C_{\varepsilon2} = 1.92$. Many authors report that, in stirred tank simulations, the standard k-ε model can accurately predict the mean velocity, but not k, ε and the derived quantities, such as the power number (Bartels et al., 2000; Alexopoulos et al., 2002; Bartels et al., 2002; Aubin et al., 2004; Murthy and Joshi, 2008; Singh et al., 2011). This is generally attributed to the isotropic assumption and to the model insensitivity to flow rotation. Some variants derived from the standard k-ε, e.g. the Renormalisation Group (RNG) k-ε (Yakhot and Orszag, 1986) and the Realisable k-ε (Shih et al., 1995) models, provide only marginally better or even worse predictions (Ranade et al., 2001; Aubin et al., 2004; Chtourou et al., 2011). Another limitation of the k-ε models is their inaccuracy at low Reynolds numbers and in the wall viscous layer (Menter, 2009).

In the aeronautics community of the 90's, the most popular alternative to the k-ε was the k-ω model (Wilcox, 1988). The equation for ε is replaced by an equation for $\omega = \varepsilon/(C_\mu k)$, that is the specific rate of energy dissipation (frequency, s^{-1}):

$$\nu_T = \frac{k}{\omega}, \qquad \textit{Eq. II-28}$$

$$\frac{\partial k}{\partial t} = \nabla \cdot \left(-k\bar{\mathbf{u}} + \left(\nu + \frac{\nu_T}{\sigma_k} \right) \nabla k \right) + 2\nu_T \bar{\mathbf{S}} : \bar{\mathbf{S}} - \beta^* k\omega, \qquad \textit{Eq. II-29}$$

$$\frac{\partial \omega}{\partial t} = \nabla \cdot \left(-\omega\bar{\mathbf{u}} + \left(\nu + \frac{\nu_T}{\sigma_\omega} \right) \nabla \omega \right) + 2\alpha \frac{\omega}{k} \bar{\mathbf{S}} : \bar{\mathbf{S}} - \beta\omega^2. \qquad \textit{Eq. II-30}$$

This model works well in the wall layer. However, it is extremely sensitive to the freestream value specified for ω. It can be verified that *Eq. II-27* and *Eq. II-30* only differ for the so-called *cross-diffusion* term, proportional to $(\nabla k \cdot \nabla \omega)/\omega$, appearing in the k-ε model only (till successive revisions of the k-ω, see Wilcox, 2008). Therefore, the k-ε model can be converted into the k-ω, and vice versa, by simply switching on/off this term. The shear stress transport (SST) model (Menter, 1994) combines the robustness of k-ε model in the bulk with the near-wall accuracy of k-ω by using a blending function for the cross-diffusion term and the model constants. Also, a numeric limiter bounds the turbulence production in stagnation regions, providing better accuracy in case of flow separation. Successive enhancements include the streamline curvature correction, SST-CC (Smirnov and Menter, 2009), changes in the ω equation (Menter, 2009) and the possibility to run the simulation in scale adaptive mode, SST-SAS (Menter and Egorov, 2005). In SST-SAS, the resolution of flow structures is adjusted dynamically, resulting in LES-like behaviour in the unsteady flow regions, e.g. the impeller stream (Singh *et al.*, 2011; Zamiri and Chung, 2018). This comes at the price of a larger computational expense – about 20 times higher than the standard k-ε and SST models (Singh et al., 2011). In some cases, the SST models have been proved superior to k-ε for stirred vessels simulations (Singh et al., 2011; Xiao et al., 2014; Lane, 2017; Tamburini et al., 2021).

In general, all two-equation eddy viscosity models assume that the effects of turbulence on the mean flow can be modelled based on two transport equations. Whilst the k equation is exact,

the second equation, for ε or ω, is based on dimensional and intuitive arguments and is considered the weak link of two-equation RANS models.

In the Reynolds Stress Model (RSM), originally proposed by Hanjalić and Launder (1972), seven transport equations are solved to close the momentum problem, six for the components of **R** and one for ε. For the Reynolds stresses, the equation has the general form

$$\frac{\partial \overline{u_i' u_j'}}{\partial t} = C_{ij} + D_{ij} + \varepsilon_{ij} + R_{ij} + S_{ij}. \qquad \textit{Eq. II-31}$$

The terms on the right-hand side represent convection, diffusion, dissipation, redistribution and an optional user-defined source. The terms D_{ij}, ε_{ij} and R_{ij} are modelled. The Boussinesq hypothesis is avoided, and the model resolves the directionality of Reynolds stresses. However, the weakness of ε transport equation remains. For this reason, the RSM not always yields better results compared to simpler models (Haque et al., 2011; Singh et al., 2011; Tamburini et al., 2021), and the larger computational cost might be unjustified. Furthermore, the RSM suffers convergence issues (Aubin et al., 2004; Lane, 2017).

II.3.1.3. LES

In LES, the contribution of the large anisotropic eddies to momentum transfer is computed explicitly, while the effect of the isotropic small scales is modelled. This represents a compromise between DNS resolutions and RANS affordability. The large scales are separated from the smaller ones by applying a low-pass grid filter to the governing equations:

$$\nabla \cdot \tilde{\mathbf{u}} = 0, \qquad \textit{Eq. II-32}$$

$$\frac{\partial \tilde{\mathbf{u}}}{\partial t} = \nabla \cdot \left(-\tilde{\mathbf{u}}\,\tilde{\mathbf{u}} - \frac{\tilde{p}}{\rho}\mathbf{I} + 2\nu\tilde{\mathbf{S}} + \mathbf{G} \right) + \tilde{\mathbf{g}}, \qquad \textit{Eq. II-33}$$

The subgrid stress tensor, $\mathbf{G}$, represents the effect of the subgrid flow on the large-scale flow. In the standard Smagorinsky model (Smagorinsky, 1963),

$$\mathbf{G} - \frac{2}{3}k_{SG}\mathbf{I} = 2\nu_{SG}\tilde{\mathbf{S}}, \qquad \textit{Eq. II-34}$$

$$k_{SG} \equiv \frac{1}{2}(\widetilde{u_\iota u_\iota} - \tilde{u}_\iota \tilde{u}_\iota) = \left(\frac{\nu_{SG}}{C_K \Delta}\right)^2. \qquad \textit{Eq. II-35}$$

$$\nu_{SG} = {C_S}^2 \Delta^2 \sqrt{2\tilde{\mathbf{S}}:\tilde{\mathbf{S}}}. \qquad \textit{Eq. II-36}$$

The scalar ν_{SG} is analogous to the eddy viscosity in RANS, while the grid size Δ is chosen so that the corresponding wavenumber lies in the inertial subrange of the turbulence energy spectrum. The constants are typically $C_S = 0.1$ and $C_K = 0.094$. In more advanced models, k_{SG} is calculated through a dedicated transport equation.

LES of stirred tanks provides better quantitative predictions of turbulence quantities than RANS (Yeoh et al., 2004; Alcamo et al., 2005; Delafosse et al., 2008, 2009; Zadghaffari et al., 2010; Kysela et al., 2017). However, it remains unpractical in industrial environments with limited computational budgets. In fact, a characteristic weakness of LES is that turbulence is not appropriately resolved in the boundary layers unless extremely fine grids are used. For example, Gillissen and Van den Akker (2012) observed that k and ε were underpredicted in the volume swept by a Rushton impeller, due to under-resolved velocity gradients, despite their LES was conducted in a mesh of 16.8 million CVs. This led to the development of hybrid models called Detached Eddy Simulations (DES), in which LES and RANS are performed in the bulk flow and in the boundary layer, respectively. DES of agitated vessels provides better predictions than RANS, without the excessive resolution requirements of LES at the wall (Singh et al., 2011; Gimbun et al., 2012; Lane, 2017).

II.3.1.4. Laminar simulations

Laminar simulations solve the equations of motion in terms of instantaneous quantities. However, unlike DNS, turbulence initialisation is not required, and steady state mode can be selected for time-independent flows. Laminar simulations can accurately predict the hydrodynamics and power requirement of laminar flows in agitated vessels, even with complex fluid rheology (Anne-Archard et al., 2006; Xiao et al., 2014; Patel et al., 2015a; Cortada-Garcia et al., 2017). Some authors have used a laminar solver to simulate stirred tank operations in the low and mid transitional regime, up to a Reynolds number of a few hundred (Zalc et al., 2001; Kelly and Gigas, 2003; Ameur and Bouzit, 2012; Patel et al., 2015a; Mendoza et al., 2018). The agreement with experimental data worsens as the Reynolds number increases.

II.3.2. FVM grids and discretisation

The most used discretization method in engineering applications is the finite volume method (FVM). Other approaches, not discussed here, are the finite differences (FDM), finite element (FEM) and the Lattice-Boltzmann (LBM) methods.

In FVM, the domain is domain divided in a grid of many control volumes (CV). Each CV contains a computational node, in which the flow variables will be stored. The integral transport equation for the generic quantity ϕ is:

$$\iiint_{\mathrm{CV}} \frac{\partial}{\partial t}\rho\phi \, dV + \iint_{\mathrm{CS}} (\rho\phi\mathbf{u}) \cdot \mathbf{n} \, dA + \iint_{\mathrm{CS}} \left(-\Gamma_\phi \nabla\phi\right) \cdot \mathbf{n} \, dA - \iiint_{\mathrm{CV}} S_\phi \, dV = 0. \quad \textit{Eq. II-37}$$

Here CS stands for control surface, that is the boundary of the CV. The discretisation of the equations involves three levels of approximation:

i. *Differentiation*. Derivatives are approximated with finite differences.

ii. *Integration*. Surface and volume integrals are approximated in terms of the variable value at specific locations in the CV, namely the node and the CS faces.

iii. *Interpolation*. Face values are approximated in terms of neighbouring nodal values.

Therefore, the nodal value in the i-th CV is related to the values at many neighbouring nodes, i.e.

$$a_i \phi_i = \sum_{j \neq i} a_j \phi_j + b_i. \qquad \textit{Eq. II-38}$$

This set of algebraic equations is rearranged in the matrix form

$$[\mathrm{A}][\phi] = [\mathrm{b}] \qquad \textit{Eq. II-39}$$

and solved iteratively. The structure of the coefficient matrix [A] depends on the computational grid topology. In structured grids, each CV is uniquely identified by 2 (in 2D) or 3 (in 3D) indices and has exactly 4 or 6 neighbours. This produces poly-diagonal matrices and speeds up calculations. However, structured grids are limited to simple domains. Complex geometries must be split in sub-domains, which are meshed individually. In unstructured meshes, cells can have any shape, hence neighbour indexing is impossible. Polyhedral cells can have many neighbours (typically ~10), increasing the accuracy in gradients computation. However, unstructured meshes produce sparse matrices and lead to larger computational costs.

The characteristic mesh size, Δx, influences greatly the resolution and computational cost of a simulation. The appropriate grid size is determined by performing simulations on successively refined grids until no significant differences are observed in the relevant variables. In the literature, meshes used for RANS of agitated vessel flows typically range from ~10^4 to ~10^6 CVs (Deglon and Meyer, 2006), although Lane (2017) found that much finer grids were necessary to reach mesh-independence of the energy dissipation in a vessel operated at $Re = 75{,}000$ (***Table II-5***). LES and DNS require finer grids, depending on the Reynolds number.

***Table II-5**: Effect of the mesh size on the resolution of energy dissipation in a vessel operated at Re = 75,000, as simulated by Lane (2017). Even with extremely fine meshes, the energy dissipation was not completely mesh-independent.*

Configuration	Mesh size	Turbulence model	Total dissipation as % of expected power input
Full tank	3.2×10^6	k-ε	80%
Full tank	3.2×10^6	SST	68%
1 impeller blade, 1/2 tank	3.4×10^6	SST	73%
1 impeller blade, 1/2 tank	10.4×10^6	SST	84%
1 impeller blade, 1/2 tank	21.5×10^6	SST	81%
1 impeller blade, 1/3 tank	13.1×10^6	DES	69%

The overall accuracy of the spatial discretisation is determined by the least accurate of the approximation steps, which in practice is the face-value interpolation. The interpolation is said of n-th order if the truncation error, ϵ, scales as Δx^n. In first order schemes, ϵ is proportional to $\nabla\phi$ and resembles a diffusive flux (*numerical diffusion*). High order schemes are less sensitive to numerical diffusion, but they are computationally demanding and may suffer convergence issues. Some common interpolation schemes are listed in ***Table II-6***. The examples refer to the linear mesh illustrated in ***Figure II-12***. A few authors have investigated the impact of the discretisation scheme on the predicted flows in stirred tanks. In most cases, little effect was observed on the mean velocities, but a first order scheme exacerbated the errors in the turbulent scalars and power number (Aubin et al., 2004; Deglon and Meyer, 2006; Coroneo et al., 2011).

***Table II-6**: Common face-value interpolation schemes used in CFD.*

Scheme	Order	Equation (the λ's are weighting coefficients)	Notes
Upwind	1	$\phi_f = \phi_U$	Suitable for flows aligned to the grid and dominated by

			convection. Stable. Good for starting a simulation.
Linear interpolation (centred differences)	2	$\phi_f = \lambda\phi_U + (1-\lambda)\phi_D$	Good for flows dominated by diffusion.
Linear upwind	2	$\phi_f = \lambda_{UU}\phi_{UU} + \lambda_U\phi_U$	Good for full range of convection/diffusion ratios.
Quadratic upwind (e.g. QUICK)	3	$\phi_f = \lambda_{UU}\phi_{UU} + \lambda_U\phi_U + \lambda_D\phi_D$	Good for full range of convection/diffusion ratios. Mesh sensitive.

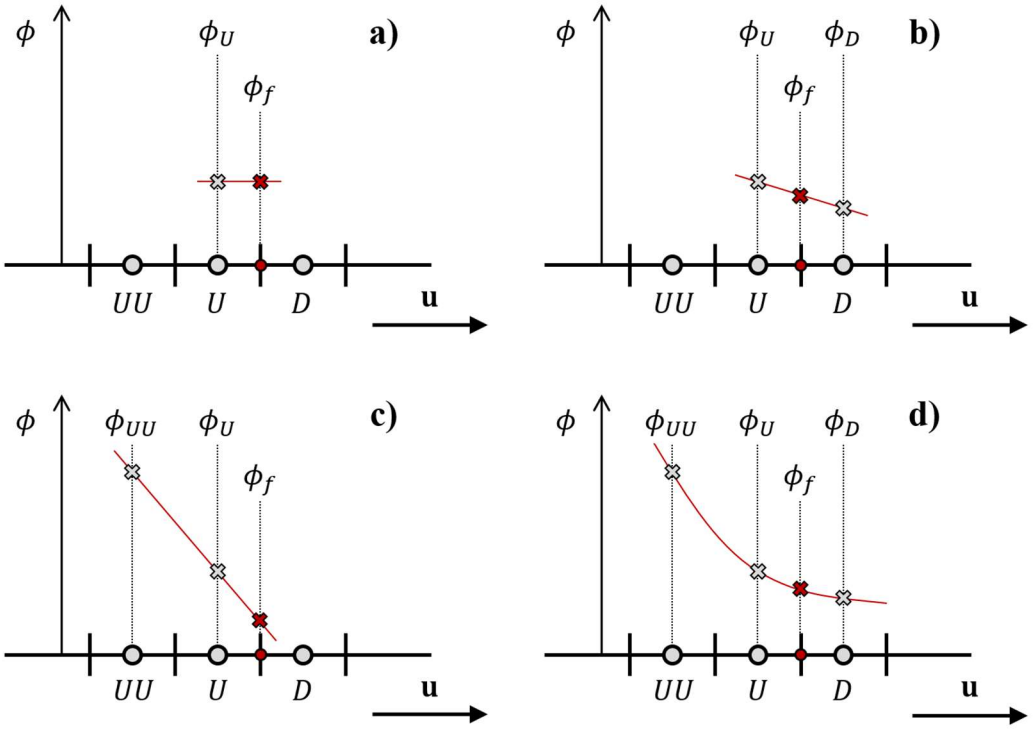

***Figure II-12**: Graphic representation of common face-value interpolation schemes used in CFD. (a) upwind; (b) linear interpolation; (c) linear upwind; (d) QUICK.*

II.3.3. Solver algorithm and convergence criteria

The system arising from *Eq. II-39* must be solved iteratively, because the momentum equations are not linear in the velocity and no transport equation for the pressure is available. The most used algorithm is the Semi-Implicit Method for Pressure Linked Equations (SIMPLE) by

Patankar and Spalding (1972), schematised in ***Figure II-13***. SIMPLE exploits a pressure-correction equation derived from the mass equation, since only the correct pressure field gives the correct velocity field. However, the pressure equation is approximated and suffers numerical instability. For this reason, under-relaxation factors are used to update the pressure and velocity gradually and facilitate convergence. Alternatives to SIMPLE are its revisions (e.g. SIMPLEC and SIMPLER) or the PISO (Issa, 1986).

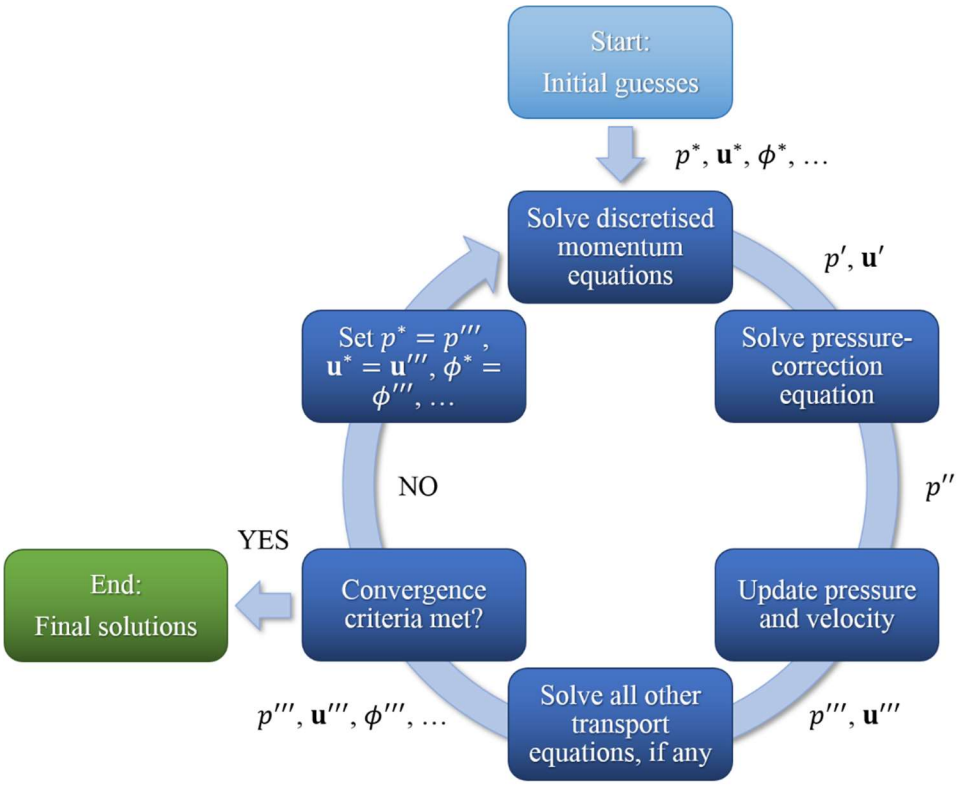

Figure II-13*: Structure of the SIMPLE algorithm.*

The equation residuals measure, in each CV, the local imbalance in the computed variable $\hat{\phi}$ after m iterations:

$$R_i(m) = a_i\hat{\phi}_i(m) - \sum_{j \neq i} a_j\hat{\phi}_j(m) - b_i. \qquad \textit{Eq. II-40}$$

The normalised sum of residuals is often used to monitor the solution convergence and decide when to stop the iterations. In stirred vessel simulations, normalised sums of ~10^{-4} or less are

typical (Aubin et al., 2004). Also, all physical quantities must reach independence from further iterations.

II.3.4. Boundary conditions

II.3.4.1. Solid walls

In real flows, the fluid velocity at solid walls equals the wall velocity (*no-slip condition*) and the flux of momentum through the wall is null. The thin fluid layer between the wall and the bulk is a complex region, characterised by strong gradients. Experiments and DNS show that the velocity profile in the boundary layer has a universal shape in terms of the normalised wall units. In ***Figure II-14***, y is the coordinate normal to the wall surface, u is the parallel component of the velocity and τ_w is the shear stress at the wall. In simulations of engineering flows, the near-wall model is of equal importance as the turbulence model (Menter, 2009). There are two possible approaches.

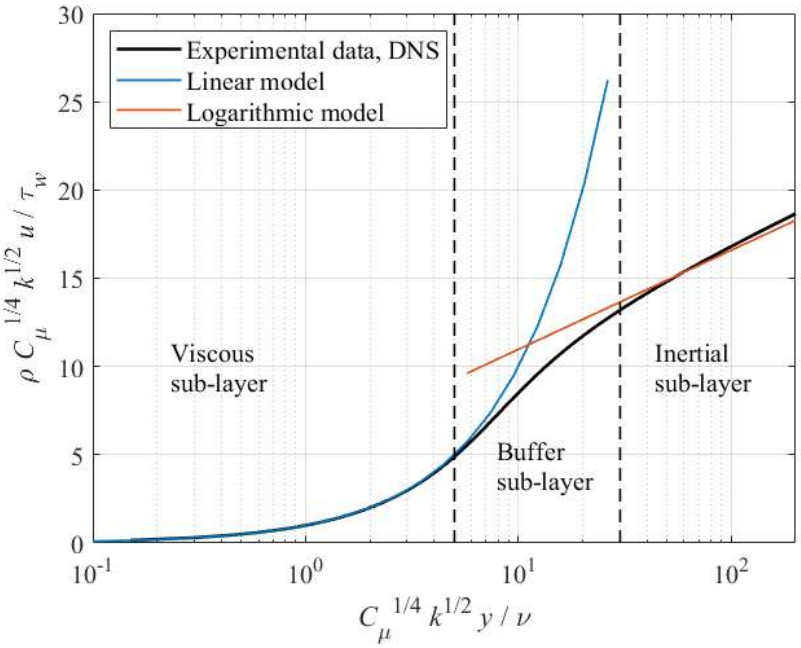

***Figure II-14**: Velocity profile of the near-wall layer.*

Integration of the transport equations through the boundary layer is referred to as *low-Reynolds approach* and requires extremely fine meshing ($y^*\sim1$, see definition below) to resolve all three sub-layers. The k-ω models are specifically designed for this method. Other models, such as k-ε, can also run in low-Reynolds mode, through damping functions that limit the production and dissipation effects of eddy viscosity. However, damping functions are generally inaccurate.

Conversely, the use of empirical correlations allows the velocity profiles to be modelled with much larger grids ($y^* > 30$). For example, the standard k-ε wall functions are based on the *law-of-the-wall* and the work of Launder and Spalding (1974):

$$U^* = \begin{cases} y^* & \text{for } 0 < y^* < 11.25, \\ \frac{1}{\kappa}\ln(Ey^*) & \text{for } 11.25 < y^* < 200. \end{cases} \qquad \textit{Eq. II-41}$$

$$y^* \equiv \frac{{C_\mu}^{1/4}{k_P}^{1/2}}{\nu} y_P, \qquad \textit{Eq. II-42}$$

$$U^* \equiv \frac{{C_\mu}^{1/4}{k_P}^{1/2}}{\tau_w/\rho} u_P. \qquad \textit{Eq. II-43}$$

The subscript P indicates a wall-adjacent cell, $\kappa = 0.418$ is the von Kármán constant and E is a roughness parameter ($E \approx 9$ for smooth surfaces). Since both the linear and logarithmic models are inaccurate in the buffer sub-layer, wall-adjacent cells in the range $5 < y^* < 30$ should be avoided. The following steps are carried out within each iteration of the solver algorithm and for each wall-adjacent cell:

i. u_P and k_P are available from previous iteration.

ii. y^* is calculated from *Eq. II-42*.

iii. $\tau_w/\rho \equiv \nu(\partial u/\partial y)_w$ is expressed as $\tau_w/\rho = \nu_w u_P/y_P$, where ν_w is a modified viscosity that ensures the correct stress even though $(\partial u/\partial y)_w \neq u_P/y_P$. If P is in the

linear region, simply $\nu_w = \nu$. In the logarithmic region, $\nu_w = {C_\mu}^{1/4} {k_P}^{1/2} y_P \kappa \,/\, \ln(E y^*)$.

iv. ν_w is used to solve the momentum equation and obtain the new u_P. The no-slip and no-flux conditions are imposed at the wall-face.

v. The k transport equation is solved to obtain the new k_P. Zero-value and zero-flux conditions are imposed at the wall-face. Turbulence production and dissipation are assumed at equilibrium.

vi. The energy dissipation is set as $\varepsilon_P = {C_\mu}^{3/4} {k_P}^{3/2} / \, y_P \kappa$. This expression arises from the equilibrium assumption, which is necessary because no boundary conditions are available to solve the ε transport equation in the wall-adjacent cell.

vii. Restart from step i.

The wall function approach is unreliable in presence of strong pressure gradients, because the equilibrium assumption is inaccurate.

In the past, most commercial CFD solvers used the wall units y^+ and U^+. Their definition is slightly different from y^* and U^*, thus their use involves an iteration sub-loop and is computationally expensive. For this reason, all modern solvers now use y^* and U^* by default. Nevertheless, it is still common practice in the CFD community to report y^+ as a post-processing mesh quality index.

II.3.4.2. Free surface

The fluid free surface in agitated vessels can deform significantly under the effect of pressure forces leading to vortex formation. This is particularly relevant to unbaffled vessels. In an early study, Ciofalo et al. (1996) developed an iterative method in which a body-fitted mesh was generated at each new iteration, based on the current flow solution. The surface pressure was used to calculate the liquid surface shape, and the procedure was repeated until independence

was reached. However, this approach was extremely expensive. The volume of fluid (VOF) model, which involves the simulation of a volume of air above the liquid surface, was firstly applied by Serra et al. (2001) to solve surface deformation. This method solves the transport equation of the volume fraction of the fluids. In most numerical studies, the free surface is modelled as flat, with a zero-stress and zero-flux condition (Aubin et al., 2004, 2006; Cortada-Garcia et al., 2017; Lane, 2017; Mendoza et al., 2018), or a lid is used to cover the vessel, thus introducing a wall (Hartmann et al., 2006; Coroneo et al., 2011; Huang and Li, 2013).

II.3.4.3. Modelling the rotating impeller

In the case of unbaffled tanks, a rotating frame of reference (RF) can be adopted, so that the impeller is stationary, and the walls rotate. In baffled vessels, the impeller phase relative to the baffles needs to be resolved. Historically, the impeller region has been modelled as a *black box* source of momentum, by imposing experimental conditions at its boundary. This approach was conditional on specific data availability and sensitive to their accuracy (Brucato et al., 1998).

Two modern impeller models are the sliding mesh (SM) and multiple frames of reference (MFR) approaches. The vessel is divided in two non-overlapping sub-domains, an outer region which includes the stationary elements and an inner cylinder around the impeller. The two regions interact through their common interface. The SM technique (Luo et al., 1993) is used in transient simulations to resolve the impeller-baffle interactions and pseudo-turbulence. At each time step, the inner region rotates, and the solution is recomputed according to the new impeller position. Non-conformity at the interface (inner and outer cell faces may not match) is handled with an interpolation algorithm. In the MFR approach (Luo et al., 1994), the flow equations in the inner region are solved in a rotating frame of reference, so that both the inner and outer flows are assumed steady in their own reference frame. If all quantities do not change azimuthally at the interface, i.e. the outer-inner interactions are negligible, the MRF solution

represents a snapshot of the physical flow. This method requires the interface position to be defined sensibly. MRF solutions are also commonly used to initialise SM simulations and avoid the computation of the transient between fluid at rest and pseudo-steady state (Campolo et al., 2003). Despite the MFR approach does not capture the impeller-baffle interactions, many researchers have reported no significant differences in the mean velocities and flow patterns obtained with MFR and SM (Aubin et al., 2004; Patel et al., 2015a; Lane, 2017), indicating that the higher cost of the latter method can be avoided. However, turbulent quantities are sensitive to the impeller model, the SM being more accurate (Aubin et al., 2004). The differences between MRF and SM solutions might depend on the choice of the turbulence model. In his research work, Lane (2017) compared k-ε and k-ω SST RANS of the turbulent flow in a stirred tank, using both the MRF and SM approaches. With the k-ε model, the MRF solution and the time-averaged SM solution were essentially identical. Due to its sensitivity to flow separation, the SST model was able to predict a secondary recirculation loop in the top half of the vessel, the size of which depended on the angle between the impeller blade and the baffle. This produced, even in the case of the MRF simulation, an asymmetric velocity field. Clearly, this snapshot did not represent the mean flow correctly, and the author concluded that only the SM method was suitable for the SST model.

II.4. Closing remarks and knowledge gaps

Fluid mixing in mechanically agitated vessels is an active field of scientific research. More than 200 scientific papers related to fluid mixing have been reviewed to identify the gaps in the current knowledge and the research open questions. Recent publications represent a significant share of the literature survey. The main findings are summarised below.

Many tank configurations and mixer geometries have been developed to achieve different process objectives. The Rushton turbine is one of the most common impeller geometries and it has been studied extensively. Quantitative data for the RT are widely available in the literature, and the agreement between different sources is typically good. For this reason, the RT can be considered the ideal geometry for validating new research methods.

Most of the published works regarding agitated vessels focus on fully turbulent or fully laminar conditions. The transitional flow regime, characterised by the simultaneous presence of viscous and inertial effects and by complex hydrodynamics, is still not well understood. Transitional flows may show turbulent and laminar behaviour in different zones of the vessel, but they are different from fully turbulent and fully laminar flows on a global level. Laminar stirred tanks are commonly designed in terms of an effective shear rate proportional to the impeller speed (Metzner-Otto model). This allows the power data of any fluid to be condensed in a single curve, regardless of the fluid Newtonian or non-Newtonian rheology. However, the applicability of the Metzner-Otto model to transitional vessels is still debated in the literature. On the other hand, some authors have shown that, under transitional flow conditions, the velocity and energy dissipation do not scale as in the turbulent regime. Thus, the scale-up of transitional flows in agitated vessels is still a challenging task, often conducted by trial and error. More studies are needed for a better understanding of fluid agitation under transitional conditions and for the development of adequate scale-up strategies.

Today, accurate and reliable measurements of fluid flows can be obtained through various experimental techniques. Although mixing is an inherently Lagrangian process, it has so far been studied mostly from a Eulerian perspective, due to the characteristics of the best available measurement technologies. Traditional optical techniques, such as LDV, PIV and PLIF, have greatly contributed to the current knowledge of fluid agitation in stirred tanks. CARPT and

PEPT have been used successfully to investigate opaque systems and fluids. For all these techniques, well-established experimental procedures and guidelines are available. PTV is one of the oldest flow visualisation techniques, based on the individual tracking of many Lagrangian flow tracers. However, its sensitivity to image noise limited its application until the necessary software and hardware improvements were achieved. In the last two decades, PTV has been used to study many flow applications involving small observation volumes. This technique is very effective in investigating the turbulence statistics at small scales. Its application to stirred vessel flows has been prevented by many difficulties, including the large volumes and wide range of velocity involved and data sparsity. Recently, a promising validation of PTV against PIV measurements in a lab-scale tank has been conducted by Alberini et al. (2017). This publication paved the way for a hitherto unexplored area of mixing research.

Numerical simulations can provide access to information that would be difficult to obtain experimentally. CFD studies are always a compromise between satisfactory accuracy and affordable computational costs, and validation against experimental data is always required. The RANS approach to turbulence modelling is the most common method used in research. Many RANS models have been developed, each one with intrinsic strengths and limitations. In general, the mean flow in stirred tanks can be determined with good accuracy even with the MRF approach. However, the turbulent quantities are extremely sensitive to the grid spacing, the turbulence model, the discretisation scheme and the impeller model. The simulation of transitional flows in stirred tanks is particularly challenging, because common turbulence models were developed for fully turbulent conditions. As a consequence, the number of published CFD studies of transitional vessels is quite small, and even smaller when non-Newtonian fluids are involved. The best practices for simulating these systems are not yet

clearly defined, and more studies are needed to fully address the role of the turbulence model and other modelling parameters.

Chapter III

DEVELOPMENT AND APPLICATION OF 3D-PTV MEASUREMENTS TO LAB-SCALE STIRRED VESSEL FLOWS

Abstract

Guidelines for reliable 3D-PTV measurements of fluid flows in stirred vessels at the lab-scale have been developed. The flow of water at $Re = 12{,}000$ in a flat bottom cylindrical tank ($T = 180$ mm) stirred with a 6 blades Rushton turbine ($C = D = T/3$) has been measured at different camera frame rates (125 – 3,600 fps) and tracer concentrations (0.001 – 0.010 px^{-2}). The best compromise between the total number of individual data points, tracking efficiency and CPU time (206 frame^{-1}, 39% efficiency, 0.026 min frame^{-1}) has been obtained at 125 fps and 0.002 px^{-2}. These results can be expressed in terms of the normalized parameters $\varphi \sim 0.5$ and $p \sim 2$ and scaled to different experimental conditions. The Savitzky-Golay filter, used to enhance the measurements signal-to-noise ratio, has been optimized by testing different values of the polynomial order (0 – 3) and filter width (3 – 21 data points). A 2nd order, 11-points filter gave the best results, based on considerations regarding the reduced Chi-squared and velocity distributions. Finally, an unbiased distribution of the flow decorrelation time has been determined from the velocity autocorrelation functions along the trajectories longer than 6 impeller revolutions.

III.1. Introduction

The capability to map flow velocity fields accurately and reliably is of critical importance to enable understanding of flows in both academia and in industry applications, such as mixing of fluids in agitated vessels. Laser-based imaging techniques, namely Particle Image Velocimetry (PIV) and Laser Doppler Velocimetry (LDV), are the most widely used (Li et al., 2018a) and the current benchmarks for any competing technique where optical access is possible. Both these techniques are Eulerian, meaning that the velocity is measured at specified positions in space. Consequently, most of the existing knowledge about fluid mixing in agitated vessels is based on Eulerian quantities, e.g. velocity profiles, shear rate, vorticity, turbulent kinetic energy and energy dissipation rate. However, the cost of a PIV or LDA experimental rig can be prohibitive, mainly due to the investment costs associated to laser illumination facilities.

3D-PTV is a Lagrangian technique which enables the 3D Lagrangian velocity field to be obtained through individual tracking of many flow tracers and with relatively simple hardware. The use of particles larger than ~200 μm can obviate the need for laser illumination. Consequently, the cost of a PTV rig can be much lower than PIV or LDA facilities. This is particularly attractive for industrial R&D sectors with limited budgets. JM invested in a PTV rig before the start of this EngD project, with the pioneering aim to study fluid mixing in agitated vessels by means of PTV. This had never been attempted before, due to the large volumes and wide ranges of velocity involved. A comparison between PTV and PIV velocity measurements in lab-scale agitated vessels has been conducted by Alberini et al. (2017). Newtonian and non-Newtonian fluids were studied under low and mid transitional ($Re \sim 70$ and $Re \sim 1{,}000$) and fully turbulent conditions ($Re \sim 33{,}000$). However, the procedures of PTV data acquisition, processing and post-processing were not optimised and the analysis was limited to

a comparison of interpolated Eulerian velocity against PIV data. Still, the agreement between the two techniques was promising.

In this chapter, 3D-PTV measurements have been conducted in a similar vessel operated at $Re \sim 12{,}000$. This Reynolds number has been chosen because the experiments described in the next chapters would be conducted in the low and mid-transitional flow regime and at comparable impeller speeds. The effects of the tracer concentration and frame rate on the tracking efficiency and CPU time have been assessed. In order to obtain precise velocity measurements, the coordinates have been filtered with a Savitzky-Golay filter before discrete differentiation. Different combinations of the filter width and order have been tested. The best choice has been determined by comparing the resulting distributions of the velocity and of the reduced Chi-squared. This is a standard procedure to evaluate the goodness of fitting. Finally, the macroscopic time scales of the flow have been quantified in terms of velocity decorrelation time. The results discussed in this chapter will provide the basis for future 3D-PTV experiments in lab-scale agitated vessels, both in terms of in-lab operating conditions and post-processing of the data.

III.2. Materials and methods

III.2.1. Vessel geometry and flow conditions

All measurements were conducted in an unbaffled cylindrical vessel of diameter $T = 180$ mm and a liquid height $H = T$. The impeller was a 6 blades Rushton turbine of diameter $D = T/3$, placed with a clearance $C = T/3$. The impeller blades had width $D/4$ and height $D/5$. To avoid refraction effects at the curved wall, the cylindrical vessel was immersed in a larger square tank filled with the same liquid. The two vessels were made from polymethylmethacrylate, and the

thickness of the walls was 4 mm. The working fluid was demineralised water at room temperature, having density $\rho = 1.0 \cdot 10^3$ kg m^{-3} and viscosity $\mu = 1.0 \cdot 10^{-3}$ Pa s. The impeller rotational speed was 200 rpm, corresponding to a tip speed $U_{ti} = 0.63$ m s^{-1} and a Reynolds number of $Re = 12{,}000$.

After the image calibration (see **§III.2.3**), the fluid was seeded with polyethylene microspheres (Cospheric, US) for 3D-PTV measurements. The tracers were neutrally buoyant (density: 1.0×10^3 kg m^{-3}) and 750 – 820 µm in size. Their Stokes number was $St = 1.46 \times 10^{-2}$.

III.2.2. Image acquisition and processing

The raw images of the flow were acquired with a high-speed camera (Fastcam SA4, Photron Ltd., JP) equipped with a macro lens fit (Sigma 24-70 mm f2.8 EX DG Macro, Nikon, JP) and a system of mirrors (LINOS adjust.X, Qioptiq, UK). These allowed the inner vessel to be visualised from two viewing orientations in a single image (***Figure III-1***). LED lights (Marathon multiLED LT, GSVitec GmbH, DE) were used for the illumination. This is the same hardware used in the work of Alberini et al. (2017).

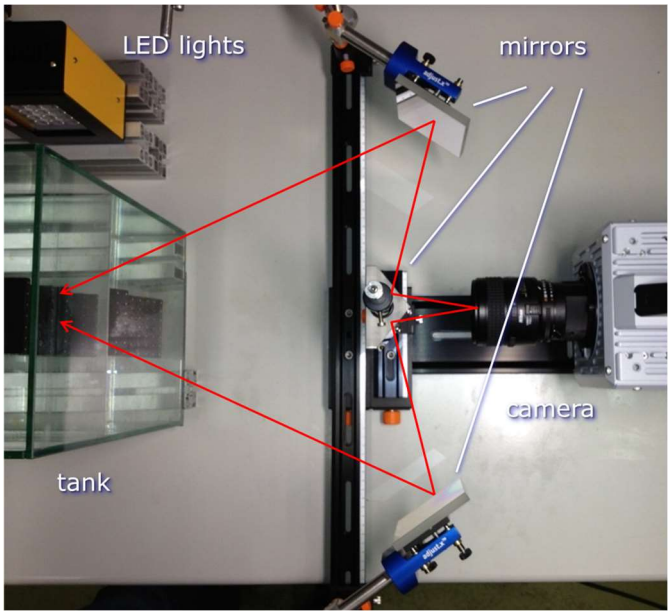

Figure III-1*: Schematic of the PTV camera arrangement.*

The raw images were encoded in a 8-bits greyscale, so that each pixel level could assume any value between 0 (true black) and 255 (true white). The image size was 1024×1024 px^2, corresponding to a digital resolution of ~350 μm px^{-1}. The camera could record a maximum of 3,600 frames per second (fps) and store approximately 5.4 GB of data (5,400 frames) in a single recording. The shutter time could be chosen among a list of default values.

The raw images were converted to matrices of double-precision floating point numbers in MATLAB environment and split in the two viewing orientations, which were processed individually. The ensemble average image of the sequence was subtracted from the individual images, in order to remove the static background and reduce random noise. The images were then converted back to the 8-bit format. This step was not required for single calibration images. At this point, the moving particles appeared as bright blurs on a dark background. According to Kähler et al. (2012a), the resolution of the centroids is independent of the blur size, as long as the particle images do not overlap. With modern algorithms, the precision is also independent, if the blur diameter is larger than 2×2 px^2 (Nobach et al., 2005). The typical size of the blurs was between 3×3 and 4×4 px^2 for the tracers and between 4×4 and 5×5 px^2 for the calibration dots. A high pass filter was applied, and the blurs were detected with a cluster search algorithm developed by Lei et al. (2012) which identifies clusters in the pixel levels larger than a threshold size. By doing so, random bright pixels were not mistakenly recognised. The blur centroids were determined with subpixel precision by weighting the pixel levels (Lei et al., 2012). For each viewing orientation and time step, a file containing all the centroid coordinates was produced. These files represented the input to the 3D-PTV algorithm. With the current setup, the typical repeatability of the centroid calculation was ~0.014 px (~5 μm) on each of the image coordinates. This has been determined by taking 15 ideally identical pictures of the reference geometry in ***Figure III-2a*** and calculating the standard deviation over the 15 measured coordinates, then averaging over each reference dot.

III.2.3. Image calibration

III.2.3.1. Procedure

The image calibration was conducted using a reference geometry with a 3D grid of 147 control dots (***Figure III-2***). The grid extends for 60 mm, 200 mm and 55 mm in x (width), y (height) and z (depth). The target was put at a known position within the vessel, filled with fluid in absence of agitation, before the actual PTV experiments. A single stereo-picture was taken, and the two half-images were processed as described in the previous section. For each view, the projection matrix that links the 2D image coordinates to the 3D world coordinates was determined, in the least square sense, from the 147 correspondences between the dot centroids in the images and their known positions in the vessel. The knowledge of the two projection matrices allowed the 3D position of any point in the observation volume to be reconstructed by triangulation of its 2D coordinates in the images.

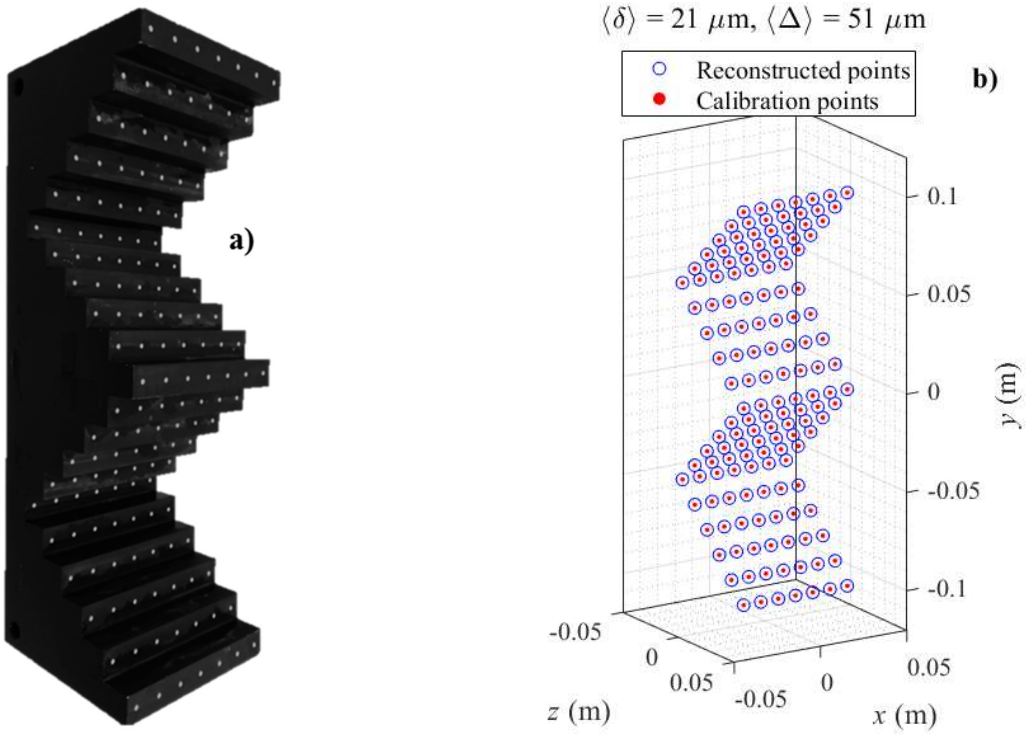

Figure III-2*: Reference geometry for 3D-PTV image calibration (a) and an example of 3D reconstruction from images (b).*

III.2.3.2. Statistics of the measurement error

The reconstruction error of the tracer particle positions will be statistically determined by the quality of calibration. Since the projection matrices are calculated from real data, biases are inevitably present. In addition, any blur centroid can only be determined within the experimental uncertainty. Consequently, once a stereo-correspondence is established, the two sight lines do not cross at the true position in 3D space. The reconstructed point is placed at the centre of the distance between the sight lines. The quality of calibration can be described by two quantities. The first, δ, is the distance between the two sight lines of each control dot and measures the uncertainty in the 3D reconstructions. The second, Δ, is the distance between the reconstructed control dots and their true positions, i.e. the reconstruction error. Note that, in experiments with tracers, δ is measurable but Δ is not, since the true positions are unknown. A theoretical discussion about δ and Δ can be found in **§A.1.4**.

The calibration in the present study produced the log-normal distributions of δ and Δ pictured in ***Figure III-3***. The mean values, calculated in the logarithmic space and then converted back to linear scale, were $\langle\delta\rangle = 21$ µm and $\langle\Delta\rangle = 51$ µm. The maximum observed value and the 98th percentile of the error were $\Delta_{max} = 499$ µm and $\Delta_{98} = 255$ µm, respectively. The z-component dominated the total error, with $\langle\Delta_z\rangle \approx 5\langle\Delta_x\rangle \approx 5\langle\Delta_y\rangle$. It should be pointed out that the moving particles are worse targets than the static control dots, and the average error obtained with the reference geometry may underestimate the error in real flow conditions (Maas et al., 1993). Still, the average error in the flow measurements is expected to be in the order of magnitude between $\langle\Delta\rangle$ and Δ_{max}. Finally, δ and Δ were not correlated to each other (***Figure III-4***; the Pearson's correlation coefficient, PCC, between their logarithms was 0.104), nor autocorrelated over distances in space of 10 mm (the distance between adjacent control dots).

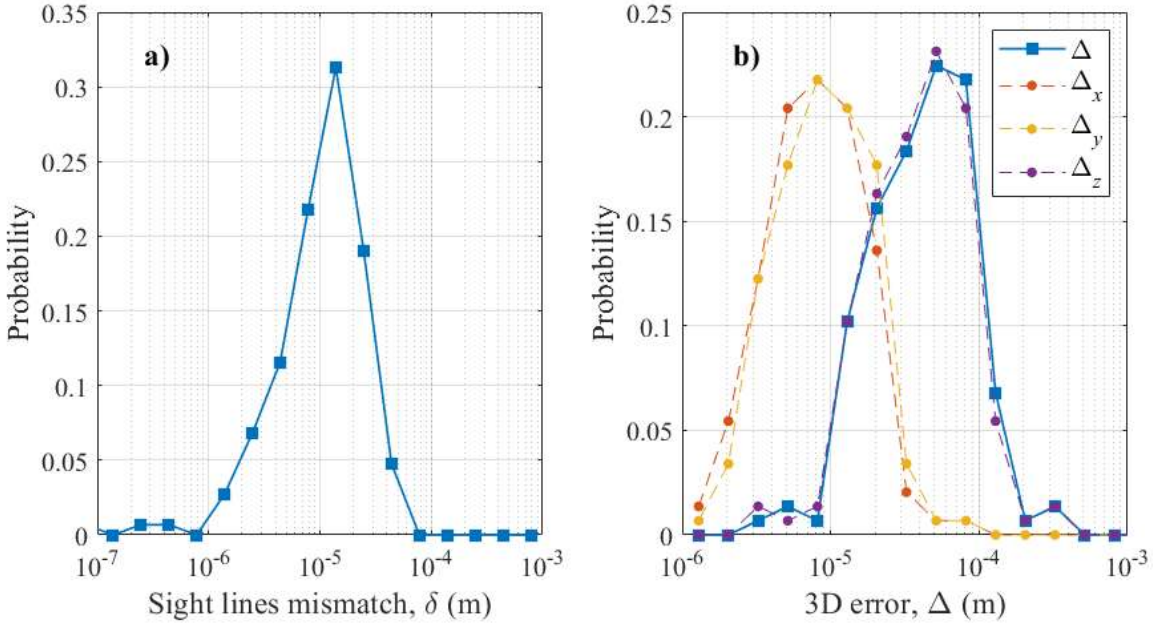

***Figure III-3**: Distributions of δ and Δ.*

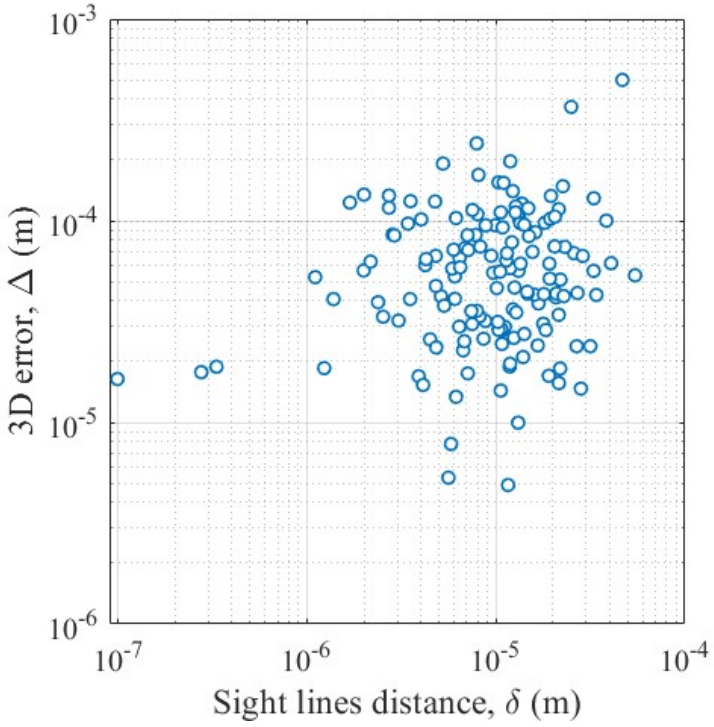

***Figure III-4**: Scatter of δ against Δ.*

III.2.4. 3D particle tracking

III.2.4.1. Preliminary considerations on frame rate and tracer concentration

As discussed in **§II.2.6**, the frame rate and tracer concentration are two crucial variables for obtaining good quality PTV measurements. Also, the goal of a PTV experiment is to obtain as many data as possible, for the sake of statistical representativeness of the results. The mixing experiments described in this section were aimed at finding a good operational window for 3D-PTV measurements in lab-scale stirred vessels.

In agitated vessels, the velocity can vary by many orders of magnitude within the volume. High values in the order of ~80% of the tip speed are found close to the impeller. Although the high velocities occupy a small fraction of the vessel volume, they contribute significantly to the total energy dissipation (Ng and Yianneskis, 2000; Micheletti et al., 2004). Since the tracers move out of these small regions rapidly, particle occupancy is crucial for obtaining enough data and measuring the flow reliably. In the fluid bulk, which represents most part of the tank volume, the velocity can be less than 1% of the tip speed, e.g. when viscous fluids are mixed. The minimum distance travelled by the particles between consecutive frames, $U_{min}\Delta t$, should be larger than the experimental error, Δ. This leads to

$$f \ll U_{min}\Delta^{-1}, \qquad \textit{Eq. III-1}$$

where U_{min} is the minimum velocity of interest in the flow and $f = \Delta t^{-1}$ is the frame rate. This equation represents a constraint to the frame rate based on the experimental error and the flow conditions. In particular, the frame rate should be scaled linearly with the flow characteristic velocity. The limit rate at which *Eq. III-1* becomes an equality is

$$f_{max} = U_{min}\Delta^{-1}. \qquad \textit{Eq. III-2}$$

The main issues related to the tracer concentration have already been introduced in **§II.2.6**. Given n_p particles uniformly distributed in a volume V, they all have the same distance from the nearest neighbour. This is

$$d_0 = \left(\frac{n_p}{V}\right)^{-\frac{1}{3}}. \qquad \textit{Eq. III-3}$$

In a 3D-PTV experiment, the tracers are randomly distributed, hence the average nearest neighbour distance is $\langle d \rangle < d_0$. The distribution of d/d_0 in a cylinder is log-normal with $\langle \ln(d/d_0) \rangle \approx -0.6$ and a standard deviation $\sigma_{\ln(d/d0)} \approx 0.5$. These values have been obtained from 45 randomly generated data sets of particle positions (15 repetitions at 3 concentrations) and are identical to those obtained by Malik et al. (1993) through Gaussian Kinematic Simulation of a turbulent flow. Following their analysis, a conservative nearest neighbour distance is $d^* = d_0/3$. This is defined as one standard deviation below the mean, i.e. $\ln(d^*/d_0) = -1.1$. The condition on the tracking parameter introduced in *Eq. II-14* can be written as

$$p = \frac{d^*}{\Delta l_{max}} = \frac{1/3\ d_0}{U_{max}\ \Delta t} = \frac{1}{3}\left(\frac{n_p}{V}\right)^{-\frac{1}{3}} \frac{f}{U_{max}} \gg 1. \qquad \textit{Eq. III-4}$$

In this case, a high f is desirable. The frame rate can be expressed as a fraction φ of the maximum rate $f_{max} = U_{min}\Delta^{-1}$ defined above, and *Eq. III-4* becomes

$$\frac{n_p}{V} \ll \left(\frac{\varphi}{3\Delta}\frac{U_{min}}{U_{max}}\right)^3. \qquad \textit{Eq. III-5}$$

Eq. III-5 represents a constraint on the tracer concentration based on the experimental error, the flow characteristics and the chosen frame rate. The ratio U_{max}/U_{min} is therefore an indicator of tracking difficulty. As already stated, this ratio can be very large in stirred tanks.

III.2.4.2. Investigated operational conditions

The operational conditions of the 3D-PTV experiments have been varied as shown in ***Table III-1***. Experiments B, C and D have been repeated three times. The values of $d^* = d_0/3$ for the investigated tracer concentrations are listed in ***Table III-2***. The observed velocity in the flow ranged between ~10% $U_{tip} = 0.063$ m s^{-1} and ~70% $U_{tip} = 0.44$ m s^{-1} (***Figure III-7***). Taking $\Delta = \Delta_{98} = 255 \cdot 10^{-6}$ m as the characteristic error, *Eq. III-2* gives $f_{max} = 246$ s^{-1}. The acquisition rates of experiments E and F were intentionally higher. For $f = 125$ s^{-1} ($\varphi = 0.51$), *Eq. III-5* gives $n_p/V \ll 570$ L^{-1}, that is exactly the concentration of experiments D.

Table III-1*: Operational conditions of the 3D-PTV mixing experiments.*

Experiment	Image particle concentration	Acquisition rate	Number of frames	Overlapping particles (Maas, 1992)	p (*Eq. II-14*)
A	0.001 px^{-2}	125 s^{-1}	5,400	0.2% - 0.6%	2.46
B1, B2, B3	0.002 px^{-2}	125 s^{-1}	5,400	0.3% - 1.2%	1.95
C1, C2, C3	0.006 px^{-2}	125 s^{-1}	5,400	0.9% - 3.7%	1.35
D1, D2, D3	0.010 px^{-2}	125 s^{-1}	5,400	1.5% - 6.0%	1.14
E	0.002 px^{-2}	500 s^{-1}	5,400	0.3% - 1.2%	7.82
F	0.002 px^{-2}	3,600 s^{-1}	5,400	0.3% - 1.2%	56.2

Table III-2*: Nearest neighbour distances for particles in a 4.6 L tank, visualized in a 512×512 image, at four tracer concentrations.*

Image particle concentration	*Number of particles, n*	*Volumetric particle concentration, n_p/V*	$d_0/3$
0.001 px^{-2}	~ 262	57 L^{-1}	8.6 mm
0.002 px^{-2}	~ 524	114 L^{-1}	6.8 mm
0.006 px^{-2}	~ 1573	342 L^{-1}	4.7 mm

0.010 px^{-2}	~ 2621	570 L^{-1}	4.0 mm

The best operational conditions have been determined by comparing the particle detection efficiency, the tracking efficiency and the CPU time required for the 3D reconstruction and particle tracking steps. The overall particle detection efficiency was calculated as the number of detected blurs, averaged over the 5,400 frames and two orientations, divided by the number of particles present in the system. The overall tracking efficiency was calculated as the total number of established links, divided by the number of frames, and again by the number of particles in the system. Image processing (i.e. views splitting, ensemble average subtraction and blur detection) was not considered in the measurement of the CPU time, as this procedure only includes operations between pixel values, regardless the tracer concentration and frame rate.

III.2.4.3. Particle tracking algorithm

The data processing was conducted in MATLAB environment on a computer equipped with 32 GB of RAM and an Intel® Xeon® E5-2650 CPU working at a maximum frequency of 2.00 GHz. Since only two views of the flow were available, numerous ambiguities could occur at the particle 3D stereo-matching stage by the method of epipolar lines, even at the lowest tracer concentration. To overcome this problem, the PTV algorithm developed by Willneff (2003) was used. This is based on the simultaneous use of 2D image and 3D object space information to solve stereoscopic ambiguities. The correct link in case of many temporal candidates was determined by minimizing the change in Lagrangian acceleration: the new position was predicted through a second order polynomial fitting of the past coordinates (constant acceleration) and the candidate closest to the prediction was chosen. Wrong matches were unlikely but still virtually possible, if a wrong candidate happened to be closer to the prediction.

However, most likely, the wrong matches could not be tracked further, leading to trajectory interruptions. For this reason, points that could not be linked to the next time steps were discarded. Also, all the trajectories shorter than 21 time steps were discarded. Willneff's algorithm also allows to bridge the gaps in the trajectories when only a few time steps are not available, thus leading to longer trajectories and enhancing the quality of the final velocity field.

III.2.5. Data post-processing

III.2.5.1. Signal-to-noise ratio enhancement of 3D-PTV data

The Savitzky-Golay filter (Savitzky and Golay, 1964) is a popular method for enhancing the signal-to-noise ratio of experimental data sequences and allows the derivatives to be calculated with more precision. It has been used successfully by some authors for PTV data smoothing (e.g. Hoyer et al., 2005; Lüthi et al., 2005; Kreizer and Liberzon, 2011; Krug et al., 2014). The filter is based on the convolution of each coordinate sequence along a trajectory with a polynomial of time. The coordinate at time t_i is $\xi_i \equiv \xi(t_i)$, where ξ can be x, y or z. The sequence of $w = (2k + 1)$ data points that goes from ξ_{i-k} to ξ_{i+k} is expressed with a Taylor expansion centred at ξ_i:

$$\xi_j \approx c_0 + c_1 \Delta t_j + c_2 \Delta t_j^2 + \cdots + c_o \Delta t_j^o . \qquad \textit{Eq. III-6}$$

Here w is the width of the filter, o is the order, j goes from $(i - k)$ to $(i + k)$ and $\Delta t_j \equiv (t_j - t_i)$. If $w > (o + 1)$, *Eq. III-6* generates an overdetermined system of w equations in $(o + 1)$ unknowns:

$$[\mathrm{T}][c] = [\xi], \qquad \textit{Eq. III-7}$$

with

$$[\mathrm{T}] \equiv \begin{bmatrix} 1 & \Delta t_{i-k} & \dots & \Delta t_{i-k}^{o} \\ 1 & \Delta t_{i-(k-1)} & \dots & \Delta t_{i-(k-1)}^{o} \\ \dots & \dots & \dots & \dots \\ 1 & \Delta t_{i} & \dots & \Delta t_{i}^{o} \\ \dots & \dots & \dots & \dots \\ 1 & \Delta t_{i+k} & \dots & \Delta t_{i+k}^{o} \end{bmatrix}, \qquad [c] \equiv \begin{bmatrix} c_0 \\ c_1 \\ \dots \\ c_o \end{bmatrix}, \qquad [\xi] \equiv \begin{bmatrix} \xi_{i-k} \\ \xi_{i-(k-1)} \\ \dots \\ \xi_{i} \\ \dots \\ \xi_{i+k} \end{bmatrix}. \qquad \textit{Eq. III-8}$$

The least square solution is

$$[\hat{c}] = ([\mathrm{T}]^{\mathrm{T}}[\mathrm{T}])^{-1}[\mathrm{T}]^{\mathrm{T}}[\xi]. \qquad \textit{Eq. III-9}$$

The filtered coordinates can be expressed as:

$$\widehat{\xi_j} \equiv \widehat{c_0} + \widehat{c_1}\Delta t_j + \widehat{c_2}\Delta t_j^2 + \cdots + \widehat{c_o}\Delta t_j^o. \qquad \textit{Eq. III-10}$$

In particular, when $j = i$, $\Delta t_i = 0$. Hence $\widehat{\xi_\imath} = \widehat{c_0}$ is the filtered coordinate at the centre of the sequence, while $\widehat{c_n}$ is the filtered n-th order derivative at the centre of the sequence. As the index i moves along the trajectory, all the filtered coordinates are obtained.

The points at the beginning and at the end of the trajectories need a different treatment, because there are not enough data available backwards or forwards. There are many ways to deal with first and last points. The method used here was to reduce the width as needed.

The convolution reduces the noise in the original signal but also affects the information contained in it (distortion). Both the signal-to-noise enhancement and the signal distortion decrease with the order o and increase with the width w. When applied to a signal containing white noise with constant standard deviation σ, a second order SGF reduces the standard deviation in the filtered signal to

$$\hat{\sigma} = \sqrt{\frac{3(3w^2 - 7)}{4w(w^2 - 4)}}\sigma. \qquad \textit{Eq. III-11}$$

If w is large enough, $\hat{\sigma} \sim \sqrt{1/w}\,\sigma$, similarly to the standard error of the mean. Note that the convolution of PTV data with a second order polynomial is equivalent to assuming uniformly accelerated motion in the neighbourhood of each data point. Malik et al. (1993) found that, even in presence of turbulence, this assumption holds for small enough time intervals (25 fps, in their case). For this reason, there is no practical need to use $o \gg 2$ for PTV data smoothing. Another important advantage of the SGF is that the error in the filtered coordinates becomes highly autocorrelated, because consecutive coordinates are calculated from many common data points. Thus, only a small share of uncorrelated error propagates through finite differentiation.

The SGF can be thought as a data fitting, and the reduced Chi-squared statistic is a common measure of the *goodness of fitting*. It is defined as the Chi-squared per degree of freedom:

$$\frac{\chi^2}{\nu} \equiv \frac{1}{\nu}\sum_i \frac{\left(\widehat{\xi_i} - \xi_i\right)^2}{\sigma_i^2}, \qquad \textit{Eq. III-12}$$

where ν is the degree of freedom (the number of observations minus the number of fitted parameters); $\widehat{\xi_i}$ is the i-th fitted data; ξ_i is the i-th observation; σ_i is a metric of the uncertainty in the i-th observation. The Chi-squared can be interpreted as the ratio between the average squared fitting residual over the averaged squared uncertainty. This leads to the following considerations, depending on the scenario:

(i) If the measurements uncertainty is known a priori, but the fitting model is not, then
   a. if $\chi^2/\nu \gg 1$, the residuals are much greater than the measurement uncertainty, that is the model does not fit the data adequately;
   b. if $\chi^2/\nu \ll 1$, the measurement uncertainty is much greater than the fitting residuals, meaning that the model is improperly fitting noise (overfitting);
   c. if $\chi^2/\nu \approx 1$, then the model is a good fitting for the data, given their level of uncertainty.

(ii) If the measurement uncertainty is not known, but it is known that the data should follow a certain model, then the uncertainty can be roughly estimated with s such that

$$\frac{\chi^2(s)}{\nu} = \frac{1}{\nu}\sum_i \frac{\left(\widehat{\xi_i} - \xi_i\right)^2}{s^2} = 1. \qquad \textit{Eq. III-13}$$

Five Savitzky-Golay filters have been tested on the data obtained from experiment B1 as the width and the order of the filter were varied. The dataset consisted of 1,115,409 coordinates grouped in 21,124 individual trajectories. The goodness of fitting of each filter has been measured in terms of reduced Chi-squared. The filters tested in this paper are defined in ***Table III-3***. A first guess value of $\sigma = \Delta_{98} = 255$ µm has been used for the measurement error. The best filter has been identified by comparing the distributions of the reduced Chi-squared. Then, the randomness of the fitting residuals has been checked. The results are shown in **§III.3.2**.

Table III-3*: The SGFs tested in this work.*

Filter	Width, w	Order, o
SGFa	21	3
SGFb	11	2
SGFc	7	2
SGFd	5	1
SGFe	3	0

III.2.5.2. Velocity autocorrelation and decorrelation time along trajectories

Bashiri et al. (2016a) have used the autocorrelation functions (ACFs) of the tracer position vectors to determine the flow time scales. The ACF of a time series measures how much the signal is correlated with a delayed version of itself, as a function of the delay. The decorrelation time quantifies the time required for the series to lose memory of the past values. The simplest

way to define it is to take the time at which the ACF crosses the 0 line for the first time. A similar approach to the method proposed by Bashiri et al. (2016a) has been applied to the PTV filtered trajectories, with some necessary modifications.

Firstly, the motion in the unbaffled vessel was mainly rotational, i.e. in the azimuthal direction. As a consequence, the ACF of the position vectors in a Cartesian frame of reference, $\{x, y, z\}$, would have a pronounced sinusoidal behaviour. This feature is not informative and would hide more relevant dynamics. For this reason, the ACF of the velocity in cylindrical coordinates would be a more sensible quantity to investigate. Secondly, the decorrelation time is biased by a finite measurement effect. Reasonable estimates can only be obtained from long trajectories.

The velocity data of experiment B1 have been converted to cylindrical components, U_r, U_θ and U_y. In order to reduce the bias due to the finite trajectory length, only the 188 trajectories longer than 6 impeller revolutions ($T > 225$ time steps) have been analysed. This choice has been validated later. The autocorrelation coefficients have been calculated along each long trajectory according to

$$R_{\mathbf{U}}(l) = \frac{\sum_{j=1}^{T-l}\left(\mathbf{U}_j - \overline{\mathbf{U}}\right) \cdot \left(\mathbf{U}_{j+l} - \overline{\mathbf{U}}\right)}{\sum_{j=1}^{T}\left(\mathbf{U}_j - \overline{\mathbf{U}}\right)^2}. \qquad \textit{Eq. III-14}$$

In *Eq. III-14*, l is the lag, T is the trajectory length, $\mathbf{U}_j$ is the velocity vector at the time step j, $\overline{\mathbf{U}}$ is the average velocity and the symbol "$\cdot$" denotes the scalar product. By calculating the coefficients $R_{\mathbf{U}}(l)$ for each lag $l = 1, 2, \dots, (T-1)$, the autocorrelation curves were obtained, and the trajectory decorrelation time was calculated.

Because the Lagrangian velocity was expressed in cylindrical coordinates, the corresponding decorrelation time acquires a specific physical interpretation. A solid-body rotation would be characterized by constant tangential velocity, the other components being zero. Since a perfectly constant velocity signal would have zero variance and create a singularity in *Eq. III-*

14, we consider the limit of extremely small variance instead. In this case, the autocorrelation coefficient would stay almost constant, i.e. $R_{\mathbf{U}} \sim 1$, decreasing very slowly with lag. On the other hand, the coefficient of a random process would drop to zero immediately. Therefore, the deviation from a unit autocorrelation coefficient reflects the deviation of the flow from a solid-body rotation and the degree of randomness of the flow dynamics. In an unbaffled vessel, if the Lagrangian velocity is measured starting at t_0, the values immediately after will be relatively similar to a solid-body rotation. However, they will progressively diverge from this behaviour due to random forces acting on the fluid elements. After a while, when $R_{\mathbf{U}} = 0$, the velocity will be statistically independent of the past values, thus from the solid-body behaviour. Therefore, the decorrelation time, t^*, can be intended as an indicator of macro-mixing performance. Note that this concept can be generalized to any flow in which the Lagrangian velocity is expected to be ideally constant relatively to an appropriate frame of reference. For instance, the velocity in an infinite length pipe is constant if expressed in Cartesian coordinates.

III.3. Results

III.3.1. Effect of tracer concentration and acquisition rate on the tracking performance

Figure III-5 shows some of the particle trajectories obtained from experiment B1. Due to the unbaffled configuration of the tank, the trajectories were mainly circular with small vertical motion. The performance measures of the tracking algorithm are listed in ***Table III-4***. Different repetitions of experiments B, C and D showed very similar results.

Although the number of data points increased with the tracer concentration, both the detection efficiency, i.e. the average percentage of particles detected per frame, and the tracking

efficiency, i.e. the average percentage of particles linked per frame, decreased linearly with the square of tracer concentration (***Figure III-6a***). This was caused by the increasing number of indistinguishable particles in the images. Even a low percentage of overlapping particles (< 6.0% estimated at the highest tracer concentration) has dramatic effects on PTV trajectory reconstruction, particularly if only two views are used. Three or four views algorithms are more robust, as they increase the probability that each particle is visible in at least two images.

The CPU cost increased more than linearly with the concentration (***Figure III-6b***), because more combinations had to be processed at the stereo-matching and trajectory reconstruction steps. Experiments B showed the minimum CPU time required per data point (7.7 ms).

Reducing the tracer concentration from 0.002 (experiments B) to 0.001 particles per pixel (experiment A) did not lead to significant advantages in terms of efficiency and computational costs. On the other hand, the absolute number of valid links was significantly reduced, as expected. Similar performances were also obtained by increasing the frame rate from 125 fps (experiments B) to 500 and 3,600 fps (experiments E and F), while maintaining the same tracer concentration. However, the relative error in the velocities would be higher because of the smaller Δt. This demonstrates the need to not exceed the recommended frame rate (*Eq. III-2*). In conclusion, the conditions of Experiment B were the preferable choice for this flow.

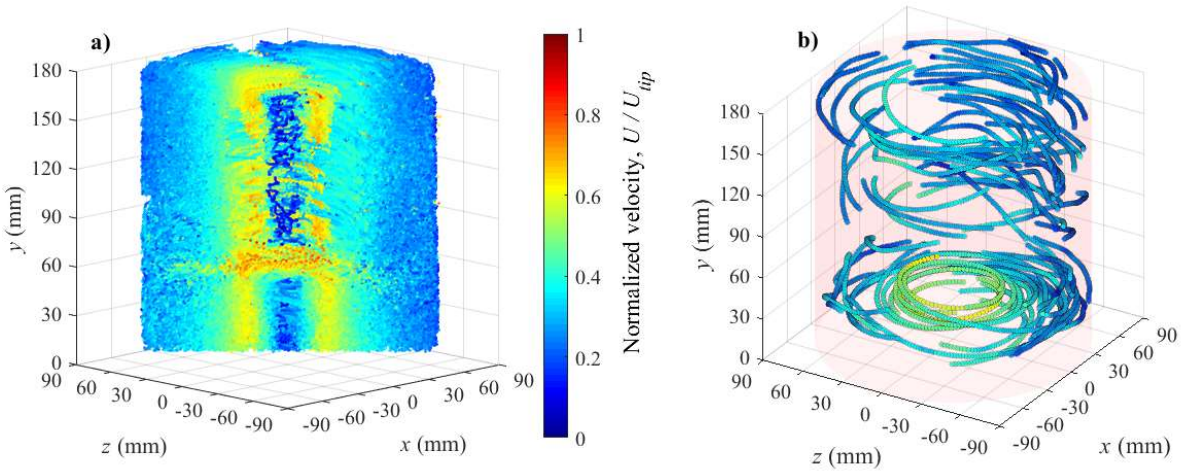

***Figure III-5**: Lagrangian trajectories obtained from experiment B1. (a): Cross section. (b): Selection of the trajectories longer than 0.5 s within the first 1 s of experiment (0.6% of total data set).*

***Table III-4**: Performance measures of the tracking algorithm.*

Experiment	Average fraction of detected particles ($\pm 3\ \sigma$)	Number of obtained links	Average fraction of tracked particles	CPU time (stereo-matching and tracking)
A	77.4% (±12.6%)	583,373	41.2%	112 min
B1	77.9% (±7.4%)	1,115,409	39.4%	141 min
B2	77.0% (±7.9%)	1,088,760	38.5%	144 min
B3	78.4% (±7.3%)	1,134,957	40.1%	144 min
C1	73.1% (±3.8%)	2,365,631	27.9%	876 min
C2	72.0% (±3.8%)	2,338,387	27.5%	895 min
C3	70.6% (±4.0%)	2,296,014	27.0%	866 min
D1	66.2% (±2.9%)	2,561,380	18.1%	2104 min
D2	66.2% (±2.9%)	2,599,979	18.4%	2119 min
D3	67.5% (±2.8%)	2,619,341	18.5%	2194 min

E	78.3% (±7.1%)	1,178,112	41.6%	134 min
F	76.4% (±7.8%)	1,102,631	38.9%	121 min

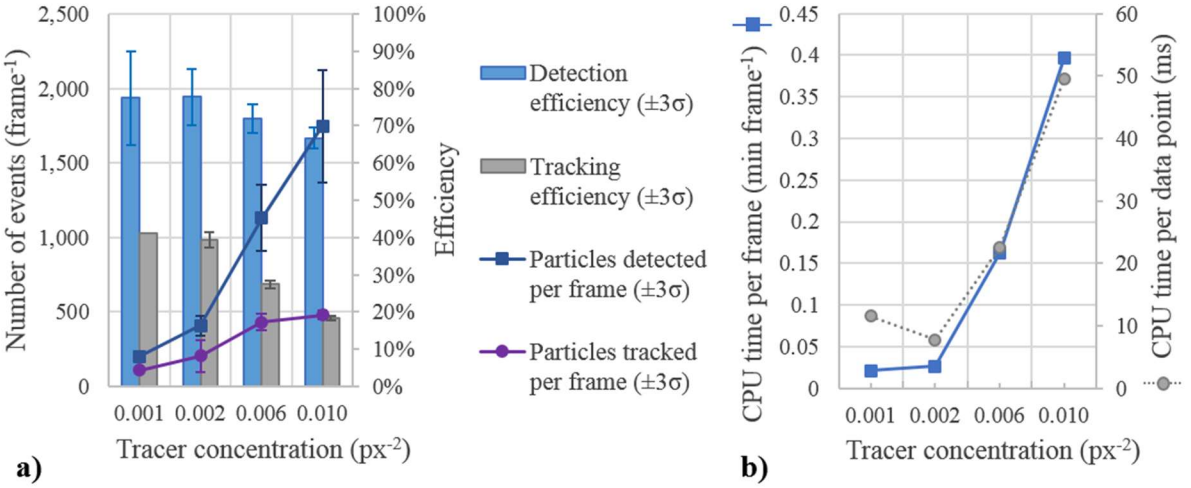

***Figure III-6**: Performance measures of the tracking algorithm comparing experiments A, B, C and D. (a): Particle detection and tracking efficiency. (b): CPU cost against the tracer concentration.*

III.3.2. Signal-to-noise ratio enhancement and velocity statistics

The distributions of the reduced Chi-squared of the filters, tested on the z coordinate from experiment B1, are plotted in ***Figure III-7a***. For SGFd and SGFe, $\mathrm{Mo}(\chi^2/\nu) \gg 1$, where Mo indicates the mode. These filters did not fit the data adequately, due to the low order of the polynomial: SGFe corresponded to a 3-point moving average and SGFd was a 5-point linearization. SGFa, SGFb and SGFc had similar modes, equal to 0.88, 0.93 and 0.73 respectively. In particular, SGFa and SGFb produced two very similar distributions of the reduced Chi-squared, while SGFc had a slightly broader distribution, hence a higher presence of badly fitted and overfitted data. Note that increasing o from 2 to 3 did not have a significant impact on the filter performance. This confirmed that, for this flow system, the assumption of uniformly accelerated motion of the tracers is valid. ***Figure III-7b*** shows that the resulting

velocity magnitude distributions of SGFa, SGFb and SGFc were very similar. SGFa had a stronger smoothing effect, as can be seen by the higher probability around the mode. In the light of the above, SGFb was the best option. According to *Eq. III-11*, this filter would reduce the amplitude of white noise to ~45% of the original value.

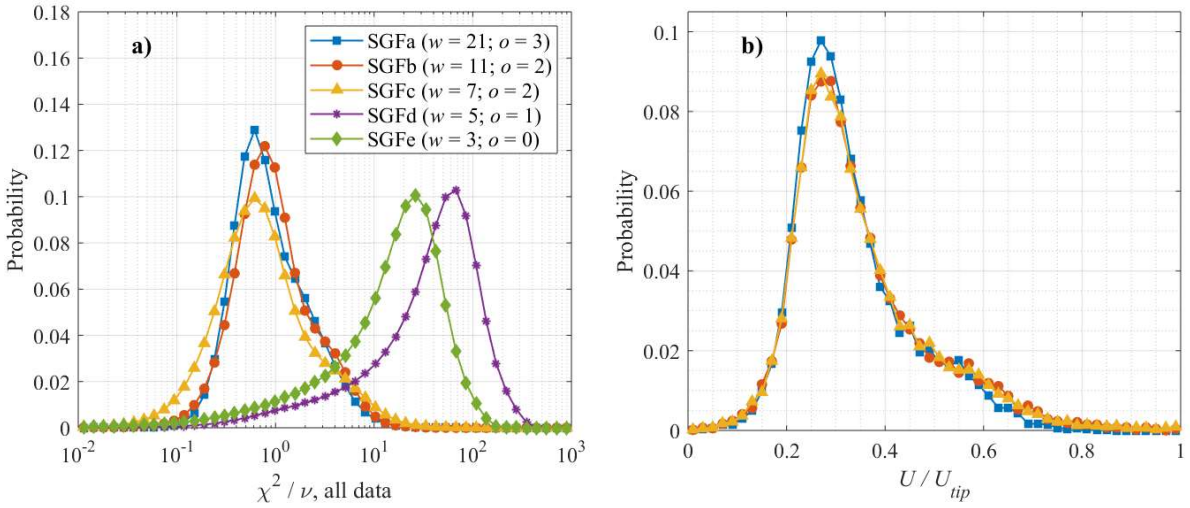

Figure III-7 *(a): Distributions of the reduced Chi-squared of the filters applied to the z coordinate. (b): Resulting distributions of the normalised velocity.*

The following considerations refer to SGFb. The fitting residuals on z (***Figure III-8a***) were normally distributed, with zero mean and RMS of $\pm$249 µm. Note that, with an ideal perfect filter ($\chi^2/\nu = 1$), the residuals would be equal to the measurement error. The RMS residuals on x and y were $\pm$38 µm and $\pm$42 µm, i.e. ~6 times smaller than the residuals on z. This reflects the fact that the error in the depth coordinate was predominant, as discussed in **§III.2.3.2**. The 3D residuals (signless), calculated as $r = \sqrt{{r_x}^2 + {r_y}^2 + {r_z}^2}$, were distributed as pictured in ***Figure III-8b***, with mode at ~157 µm and RMS of 255 µm, which is equal to the guessed error only by accident.

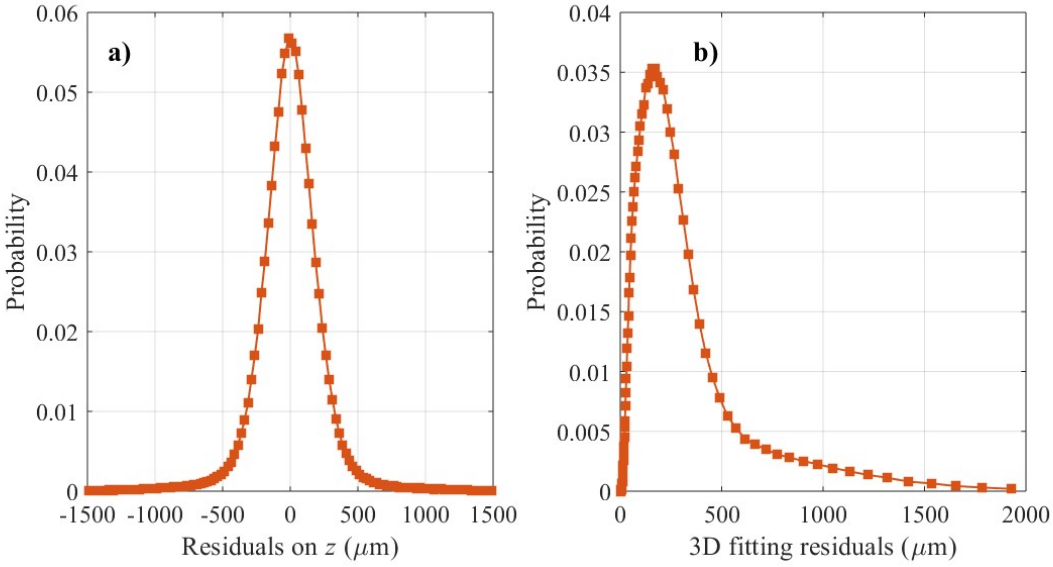

Figure III-8*: Fitting residuals of SGFb. (a): z component of the residuals. (b): 3D (signless) residuals.*

The residuals were further investigated along the longest trajectory of the experiment (***Figure III-9a***). This consisted of 479 data points (~3.82 s), that are enough to be statistically representative. The filtered data in 3D space tended to be inside the uncertainty region centred at the unfiltered data (***Figure III-9b***). The residuals did not show positive autocorrelation. This can be observed by plotting the residuals sequence along the trajectory (***Figure III-10a***) or by scattering each residual against the consecutive one in a lag plot (***Figure III-10b***). In the lag plot, the points were clustered around the origin with absence of patterns. Since the fitting residuals where normally distributed and not autocorrelated, they were random. This observation allows to conclude that the SGF reduced random noise and the experimental errors in the coordinates were in the same order of magnitude of the RMS fitting residuals.

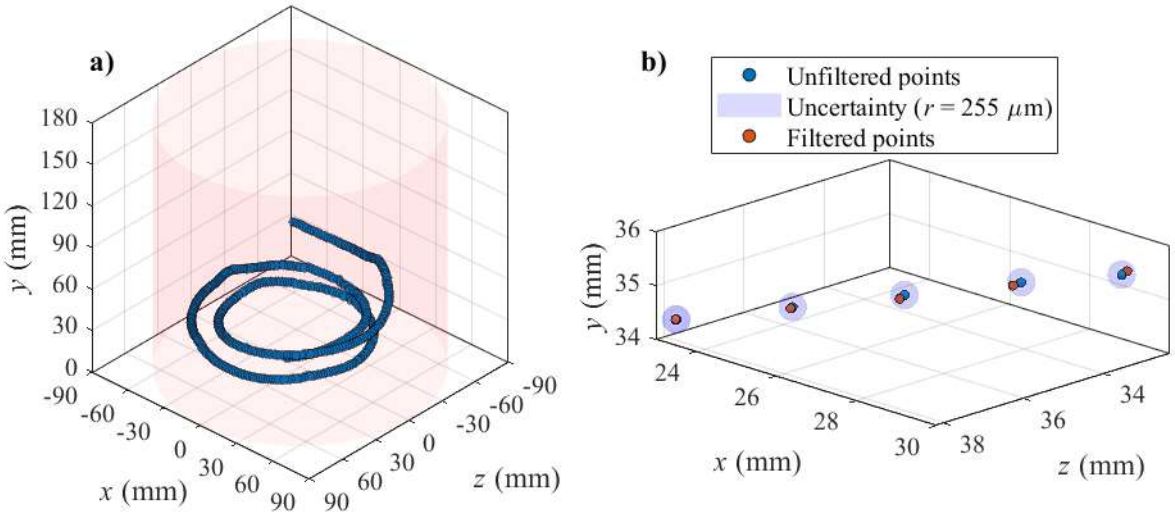

***Figure III-9**: Trajectory in the tank volume selected for residual analysis (a) and zoom on some data points in 3D space (b).*

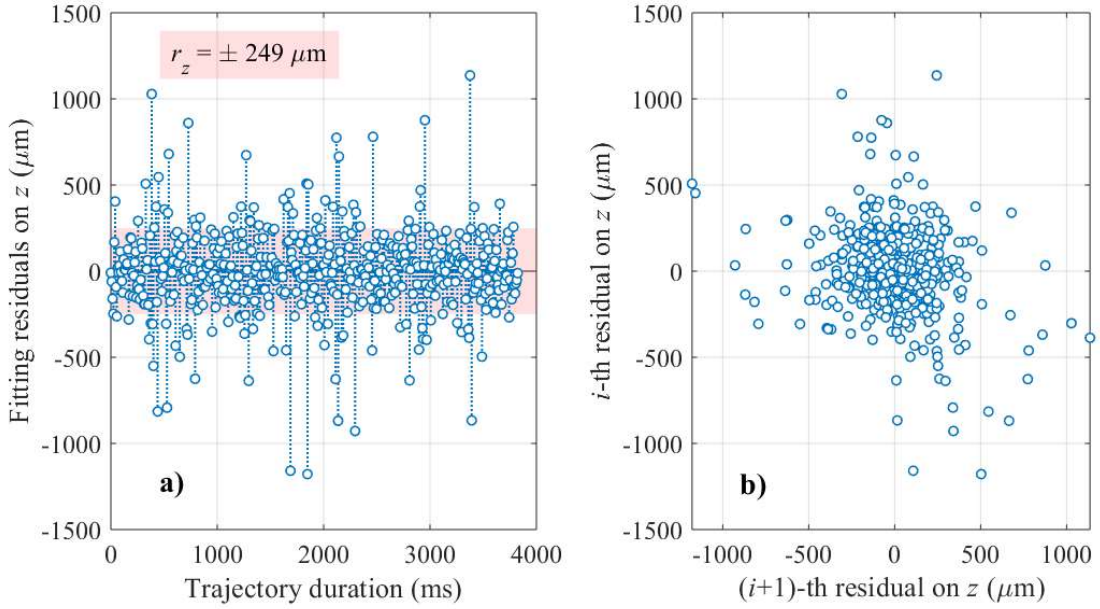

***Figure III-10**: Residuals along the longest trajectory (a) and 1-lag plot (b).*

III.3.3. Velocity autocorrelation along trajectories

Figure III-11 displays an example of velocity autocorrelation coefficient, for the case of the trajectory already shown in ***Figure III-9a***. Note that R_U is not exactly 0 after it crosses the 0 line for the first time. This does not automatically indicate a periodic component of the signal.

Even the $R_{\mathbf{U}}$ of random noise oscillates above and below 0, as it is estimated from a finite length sample. Therefore, while periodicity cannot be excluded with certainty, if such a periodic component was present, it would be very weak. Where $R_{\mathbf{U}}$ is outside the red transparent region, the null hypothesis that there is no correlation at and beyond that lag is rejected with a significance level of 95%. Instead, the null hypothesis cannot be rejected if $R_{\mathbf{U}}$ is within the band. The band was calculated according to the following formula:

$$b_{95\%}(l = 1) = \pm 1.96 \sqrt{\frac{1}{T}};$$

$$b_{95\%}(l \geq 2) = \pm 1.96 \sqrt{\frac{1}{T}\left(1 + 2\sum_{j=1}^{l-1} R_{\mathbf{U}}(j)^2\right)}.$$

Eq. III-15

The coefficient 1.96 is the 95% quantile of the standard normal distribution and the expression under square root is Bartlett's expression for the standard error.

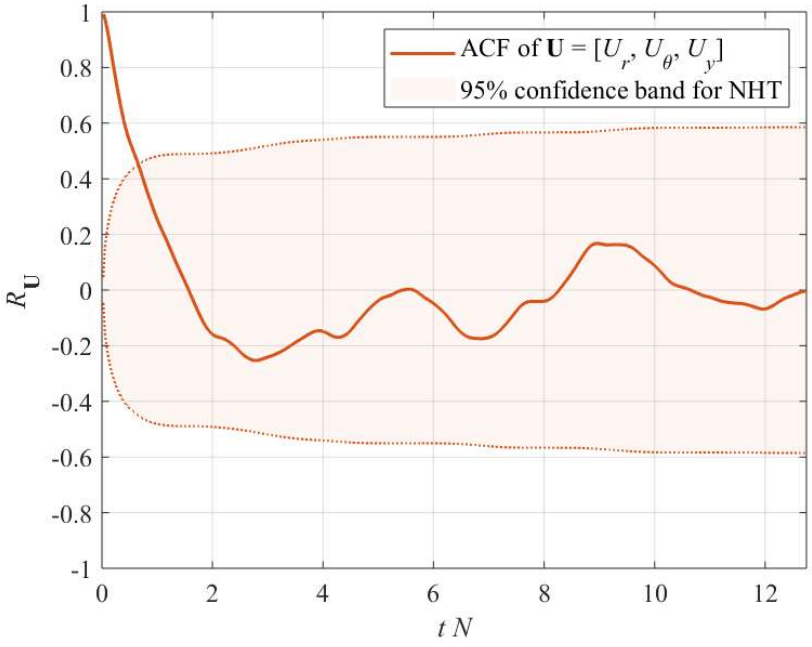

Figure III-11*: Example of the velocity autocorrelation curve for the trajectory shown in Fig. 9a.*

For that specific trajectory, the decorrelation time was 1.6 impeller revolutions, corresponding to ~0.48 s. ***Figure III-12a*** shows how the decorrelation time of the 188 investigated trajectories (on the horizontal axis) were distributed against the trajectory length (on the vertical axis) and the average velocity magnitude (in the colour bar). The absence of evident patterns indicates that the decorrelation time calculated with the proposed method was unaffected by the finite length of the trajectories ($\mathrm{PCC} = 0.13$). Therefore, the decorrelation time distribution in ***Figure III-12b*** was unbiased and characteristic of the flow. Instead, it was not possible to exclude an effect of the average velocity ($\mathrm{PCC} = -0.35$). Reasonably, shorter decorrelation times can be expected in the zones of the tank where the velocity is higher. Additional investigations should be carried out to address the role of velocity.

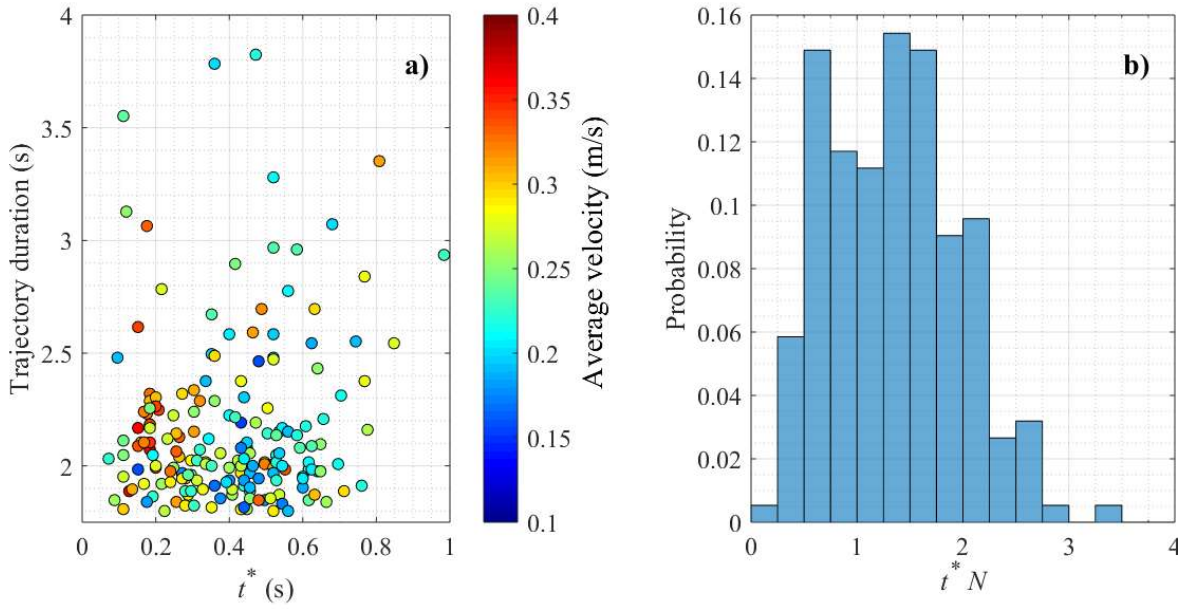

Figure III-12 *(a): Scatter of the decorrelation time against the trajectory duration, coloured in function of the average velocity along the trajectory. (b): Distribution of the normalised decorrelation time in the flow.*

III.4. Summary and conclusions

3D-PTV measurements have been conducted in a lab-scale tank operated in the high-transitional regime ($Re = 12{,}000$) and stirred with a Rushton turbine. The experimental rig consisted of a single camera setup with a two-view splitter. The capability of the 3D-PTV facility to measure the flow field in the vessel has been investigated.

The average error in the reconstructed coordinates, determined by means of the reference geometry used for image calibration, was 51 μm. The 98-th percentile, a more conservative statistic, was 255 μm. The error component in the depth, z, was about 5 times worse than those in x and y. The knowledge of the measurement error is of crucial importance in PTV experiments, as the frame rate and tracer concentration should be chosen accordingly.

The PTV operational variables have been optimized. It has been found that the best choice was to operate with 0.002 tracers per pixel. Higher concentrations (0.006 and 0.010 px^{-2}) led to a significant decrease in detection and tracking efficiency and higher computational cost. A lower value (0.001 px^{-2}) did not lead to higher efficiency, while of course it reduced the number of velocity vectors obtained. The best choice for the acquisition rate, given an impeller tip speed of $0.63\ m\ s^{-1}$, was 125 fps ($\varphi = 0.51$). Higher rates (500 and 3,600 fps) did not lead to higher tracking efficiency, while the error in the velocities would have been larger because of the smaller Δt. Values of the frame rate smaller than 125 fps have not been tested. The camera could potentially record at 60 fps, a too low acquisition rate for tracking the high-velocity particles in the impeller region. At the optimal conditions, the particle spacing displacement ratio (*Eq. III-4*) was $p = 1.95$. These results can be generalized for future measurements of similar flows. The optimal conditions can be adjusted by keeping the same normalised parameters $\varphi \sim 0.5$ and $p \sim 2$. In particular, the frame rate will scale linearly with the characteristic flow velocity (*Eq. III-2*), while the particle concentration will decrease with the

cubic power of the characteristic velocity (*Eq. III-4*). At the same time, it must be ensured that *Eq. III-1* and *Eq. III-5* are satisfied. Because these two equations represent two conflicting requirements, it is possible that only a limited range of flow velocities can be measured effectively for challenging experimental conditions.

The 3D Lagrangian coordinates obtained with the best operational conditions have been smoothed with five Savitzky-Golay filters of different width and polynomial order. The comparison of the reduced Chi-squared distributions of the filters suggested that a second order, 11-point filter was the best option among those investigated. Interestingly, a third order, 21-point filter did not perform better, suggesting that the Lagrangian acceleration is enough to describe the flow dynamics locally. The fitting residuals of the three spatial coordinates were normally distributed and not autocorrelated, with RMS of ± 38, ± 42 and ± 249 μm in x, y and z. The resulting 3D residuals were approximately log-normally distributed with mode at ~157 μm and RMS of 255 μm. In general, the choice of optimal filter could be different based on the flow characteristics and experimental conditions. However, the analysis of the Chi-squared distributions is an easy and quick task (the computations for ~10^6 data require a few minutes on a personal laptop). Thus, the best filter parameters can be determined with low efforts.

It has been shown that 3D-PTV can be used to obtain flow measurements in agitated vessels of lab-scale, provided that the operational variables are chosen correctly and the experimental error in the Lagrangian coordinates is reduced. Note that the velocity sequences can be filtered themselves, further enhancing the SNR and allowing the Lagrangian accelerations to be calculated. Velocity and acceleration data can be immensely useful for better understanding the flow dynamics inside agitated tanks. A method for estimating the flow decorrelation time scales from the autocorrelation of the velocity vectors has been proposed. This analysis requires a sufficient number of long trajectories. This approach could be used to compare flows as the

Reynolds number is changed, or with different impeller geometries, fluid rheology and tank scales.

The observations reported in this chapter can be easily generalized and represent a useful guideline for future PTV investigations in agitated vessels.

Chapter IV

3D-PTV FLOW MEASUREMENTS OF NEWTONIAN AND NON-NEWTONIAN FLUID BLENDING IN A BATCH VESSEL IN THE TRANSITIONAL FLOW REGIME

Abstract

Lagrangian trajectories obtained through 3D-PTV measurements have been used to visualize the flow field of Newtonian and non-Newtonian fluids in a flat-bottomed vessel. The vessel, of diameter $T = 180$ mm, was equipped with a 6-blade Rushton turbine of diameter $D = T/3$ and four baffles of width $B = T/10$. The experiments have been carried out in the transitional flow regime ($73 \leq Re \leq 1{,}257$). The velocities and Lagrangian accelerations in the flows have been calculated from the time-resolved tracer coordinates. Non-Newtonian fluids exhibited a smaller normalised flow rates compared to Newtonian fluids. The distributions of shear rate have been obtained via binning of the Lagrangian velocity data on a 3D Eulerian grid. In the impeller region, the mean shear rate was, to a first approximation, proportional to the impeller rotational speed, although a more detailed analysis revealed influences of both rheology and Reynolds number. The mean Lagrangian acceleration scaled with the mean shear rate raised to the power of 1.8.

IV.1. Introduction

As discussed in **§II.1.5**, industrial mixing operations in stirred vessels are frequently carried out under transitional flow conditions. However, most experimental and numerical studies reported in the literature focus on fully laminar or fully turbulent flows (Mendoza et al., 2018). Therefore, the transitional regime is still not well characterised (Machado et al., 2013), particularly when non-Newtonian rheology is involved. Furthermore, most experimental studies in agitated vessels have been carried out by means of Eulerian techniques, including PIV, LDA and Planar Laser Induced Fluorescence (PLIF). Lagrangian investigations of fluid mixing in stirred tanks have been rather limited. Some examples include the works by Rammohan et al. (2001, 2003) with Computer Automated Radioactive Particle Tracking (CARPT) and Chiti et al. (2011) using Positron Emission Particle Tracking (PEPT). Alberini et al. (2017) have applied PTV to transitional flows of non-Newtonian fluids in agitated vessels, but their analysis was limited to a comparison of the binned Eulerian velocity against PIV data. This chapter presents a novel investigation of the agitation of Newtonian and non-Newtonian fluids in a lab-scale vessel equipped with a Rushton turbine under transitional flow conditions using 3D-PTV. The effects of the fluid rheology on the flow dynamics have been assessed in terms of mean flow patterns, impeller flow numbers and distributions of shear rate and Lagrangian acceleration. A study of the volume-averaged shear rate in the impeller region has been carried out to test the validity of Metzner-Otto's assumption (*Eq. II-7*) in the low and mid transitional flow regime. This analysis is similar to those carried out by Ramírez-Muñoz et al. (2017) and Márquez-Baños et al. (2019), but is based on experimental data rather than numerical simulations. To the best of the candidate's knowledge, this is the first time that PTV has been applied to fluid mixing in agitated vessels in a wide range of experimental conditions.

Some of the measurements described here will be used in the next chapters for PTV-CFD cross-validation (**Chapter V**) and sale-up analysis (**Chapter VI**).

IV.2. Materials and methods

IV.2.1. Flow systems and experimental conditions

The flows investigated in this work were obtained by agitating different fluids in a transparent flat-bottomed cylindrical vessel of diameter $T = 180$ mm and height $H = T$. The tank was equipped with four baffles, of width $B = T/10$, and a 6-blade Rushton disc turbine, of diameter $D = T/3$ and placed at a clearance $C = T/3$ from the bottom. The impeller blades had width $D/4$, height $D/5$ and thickness of 2 mm. The geometry of the flow system is pictured in ***Figure IV-1***. The main vessel was immersed in a larger transparent square tank, filled with the same liquid, in order to minimize refractive distortion at the curved wall.

The six working fluids used were aqueous solutions of glycerol (75% and 80% wt. concentration), carboxymethylcellulose (CMC, 0.5% and 1.0% wt.) and polyacrylic acid (Carbopol 940, 0.1% wt. at pH 5.5 and 0.15% wt. at pH 5.0) at room temperature. The materials have been purchased from Sigma-Aldrich, US. The two glycerol solutions exhibited Newtonian rheology, as expected. The power-law model (*Eq. II-4*) and the Herschel-Bulkley model (*Eq. II-5*) have been used to describe the rheology of the CMC and Carbopol solutions, respectively. The rheological parameters of the fluids (***Table IV-1***) have been measured, immediately after the PTV image acquisition, with a rheometer (Discovery HR-1, TA Instruments, UK) equipped with a 40 mm flat plate geometry. K and n have been obtained through fitting of the flow sweep curves, while τ_0 has been determined at the crossover point

of the loss and storage moduli, through amplitude sweep measurements at a frequency of 10 Hz. The rheological data are given in **§A.6.1**.

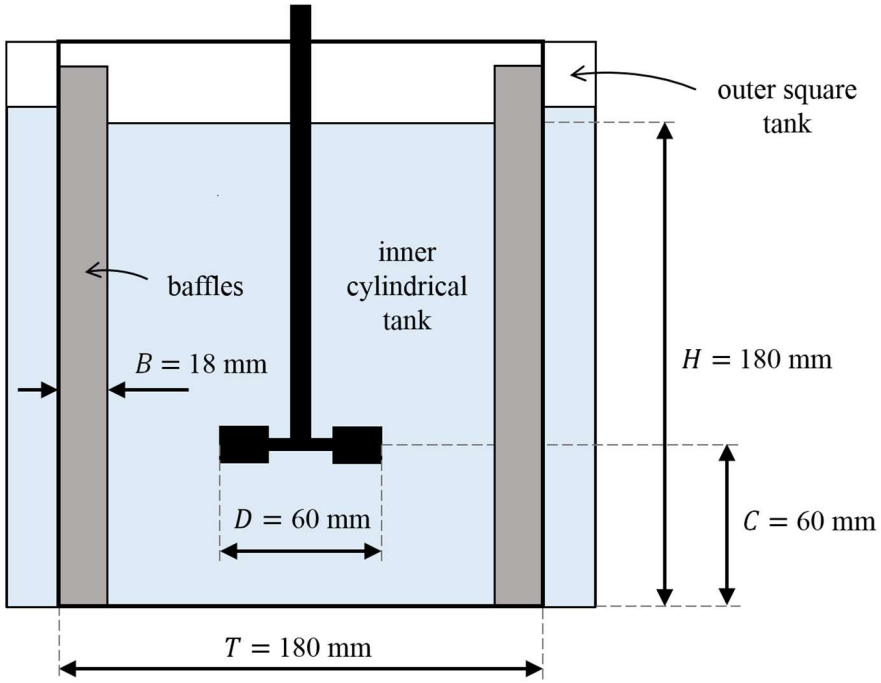

***Figure IV-1**: Schematic of the agitated vessel.*

***Table IV-1**: Density and rheological parameters of the working fluids.*

Label	Composition (in water)	ρ (kg m^{-3})	K (Pa s^n)	n	τ_0 (Pa)
NW1	Glycerol 75% wt.	$1{,}1\times10^3$	0.046	1	0
NW2	Glycerol 80% wt.	$1{,}2\times10^3$	0.17	1	0
PL1	CMC 0.5% wt.	$1{,}0\times10^3$	0.20	0.7	0
PL2	CMC 1.0% wt.	$1{,}0\times10^3$	0.70	0.7	0
HB1	Carbopol 0.10% wt. (pH 5.5)	$1{,}0\times10^3$	1.1	0.5	4.2
HB2	Carbopol 0.15% wt. (pH 5.0)	$1{,}0\times10^3$	4.4	0.5	43

Each liquid was mixed at various impeller speeds to obtain observations at different Reynolds numbers (***Table IV-2***). Although the flow regime was transitional, the Metzner-Otto model ($k_s = 11.5$) was used to estimate the apparent viscosity and Reynolds number of non-Newtonian fluids.

***Table IV-2**: Experimental conditions.*

Experiment	Fluid	Impeller speed (rpm)	Camera frame rate (s^{-1})	μ_e (Pa s)	Re
NW1a	NW1	400	250	4.60×10^{-2}	629
NW1b		600	500		943
NW1c		800	500		1,257
NW2a	NW2	200	125	1.70×10^{-1}	86
NW2b		600	250		258
PL1a	PL1	100	60	8.25×10^{-2}	73
PL1b		200	125	6.70×10^{-2}	179
PL1c		400	250	5.44×10^{-2}	441
PL1d		800	500	4.42×10^{-2}	1,086
PL2a	PL2	400	125	1.90×10^{-1}	126
PL2b		800	250	1.55×10^{-1}	310
HB1a	HB1	400	125	1.80×10^{-1}	133
HB1b		600	250	1.39×10^{-1}	259
HB1c		800	250	1.16×10^{-1}	413
HB1d		1,000	500	1.01×10^{-1}	592
HB2a	HB2	1,200	500	4.77×10^{-1}	151
HB2b		1,500	1,000	4.09×10^{-1}	220

IV.2.2. 3D-PTV measurements

IV.2.2.1. Tracer particles

Polyethylene microspheres (Cospheric, US) have been used as tracer particles. Their size was 750 – 820 μm. The tracers utilized with the CMC and Carbopol solutions had a density of 1.0×10^3 kg m^{-3}. For the glycerol solutions, the tracer density was 1.1×10^3 kg m^{-3}. Buoyancy effects were negligible. In all experiments, the tracers' Stokes number was small (maximum value was 1.1×10^{-1} in experiment PL2b), and the effects of Magnus force (F_M), Basset force (F_B) and Saffman force (F_S) were negligible compared to the drag force (F_d). Thus, the tracers

could adequately follow the fluid element trajectories and resolve the mean flow features down to a scale of ~820 μm. Turbulent scales were not investigated, as the current PTV setup could not resolve them. A complete assessment of the Stokes numbers and force effects in the experiments can be found in **§A.4**. ***Table IV-3*** lists the final estimations, which are highly conservative.

The tracer concentration was roughly 114 L^{-1}, which corresponded to a blur image density of 0.002 px^{-2}. With a particle image size between 3 and 4 px, the ratio of indistinguishably overlapping particles was between 0.7% and 1.2% (Cierpka et al., 2013).

Table IV-3*: Stokes number and force ratios in the PTV experiments. Maxima in bold*

Experiment	St	$\frac{F_M}{F_d}$ (small Re_p)	$\frac{F_M}{F_d}$ (large Re_p)	$\frac{F_B}{F_d}$	$\frac{F_S}{F_d}$ (small Re_p)
NW1a	3.17E-02	5.05E-04	8.22E-03	9.06E-03	2.06E-02
NW1b	4.70E-02	7.57E-04	1.23E-02	1.34E-02	2.52E-02
NW1c	6.20E-02	1.01E-03	1.64E-02	**1.78E-02**	2.92E-02
NW2a	4.40E-03	6.83E-05	4.11E-03	1.44E-03	7.58E-03
NW2b	1.31E-02	2.05E-04	1.23E-02	4.28E-03	1.31E-02
PL1a	8.19E-03	1.28E-04	2.06E-03	5.01E-04	1.04E-02
PL1b	1.99E-02	3.15E-04	4.11E-03	1.22E-03	1.63E-02
PL1c	4.80E-02	7.74E-04	8.22E-03	2.94E-03	2.55E-02
PL1d	**1.14E-01**	**1.91E-03**	1.64E-02	6.97E-03	**4.01E-02**
PL2a	1.41E-02	2.21E-04	8.22E-03	8.63E-04	1.36E-02
PL2b	3.41E-02	5.45E-04	1.64E-02	2.09E-03	2.14E-02
HB1a	2.93E-02	4.67E-04	8.22E-03	1.80E-03	1.98E-02
HB1b	5.42E-02	8.78E-04	1.23E-02	3.32E-03	2.72E-02
HB1c	8.31E-02	1.37E-03	1.64E-02	5.09E-03	3.40E-02
HB1d	2.70E-02	4.29E-04	2.06E-02	1.65E-03	1.90E-02
HB2a	3.58E-02	5.74E-04	2.47E-02	2.19E-03	2.20E-02
HB2b	5.05E-02	8.16E-04	**3.08E-02**	3.09E-03	2.62E-02

IV.2.2.2. Image acquisition and processing

The raw images of the flows were acquired by means of the hardware described in **§III.2.2**. Each experiment consisted of 5,400 frames. The acquisition rate (***Table IV-2***) has been selected depending on the impeller speed and an estimation of the experimental error, following the guidelines discussed in **§III.2.4.1**. The distance travelled by the tracers between consecutive time steps was in the order of 1 – 10 mm, depending on their velocity. The exposure time was 1/2000 s for the two CMC solutions and 1/3600 s for all other fluids, so that tracers appeared spherical in the images.

The images were processed as described in **§III.2.2**. The output of this step consisted in a list containing the image coordinates of the detected tracers, in each half-image and each time step.

IV.2.2.3. Image calibration and coordinate reconstruction error

The calibration routine has been conducted as described in **§III.2.3**. The error in the reconstructed tracer coordinates was determined by the quality of the image calibration. This was influenced by the properties of the multi-media optical path, the fluid opaqueness in particular. The glycerol and Carbopol solutions were highly transparent, and the reference dots were reconstructed with an average error of ~60 μm. In the case of the CMC solutions, which were slightly opaque, the average reconstruction error was ~180 μm. These errors were reduced before the computation of velocity and acceleration by means of a Savitzky-Golay filter, as described in **§III.2.5.1**.

IV.2.2.4. 3D particle tracking, velocity and acceleration determination

The tracking algorithm developed by Willneff (2003) has been used. Only the trajectories longer than 21 time steps were kept, in order to minimize the chance of wrong stereo and temporal links. In addition, only the data in the front half of the tank ($z < 0$) were used. This was because the coordinates at the back ($z > 0$) were determined with a larger uncertainty, due

to perspective size reduction of the tracers and attenuation of the scattered light through the longer optical path.

The velocity components along the individual trajectories have been obtained by finite differentiation of the coordinates. To avoid amplification of the experimental error, a second order, 11-point Savitzky-Golay filter has been applied. The velocity components along the trajectories have been calculated with a centred differences scheme from the corresponding coordinates (*Eq. IV-1*), and then filtered themselves. In the same way, the Lagrangian acceleration components have been obtained through differentiation of the velocities (*Eq. IV-2*) and then filtered.

$$u_j = \frac{x_{j+1} - x_{j-1}}{t_{j+1} - t_{j-1}}. \qquad \textit{Eq. IV-1}$$

$$a_j = \frac{u_{j+1} - u_{j-1}}{t_{j+1} - t_{j-1}}. \qquad \textit{Eq. IV-2}$$

In the equations above, the subscript j indicates the time step. The Lagrangian acceleration is a measure of the force acting on an infinitesimal element of fluid which moves with the local and instantaneous flow. It is responsible for stretching, contraction and curvature of the fluid element. The statistics of Lagrangian acceleration are of great importance in turbulence research, as they are related to the intermittent bursts of vorticity and strain that characterize turbulent flows (Zeff et al., 2003). Large values of acceleration and energy dissipation are strongly correlated (Reynolds et al., 2005). Acceleration data can also be used to calculate instantaneous pressure fields by integration of the pressure gradient term in the Navier–Stokes equations for incompressible flow (van Gent et al., 2017; Shaffer et al., 2021). To the best of the candidate's knowledge, experimental data of instantaneous acceleration along real Lagrangian trajectories in stirred tanks have never been reported before this work.

IV.2.3. Data post-processing

IV.2.3.1. Impeller flow rates

The impeller flow rates have been calculated, according to *Eq. II-11*, at a distance $D/2$ from the impeller tip, that is halfway between the impeller tip and the tank wall ($r = T/3$). This choice was motivated by the following considerations. In the region very close to the impeller, the tracking efficiency, i.e. the number of obtained velocity data per volume, was low due to the presence of the impeller and to the longer optical path of the light scattered by the tracers through the fluid. On the other hand, the extension of the impeller discharge jet diminished with the viscosity of the fluid, and in the case of cavern formation the velocity at large r was essentially null. In the literature, the flow rates are typically evaluated very close to the impeller tip ($r = T/6$). In order to account for the different radial coordinate, the flow rates have been scaled by a factor of 2. Then the flow rates have been normalised by D^3N as per *Eq. II-10*. A perfect match with the impeller flow numbers reported in the literature is not expected, because the impeller jet is quite diffusive, and the radial velocity decreases quickly with the distance from the impeller. Nevertheless, this analysis allowed the effects of fluid rheology and Reynolds number on the impeller pumping capacity to be assessed.

IV.2.3.2. Shear rate

The Lagrangian velocity data have been interpolated on a 3D Eulerian grid to obtain the mean 3D velocity fields. The grid was equi-spaced in the three Cartesian directions. This allowed the spatial derivatives of the velocity to be calculated with a centred difference scheme, and the full gradient tensor to be obtained in each node. Then, the shear rate was calculated in each node as

$$\dot{\gamma} = \sqrt{2\,\mathbf{S}:\mathbf{S}}\,, \qquad \textit{Eq. IV-3}$$

where **S** is the symmetric part of the gradient. Since the non-Newtonian fluids formed pseudo-caverns and caverns, not only the shear rate distributions in the whole tank were calculated, but also those limited to an arbitrarily defined impeller region, i.e.:

$$\begin{cases} r \leq D \\ C - \frac{D}{4} \leq y \leq C + \frac{D}{4} \end{cases}. \qquad \textit{Eq. IV-4}$$

This also allowed the validity of Metzner-Otto's approach under transitional flow conditions to be assessed. *Eq. IV-3* is expected to underestimate the true shear rate due to the finite grid spacing, particularly in those regions at higher turbulence intensity. The grid spacing is therefore a compromise between the resolution of sharper gradients and their statistical reliability. With a 3 mm grid spacing, 87,901 nodes were used for the half tank and 7,139 nodes for the half impeller region. This allowed more than 10 velocity events to be typically binned in each cell, although a lesser number was present in some cells very close to the impeller and to the tank walls. Since the shear rate maps were determined from the mean velocities, the uncertainty associated to the shear rate was essentially due to the variance in the collections of velocity events within each cell. The standard error was selected as a metric for the shear rate uncertainty. With a 3 mm spacing, the standard error was in the order of a few percent of the shear in most of the vessel, while values close to ~10% were observed in the impeller jet, where the velocity variance was higher. In order to assess the effect of the finite spacing on the shear rate estimation, a grid of 2 mm has also been tested (293,566 nodes for the half vessel, 21,615 in the impeller region). Considering the experiments with fluids PL1, PL2, HB1, and NW2, the mean shear rate in the impeller region was, on average, 4.9% higher than that calculated with the 3 mm spacing; for fluid NW1, the differences between the two grids were larger (+12% to +18% with the 2 mm grid). For fluid HB2, the average shear rate was 1.6% lower using the 2 mm grid (this was probably just a binning effect, as shear decrease with grid refinement is not physically meaningful). However, with the smaller spacing, the number of velocity vectors per

node obviously reduced, resulting in a few empty nodes and a noisy interpolation (over-binning). Consequently, the uncertainty in the mean velocities (hence in the shear rate) was unacceptable. For this reason, it has been decided to use the 3 mm grid. Note that the current spacing limitation is not related to PTV resolution and could be overcome by extending the size of the data set and ensuring a large number of velocity data per node. This could be achieved in many ways – one is to increase the number of recorded frames to more than 5,400.

IV.2.3.3. Statistical convergence of the velocity measurements

The statistical convergence of the velocity measurements has been validated by monitoring its ensemble average and ensemble standard deviation in three sample volumes as a function of the number of events. The sample volumes were semi-annular voxels of volume $V_s = 0.1\%\ (V_{tank}/2) = 2.3\ \text{cm}^3$ located in the impeller region, close to the vessel wall and in the bulk flow. In all experiments, both the average and the standard deviation were independent of the number of events. This analysis if thoroughly described in **§A.2.2**.

IV.2.3.4. Mean Square Displacement

An interesting quantity that can be calculated from 3D-PTV Lagrangian data is the Mean Square Displacement (MSD) of the particles passing through a control volume, as a function of time. The MSD is defined as:

$$\text{MSD}(t) = \frac{1}{m}\sum_{i=1}^{m}\left(\mathbf{x}_i(t) - \mathbf{x}_i(t_0)\right)^2. \qquad \textit{Eq. IV-5}$$

Here the index i identifies the tracer, $\mathbf{x}$ is the position vector, t is time and t_0 is the reference time. The MSD can be used to quantify long range dispersion (La Forgia et al., 2022) and self-diffusion coefficients (Wildman et al., 1999; Windows-Yule and Parker, 2014) from time-resolved Lagrangian data. For each PTV experiment, the MSD has been calculated using the trajectories entering the three sample volumes described in **§IV.2.3.3**.

IV.3. Results and discussion

IV.3.1. Flow fields visualisation

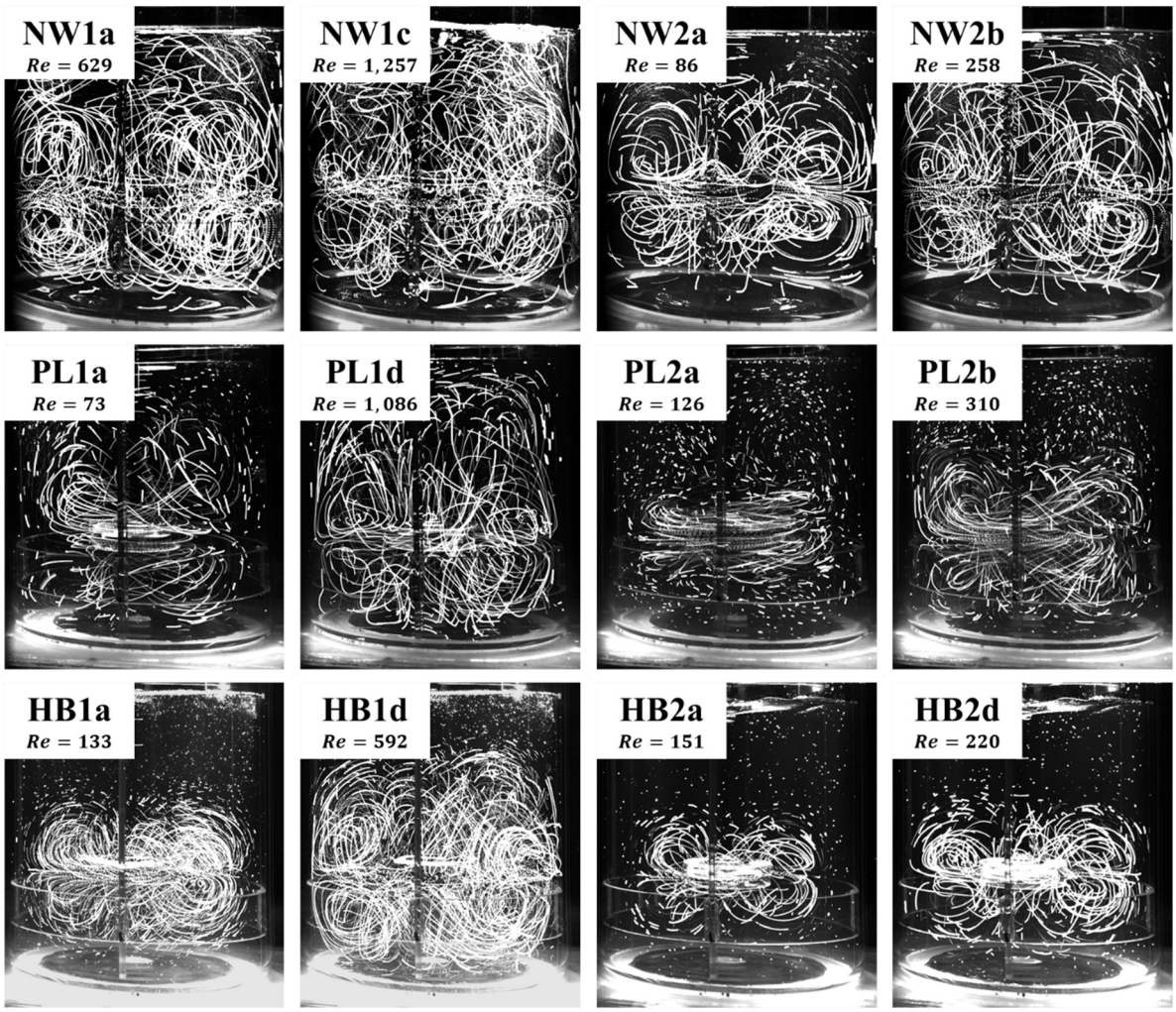

***Figure IV-2**: Tracer path lines obtained by superimposition of the raw images. The labels indicate the experiment.*

A qualitative visualisation of the investigated flows, obtained by superimposing the raw Lagrangian trajectories over four impeller revolutions, is given in ***Figure IV-2***. The white stripes represent the paths taken by the tracers and illustrate the overall flow patterns in the vessel. At low values of Re, the power-law fluids formed pseudo-caverns and showed low axial circulation, whereas the Herschel-Bulkley solutions formed caverns, with the flow remaining effectively stagnant outside the cavern volume.

Figure IV-3 shows some examples of 3D trajectories obtained after PTV data processing. The colour denotes the magnitude of the velocity, normalized by the tip speed. To facilitate visualisation, only reduced samples of trajectories are shown, i.e. 5% - 8% of the original data sets. For the two Newtonian fluids, the overall flow patterns were independent of the Reynolds number in the investigated range. The tracers entering the impeller region were discharged radially and followed one of the two recirculation loops, above or below the plane of the impeller. The lower loop reached the tank bottom, while the upper loop extended to about two thirds of the vessel height. The flow interacted significantly with the tank wall and the baffles, creating systematic paths (***Figures IV-3a*** and ***IV-3b***). Such features were present in all the Reynolds numbers investigated. In the region downstream of the baffles, a small portion of fluid moved downward at low velocity (~5% of the tip speed), met the upper circulation loop and gained tangential velocity. Upstream of the baffles, the liquid flowed upwards to feed the upper circulation loop. This mechanism was responsible for the material turnover with the top of the tank. As the Reynolds number was increased, a slight increase in velocity magnitude was only observed close to walls and baffles.

With the two power-law fluids, the flow features and local velocity components changed completely with the Reynolds number. This was already visible in ***Figure IV-2***. In experiment PL1a, the near-impeller flow was almost completely tangential, with very low circulation in the radial and axial directions (***Figure IV-3c***). In this case, the degree of agitation was not enough to maintain a substantial convection of fluid between the lower and the upper part of the tank. This was due to the shear thinning behaviour of the fluid, which dampened the momentum transfer. The extension of the impeller discharge stream, the magnitude of radial velocity in it and the intensity of the two circulation loops increased gradually with the rotational speed. The downflow behind the baffles, observed with the Newtonian fluids, was only present in experiment PL1d (***Figure IV-3d***), but with a much smaller velocity (~1% of

the tip speed). Dead zones of low velocity were present at the top of the vessel and in the proximity of the baffles. ***Figure IV-4*** illustrates the effect of the Reynolds number on the extension of the pseudo-caverns formed by the fluids. As in the work by Adams and Barigou (2007), the boundaries have been identified as the isoline corresponding to a fluid velocity equal to 1% of the tip speed.

With the two Herschel-Bulkley fluids, the tracer particles were only tracked within the caverns around the impeller. No fluid exchange occurred with the region outside. At low Reynolds number, the fluid discharged by the impeller reached the cavern boundary and simply flowed back towards the impeller along two circulation paths, one above and one below the impeller plane (***Figure IV-3e***). As the Reynolds number increased, the caverns expanded in size (***Figure IV-4***), reaching the vessel bottom and the wall (***Figure IV-3f***). However, since the fluid at the top of the vessel was still, the downflow behind the baffles was not observed. In the literature, the models used to predict the cavern size assume a spherical, toroidal or cylindrical shape of the cavern (Amanullah et al., 1998). Clearly, the caverns shown in ***Figure IV-4*** have a much more complex shape. Adams (2009) compared PEPT measurements and CFD predictions of caverns formed by complex fluids. While the agreement between experimental and numerical data was satisfactory, theoretical models predicted the cavern size and shape very poorly.

Since both the pseudo-cavern and cavern boundaries were defined according to the same criterion of velocity threshold, a comparison can be made between the four non-Newtonian liquids. Interestingly, different fluids showed different cavern extensions at similar Reynolds conditions (***Figure IV-4***), indicating that the phenomenon of (pseudo-) cavern formation is rheology dependent. In particular, the experiments PL2a ($Re = 126$) and PL1b ($Re = 179$) show extreme differences. Between the experiments HB1a ($Re = 133$) and HB2a ($Re = 151$), the differences are smaller. Therefore, ***Figure IV-4*** seems to indicate that the higher the flow index (n), the larger the effects of the consistency index (K) on the (pseudo-) cavern extension.

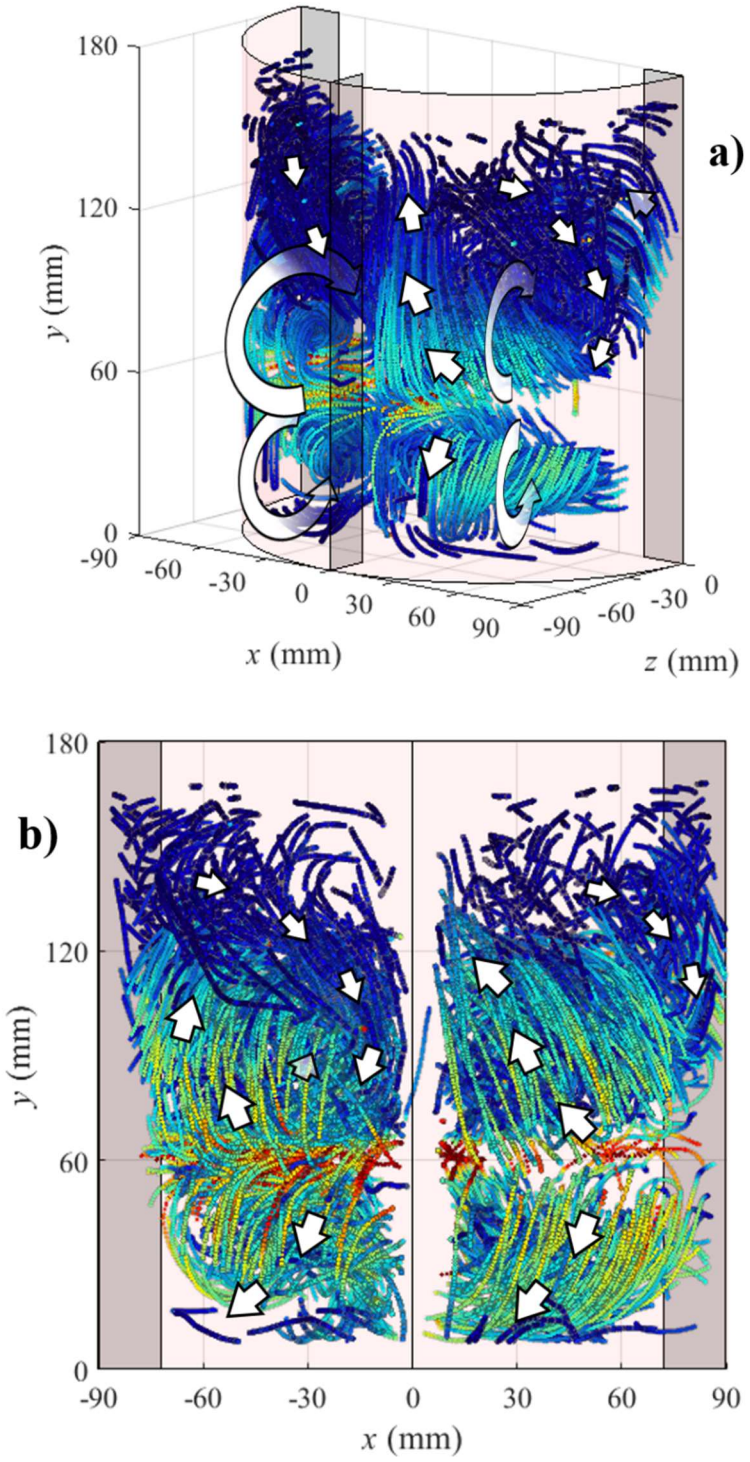

Figure IV-3*: Examples of 3D-PTV trajectories sampled from experiments. (a): NW2b, Re = 258; (b): NW1a, Re = 629; (c): PL1a, Re = 73; (d): PL1d, Re = 1,086; (e): HB2a, Re = 151; (f): HB1c, Re = 413. The impeller rotates clockwise. (Continues in the next pages).*

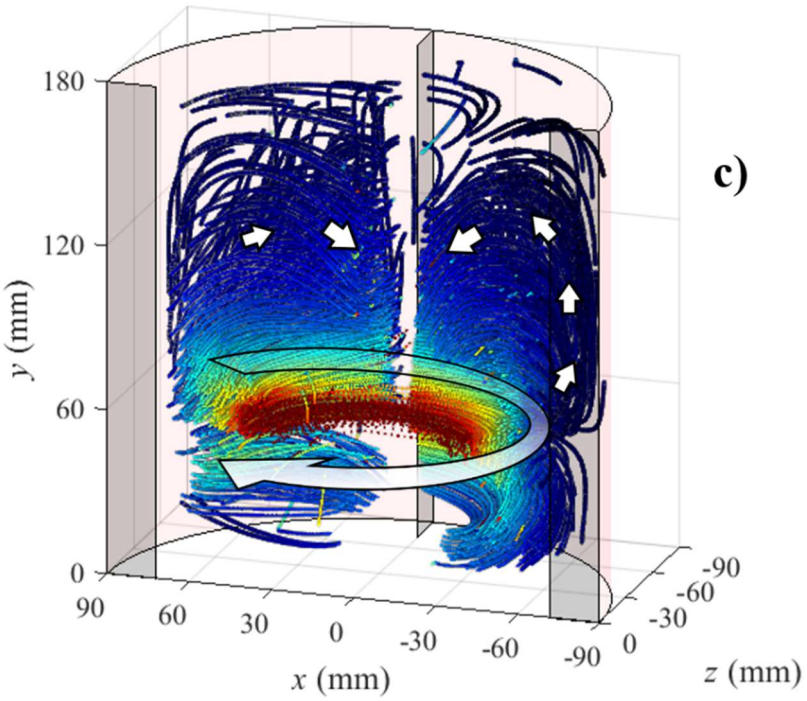

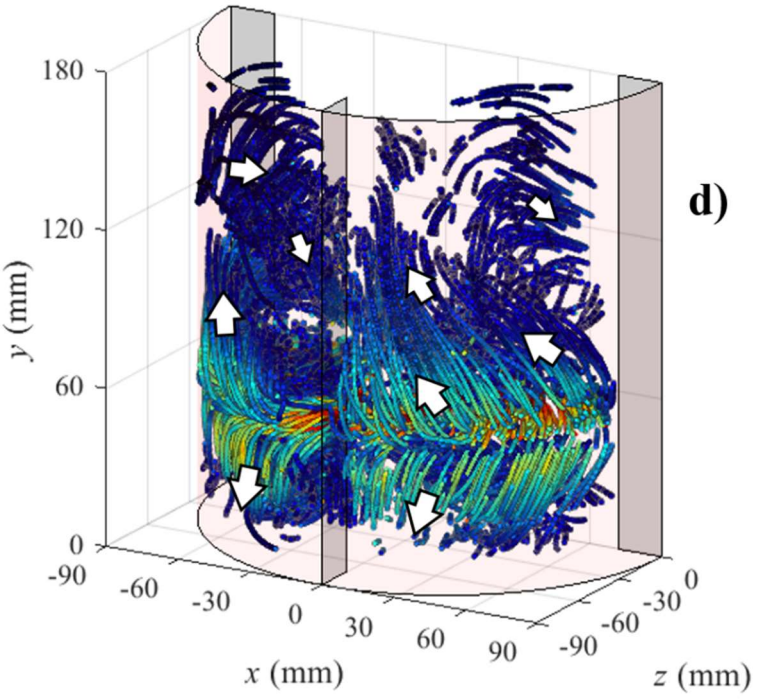

Figure IV-3 *(continues).*

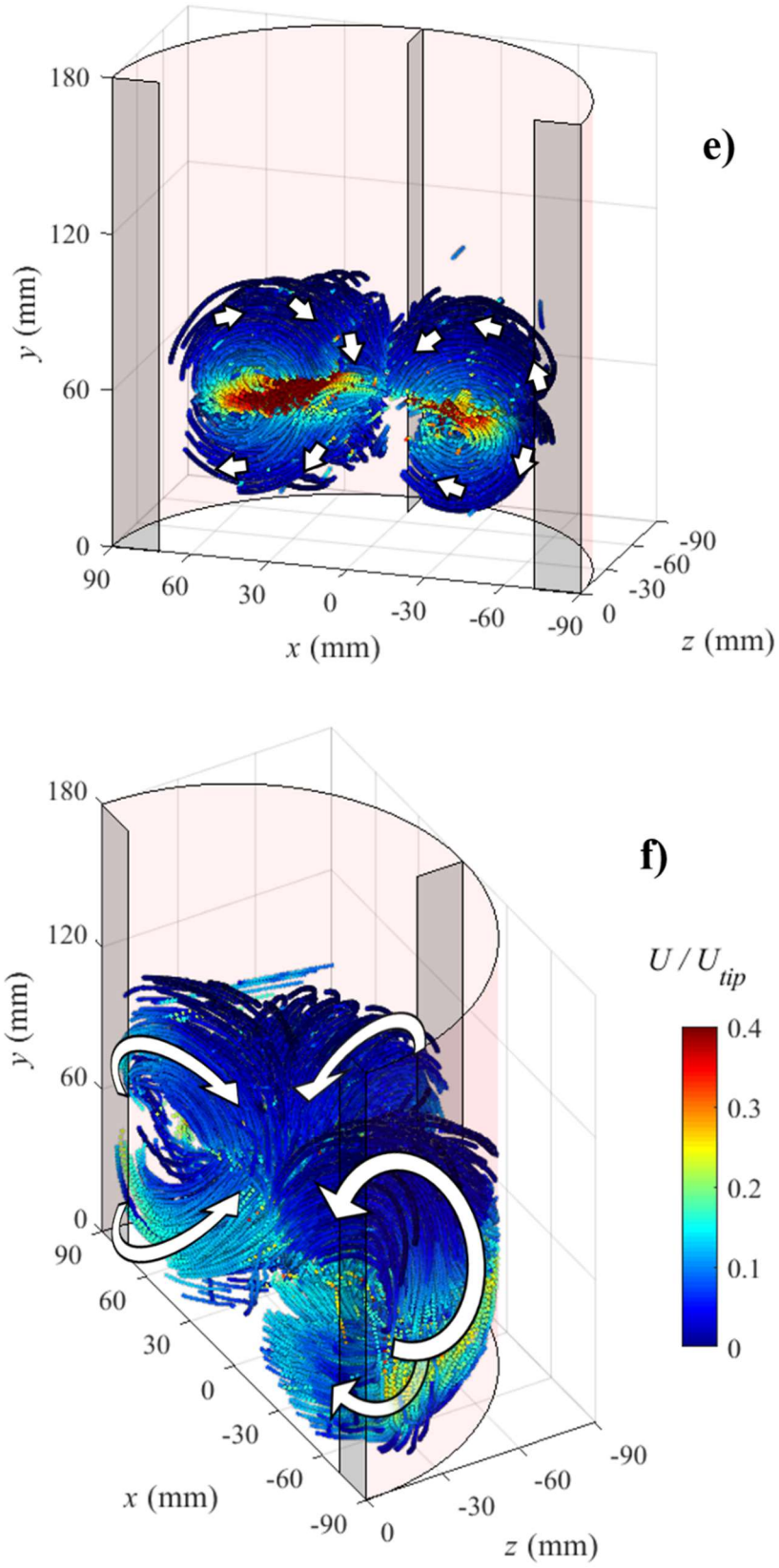

Figure IV-3 *(continues).*

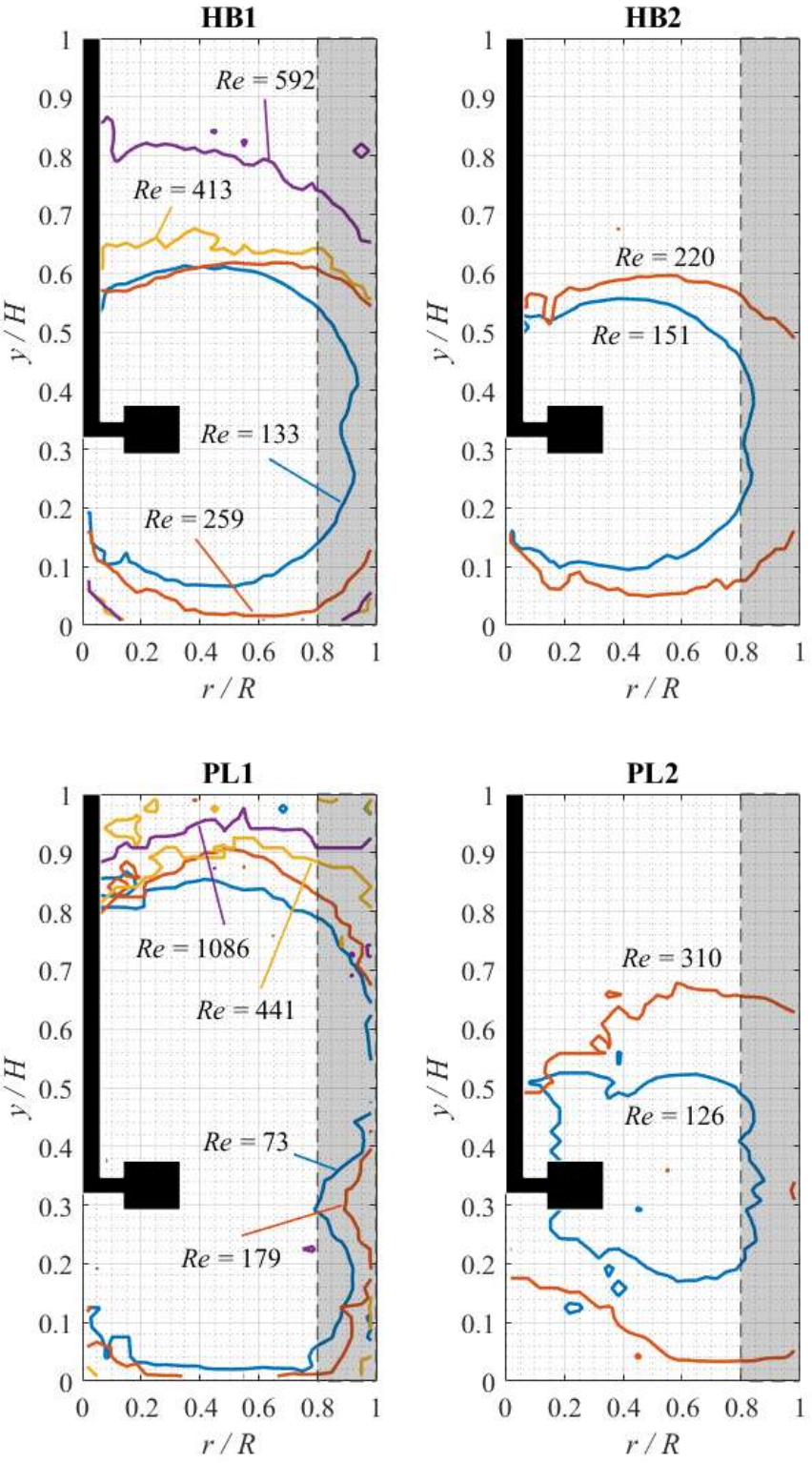

***Figure IV-4**: Pseudo-cavern and cavern boundaries as measured form PTV velocity data.*

IV.3.2. Impeller flow rates

In ***Figure IV-5a***, the flow rates are plotted against the group $ND^{2.2}W(\rho/\mu_a)^{0.5}$, which was used by Norwood and Metzner (1960) to fit their measurements (*Eq. II-12*). Here $\mu_a = K\dot{\gamma}_e^{n-1}$ is the 'adjusted' viscosity due to shear, in which yield stress is not considered. It only differs from the Metzner-Otto effective viscosity in the case of the yield stress fluids. The reason for this modification is that the flowing fluid does not experience the effects of the yield stress, hence the volumetric flow rate only depends on shear rate. The proportionality fitting in ***Figure IV-5a*** gave a coefficient of determination of 0.76, which is reasonably high for 17 experimental measurements at various conditions. ***Figure IV-5b*** shows the normalised flow numbers measured against the adjusted Reynolds number, $Re_a = \rho D^2 N/\mu_a$. Since the flow rates were calculated at $r = T/3$ instead of the typical $r = T/6$, the values were slightly lower than those reported in the literature. Nevertheless, their trends were very informative. For the Newtonian fluids, the normalised flow rate scaled as ${Re_a}^{0.036}$. A very similar scaling (${Re_a}^{0.034}$) was reported by Venneker et al. (2010) in the transitional regime. At high Re, the flow number of the RT should reach about 0.7 and become constant (Hemrajani and Tatterson, 2003). Non-Newtonian fluids were characterized by smaller normalised flow rates than Newtonian fluids. For $Re_a < \sim 400$, Q/ND^3 increased as ${Re_a}^{1.1}$. For $Re_a > \sim 400$, Q/ND^3 was proportional to ${Re_a}^{0.23}$, approaching the curve of the Newtonian fluids. The exponents agree with those obtained by Koutsakos et al. (1990) and Dyster et al. (1993). Flow rate data, together with previous observations, suggest that a gradual change in the non-Newtonian flow dynamics occurred around $Re \sim 400$, due to the incipient interactions between the inner flow around the impeller and the outer flow close to the baffles and walls. In a previous study using DNS data (Tamburini et al., 2018), the same mechanism was evoked to explain the gradual transition from laminar to turbulent flow, in the range of Re between 150 and 600, and the different behaviour the flow between baffled and unbaffled vessels. It can be concluded that the capacity

of a Rushton turbine to pump a non-Newtonian fluid around a vessel becomes very poor below $Re{\sim}400$. For Newtonian fluids, previous works report a similar decrease in pumping capacity for $Re_a < {\sim}100$ (Lamberto et al., 1999; Rice et al., 2006; Venneker et al., 2010). Practitioners should take a different geometry into consideration for such mixing conditions. For example, close-clearance impellers are designed to physically turnover highly viscous fluids in the whole vessel at low Reynolds numbers (Hemrajani and Tatterson, 2003).

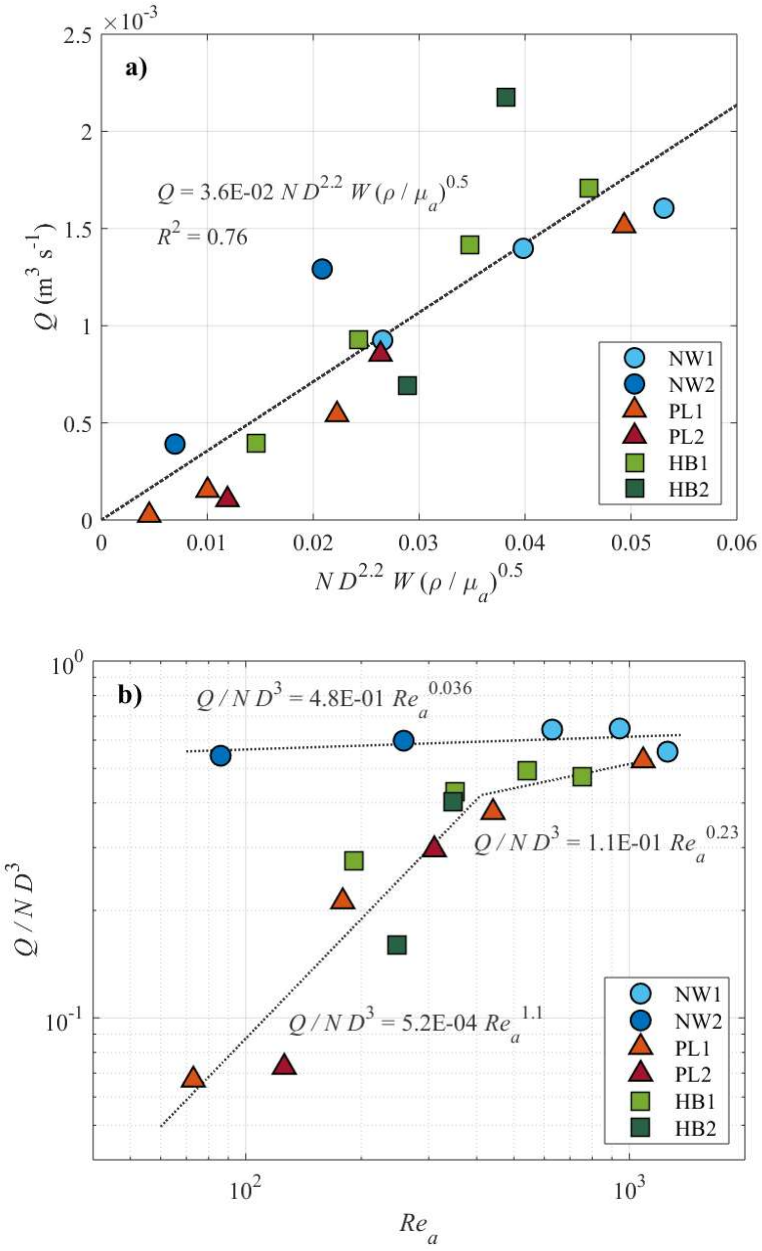

Figure IV-5*: Fitting of the flow rates against Norwood and Metzner's correlation group (a) and impeller flow number against Reynolds number (b).*

IV.3.3. Distributions of shear rate and Lagrangian acceleration

In all the experiments, both the shear rate and the Lagrangian acceleration were distributed in logarithmic space, spanning different orders of magnitude. This reflects the variety of fluid dynamics conditions at different locations within the vessel.

The shear rate was higher in the region surrounding the impeller, and the differences with the overall distribution were particularly significant with the non-Newtonian fluids (***Figures IV-6a-c*** and ***IV-7a***), due to the larger spatial variability of the flows. In the case of Newtonian fluids, the shear rate was distributed log-normally both in the impeller region and in the entire vessel. It is being understood that the shear rate decreases with distance from the impeller blade, this transition was smooth, and the fluid remained sufficiently and uniformly sheared also in the bulk, where $\dot{\gamma} \sim N$. Instead, the distributions of the non-Newtonian fluids in the entire vessels tended towards bimodality, due to pseudo-cavern and cavern formation. Shear rate decreased very quickly – more than one order of magnitude – close to the (pseudo-) cavern boundary. With the power law fluids, the flow occurred even outside of the pseudo-caverns, which is a significant fraction of the vessel volume, albeit with very low velocities and shear rates ($\dot{\gamma} \sim 10^{-1}\, N$). Instead, with the Herschel-Bulkley fluids, very low shear rates were confined close to the cavern boundary. As anticipated in **§IV.2.3.2**, the standard error associated to the shear rate maps was in the order of a few percent in most of the tank and about ~10% in the impeller discharge region, due to the higher velocity variance there. These values could be reduced by increasing the size of the datasets. One example of error map is pictured in ***Figure IV-6d***. Three examples of shear distributions are illustrated in ***Figure IV-7a***. Clearly, the curves were dependent on fluid rheology for the reasons discussed above. However, the means of the curves were relatively close, therefore some fitting models were attempted. The analysis focused on the impeller region because of its importance to the mixing process and to assess the validity of Metzner-Otto's assumption. Considering all working fluids, the best

power-law fitting of the average shear rate against the impeller rotational speed gave an exponent of 1.08 (***Figure IV-8a***). The bars in ***Figure IV-8*** represent one standard deviation of the individual shear distributions in logarithmic space, therefore they should not be intended as confidence intervals (due to the large data sets, the standard error of the mean was extremely small). A simple proportionality law, i.e. $\langle\dot{\gamma}\rangle = 6.1\,N$, still predicts the mean shear rate characterising the near-impeller flow with reasonable accuracy ($R^2 = 0.85$). As already pointed out, the value of the proportionality constant, $k_S^* = 6.1$, depends on the volume and shape of the impeller region, which was defined arbitrarily. The impeller region used in this paper is comparable to the control volume labelled 'ESV' in the work by Ramírez-Muñoz et al. (2017), although some differences were present. The exact dimensions of ESV were not reported (ESV appears smaller than the impeller region here), their tank had a curved bottom and the flow regime was laminar. In ESV, Ramírez-Muñoz et al. (2017) measured $k_S^* = 7.2$.

The high coefficients of determination ($R^2 = 0.92$ and $R^2 = 0.85$) of the 'all-fluids' fittings suggest that rheology effects, if present, were small compared to the variation of shear rate attributable to the impeller speed. However, the shear rate measured with the Newtonian fluids was systematically higher than with non-Newtonian fluids, N being the same. For this reason, the data have been categorised as Newtonian or non-Newtonian and two additional fittings have been calculated separately (***Figure IV-8a***). Indeed, these have higher coefficient of determination than the overall fittings, meaning that the classification into two subsets based on fluid rheology has helped explain a larger share of variance in the data. In the case of Newtonian fluids, $k_S^* = 8.4$ ($R^2 = 0.94$), while $k_S^* = 5.6$ ($R^2 = 0.97$) for the non-Newtonian fluids. Further to this analysis, a dependency of $k_S^* = \langle\dot{\gamma}\rangle/N$ on Re was also tested (***Figure IV-8b***). Again, Newtonian and non-Newtonian data were fitted separately (*Eq. IV-6* and *IV-7*). A linear model was chosen because k_S^* is expected to become constant in the limit of low Re, that is under fully laminar conditions.

$$\langle \dot{\gamma} \rangle_N = (6.8 + 2.0 \cdot 10^{-3}\, Re)\, N; \qquad \textit{Eq. IV-6}$$

$$\langle \dot{\gamma} \rangle_{NN} = (4.8 + 1.6 \cdot 10^{-3}\, Re)\, N. \qquad \textit{Eq. IV-7}$$

In the first case, the predicted normalised shear rate changed from 6.9 to 9.3 in the range of Re between 86 (experiment NW2a) and 1,257 (NW1c). With the non-Newtonian fluids, the predicted k_s^* changed from 4.9 to 6.5 in the range of Re between 73 (experiment PL1a) and 1,086 (PL1d). Numerically, the effects of the Reynolds number become increasingly significant when $Re > \sim 300$. This reflects the gradual deviation from Metzner-Otto's scaling rule as Reynolds number increases. Note that the coefficients of determination of *Eq. IV-6* and *Eq. IV-7* refer to the residual variance in the data, once the variation of shear due to the impeller speed has already been accounted for by fitting $\langle \dot{\gamma} \rangle / N$ as a dependent variable.

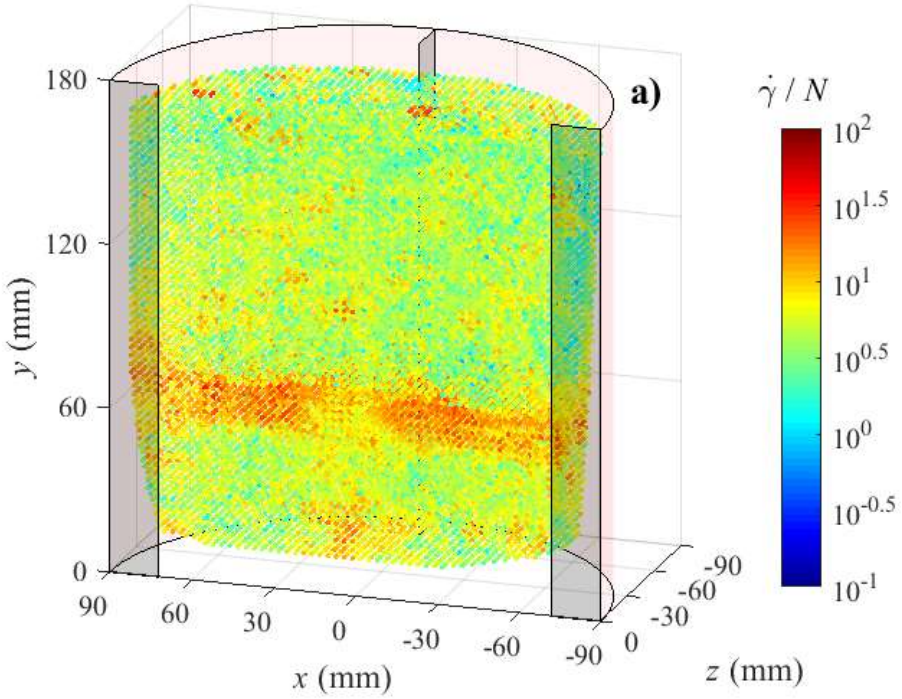

Figure IV-6*: Examples of normalised shear rate maps in the vessel. (a) experiment NW1c; (b) experiment PL2a; (c) experiment HB2a. Subfigure (d) shows the standard error of the shear rate for experiment NW1c. (Continues in the next pages)*

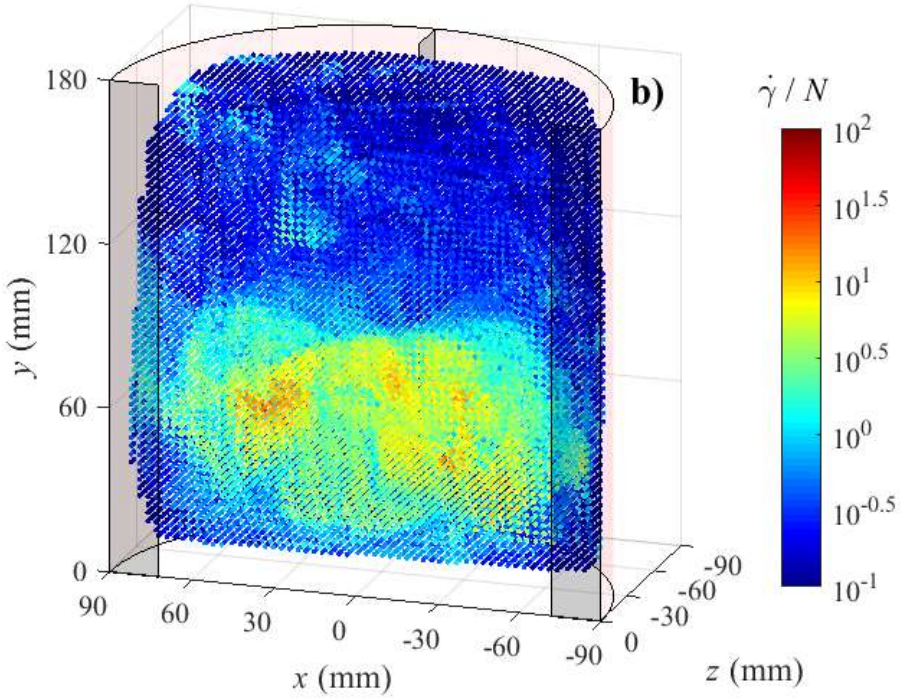

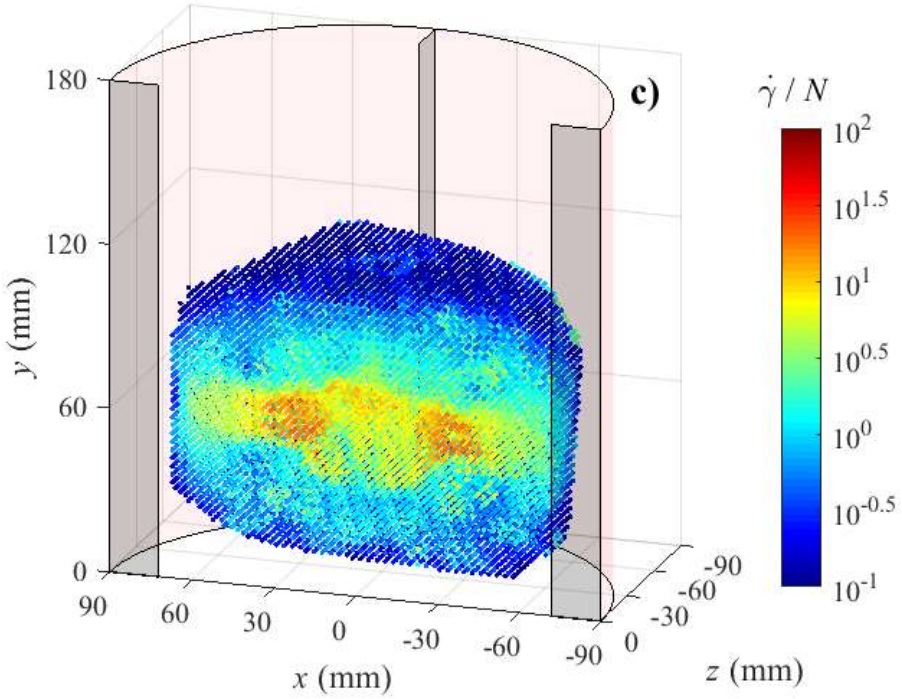

Figure IV-6 *(continues).*

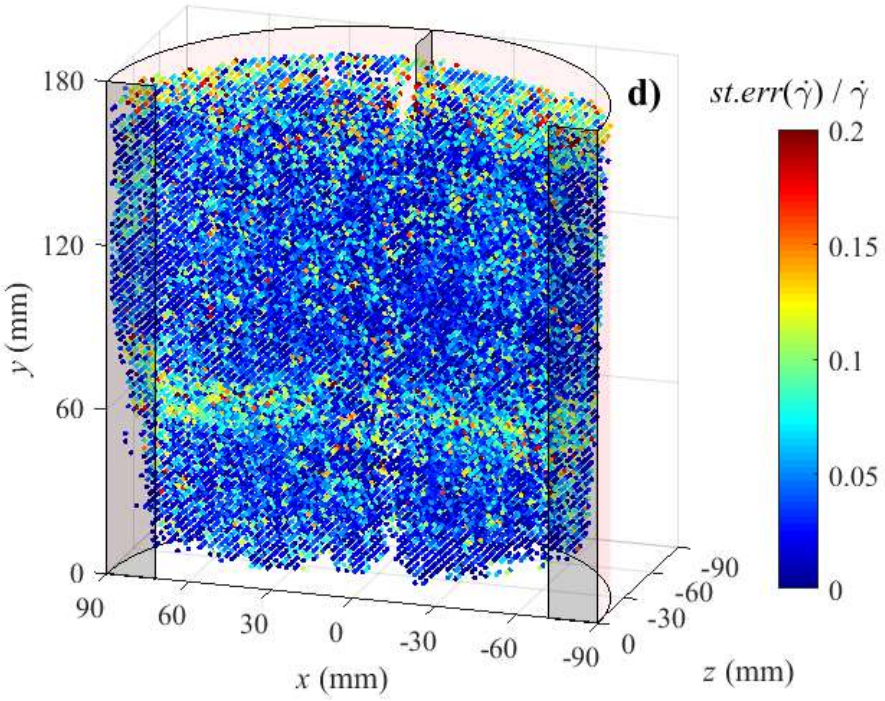

Figure IV-6 *(continues).*

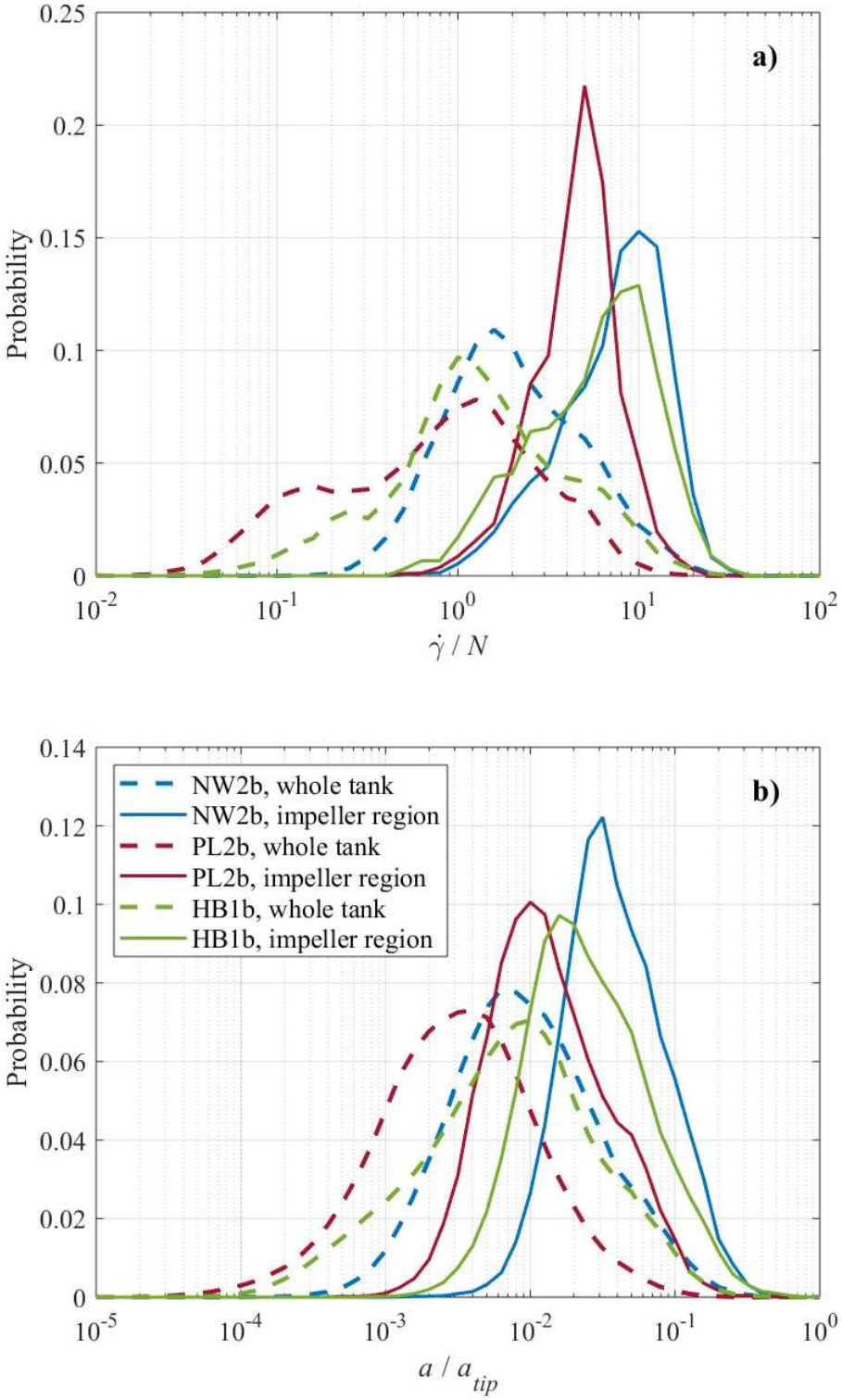

***Figure IV-7**: Examples of distributions of normalised shear rate (a) and normalised Lagrangian acceleration (b) for three experiments at comparable Reynolds number.*

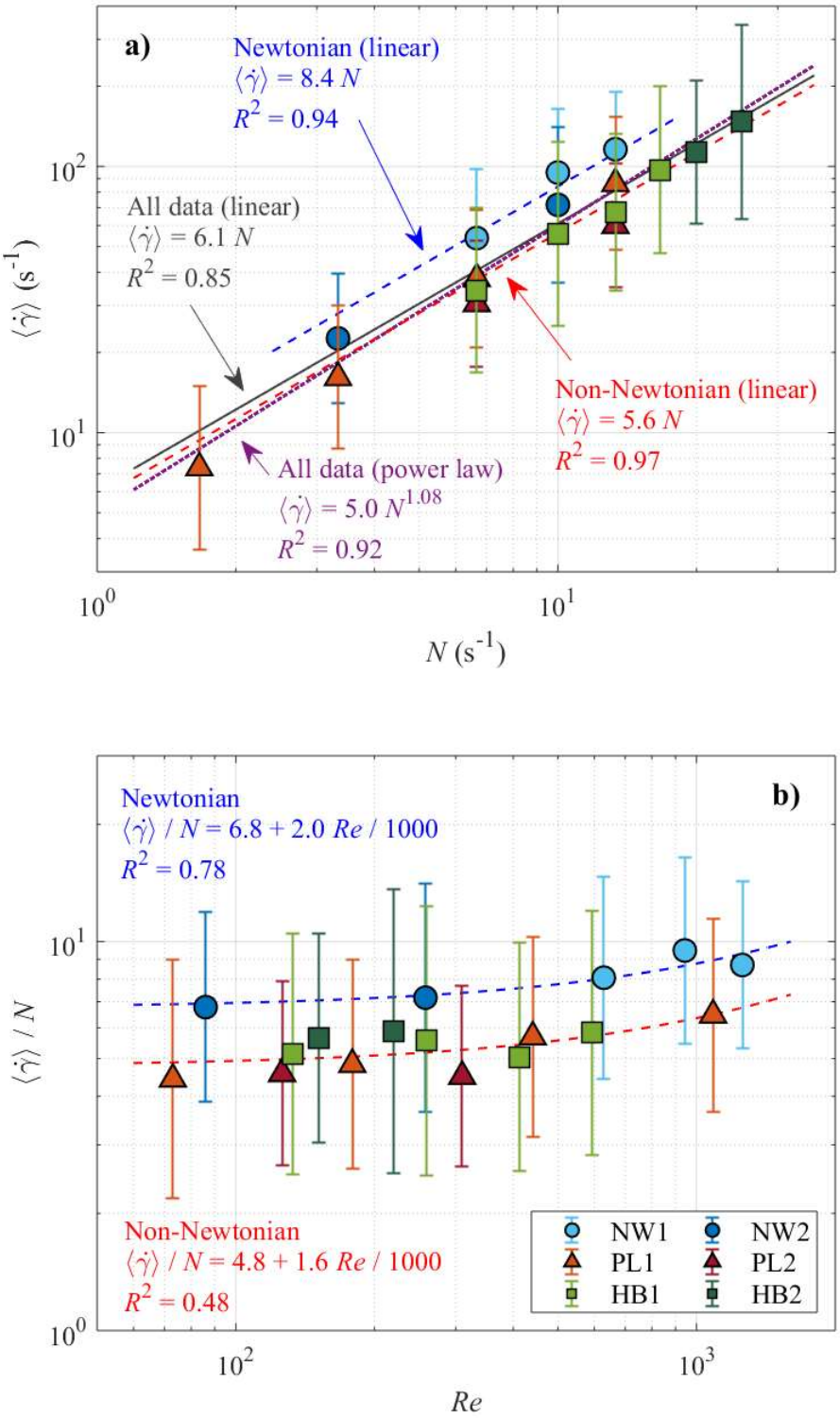

***Figure IV-8**: Average shear rate in the impeller region against the impeller speed (a) and its ratio over the impeller speed against the Reynolds number (b).*

Three examples of normalised acceleration distributions, normalised with the centripetal acceleration at the impeller tip, $a_{tip} = 2\,{U_{tip}}^2/D$, are pictured in ***Figure IV-7b***. The

distributions were approximately log-normal. The mean acceleration in the impeller region was one or more orders of magnitude larger than in the entire vessel. In the impeller region, the average Lagrangian acceleration scaled with the average shear rate to the power of 1.8 (***Figure IV-9***). The coefficient of determination of the fitting was $R^2 = 0.96$. The high degree of correlation between the two quantities has two important implications. Firstly, acceleration, which is easily measured with 3D-PTV, can be used as an indicator of the local degree of mixing, similarly to shear rate. This eliminates the difficulties related to PTV data binning when estimating the shear rate. In fact, the average shear rate is commonly used as an indicator of overall mixing efficiency, for example for scale-up. Since the average acceleration is highly correlated with the average shear rate, it is correlated to overall mixing efficiency. Note that this might not be true in general, e.g. in non-chaotic steady flows, if all streamlines move with the same acceleration and no convective mixing occurs. However, this is not the case of stirred tank flows, even at low Re. Secondly, as for the shear rate, the forces acting on the fluid elements are determined by the impeller speed, the Reynolds number and the fluid rheology in combination. Therefore, practitioners should take into consideration that transitional flows at the same Reynolds number are not necessarily dynamically equivalent.

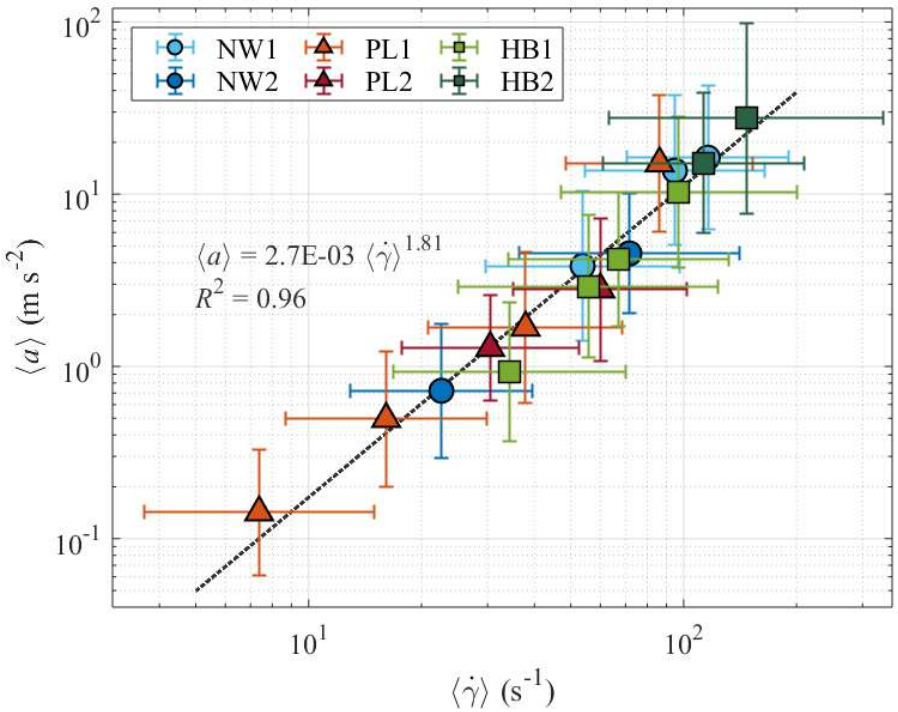

***Figure IV-9**: Average Lagrangian acceleration against average shear rate in the impeller region.*

IV.3.4. Mean square displacement

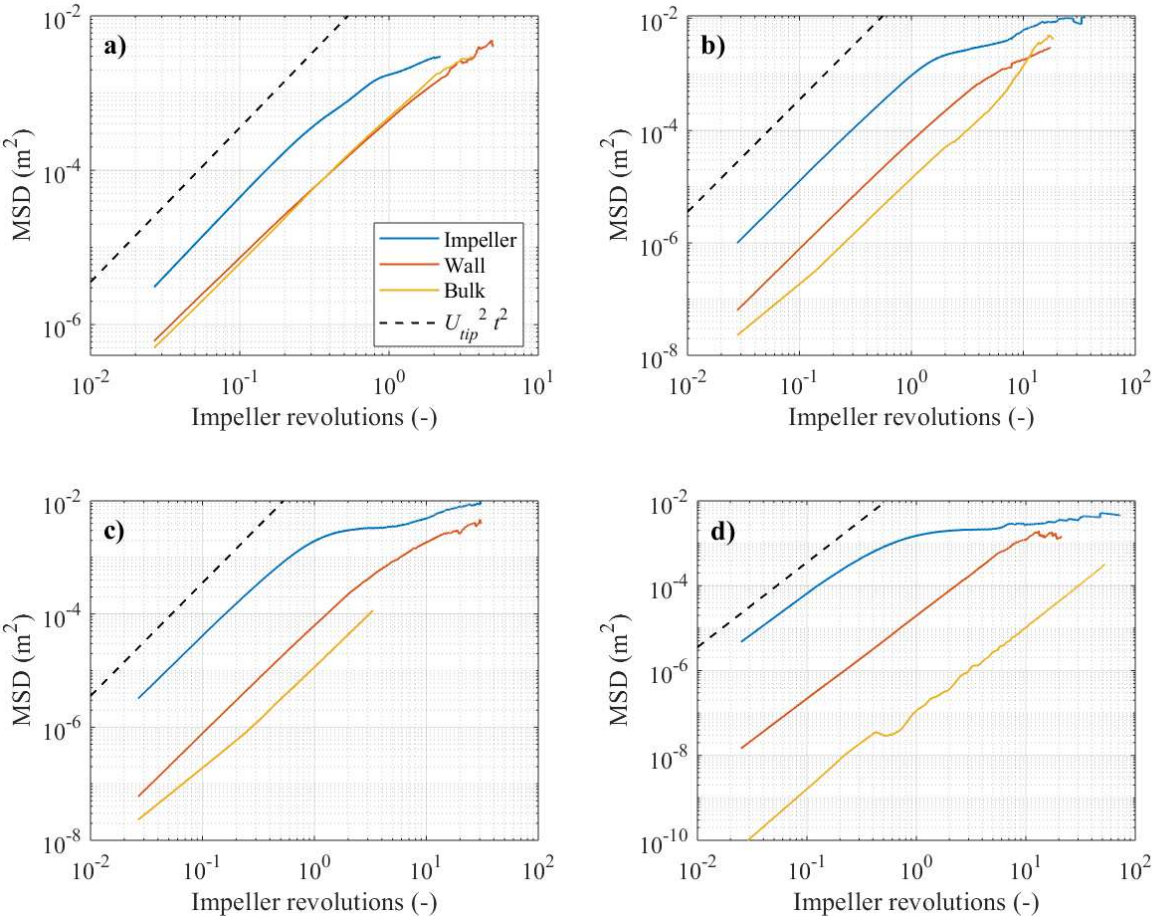

***Figure IV-10**: MSD against time in three control volumes. (a): NW1b, Re = 943; (b): PL1a, Re = 73; (c): PL1c, Re = 441; (d): HB2b, Re = 220.*

Some examples of the evolution of the MSD against time are displayed in ***Figure IV-10***. The dashed black lines indicate the ideal MSD of tracers travelling at constant velocity U_{tip}. As could be expected, the MSD was highest close to the impeller. For all three control volumes, the MSD initially increases with t^2, because the fluid circulated by convection. After a time of the order of the impeller period, the slopes of the curves (particularly those referring to the impeller control volume) start decreasing. If the tracers entering the control volumes could be tracked for a very long time, they would eventually meet a recirculation loop and return close to the starting point, so the curves would show a periodic pattern. ***Table IV-4*** lists the MSD of

the tracers passing through the impeller control volume, after one impeller period ($t = 1/N$). This value is indicated as MSD*. The average acceleration in the impeller region was highly correlated to the MSD* multiplied by N^2 (***Figure IV-11***). This indicates that, in the impeller region, the Lagrangian acceleration is linked to the fluid pumping rate.

***Table IV-4**: MSD of the tracers passing through the control volume close to the impeller, after one impeller period* ($t = 1/N$).

Experiment	MSD* (m^2)
NW1a	2.11E-03
NW1b	2.14E-03
NW1c	1.74E-03
NW2a	2.22E-03
NW2b	2.37E-03
PL1a	2.33E-03
PL1b	1.84E-03
PL1c	1.92E-03
PL1d	2.69E-03

Experiment	MSD* (m^2)
PL2a	1.23E-03
PL2b	8.05E-04
HB1a	9.58E-04
HB1b	1.97E-03
HB1c	2.02E-03
HB1d	2.48E-03
HB2a	9.79E-04
HB2b	1.51E-03

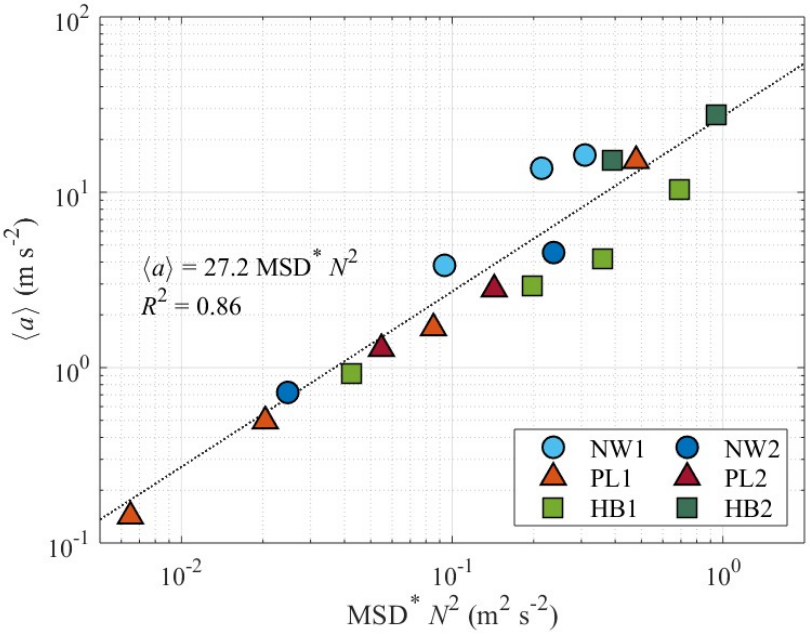

***Figure IV-11**: Plot of the average Lagrangian acceleration in the impeller region against MSD* multiplied by N^2.*

IV.4. Summary and conclusions

The flow fields of six fluids in a 4.6 L cylindrical tank stirred with a Rushton turbine and operated in the transitional regime (Re from 73 to 1,257) have been measured by means of 3D-PTV. The working fluids had different rheology, namely Newtonian, shear-thinning and Herschel-Bulkley.

Newtonian fluids showed very similar flow patterns in the range of Reynolds number from 86 to 1,257. Non-Newtonian flow patterns changed dramatically in the range of Reynolds number investigated. Non-Newtonian fluids formed pseudo-caverns and caverns around the impeller, the size of which was rheology dependent and increased with Reynolds. The impeller flow rates have been calculated from azimuthally averaged radial velocity data. For practical reasons, they have been evaluated at a radial coordinate $r = T/3$ instead of $r = T/6$ (impeller tip). For the Newtonian fluids, the normalised flow rate was almost constant (0.6 on average) in a range of Reynolds from 86 to 1,257. With the non-Newtonian fluids, two separate trends were observed. Q/ND^3 scaled as $Re^{1.1}$ for $Re < \sim 400$ and as $Re^{0.23}$ for $Re > \sim 400$. The Non-Newtonian rheology significantly decreased the impeller's capacity to pump the fluid around the vessel when $Re < \sim 400$. Low fluid circulation and (pseudo-) cavern formation have detrimental effects on macromixing. High impeller velocities could potentially guarantee substantial flow in the whole vessel. However, the resulting power drawn would be too high for industrial purposes. Close-clearance impellers, such as anchors and ribbons, could be a better solution for non-Newtonian fluid agitation at low Reynolds number.

The shear rate maps have been obtained by interpolating the velocity vectors in a Cartesian grid. The shear rate distributions were approximately log-normal. For practical purposes, the volume-averaged shear in the impeller region can be assumed to scale as $\langle \dot{\gamma} \rangle = 6.1\, N$ with reasonable accuracy ($R^2 = 0.85$). This proportionality law clearly resembles the Metzner-

Otto's assumption, valid in the laminar regime. The model has been refined by fitting Newtonian and non-Newtonian shear data separately and by expressing k_s^* as a function of the Reynolds number. This accounts for rheology effects and reflects the growing contribution of turbulence to shear generation as the flow deviates from fully laminar conditions. *Eq. IV-6* or *IV-7* can be used by practitioners to predict the mean shear conditions of a mixing process in the transitional regime, with higher accuracy than a simple proportionality law. However, it is important to remember that (a) the value of all fitting parameters depend on the volume and shape of the impeller region, which was defined arbitrarily, thus consistent procedures must be adopted when comparing different mixing systems, (b) individual shear rate realisations may be much greater or smaller than the mean, because this quantity is distributed over many orders of magnitude and (c) fluid rheology strongly affects the shear distribution in the vessel (with power-law fluids, the shear can be $\dot{\gamma} \sim 10^{-1}\ N$ in a substantial fraction of the vessel volume).

The acceleration was also distributed log-normally within the vessel. In the impeller region, the mean acceleration scaled as the volume-averaged shear to the power of 1.8 ($R^2 = 0.96$). This suggests that acceleration, measured directly with PTV, is a good indicator of local mixing intensity.

To the candidate's knowledge, this is the first time that PTV is used to study stirred tank flows over a wide range of experimental conditions. Current knowledge has been confirmed with very simple hardware, and this might be extremely relevant for industrial R&D sectors with limited access to advanced experimental facilities. PTV data have provided unique information regarding the instantaneous fluid acceleration in the vessel, which has been rarely reported in the literature and is not accessible by means of traditional Eulerian techniques, such as PIV and LDV.

Chapter V

COMPARISON BETWEEN RANS AND 3D-PTV FLOW MEASUREMENTS OF NEWTONIAN AND NON-NEWTONIAN FLUID BLENDING IN A VESSEL IN THE TRANSITIONAL FLOW REGIME

Abstract

Newtonian and non-Newtonian fluid flows in a vessel ($T = H = 180$ mm) stirred with a Rushton turbine ($C = D = T/3$) have been simulated in CFD using steady RANS in the transitional regime ($183 \leq Re \leq 1{,}086$). The numerical results have been compared against 3D-PTV measurements. For Newtonian fluids, the different turbulence models predicted the same mean flow, which matched well the experimental velocity data. The standard k-ε model predicted the power numbers closest to expected values and resolved 80% (at $Re = 943$) and 89% ($Re = 86$) of the total energy dissipation. Simulations of the non-Newtonian flows presented challenges. For shear thinning rheology, the simulated mean flow patterns did not correspond to the measured ones. CFD also predicted a higher mean velocity, compared to PTV. For yield stress fluids, the numerical predictions of the cavern boundaries were in reasonably good agreement with the experimental observations.

V.1. Introduction

CFD is a powerful tool for simulating fluid flow applications, including fluid mixing in agitated vessels. As described in **§II.3**, the simulations of agitated vessels have many advantages compared to experimental measurements. However, the numerical solutions are influenced by many settings, the most impacting being the turbulence modelling approach (**§II.3.1**), the numerical discretisation scheme (**§II.3.2**) and the boundary conditions at the impeller (**§II.3.4.3**). Selecting the most appropriate models for a specific flow system is not a trivial task and requires experience. As a consequence, validation of the numerical solutions against experimental data is always required.

Despite the fact that mixing under transitional flow conditions is very common in industry, especially for products whose rheology is evolving during manufacture, most experimental studies in the literature focus on fully laminar or fully turbulent flows and involve Newtonian fluids. There is still a dearth of CFD studies involving non-Newtonian fluids in the transitional flow regime. Therefore, the best practices for simulation of these systems are not yet clearly defined. In this chapter, steady RANS simulations of an agitated vessel equipped with a Rushton turbine have been conducted in the transitional regime ($86 \leq Re \leq 1{,}086$). The effects of the turbulence model and discretisation scheme have been addressed based on two Newtonian fluids of different viscosity. Then, four non-Newtonian fluids, two with shear thinning power law rheology and two with a Herschel Bulkley rheology, have been studied. The numerical solutions have been compared against the 3D-PTV measurements presented in **Chapter IV**. Lagrangian acceleration measurements obtained through PTV and shear rate data simulated with CFD have been binned on a Eulerian grid to test the spatial correlation between the two quantities within the vessel.

The reasons for using steady RANS are discussed below.

- Transitional flows in stirred vessels are time dependent. Compared to the flow variations associated to the impeller blade passage, flow macro-instabilities (MIs) have much lower characteristic frequencies (Galletti et al., 2004a). However, transient RANS cannot predict accurately the effects of MIs, and LES or DNS are required for this task (Roussinova et al., 2000, 2003). LES and DNS could not be conducted here, because of a limited computational budget. Moreover, PTV experimental data could only be compared to CFD in terms of mean velocity fields. For this reason, it has been decided to conduct steady-state simulations, with the understanding that any effect of MIs would not be resolved.

- Flows at low Reynolds number ($Re < \sim 10^2$) can be simulated using a laminar solver, that is by solving the NS equations without any turbulence model. Unlike DNS, laminar simulations can be run in steady state mode. However, the predictions worsen rapidly as the Reynolds number increases. A Newtonian fluid flow in the low transitional regime ($Re = 86$) has been simulated with both the laminar solver and the RANS models to address how the latter perform at low Re. The turbulent quantities obtained through RANS must be interpreted carefully. In fact, the flow could be laminar in large zones of the vessel. In the laminar regions, turbulent fluctuations are not present (i.e. $k = 0$ and $\varepsilon = 0$), while RANS models would predict very low values, which should not be trusted. Instead, it is possible to verify the predictions in those regions where turbulence occurs. In fact, the integral of ε should return the expected power consumption of the mixer geometry.

V.2. Materials and methods

V.2.1. Equipment setup and flow conditions

The vessel under study was identical to that used in **Chapter IV**.

The six working fluids investigated were aqueous solutions of glycerol (NW1 and NW2), CMC (PL1 and PL2) and Carbopol (HB1 and HB2) used in **Chapter IV**. The rheological parameters of the liquids were given in ***Table IV-1***. In the CFD solver, the apparent viscosity of the Carbopol solutions has been expressed with a piecewise Hershel-Bulkley model:

$$\mu = \begin{cases} K\,[\dot{\gamma}^{n-1} - (\tau_0/\mu_0)^n\,\dot{\gamma}^{-1}] + \tau_0\,\dot{\gamma}^{-1} \text{ for } \tau > \tau_0 \\ \mu_0 \text{ for } \tau \leq \tau_0 \end{cases} \qquad \textit{Eq. V-1}$$

In *Eq. V-1*, μ_0 is the zero-shear viscosity, which is used to avoid the numerical singularity at $\dot{\gamma} = 0$ (Xiao et al., 2014; Patel et al., 2015a). Its value should be large to ensure that the fluid flow is negligible when $\tau \leq \tau_0$. In the simulations presented in this paper, the zero-shear viscosity was set conservatively as $\mu_0 = 10^4 \mu_e$, where $\mu_e = \mu(\dot{\gamma} = k_s N)$ according to the Metzner-Otto's rule and $k_s = 11.5$. ***Table V-1*** lists the flow conditions investigated in this chapter.

Table V-1*: Flow conditions.*

Label	Fluid	Impeller speed (rpm)	μ_e (Pa s)	Re
NW1b	NW1	600	4.60×10^{-2}	943
NW2a	NW2	200	1.70×10^{-1}	86
PL1d	PL1	800	4.42×10^{-2}	1,086
PL2b	PL2	800	1.55×10^{-1}	310
HB1a	HB1	400	1.80×10^{-1}	133
HB2b	HB2	1,500	4.09×10^{-1}	220

V.2.2. CFD framework

All simulations described below have been carried out in OpenFoam® on a cluster node with 32 CPUs working at 2.20 GHz. The impeller rotation has been modelled using the MRF approach and the simulations have been conducted in steady-state mode. Since experimental Eulerian information for cross-validation was available in the form of averaged PTV data, transient simulations were unnecessary. Given the fully baffled configuration of the vessel, the liquid free surface has been modelled as flat, imposing zero-stress and zero-flux conditions. Wall functions have been used with the standard k-ε and RNG turbulence models. With the SST model, the flow equations have been solved in the boundary layer. This approach has been validated retrospectively by checking that the normalised wall unit was $y^+ < \sim 1$ (see **§II.3.4.1**). This condition means that the grid was sufficiently fine to resolve the viscous sub-layer.

All turbulence model constants were set to their default values. The second order discretisation scheme was coupled with a least-square gradient scheme, a cell-based gradient limiter to avoid under- and over-shooting of the turbulent quantities and three non-orthogonality corrector loops. The solutions were considered numerically converged when the torque monitored at the impeller had become independent from further iterations and the sum of normalised residuals had dropped below 10^{-5}, with most of them being in effect less than 10^{-6}.

V.2.3. PTV velocity binning

CFD and PTV velocity data have been compared in terms of azimuthally averaged velocity at fixed positions in the vessel. This required the binning of the PTV Lagrangian velocity data on a 2D Eulerian grid. Each PTV velocity data point calculated is an average over many observations within a small voxel. The r-y vertical plane of the tank has been divided into

$30 \times 60 = 1{,}800$ voxels, each one identified by the indices i and j and having width $dr = 3$ mm and height $dy = 3$ mm. The ensemble average over all n velocity events in a given voxel, i.e.

$$\langle U \rangle_{i,j} = \frac{1}{n} \sum_{k=1}^{n} U_{i,j,k} \,, \qquad \textit{Eq. V-2}$$

is slightly based in favour of low velocity values. That is because (i) detectability and traceability of the PTV tracers are negatively correlated with their velocity and (ii) the residence time of a particle in the voxel is inversely proportional to its velocity. For this reason, an alternative method has been used, based on the following steps. The velocity events observed in the voxel were grouped in individual trajectories and a first average was calculated for each trajectory (*Eq. V-3*). Then, the final value was obtained by averaging over all the trajectories entering that voxel (*Eq. V-4*),

$$\langle U \rangle_{i,j,l} = \frac{1}{m} \sum_{k=1}^{m} U_{i,j,k,l} \,; \qquad \textit{Eq. V-3}$$

$$\langle U \rangle_{i,j} = \frac{1}{n} \sum_{l=1}^{n} \langle U \rangle_{i,j,l}. \qquad \textit{Eq. V-4}$$

The index l identifies a specific trajectory, $m(i,j,l)$ is the number of events for a specific trajectory in that voxel, and $n(i,j)$ is the number of trajectories entering that voxel. A comparison between the "trajectory-based" and the "ensemble average" methods is given in **§A.3**.

The agreement between simulations and experiments has been assessed quantitatively in terms of mean absolute difference (MAD). This is defined as

$$\mathrm{MAD} \equiv \frac{\sum_{j=1}^{M} |U_{PTV} - U_{CFD}|}{M}, \qquad \textit{Eq. V-5}$$

where M is the number of voxels. This is a linear score, which means that all differences are weighted equally in the average. Thus, it is insensitive to large relative differences occurring at small values of velocity. In terms of relative differences, the mean absolute logarithmic difference of the velocity (MALD) is a more informative score:

$$\mathrm{MALD} \equiv \frac{\sum_{j=1}^{M} |\log(U_{PTV}) - \log(U_{CFD})|}{M} = \frac{\sum_{j=1}^{M} |\log(U_{PTV}/U_{CFD})|}{M}. \qquad \textit{Eq. V-6}$$

The expression on the right shows that the MALD is directly linked to the average ratio between the two data sets.

V.2.4. Newtonian simulations

V.2.4.1. Mid transitional regime

A first Newtonian case study has been defined to conduct a mesh independence test and to assess the effects of turbulence model and discretisation scheme under mid-transitional flow conditions (NW1b, $Re = 943$). The vessel has been discretised in three meshes of approximately 1.9, 4.2 and 6.8 million cells. In each one, a cylinder of diameter $2\,T/3$ and height $T/3$ has been defined around the impeller to apply the MRF method. For each mesh, approximately 40% of the total number of cells was concentrated in this region to resolve the steep gradients. Mesh refinement was also present in the proximity of the tank walls and baffles. Maximum non-orthogonality was about 65 in all three meshes, and average non-orthogonality was about 6.

The flow has been simulated with the three grids using the standard k-ε model, standard wall functions and a first-order upwind (UW) discretisation scheme. The solutions have been

compared in terms of azimuthally averaged velocity profiles and power number. This has been calculated with two methods. The first involved the integration of the energy dissipation rate in the whole volume, that is a weighted sum based on the cell volumes, V_j:

$$Po = \frac{\langle \varepsilon \rangle_V \rho\, V}{\rho\, D^5 N^3} = \frac{\sum \varepsilon_j V_j}{D^5 N^3}. \qquad \textit{Eq. V-7}$$

The second was based on the torque, Λ (N m), experienced by the moving parts, hence on the stresses acting on the surface of impeller and shaft:

$$Po = \frac{2\pi N\, \Lambda}{\rho\, D^5 N^3} = \frac{2\pi\, \Lambda}{\rho\, D^5 N^2}. \qquad \textit{Eq. V-8}$$

Correct values of Po from *Eq. V-7* and from *Eq. V-8* indicate, respectively, the correct solution of the transport equation for ε and of the pressure equation within the SIMPLE loop (**§II.3.3**). Ideally, the two methods should provide the same result. However, it is well known that RANS simulations tend to underestimate the energy dissipation rate in agitated vessels, even with fine computational grids (Bartels et al., 2000; Alexopoulos et al., 2002; Bartels et al., 2002; Aubin et al., 2004; Singh et al., 2011; Lane, 2017). Instead, the torque on solid walls is mainly determined by the wall model. Consequently, the values of power number obtained with the two methods do not match (Murthy and Joshi, 2008). The differences depend on the mesh size and particularly on the discretisation scheme (Coroneo et al., 2011). For this reason, an additional simulation has been conducted using the intermediate mesh and a second order upwind scheme (2UW).

In order to assess the effects of turbulence modelling, the flow has also been simulated on the intermediate mesh with the k-ε RNG and k-ω SST models. Some statistics of the mesh wall unit obtained with the SST simulation are given in ***Table V-2*** to demonstrate the viability of the boundary layer resolution. For all solid walls, the condition $y^+ < \sim 1$ was met, both in terms of

average and maximum values. As could be expected, the maximum y^+ was found on the edge of the impeller blades, where turbulent energy dissipation was highest.

***Table V-2**: Average and maximum y^+ obtained with the SST simulation on a mesh of 4.2 million cells (Newtonian fluid, $Re = 943$).*

Surface	Average y^+	Maximum y^+
Vessel walls	2.9×10^{-2}	3.8×10^{-1}
Baffles	4.0×10^{-2}	9.5×10^{-1}
Impeller	1.1×10^{-1}	1.1
Shaft	8.0×10^{-2}	5.6×10^{-1}

V.2.4.2. Low transitional regime

In principle, one turbulence model may perform better than others only within a certain range of Reynolds number. Moreover, stirred tank flows at moderate Reynolds numbers are typically simulated using a laminar solver, even if the overall flow regime is transitional and some turbulence is produced by the impeller (Zalc et al., 2001; Kelly and Gigas, 2003; Ameur and Bouzit, 2012; Patel et al., 2015a; Mendoza et al., 2018). For this reason, the laminar, standard k-ε, RNG k-ε, and k-ω SST models have been applied to the flow of a glycerol-water solution (80%-20% wt.) in the low-transitional regime (NW2a, $Re = 86$). The simulations have been conducted on the intermediate mesh of 4.2 million cells and the 2UW scheme has been used. The velocity data have been compared against PTV measurements.

V.2.5. Non-Newtonian simulations

In light of the findings obtained with the two Newtonian case studies, the non-Newtonian simulations have been conducted using the standard k-ε model and the 2UW scheme on the mesh of 4.2 million cells. As for the Newtonian cases, the azimuthally averaged velocity fields have been compared against PTV data.

With the fluids HB1 and HB2, the cavern boundary has been determined as the isoline where the azimuthally averaged 2D velocity was equal to 1% of the impeller tip speed. The numerical predictions have been compared against PTV data.

V.2.6. Test of the correlation between shear rate and Lagrangian acceleration

A unique feature of Lagrangian measurement techniques, including PTV, is that the Lagrangian acceleration along the tracer trajectories can be easily obtained through finite differentiation of the coordinates with respect to time. Conversely, the precise calculation of Eulerian derivatives, such as velocity gradients and shear rate, is quite difficult, as velocity data must be binned or interpolated on a Eulerian grid. The spacing of the grid must guarantee a sufficient number of data points per cell, and this can be in CFD can be used to fill this gap, as the shear rate can be directly calculated in each cell as $\dot{\gamma} = \sqrt{2\,\mathbf{S}:\mathbf{S}}$ (*Eq. II-6*), where $\mathbf{S}$ is the symmetric part of the velocity gradient.

The simultaneous availability of acceleration and shear rate gives the capability to test whether the local values of the two quantities were spatially correlated. The data from the two Newtonian case studies have been used for this analysis, as they provided the best agreement between simulations and experiments. The shear rate and the acceleration data have been binned on a 2D Eulerian grid of 1,800 voxels (the same used for the PTV velocity data) to obtain azimuthally averaged values. Then, since the two quantities ranged within several orders of magnitude and a power law relationship was expected, the Pearson correlation coefficient (PCC) between $\mathrm{Log}_{10}\langle\dot{\gamma}\rangle$ and $\mathrm{Log}_{10}\langle a\rangle$ has been calculated. The correlation has been tested in the whole vessel, based on all the 1,800 voxels, and in a cylinder around the impeller comprising of 200 voxels and defined as

$$\begin{cases} r \leq D \\ C - \frac{D}{4} \leq y \leq C + \frac{D}{4} \end{cases}, \qquad \textit{Eq. V-9}$$

V.3. Results

V.3.1. Newtonian simulations, mid transitional regime

V.3.1.1. Mesh independence

The comparison of the azimuthally averaged velocity profiles obtained with the three numerical grids showed no significant differences; radial velocity is displayed in ***Figure V-1***. The use of a second order discretisation scheme instead of a first order led to small differences, mainly localised in the impeller discharge flow. The jet was slightly wider and the maximum velocity slightly lower in the case of the 2UW simulation.

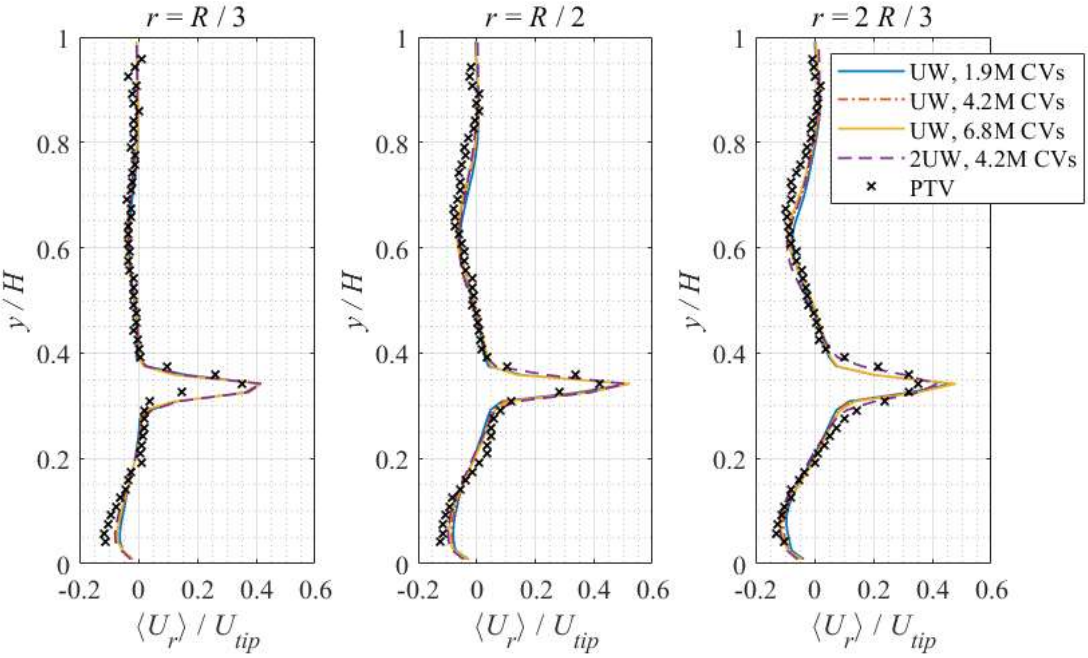

Figure V-1*: Profiles of the azimuthally averaged radial velocity at three radial coordinates (NW1b, Re = 943).*

The power numbers are listed in ***Table V-3***. With the k-ε model and the first order UW scheme, the torque on the moving parts was essentially mesh independent, but the volume averaged energy dissipation rate was significantly underestimated and kept increasing slightly as the mesh was refined. However, such differences were much smaller than those due to the discretisation scheme. With the 2UW scheme, the power number obtained from torque was very close to the expected value of about 3.5 for a Rushton turbine operated at $Re \sim 10^3$ (Distelhoff et al., 1995), meaning that the pressure field was solved correctly. The resolved energy dissipation was about 80% of the expected value. This level of resolution was in line with the figures reported by other authors (Coroneo et al., 2011; Lane, 2017) and has been considered satisfactory. For this reason, all the simulations in the remainder of the paper have been run on the intermediate mesh, coupled with a 2UW discretisation scheme.

Table V-3*: Power number in function of the mesh refinement, discretisation scheme and turbulence model (NW1b, Re = 943). Expected values taken from Distelhoff et al. (1995).*

Simulation	Po from torque (% of expected)	Po from ε (% of expected)
k-ε, UW, 1.9M cells	3.04 (93%)	1.21 (35%)
k-ε, UW, 4.2M cells	2.98 (91%)	1.38 (39%)
k-ε, UW, 6.8M cells	2.99 (91%)	1.52 (44%)
k-ε, 2UW, 4.2M cells	3.12 (95%)	2.80 (80%)
RNG, 2UW, 4.2M cells	3.14 (96%)	2.32 (66%)
SST, 2UW, 4.2M cells	3.07 (94%)	2.25 (64%)

V.3.1.2. Effects of the turbulence model

The choice of turbulence model had very little effect on the azimuthally averaged velocity fields, with the profiles matching quite well with the PTV experimental data (***Figure V-2***). Appreciable differences were only present at $r = R/3$ at the impeller tip, and in the lower recirculation loop, particularly for the tangential component. PTV measurements

underestimated the velocity very close to the impeller (up to −23%), likely due to the following reasons. Firstly, the intermittent passage of the impeller blades makes it more difficult to identify the PTV tracers in the digital images and to determine their centroids accurately. Secondly, the tracer traceability decreases significantly due to the very rapid changes in both magnitude and direction of the velocity. Chiti et al. (2011) also reported a significant underestimation of the velocity (about −50%) just off the blade tip, obtained by interpolation of PEPT Lagrangian data. Further studies are recommended to explain the differences observed in the PTV and CFD velocity values near the impeller tip.

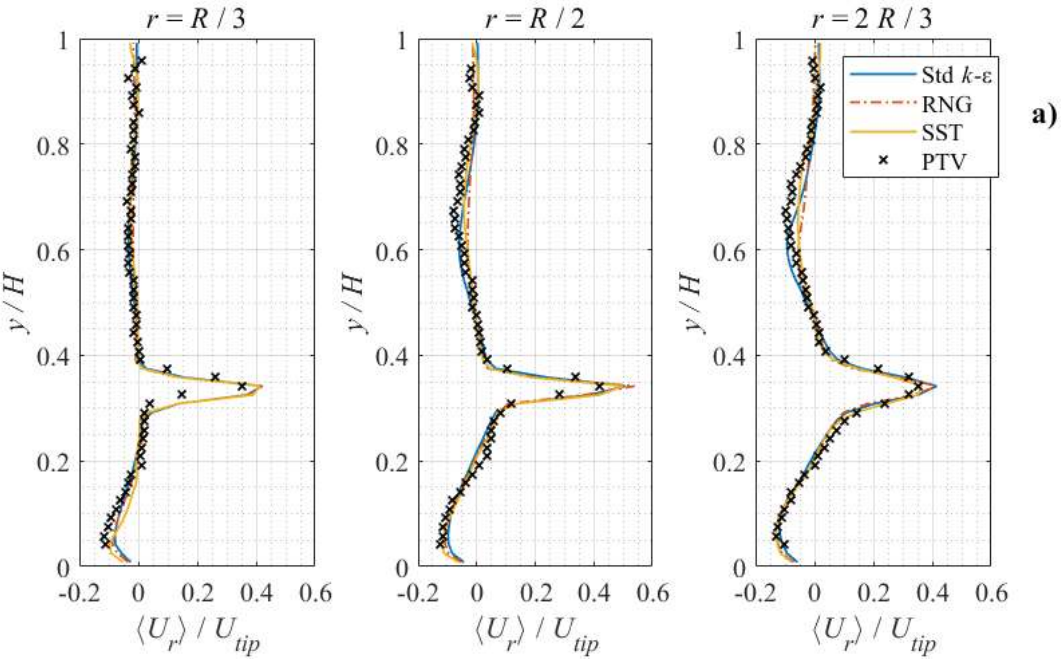

***Figure V-2**: Azimuthally averaged profiles of the radial (a), tangential (b) and axial (c) velocity components at three radial coordinates (NW1b, Re = 943). (Continues in the next page).*

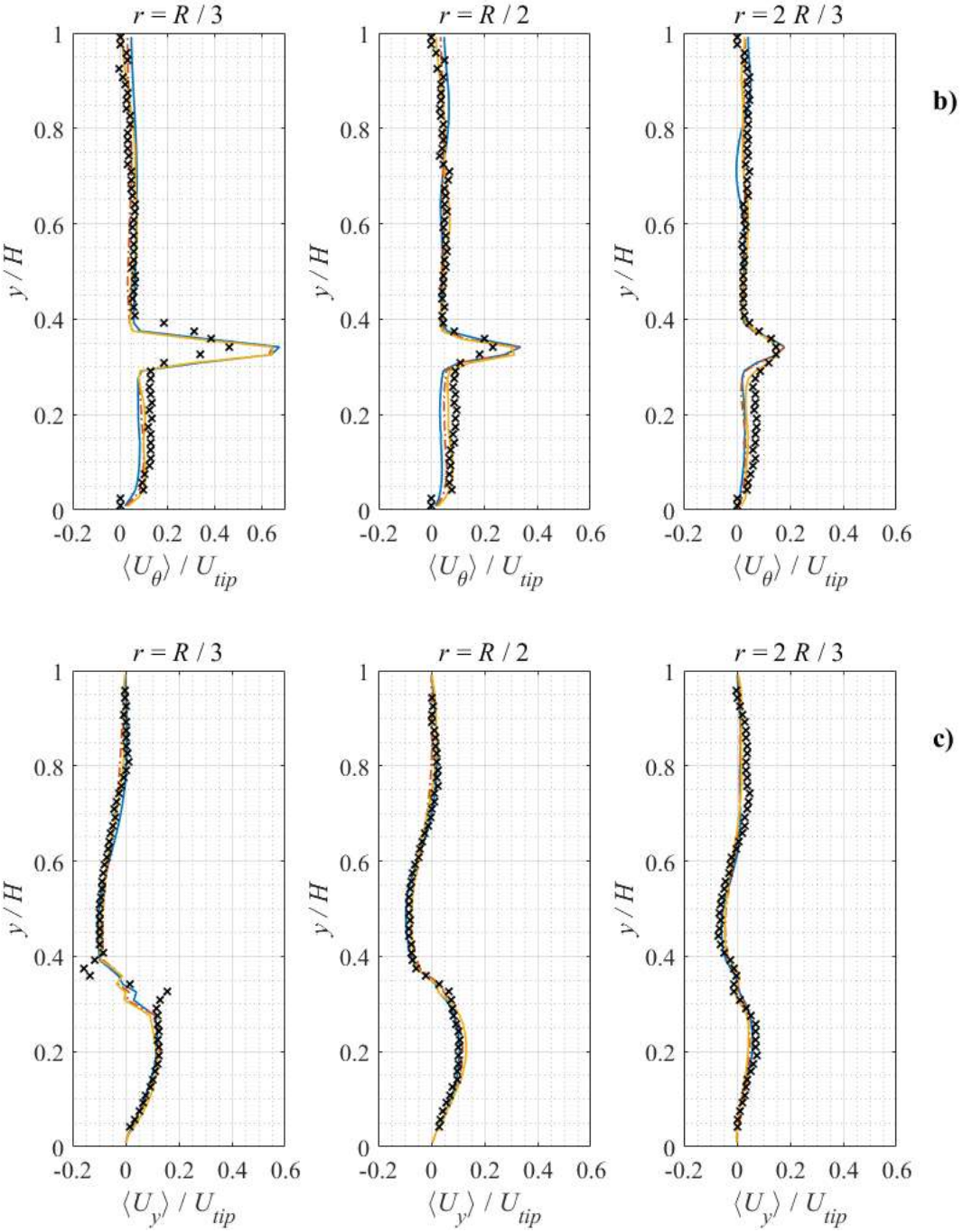

Figure V-2 *(continues).*

Good agreement was also found in the 2D maps of azimuthally averaged velocity magnitude and flow streamlines. Note that even the smallest differences in the Eulerian velocity components can lead to significant discrepancies in the resulting streamlines. ***Figure V-3*** shows the case of the k-ε simulation. The other two models gave very similar results. In particular, the

size and position of the two main recirculation loops have been predicted well. Some differences can be observed upper region of the vessel, and particularly in the flow separation region close to the wall at $y \approx 0.8\,H$. Here the fluid flows through an adverse pressure gradient and a third circulation loop is formed. As showed in **§IV.3.1**, there was a large population of Lagrangian trajectories pointing downwards in the area downstream of the baffles at $y \approx 0.8\,H$. The fluid would then meet the upper recirculation loop, gaining tangential velocity. In the upper part of the vessel, due to the low mean velocity ($< 5\%\ U_{tip}$), its relative variance was larger than in the rest of the vessel (although the absolute variance was actually smaller). The result is that, in that region, the experimental streamlines appear quite chaotic. This is just an artifact arising from the integration of the velocity components having unfavourable statistics. Flow separation was also present at the edges between the wall and the bottom, as captured by both PTV and CFD. Below the impeller, the experimental velocity magnitude was much higher than the simulated counterpart. Most of the difference was due to the tangential component.

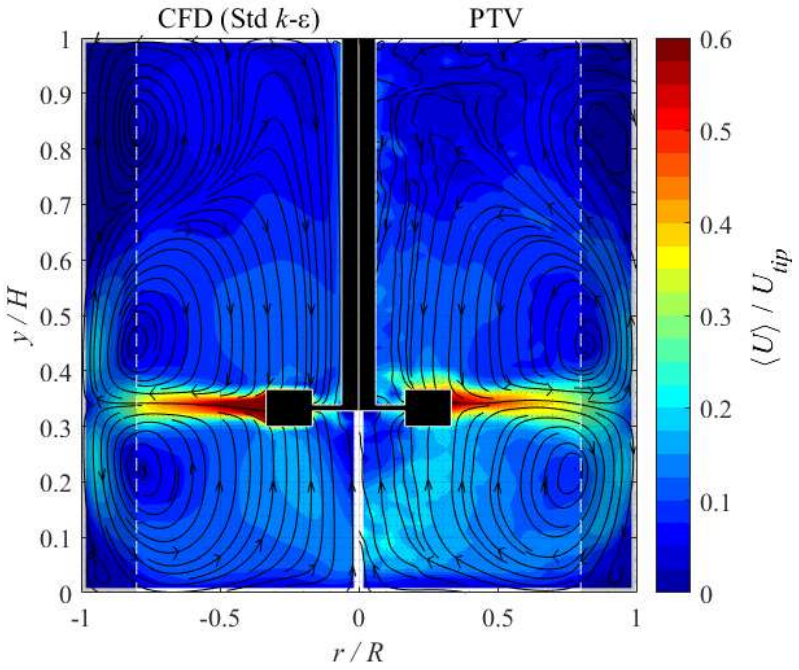

***Figure V-3**: 2D maps of the azimuthally averaged velocity magnitude and resulting streamlines, as simulated with the k-ε model and measured with PTV (NW1b, Re = 943).*

The voxel-to-voxel parity plot of the two velocity fields is illustrated in ***Figure V-4***, both in linear and in logarithmic scale. The largest absolute differences were found in the impeller jet at high values of the velocity. The MAD between the k-ε data and the experimental ones was 2.4% of the impeller tip speed. The log-log plot reveals that the largest relative differences were observed in the range of velocity between $10^{-2}U_{tip}$ and $10^{-1}U_{tip}$, located in the region below the impeller. The MALD was 0.122, corresponding to a mean ratio of $10^{\pm 0.122} = 1.3^{\pm 1}$. The MAD and MALD of the other closure models were quite similar (***Table V-5***).

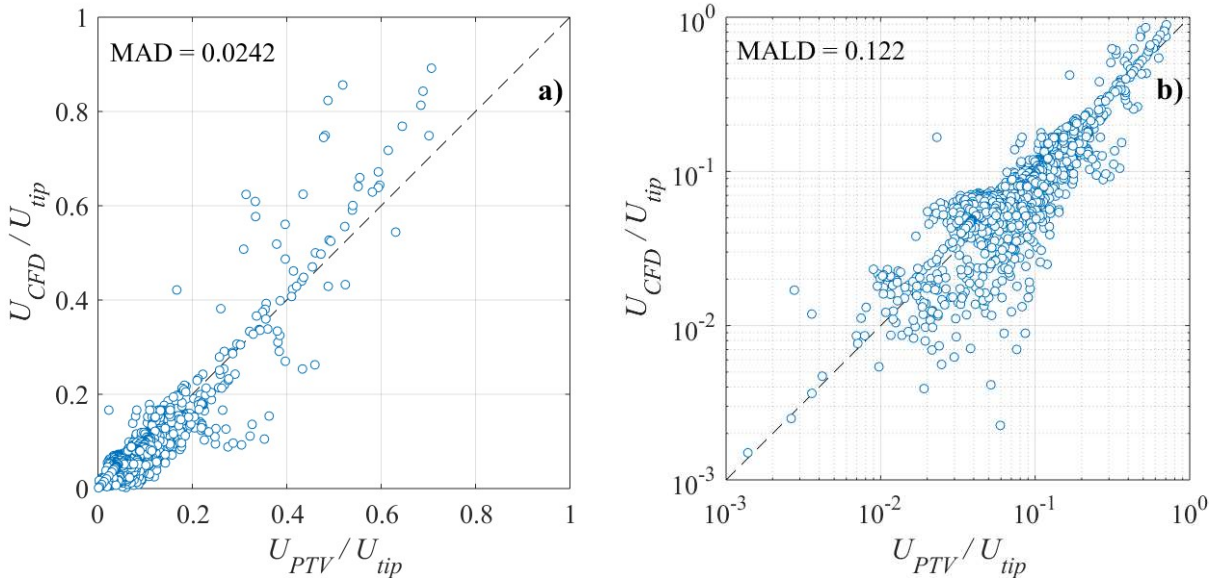

Figure V-4*: Parity plot of the azimuthally averaged velocity fields illustrated in* ***Figure V-3*** *in linear (a) and logarithmic scale (b).*

The choice of turbulence model had appreciable effects on the spatial distributions of the turbulent quantities, namely the energy dissipation rate, ε (m^2 s^{-3}), and the turbulent kinetic energy, k (m^2 s^{-2}). All models predicted $\varepsilon \sim 1\, D^2N^3$ in the impeller discharge jet, $\varepsilon \sim 10^{-2}\, D^2N^3$ in the bulk, and $\varepsilon \sim 10^{2}\, D^2N^3$ around the impeller blades (***Figure V-5***). Moderate values of energy dissipation were also present around the baffles and close to the wall at $y \approx H/3$, due to the impeller jet impinging these surfaces. These orders of magnitude agree with those reported in the literature, although most published works concerning the energy

dissipation in stirred tanks focus on fully turbulent conditions. Soos et al. (2013) conducted LES of a flow driven by a Rushton turbine at $Re = 12{,}000$ and reported phase-resolved profiles of ε spanning between $10\ D^2N^3$ and $130\ D^2N^3$. It is well-known that high values of turbulent kinetic energy and dissipation can be found in the trailing vortices behind the impeller blades (Derksen and Van den Akker, 1999; Sharp and Adrian, 2001; Escudié et al., 2004; Delafosse et al., 2009). ***Figure V-6*** shows the isosurfaces corresponding to $\varepsilon = 2\ D^2N^3$ for the standard k-ε model and $\varepsilon = 1\ D^2N^3$ for the RNG and SST models, highlighting the shape of the trailing vortices. A higher threshold was necessary for the k-ε simulation because of the higher dissipation predicted in the whole impeller discharge flow. The standard k-ε model provided also the highest integral of energy dissipation in the whole tank. This was directly reflected in the predicted power number, given in ***Table V-3***. Being much closer to the expected value, the standard k-ε model outperformed the RNG and SST models.

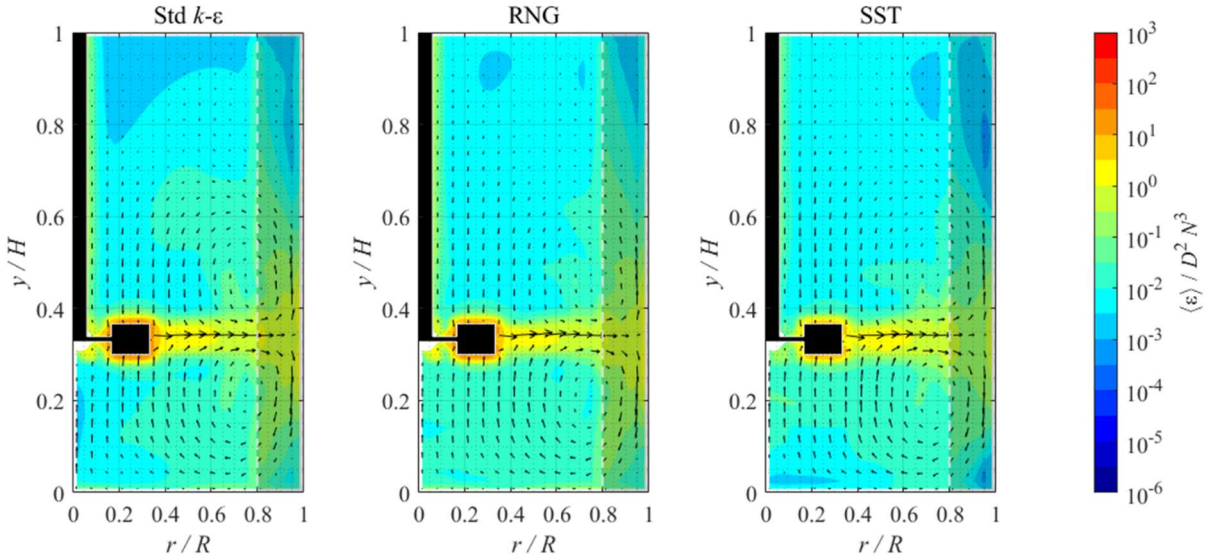

Figure V-5*: 2D maps of the azimuthally averaged energy dissipation rate, as obtained with three turbulence models (NW1b, Re = 943).*

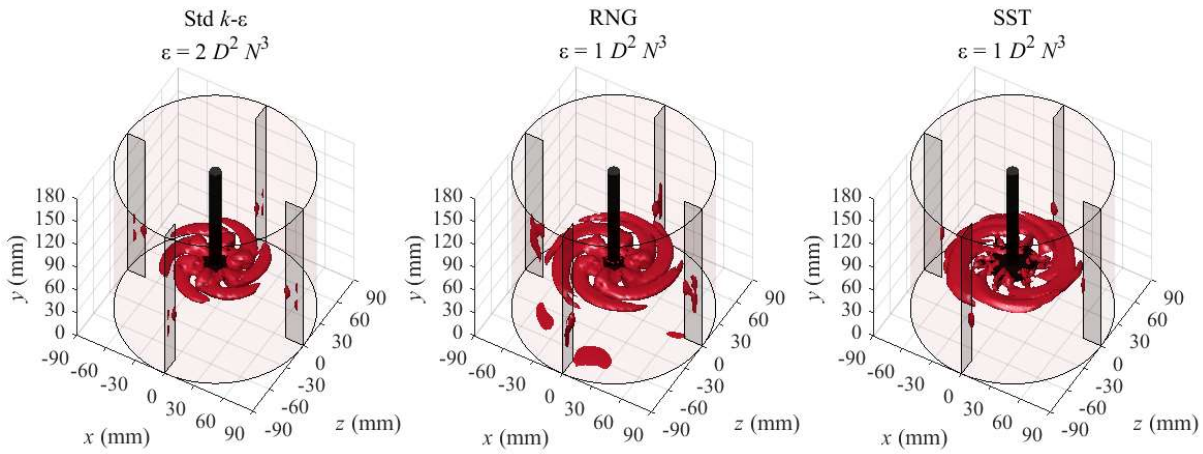

***Figure V-6**: Isosurfaces of the energy dissipation rate, highlighting the trailing vortices behind the impeller blades (NW1b, Re = 943).*

The spatial distributions of the turbulent kinetic energy (***Figure V-7***) were qualitatively similar to those of the dissipation rate, with high values close to the impeller blades ($k \sim 10^{-1}\ {U_{tip}}^2$), moderate values in the discharge jet ($k \sim 10^{-2}\ {U_{tip}}^2$) and low values in the bulk ($k \sim 10^{-3}\ {U_{tip}}^2$). There were some differences between the three turbulence models. The standard k-ε model provided the highest values in the discharge region ($k = 0.037\ {U_{tip}}^2$ at $y = H/3$ and $r = R/2$). In the SST simulation, the velocity gradients and the turbulent kinetic energy close to the wall have been determined through direct integration of the flow equations within the boundary layer. Values as low as $k \sim 10^{-5}\ {U_{tip}}^2$ can be observed in the regions of flow separation close to the peripheral wall at $y \approx 0.8\,H$ and to the vessel bottom. Although the k-ε and RNG models also predicted an adverse pressure gradient in those regions, this was not reflected strongly in the levels of turbulent kinetic energy. This may be ascribed to the use of wall functions.

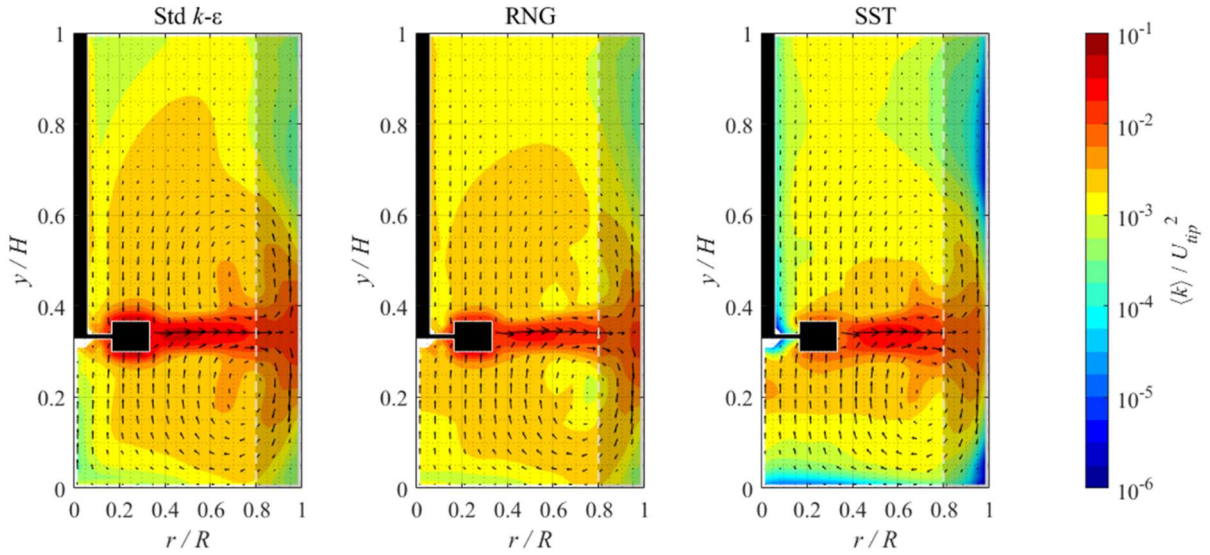

***Figure V-7**: 2D maps of the azimuthally averaged turbulent kinetic energy, as obtained with three turbulence models (NW1b, Re = 943).*

V.3.2. Newtonian simulations, low transitional regime

It is well-known that transitional flows may show turbulent behaviour close to the impeller and laminar behaviour in the bulk (Gabelle et al., 2013). The proportion between the turbulent and laminar regions changes with the Reynolds number and the fluid properties (Machado et al., 2013). At $Re = 86$, the azimuthally averaged velocity profiles obtained with the three RANS models were virtually identical and agreed very well with the PTV measurements (***Figure V-8***). The values of MAD and MALD of the different RANS models were also virtually identical (***Table V-5***). The MAD was about 1.2% of the tip speed and the average ratio over the experimental data was about $1.3^{\pm 1}$. Notably, the laminar simulation provided extremely similar results to the RANS models. That was because the ratio of the turbulent viscosity over the fluid viscosity was small ($\mu_T/\mu \sim 10^{-2}$ in the impeller jet and much lower in the bulk). This suggests that, in most parts of the tank, the flow was basically laminar and the effects of Reynolds stresses on the mean flow were negligible. The MAD/MALD concept has been applied to compare the k-ε and the laminar velocity fields. The two scores have been calculated over the

4.2 M CVs. The MAD was only 0.11% of the tip speed. The average ratio, calculated from the MALD, was $1.06^{\pm 1}$.

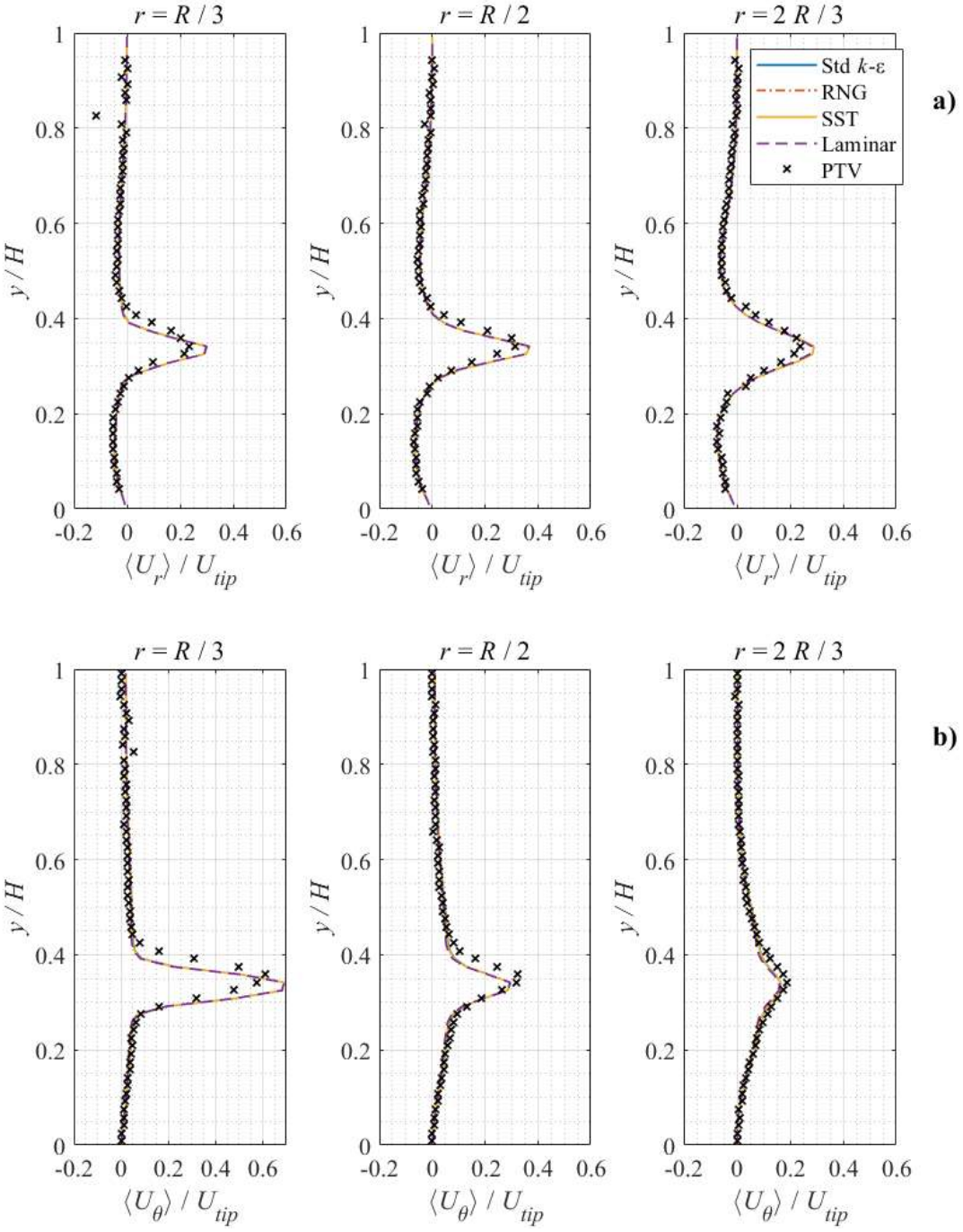

Figure V-8*: Azimuthally averaged profiles of the radial (a), tangential (b) and axial (c) velocity components at three radial coordinates (NW2a, Re = 86). (Continues in the next page).*

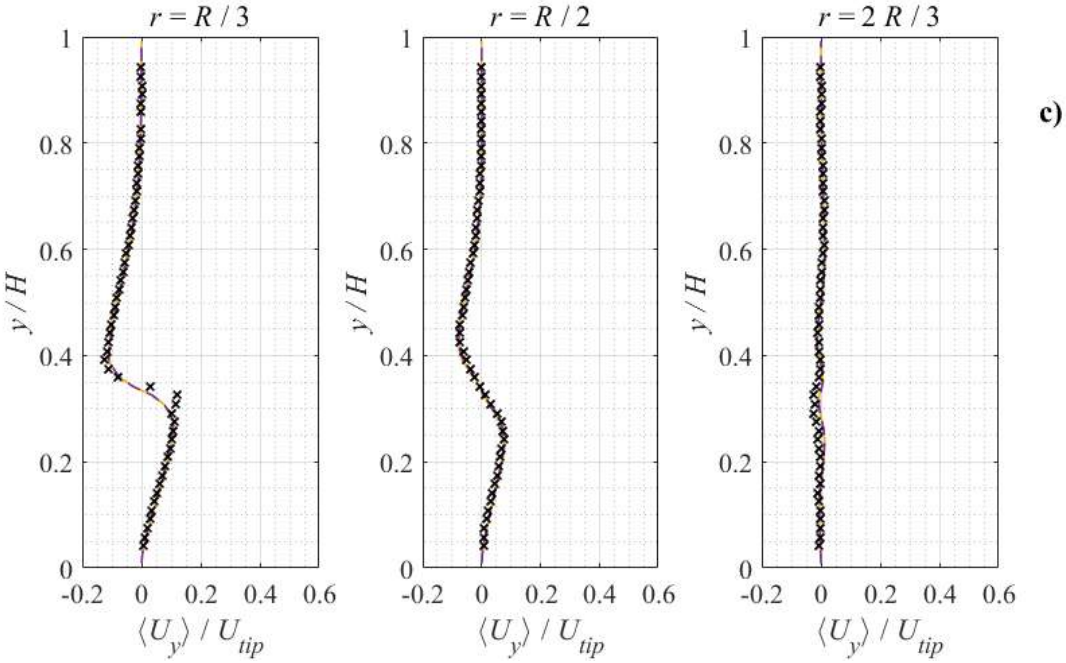

Figure V-8 *(continues).*

The distributions of normalised energy dissipation rate and turbulent kinetic energy were very different from those in the mid transitional case study. Here, turbulence was only present in the impeller jet and in those regions were the flow interacted with solid walls. For brevity, only the k-ε solution is displayed in ***Figure V-9***. High values of ε and k were only found in a small region around the impeller blades ($\varepsilon \sim 10^2\ D^2N^3$, $k \sim 10^{-1}\ {U_{tip}}^2$). Close to the baffles and peripheral wall, due to the jet impinging on the solid surfaces, $\varepsilon \sim 1\ D^2N^3$ and $k \sim 10^{-3}\ {U_{tip}}^2$. The turbulence levels in the jet were smaller than in the previous case ($\varepsilon \sim 10^{-3}\ D^2N^3$, $k \sim 10^{-4}\ {U_{tip}}^2$). As previously explained, in a purely laminar flow turbulent fluctuations are not present, and thus k and ε cannot be defined. Therefore, the very small values of k and ε obtained in the bulk flow are likely to be unphysical and should be ignored. At $Re = 86$, the expected power number for this geometry is $Po \approx 3.5$ (Distelhoff et al., 1995). This value is the same of the previous Newtonian case only by coincidence. In fact, the Po-Re curve is not monotonic in the transitional regime, and the two values are at the left and at the right side of the minimum. The simulations resolved most of the energy dissipated in the vessel (86% –

89%). This result provides some confidence that the turbulent regions have been predicted correctly. The torque on the moving parts was extremely close to the expected value (***Table V-4***). Again, the k-ε model gave the best predictions, although the differences with the other models were small.

***Table V-4**: Power numbers predicted from different turbulent models (NW2a, Re = 86). Expected values taken from Distelhoff et al. (1995).*

Simulation	Po from torque (% of expected)	Po from ε (% of expected)
k-ε, 2UW, 4.2M cells	3.42 (98%)	3.13 (89%)
RNG, 2UW, 4.2M cells	3.42 (98%)	3.09 (88%)
SST, 2UW, 4.2M cells	3.41 (97%)	3.02 (86%)
laminar, 2UW, 4.2M cells	3.42 (98%)	-

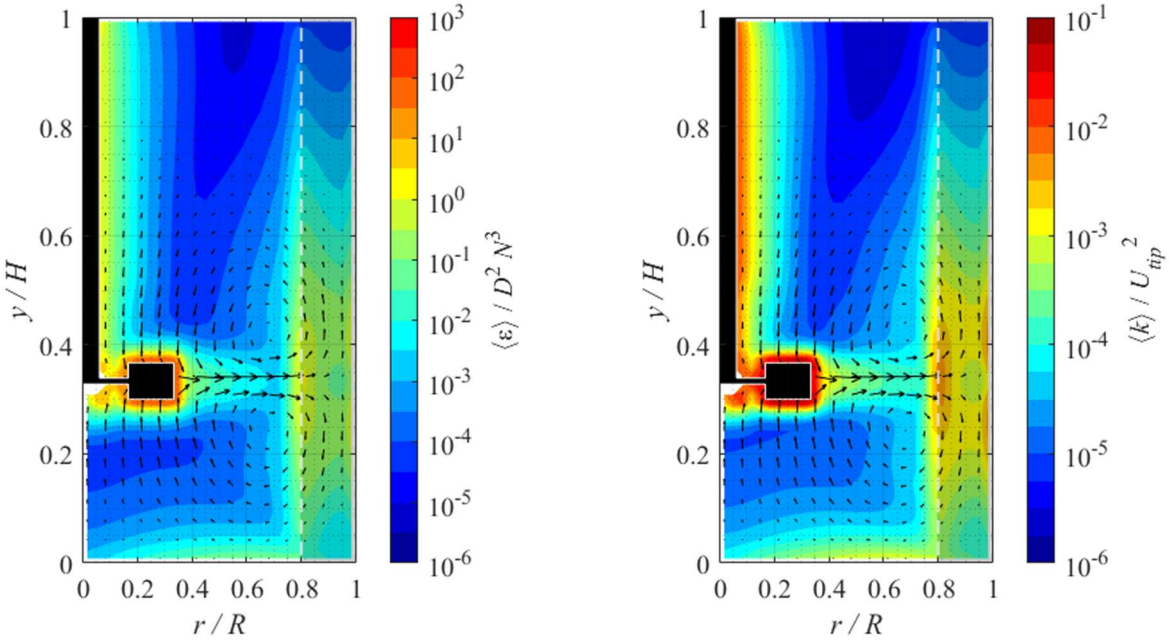

***Figure V-9**: 2D maps of the azimuthally averaged energy dissipation rate and turbulent kinetic energy, obtained with the standard k-ε model (NW2a, Re = 86).*

***Table V-5**: Root Mean Square Difference between the simulated and the numerical 2D azimuthally averaged velocity fields, in linear (Eq. V-8) and in logarithmic space (Eq. V-9).*

Flow	Simulation	MAD	MALD

NW1b	k-ε, UW, 1.9M cells	0.0317	0.159
	k-ε, UW, 4.2M cells	0.0299	0.146
	k-ε, UW, 6.8M cells	0.0287	0.141
	k-ε, 2UW, 4.2M cells	0.0242	0.122
	RNG, 2UW, 4.2M cells	0.0266	0.140
	SST, 2UW, 4.2M cells	0.0258	0.131
NW2a	k-ε, 2UW, 4.2M cells	0.0116	0.108
	RNG, 2UW, 4.2M cells	0.0117	0.109
	SST, 2UW, 4.2M cells	0.0116	0.109
	laminar, 2UW, 4.2M cells	0.0122	0.114
PL1d	k-ε, 2UW, 4.2M cells	0.0328	0.192
PL2b	k-ε, 2UW, 4.2M cells	0.0380	0.382
HB1a	k-ε, 2UW, 4.2M cells	0.0147	0.185
HB2b	k-ε, 2UW, 4.2M cells	0.0138	0.143

V.3.3. Non-Newtonian simulations

With the two power-law fluids, the velocity magnitude predicted by the simulations was higher than the experimental values in most part of the vessel, particularly in the impeller jet (the radial component is shown in ***Figure V-10***). Although in the rest of the vessel the absolute differences in the individual velocity components were not excessively large, they had dramatic effects on the resulting mean flow patterns (***Figure V-11***). In particular, the position, shape and size of the two main recirculation loops were quite different in both cases. The causes for such discrepancies are not clear and need further investigation. In the case of the flow PL2b, the agreement between numerical and experimental data was particularly poor in the range of low velocities (between $10^{-3}\ U_{tip}$ and $10^{-2}\ U_{tip}$), with large relative differences. In these voxels, the standard deviation of the velocity was about $10^{-3}\ U_{tip} \sim 2 \times 10^{-3}$ m s^{-1}, i.e. the same order of magnitude of the mean value.

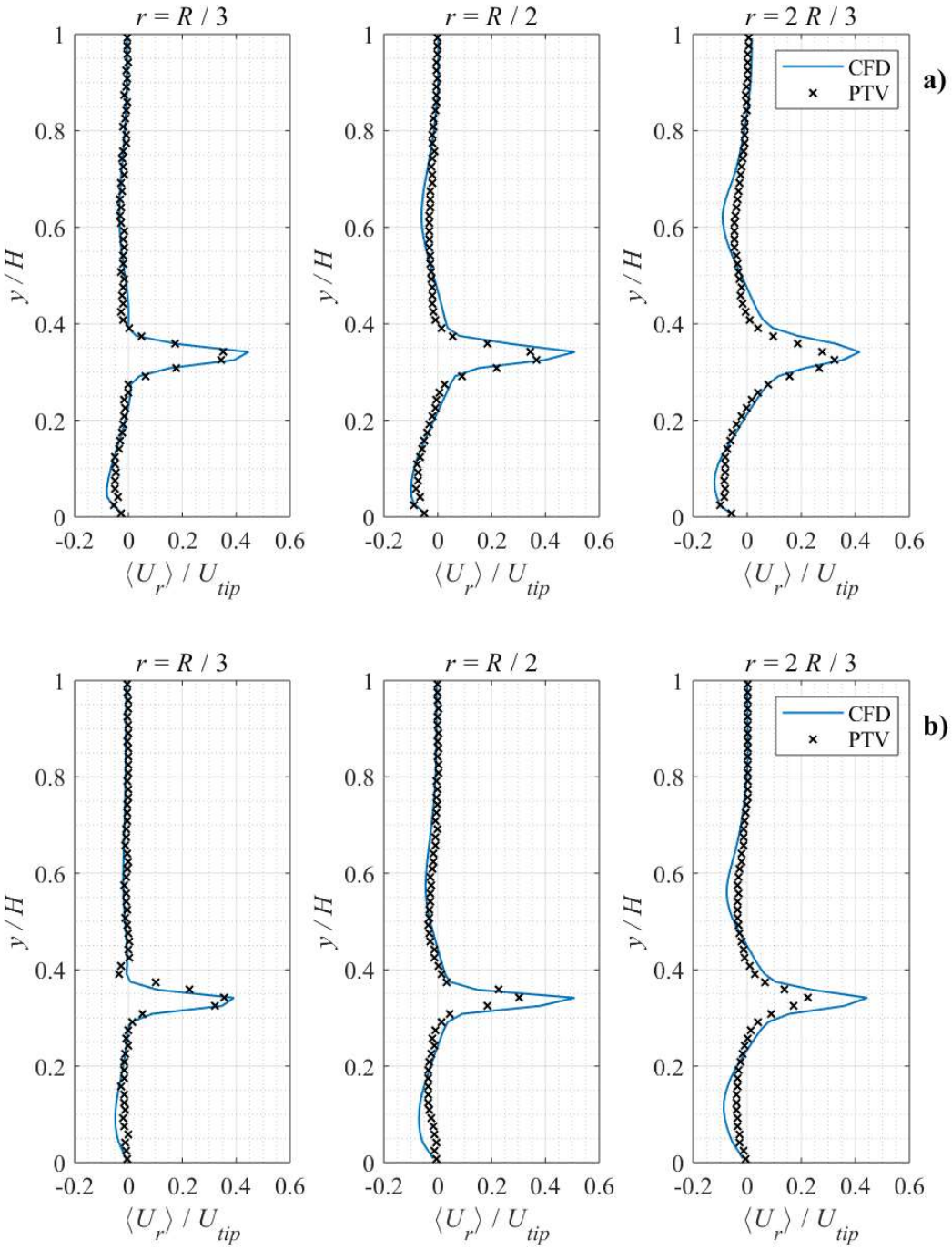

***Figure V-10**: Azimuthally averaged profiles of the radial velocity component at three radial coordinates. (a): PL1d, Re = 1,086. (b): PL2b, Re = 310.*

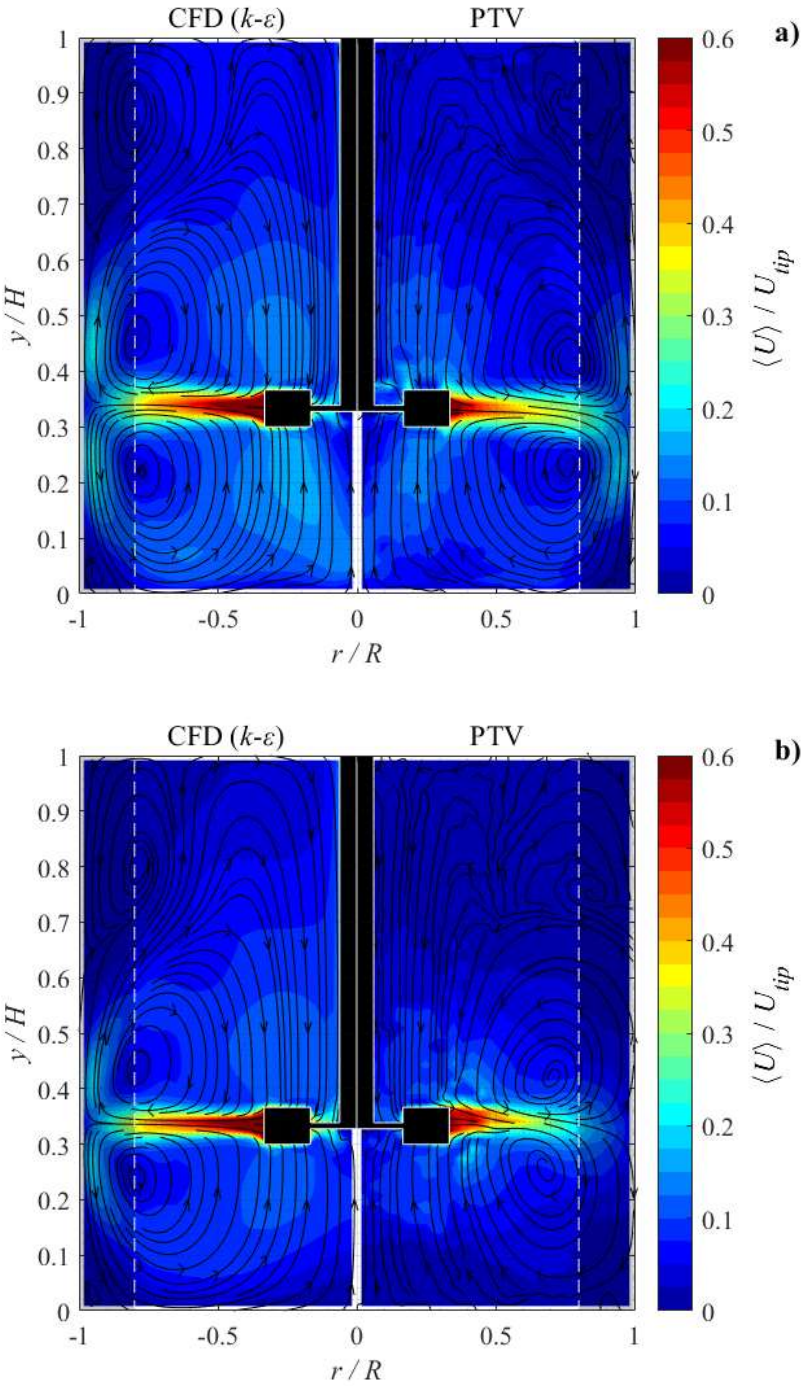

Figure V-11*: Azimuthally averaged velocity fields of the power-law fluids, as simulated with CFD and measured with PTV. (a): PL1d, Re = 1,086. (b): PL2b, Re = 310.*

The voxel-to-voxel parity plot of the experimental and numerical velocity fields is given in ***Figure V-12***. Unlike the Newtonian case (***Figure V-4***), here appreciable relative differences

could be found in the entire range of velocity values. Consequently, the RMSD was higher (***Table V-5***).

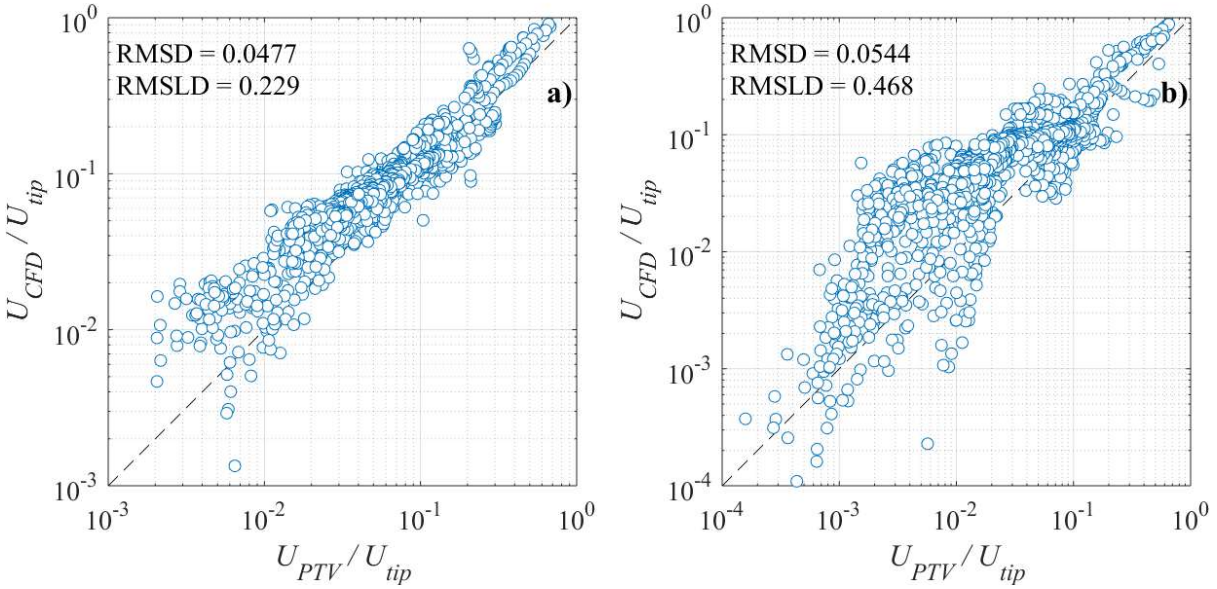

Figure V-12*: Parity plots of the azimuthally averaged velocity fields illustrated in* ***Figure V-10****. (a): PL1d, Re = 1,086. (b): PL2b, Re = 310.*

The maps of the normalised, azimuthally averaged energy dissipation rate and turbulent kinetic energy of the flow PL1d are illustrated in ***Figure V-13***. A direct comparison with results obtained for the Newtonian fluid agitated at NW1b (***Figures V-5*** and ***V-7***) reveals a strong similarity between the two flows. Although the two Reynolds numbers are very similar, it seems unlikely that the fluid rheology had so little impact on the distribution of the turbulent quantities. However, the power-law exponent of the CMC solution was $n = 0.7$, not much smaller than unity, and the fluid apparent viscosity at the Metzner-Otto shear rate was very close to that for the Newtonian glycerol solution (4.4×10^{-2} Pa s and 4.6×10^{-2} Pa s, respectively). In order to isolate the role of fluid rheology on the turbulence distribution in the vessel, future CFD simulations should involve non-Newtonian fluids with a much smaller value of power law index.

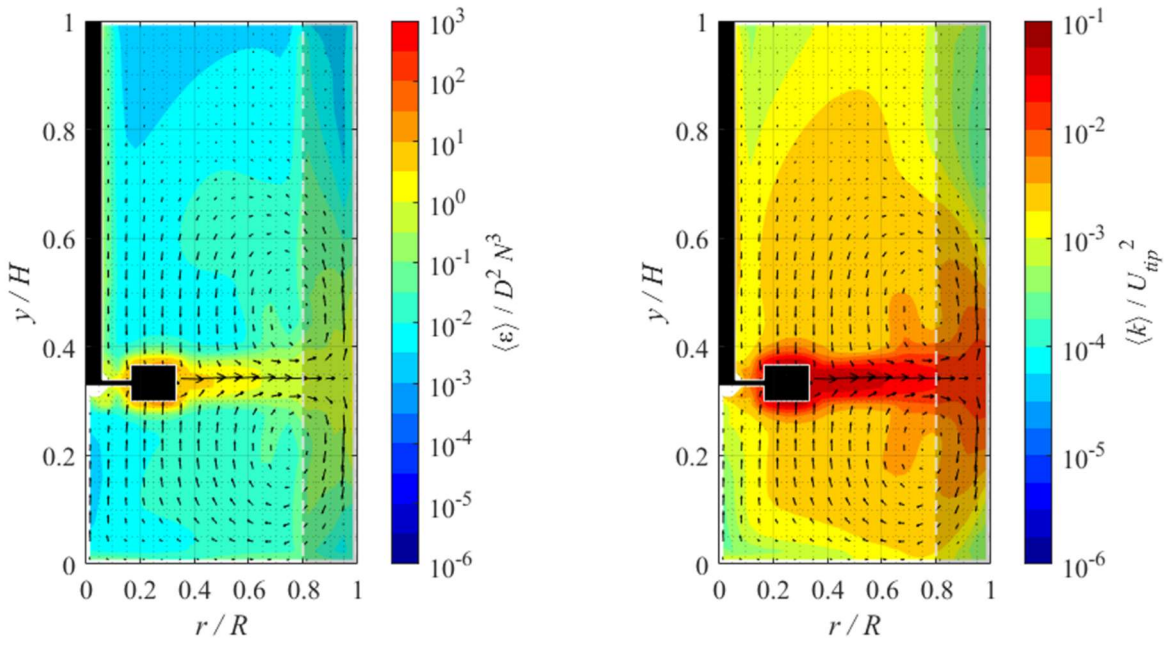

***Figure V-13**: 2D maps of the azimuthally averaged energy dissipation rate and turbulent kinetic energy (PL1d, Re = 1,086).*

The simulations of the two yield stress fluids were in reasonable agreement with the experimental data. The size and position of the two main recirculation loops have been predicted quite well, particularly at $Re = 220$. Compared to PTV, CFD slightly overestimated the cavern extension (***Figure V-14***). Roughly, CFD predicted $U_{CFD} = 2\%\ U_{tip}$ where $U_{PTV} = 1\%\ U_{tip}$ was measured. In the literature, much larger discrepancies have been reported. For instance, Xiao et al. (2014) compared six CFD turbulence models in the range $7 \leq Re \leq 163$ and found that the k-ε model overpredicted the cavern size quite significantly, particularly at $Re \leq 70$.

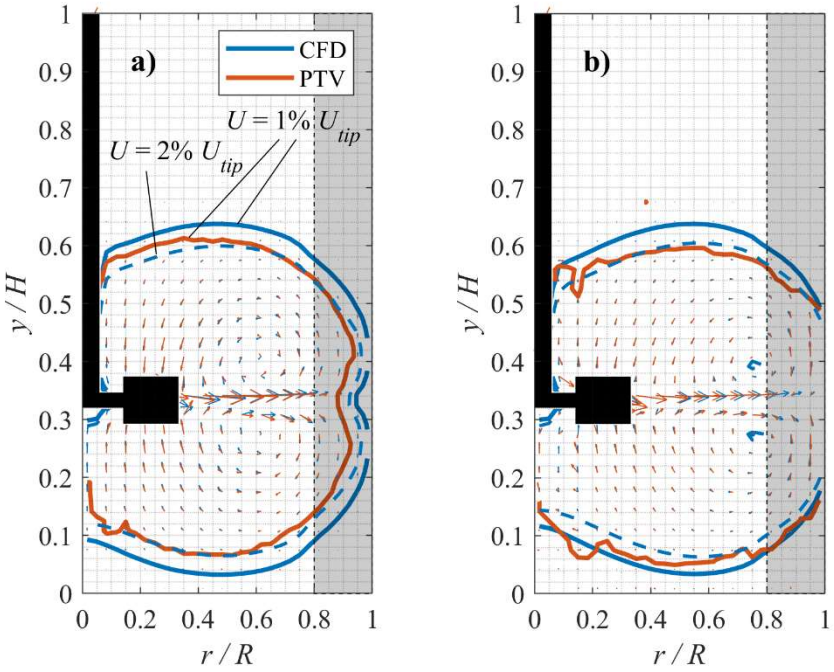

***Figure V-14**: Boundaries of the caverns formed by the two yield stress fluids and 2D velocity vectors, as simulated with CFD and measured with PTV. (a): HB1a, Re = 133. (b): HB2b, Re = 220.*

In conclusion, non-Newtonian rheology seems to amplify the difficulties associated to the RANS simulations of stirred tanks operated in the transitional regime.

V.3.4. Correlation between shear rate and Lagrangian acceleration

The analysis of the data binned on the vertical plane of the vessel revealed a strong correlation between the shear rate, obtained from CFD, and the Lagrangian acceleration, measured with PTV (***Figure V-15***). In the mid transitional regime ($Re = 943$), the Pearson's coefficient of correlation between the two quantities was PCC = 0.657. The underlying scaling rule was a power law fitting of the form $\langle a \rangle / a_{tip} = 8.3 \times 10^{-3} (\langle \dot{\gamma} \rangle / N)^{0.66}$. The correlation was even stronger in the impeller region, where PCC = 0.790 and $\langle a \rangle / a_{tip} = 14.4 \times 10^{-3} (\langle \dot{\gamma} \rangle / N)^{0.63}$. In the low transitional regime ($Re = 86$), the overall correlation coefficient was PCC = 0.756 and the scaling rule was $\langle a \rangle / a_{tip} = 6.0 \times 10^{-3} (\langle \dot{\gamma} \rangle / N)^{0.88}$. In the impeller region, PCC =

0.685 and $\langle a \rangle / a_{tip} = 14.1 \times 10^{-3} (\langle \dot{\gamma} \rangle / N)^{0.77}$. These observations indicate that Lagrangian acceleration measurements can be used to quantify local mixing intensity.

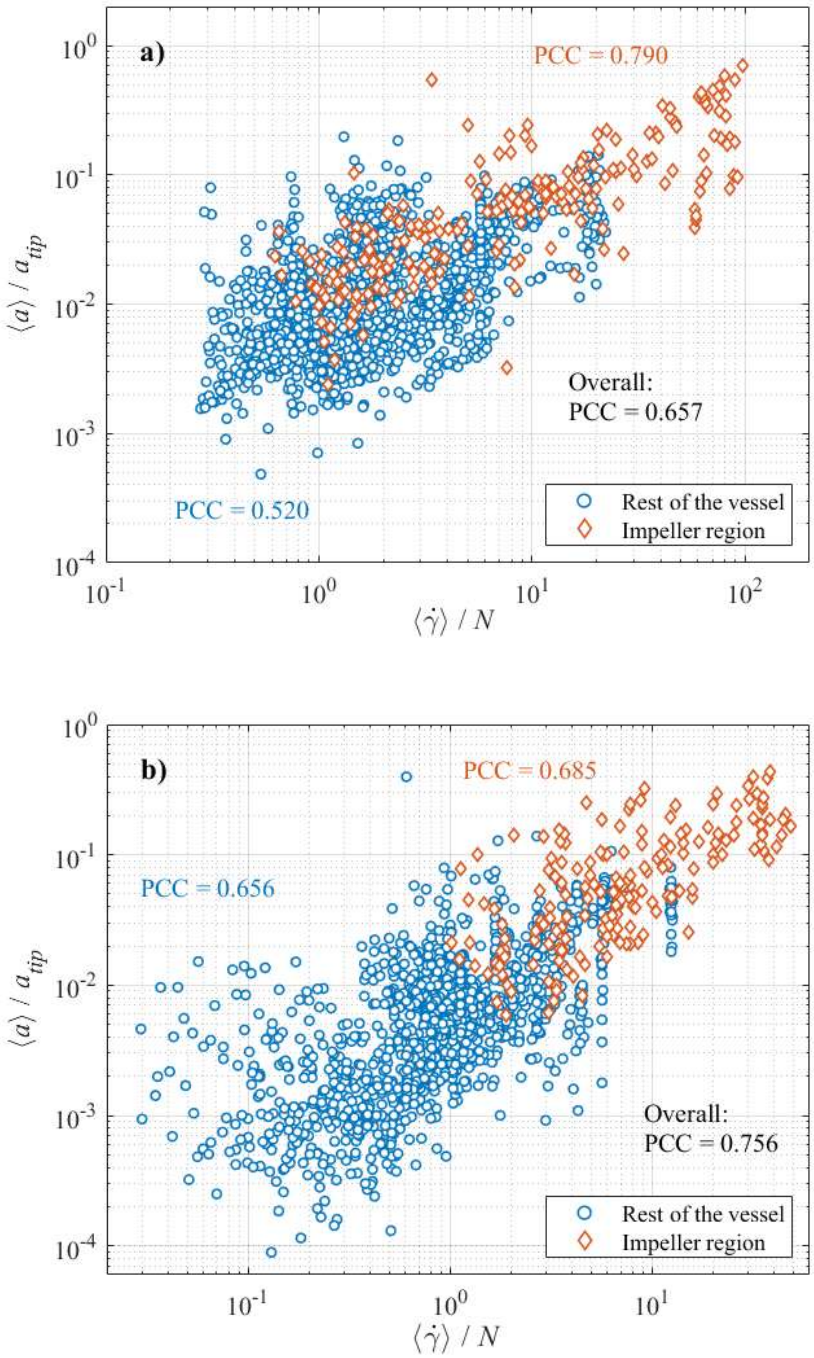

Figure V-15*: Scatter of the normalised Lagrangian acceleration against the normalised shear rate in the vessel. Newtonian fluids. (a): NW1b, Re = 943. (b): NW2a, Re = 86.*

V.4. Summary and conclusions

The transitional flows of Newtonian and non-Newtonian fluids in a lab-scale vessel stirred with a Rushton turbine have been simulated through steady RANS. Such simulations are very common, despite their limitations, because of their computational affordability. The numerical results have been compared against the PTV experiments described in **Chapter IV**. To the best of the candidate's knowledge, this is the first scientific contribution presenting a comparison between CFD and PTV data in stirred tanks. The main findings are summarised below.

The mean flow of a Newtonian fluid agitated at $Re = 943$ (NW1b) was independent from the use of a first or second order discretisation scheme. However, realistic estimations of the turbulent quantities could only be obtained with a 2UW scheme. This has been used for all subsequent simulations. The turbulence model had little effect on the mean flow. The velocity profiles predicted by the k-ε, RNG and SST models matched well the PTV measurements. Appreciable differences were only present close to the impeller tip. The cause was likely the low traceability of high velocity PTV tracers close to the impeller. The choice of the turbulence model slightly affected the distributions of the turbulent quantities. The standard k-ε model provided the power number closest to the expected value. About 80% of the total energy dissipation was resolved.

With the Newtonian fluid at $Re = 86$ (NW2a), the normalised mean velocity, energy dissipation and turbulent kinetic energy were very different from the previous case at $Re = 943$. The turbulence offset in the bulk flow was significantly lower.

Some authors have reported superior performance of the RNG and SST models over the standard k-ε in simulating stirred tank flows. In this work, the opposite has been observed both in the mid and in the low transitional flow regime. This might be a consequence to the MRF

approach to the impeller rotation. For example, according to Lane (2017), the SST model might be particularly sensitive to the position of the impeller relative to the baffles, and recommended the use of the SM approach.

With shear thinning fluids agitated at $Re = 310$ (PL2b) and $Re = 1{,}086$ (PL1d), CFD predicted a higher mean velocity in most of the tank, compared to PTV. The flow patterns and the shape of the recirculation loops did not correspond to the measured ones. The specific reason for such discrepancies is unclear. A possible, although unlikely, explanation is that the fluid rheology could not be fully described by the power-law model. Benchabane and Bekkour (2008) measured the rheological properties of CMC solutions with concentration between 0.2% and 7% wt. and observed that the power law model was not suitable to fit the data, since the log-log plots of shear stress against shear rate were not straight. However, this was only evident for concentrated solutions (> 1 wt.). Also, the researchers underlined that this finding differed from the results typically published by other authors (e.g. Ghannam and Esmail, 1997). The plots shown in **§A.6.1** demonstrate that the power-law model did fit the flow sweep data of the two CMC solutions used here, although this may not be sufficient to exclude mild viscoelasticity and thixotropy. Since the rheological tests were conducted soon after the PTV experiments, it can be excluded that the rheology of the fluids changed in the meantime, e.g. due to bacterial proliferation.

In the case of Herschel-Bulkley fluids, the flow patterns and cavern boundaries predicted by the k-ε model at $Re = 133$ (HB1a) and $Re = 220$ (HB2b) were in reasonable agreement with those obtained through PTV measurements.

Based on the Newtonian fluid data, the measured Lagrangian acceleration and simulated shear rate were correlated in space. This is a further confirm that Lagrangian acceleration measurements obtained by means of PTV can be used as indicators of local mixing intensity.

The underlying scaling rule was a power law of the form $\langle a \rangle \sim \langle \dot{\gamma} \rangle^{\beta}$. The exponent β was 0.66 and 0.88 in the two cases. More flows should be analysed to assess whether β varies consistently with the Reynolds number, fluid rheology and experimental conditions

Chapter VI

SCALE-UP STUDY OF A BATCH VESSEL IN THE TRANSITIONAL FLOW REGIME USING 3D-PTV AND CFD

Abstract

In this chapter, scale-up effects have been investigated by means of 3D-PTV and RANS simulations for two geometrically similar vessels of 4.6 L ($T_s = 180$ mm) and 21.2 L ($T_l = 300$ mm), stirred with a Rushton turbine ($C = D = T/3$). Two reference flows at the smaller scale have been selected among the experiments discussed in **Chapter IV**, one involving Newtonian rheology and one with non-Newtonian rheology. The flow conditions at the larger scale have been determined according to different scale-up criteria of the form $(N\,D^X)_l = (N\,D^X)_s$, with the scale-up index X varying between 0.33 and 2. In all cases, the flow regime was transitional. The average Lagrangian acceleration in a cylindrical region surrounding the impeller has been replicated in the larger vessel by scaling-up at $X = 1$, i.e. at equal impeller tip speed. The energy dissipation rate scaled differently based on the specific position within the vessel and on fluid rheology. For Newtonian fluids, $\varepsilon \sim D^{0.71}N^{2.34}\mu^{0.86}$ close to the impeller blade and $\varepsilon \sim D^{2.62}N^{3.27}\mu^{-3.56}$ in the jet flow. With non-Newtonian fluids, a generalised scaling rule for the energy dissipation rate has not been found. The cavern extension has been replicated by scaling-up at $X = 1$.

VI.1. Introduction

As discussed in **§II.1.6**, the scale-up of agitated vessels from laboratory to pilot and production scales is of paramount importance for the design of industrial mixing processes and for optimising the operating conditions. Preliminary tests at the laboratory scale allow the high costs and difficulties of performing research on full-scale plants to be avoided. However, finding a scale-up strategy that translates the process results at the production scale is a challenging task. Compromises are often necessary, because different process goals may have conflicting requirements (Machado et al., 2013). While geometric similarity across the different scales is typically adopted, kinematic and dynamic similarities cannot be realised concurrently. That is because mean flow velocities, turbulent fluctuations and hydrodynamic forces scale differently with the vessel size and the impeller speed. As a consequence, the scale-up criteria have a significant and complex influence on the mixing efficiency, transport coefficients, product selectivity, yield and power consumption.

Most of the scale-up rules for stirred tanks proposed in the literature have the simple form $(N\ D^X)_l = (N\ D^X)_s$ (see *Eq. II-13*), where the exponent X is chosen according to the process goals (Montante et al., 2003b). However, even for the same mixing application, the values of X reported in the literature vary broadly (Montante et al., 2003b). That is because different correlations may be suitable only within a limited range of flow conditions (Montante et al., 2003b) and for specific vessel configurations. Non-Newtonian fluid rheology complicates the scale-up task even further, because the flow variables will also depend on the fluid flow index, n. In practical applications, n often changes during the mixing process and from batch to batch. In JM, the preparation of washcoats involves many process tasks, including solid powder drawdown and dispersion and liquid blending. For this reason, the optimal X might change during the different phases of the mixing operations.

Flow hydrodynamics is undoubtedly a major factor affecting the macro-mixing performance of a stirred tank. The mean flow patterns determine the effectiveness in recirculating the fluid through the entire volume of the tank and the blending time. Therefore, it is absolutely important that the consequences of the scale-up on the vessel hydrodynamics are properly addressed (Letellier et al., 2002). However, as pointed out in **§II.1.5**, satisfactory scaling rules for a specific process objective are only available for fully turbulent and laminar mixing operations but not for the transitional regime. More data are needed to fill this knowledge gap.

This chapter presents a scale-up study of a 4.6 L vessel to a geometrically similar 21.2 L vessel, both operated under transitional flow conditions. Two reference flows at the smaller scale have been selected among those investigated in **Chapter IV**. One involved a Newtonian fluid (NW1a) and one a non-Newtonian fluid (HB1a) which possesses a yield stress. The scaling of the main flow quantities in the transitional regime have been investigated as X was varied. Experimental data obtained by means of 3D-PTV have been used to study the distributions of Lagrangian acceleration in a flow region surrounding the impeller. CFD simulations have provided access to the values of turbulent kinetic energy and energy dissipation rate at specific positions in the vessel. For the non-Newtonian fluid, the cavern extension has been determined with both experimental and numerical data.

VI.2. Materials and methods

VI.2.1. Flow conditions

The smaller vessel has been described in detail in **§IV.2.1**. The diameter and liquid height were $T_S = H_S = 180$ mm. The tank had a flat bottom and was equipped with four baffles of width $B_S = T_S/10$. The impeller was a 6-blade Rushton disk turbine of diameter $D = T/3$ placed at

a height $C_s = T_s/3$ from the bottom. The larger vessel was geometrically similar to the smaller one and had a diameter $T_l = 300$ mm. The length ratio was $S = D_l/D_s = 1.67$.

The flow conditions for the two case studies are given in ***Table VI-1***. Experiments NW1a and HB1a were the reference flows for the Newtonian and non-Newtonian case, respectively. PTV experiments and CFD simulations at the larger scale have been conducted for five values of the scale-up index X ranging from 0.33 to 2. Additional simulations have been used to validate and refine a model for predicting the energy dissipation rate based on the flow conditions and fluid rheology.

The fluids used in the larger vessel have been prepared from scratch. Therefore, the new rheological parameters have been measured with the same methods described in **§IV.2.1**. The rheological data are displayed in **§A.6.2**. In the case of the glycerol solution (NW1), the viscosity has been reproduced within ~1% deviation from the fluid used in the smaller vessel. For the new Carbopol solution (HB1), the measured yield stress was $\tau_0 = 3.2$ Pa instead of 4.2 Pa and $n = 0.52$ instead of 0.50. Such differences were inevitable, as the rheology of Carbopol solutions is very sensitive even to small variations of pH. The impact on the apparent viscosity, calculated with the Metzner-Otto method, was $\sim 7\%$ in the worst case. The numerical simulations conducted by Patel et al. (2015) showed that a small variation in the fluid yield stress had negligible effects on the fraction of fully mixed volume of the flow. Hence, the differences have been considered acceptable. The rheological parameters of fluids NW2, PL1, PL2 and HB2 used in the validation dataset were the same as in **Chapter IV**.

***Table VI-1**: Flow conditions.*

Experiment	X	Impeller speed (rpm)	μ_e (Pa s)	Re	PTV camera frame rate (s^{-1})
Newtonian case study (PTV and CFD)					
NW1a	-	400	4.6×10^{-2}	629	250
NW1a_ND^2	2	144	4.6×10^{-2}	629	125
NW1a_ND	1	240	4.6×10^{-2}	1,048	250
NW1a_ND$^{0.67}$	0.67	284	4.6×10^{-2}	1,240	250
NW1a_ND$^{0.5}$	0.5	310	4.6×10^{-2}	1,353	250
NW1a_ND$^{0.33}$	0.33	338	4.6×10^{-2}	1,475	250
Non-Newtonian case study (PTV and CFD)*					
HB1a	-	400	1.8×10^{-2}	133	125
HB1a_ND^2	2	144	3.4×10^{-1}	71	125
HB1a_ND	1	240	2.5×10^{-1}	163	250
HB1a_ND$^{0.67}$	0.67	284	2.2×10^{-1}	215	250
HB1a_ND$^{0.5}$	0.5	310	2.1×10^{-1}	247	250
HB1a_ND$^{0.33}$	0.33	338	2.0×10^{-1}	285	250
Newtonian simulations for validation and refinement of Eq. VI-2 (CFD only)					
NW1b	-	600	4.6×10^{-2}	943	-
NW1b_ND^2	2	216	4.6×10^{-2}	943	-
NW1b_ND	1	360	4.6×10^{-2}	1,572	-
NW1b_ND$^{0.67}$	0.67	426	4.6×10^{-2}	1,860	-
NW1b_ND$^{0.5}$	0.5	465	4.6×10^{-2}	2,030	-
NW1b_ND$^{0.33}$	0.33	507	4.6×10^{-2}	2,214	-
NW2a	-	200	1.7×10^{-2}	86	-
Non-Newtonian simulations for validation of Eq. VI-4 (CFD only)					
PL1d	-	800	4.4×10^{-2}	1,086	-
PL2b	-	800	1.5×10^{-1}	310	-
HB2b	-	1,500	4.1×10^{-1}	220	-

* HB1a_ND^2 *and* HB1a_ND$^{0.33}$ *studied with PTV only.*

In this study, the Reynolds number ranged from 71 to 2,214. For the yield stress fluids, the range of Bingham number was $0.33 \leq Bi \leq 0.58$.

VI.2.2. 3D-PTV measurements

VI.2.2.1. Operational variables at the larger scale

In **Chapter III**, guidelines for 3D-PTV measurements in stirred vessels at the lab-scale have been developed. In particular, the importance of selecting the correct tracer concentration and camera frame rate based on the reconstruction error has been expressed through *Eq. III-1* and *Eq. III-5*. However, as the measurement volume increased to 21 L, these two conditions could not be met in practice. The reasons will be discussed below. As a result, the PTV measurements in the larger vessel were characterised by a lower tracking efficiency.

The spatial calibration routine has been conducted as described in **§III.2.3**. Due to the larger measurement volume and smaller pixel size, the average error in the reconstructed coordinates was ~270 µm, much worse than the ~60 µm obtained with the smaller tank. According to *Eq. III-1*, the camera frame rate should decrease proportionally to the reconstruction error. However, excessively low values would prevent high-velocity tracers from being captured properly. The PTV images have been recorded at the frame rates listed in ***Table VI-2***. The shutter time was 1/3600 s and the tracers appeared spherical. Each experiment consisted of a sequence of 5,400 images.

The same particles used in **Chapter IV** have been used. Since these tracers could adequately follow the flows in the smaller tank, they were also suitable for the larger vessel. Based on *Eq. III-5*, the tracer concentration should decrease with the third power of the reconstruction error and with the frame rate. However, an insufficient number of tracers would result in unacceptably low occupancy and compromise the representativeness of the experiment. Thus,

the tracer concentration has been reduced from 114 L^{-1} to 53 L^{-1}, corresponding to a blur image density of 0.004 px^{-2}. This was a compromise between data sparsity in the measurement volume and tracking difficulty. In fact, with a blur size in the digital images between 2 and 3 px, the ratio of indistinguishably overlapping particles was between 0.6% and 1.4% (Cierpka et al., 2013), roughly the same as in the smaller vessel.

VI.2.2.2. Lagrangian acceleration

In the previous chapters, the average Lagrangian acceleration in the impeller region was found to be correlated to the average shear rate (***Figure IV-9***) and to the mean square distance travelled by the tracers in a time equal to one impeller period (***Figure IV-11***). Also, the local acceleration was moderately correlated to local shear rate (***Figure V-15***). Therefore, it was worth investigating how the mean acceleration changes when the vessel is scaled-up.

The distributions of the Lagrangian acceleration in a control volume surrounding the impeller have been used to quantify the local degree of mixing in the investigated flows. The control volume was defined as

$$\begin{cases} r \leq D \\ C - \frac{D}{4} \leq y \leq C + \frac{D}{4} \end{cases}. \qquad \textit{Eq. VI-1}$$

As in the experiments presented in **Chapter IV**, the distributions were close to log-normal. Thus, the mean and standard deviation have been calculated in logarithmic space.

VI.2.2.3. Mean square displacement

The mean square displacement (MSD) of the tracers passing through a control volume close to the impeller has been determined as described in **Chapter IV**. The control volume had a volume $V_s = 0.1\%\ (V_{tank}/2) = 10.6\ \text{cm}^3$. In the reminder, the MSD after a time equal to one impeller period is indicated with MSD^*.

VI.2.3. CFD simulations

VI.2.3.1. CFD framework

The flows have been simulated through steady RANS using a mesh of 4.2 million cells. The MRF approach has been adopted to simulate the impeller rotation. The liquid free surface has been modelled as flat, because the baffles prevented vortex formation. The turbulence model was the standard k-ε. All model constants have been kept to their default values. Wall functions have been used to model the flow in the cells adjacent to solid walls. Other numerical settings included the 2UW scheme for interpolating the face values, a least-square gradient scheme and a cell-based gradient limiter and the use of three non-orthogonality corrector loops. The simulations were stopped when the sum of normalised residuals of the simulated quantities had dropped below 10^{-5}.

VI.2.3.2. Energy dissipation and turbulent kinetic energy

The energy dissipation rate, ε, and turbulent kinetic energy, k, have been azimuthally averaged to obtain their profiles on the vertical plane of the vessel. This enabled the different profiles at the larger scale to be compared with the reference profile at the smaller scale.

For the Newtonian case study, ε and k have been monitored in two sample cells to assess the effects of the scale-up index in two specific locations. The first sample cell was near the lower edge of the impeller blade tip, at approximately $\{x, y, z\} = \{0, C - T/10, D/2\}$. The second was located within the trailing vortices shred by the impeller blade, at $\{x, y, z\} = \{0, C, T/2\}$. The position of the two cells is pictured in ***Figure VI-1***. In the image, the trailing vortices have been visualised as the isosurface corresponding to $\varepsilon = 32\ D^2N^3$ and using the data from flow NW1a. It has been checked that the values of k and ε were independent of the specific blade considered.

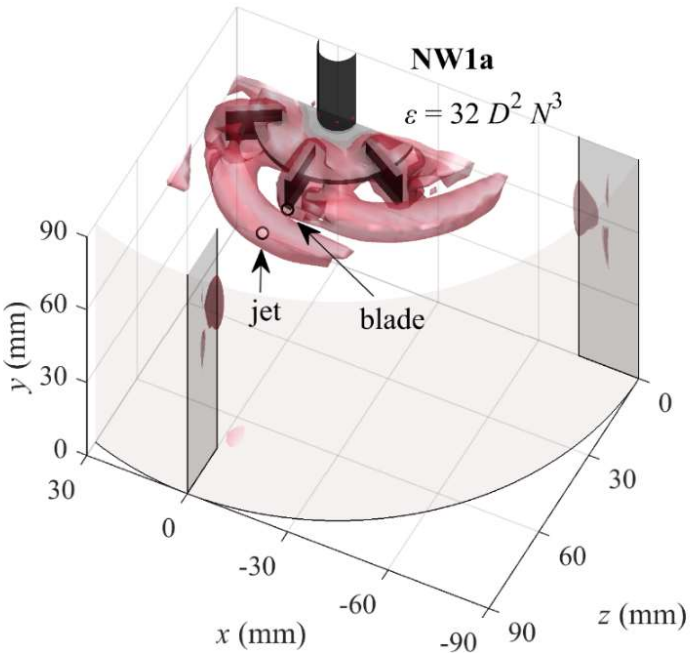

***Figure VI-1**: Location of the two sample cells for monitoring ε and k over different values of the scale-up index.*

It will be shown that, in both positions, ε did not scale with D^2N^3 (corresponding to $X = 0.66$, as expected in the fully turbulent regime), nor with N^2 ($X = 0$, as expected in the laminar regime). The values of ε in the two sample cells have been fitted through multivariate regression to assess the dependence on D and N in the transitional regime. A power-law function of the form

$$\varepsilon = \alpha\ D^{\beta} N^{\gamma} \qquad \textit{Eq. VI-2}$$

has been used. The parameters α, β and γ for the two sample cells have been determined with a least-square method. The resulting models were specific of the Newtonian fluid used. In fact, in the laminar regime, the energy dissipation increases linearly with fluid kinematic viscosity. Therefore, some effects of fluid viscosity were expected also in the transitional regime. The two models have been validated and refined in three steps, as described below.

1. First, each fitting has been validated using a set of new CFD simulations involving the same Newtonian fluid. The flow NW1b ($Re = 943$) has been selected for the smaller

scale. The flow conditions at the larger scale have been determined by setting $X = 2$, 1, 0.66, 0.5 and 0.33.

2. Then, each model has been refined to include the effects of Newtonian fluid viscosity. The numerical data of flow NW2a ($Re = 86$) have been added to the previous data set. As an intermediate behaviour between the laminar ($\varepsilon \sim N^2\ \mu/\rho$) and the turbulent ($\varepsilon \sim D^2\ N^3$) scaling rules was expected, an equation of the form

$$\varepsilon = \alpha\ D^{\beta} N^{\gamma} (\mu/\rho)^{\delta} \qquad \textit{Eq. VI-3}$$

has been used.

3. Finally, the possibility to extend the model for ε_{blade} to non-Newtonian fluids has been addressed. The energy dissipation at the impeller blade has been fitted according to

$$\varepsilon_{blade} = \alpha\ D^{\beta} N^{\gamma} (\mu_e/\rho)^{\delta}\ M^{\epsilon}, \qquad \textit{Eq. VI-4}$$

where μ_e is the effective viscosity according to the Metzner-Otto model and M is a dummy variable which enables binary categorisation of the data. Since *Eq. VI-4* is linear in logarithmic space, $M = 10^0 = 1$ for Newtonian fluids and $M = 10^1 = 10$ for non-Newtonian fluids. With this definition, the variable $\mathrm{Log}(M)$ can be switched on/off according to the fluid rheology. The model has been validated using the CFD simulations presented in **Chapter V** and corresponding to the flows PL1d, PL2b and HB2b. This analysis has been attempted only for the blade sample cell because the cell in the impeller jet could fall outside of the cavern boundaries, depending on the flow conditions.

VI.3. Results

VI.3.1. Flow fields visualisation

Figure VI-2 displays the path lines of the tracers in the vessels, obtained by superimposing the PTV trajectories over 4 impeller revolutions, and enable qualitative comparison of the investigated flows.

In the case of the Newtonian fluid NW1, the overall features of the flows appeared quite similar to the reference case at the small scale, independently of the scaling factor. Two main recirculation loops were present above and below the plane of the impeller. A third, weaker recirculation loop was formed in the top third of the vessel.

Instead, formation of caverns of increasing size can be appreciated in the case of non-Newtonian fluid HB1. At $X = 2$ ($Re = 71$), the impeller lost most of its pumping capacity. A scale-up index $X > 1$ leads to a significant reduction of the impeller rotational speed. In the case of non-Newtonian fluids with flow index $n < 1$, the Reynolds number also decreases, due to the lower effective shear rate and higher apparent viscosity. For this reason, a scale-up index $X > 1$ might have detrimental effects on mixing and should be avoided.

Two examples of Lagrangian trajectories after 3D reconstruction are given in ***Figure VI-3***. Quantitative results are presented in the next sections.

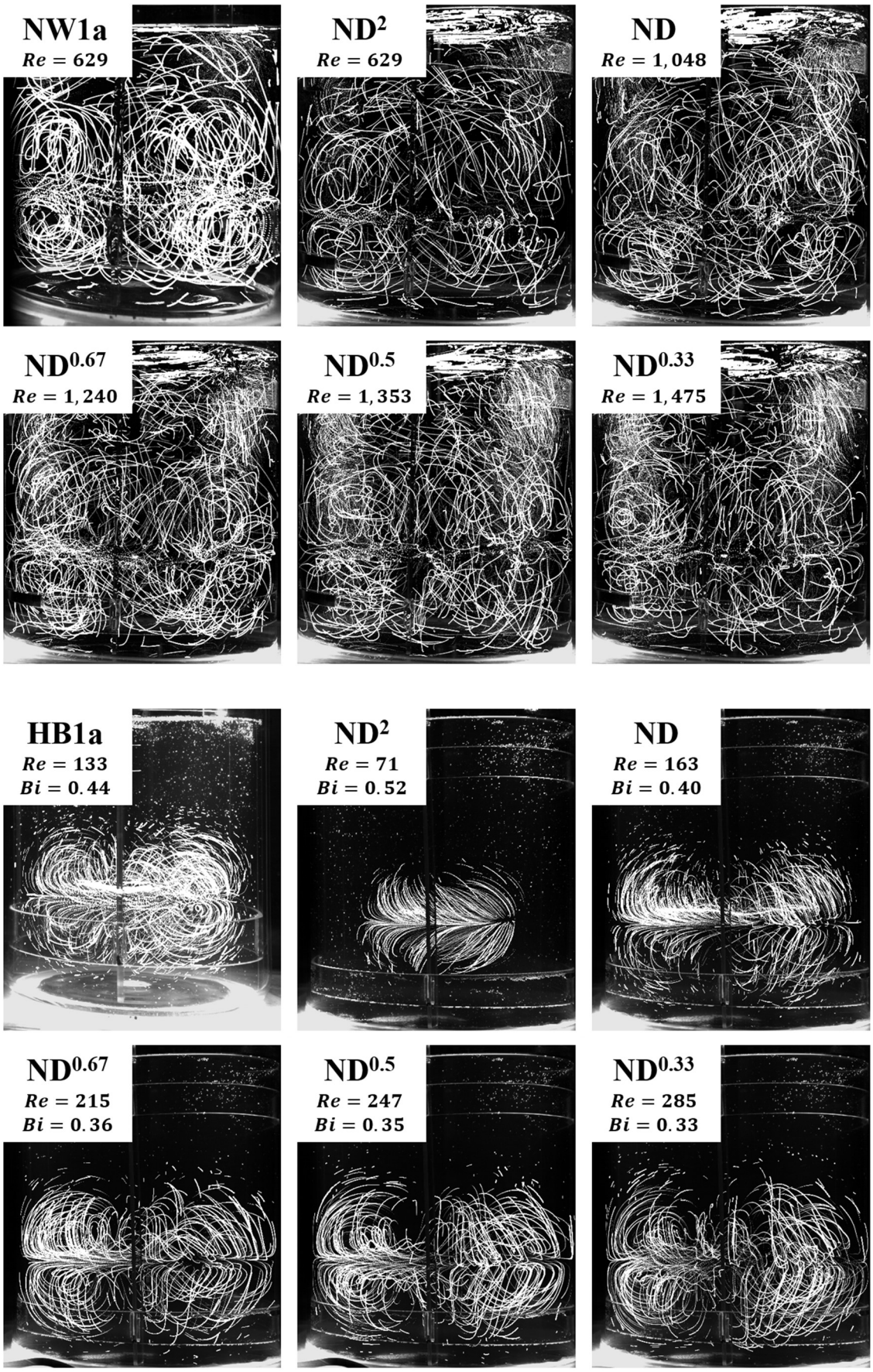

***Figure VI-2**: Tracer path lines obtained by superimposition of the raw images.*

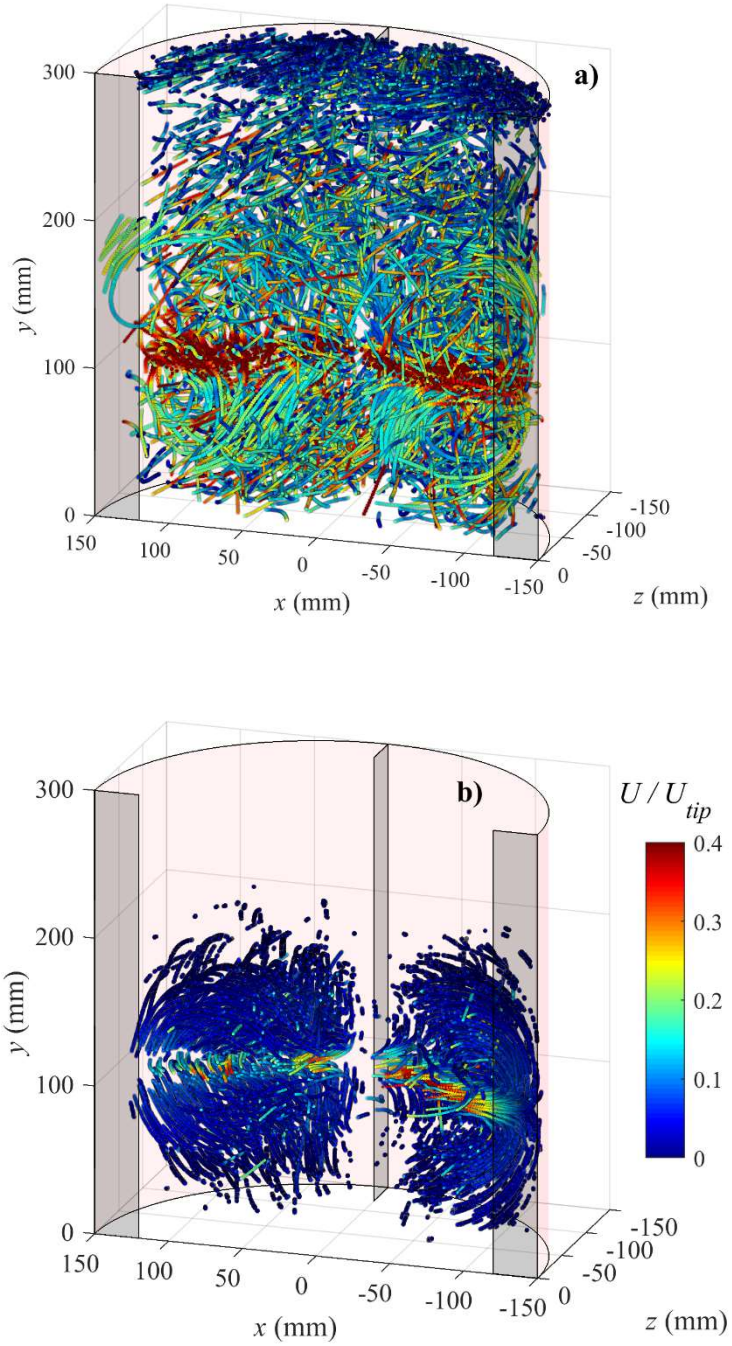

***Figure VI-3**: Selections of Lagrangian trajectories sampled from experiments NW1a_ND (a) and HB1a_ND$^{0.67}$ (b).*

VI.3.2. Scaling of the Lagrangian acceleration and mean square displacement

The Lagrangian acceleration in the vessel has been measured directly by means of 3D-PTV. As the centripetal acceleration at the impeller tip is $a_{tip} = 2\ {U_{tip}}^2/D$, the mean acceleration in the region surrounding the impeller might be expected to scale similarly to $D\ N^2$ and to stay constant for $X = 0.5$. However, the PTV measurements showed that the mean acceleration of the smaller scale and its standard deviation have been replicated in the larger vessel with $X \sim 1$ (***Figure VI-4***). This was valid for both the Newtonian fluid NW1 and the non-Newtonian fluid HB1. Higher values of acceleration were achieved for $X < 1$. In the plot, the two dashed horizontal lines represent the mean acceleration for experiments NW1a and HB1a in the smaller vessel, the markers indicate the mean acceleration at the larger scale, the coloured bands and the vertical bars indicate one standard deviation above and below the mean values.

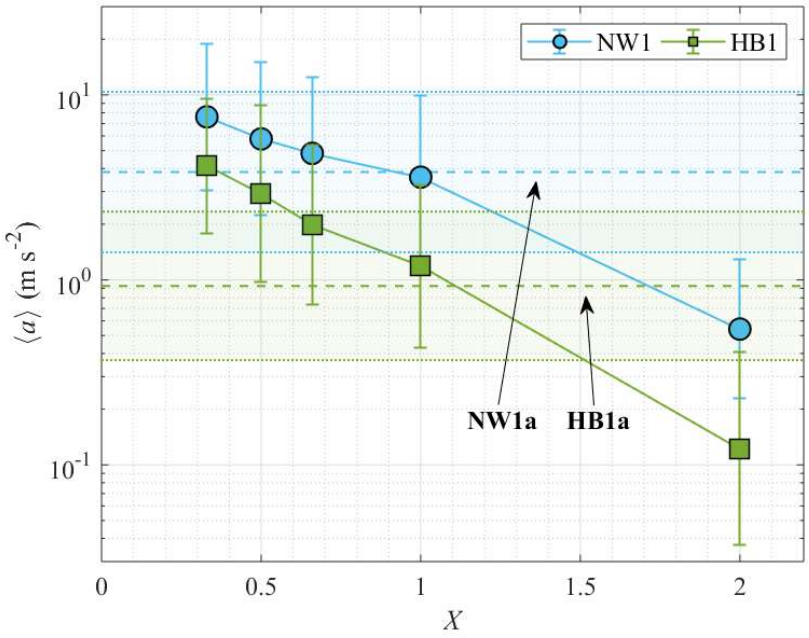

Figure VI-4*: Plot of the Lagrangian acceleration in a control volume surrounding the impeller against the scale-up index, measured with PTV.*

The MSD* of the PTV experiments and the MSD* normalised by D^2 are given in ***Table VI-2***. For the Newtonian fluid, the normalised MSD* at the large scale was essentially independent of the scaling factor and replicated the value of the reference case at the small scale (***Figure VI-5***). In fact, in a self-similar flow, the MSD* might be expected to scale as $\sim U^2t^2 \sim (D\ N)^2 N^{-2} \sim D^2$. Instead, with the non-Newtonian fluid, the normalised MSD* was smaller at lower impeller speeds, i.e. larger values of X (***Figure VI-5***). This reflects the loss of pumping of the impeller at low rotational speed. As found in **§IV.3.4**, the mean Lagrangian acceleration in the region surrounding the impeller was found to be proportional to the MSD* multiplied by N^2, regardless of the size of the vessel and the fluid rheology (***Figure VI-6***). In other words, the square distance travelled in a time span of one impeller period by a tracer that enters the impeller region is determined by the quantity $\langle a \rangle / N^2$. Note that $\langle a \rangle / N^2$ is a function of the vessel size and fluid rheological properties.

Table VI-2*: MSD and normalised MSD of the tracers passing through a control volume close to the impeller, after one impeller period* ($t = 1/N$).

Experiment	MSD* (m^2)	MSD*$/D^2$
NW1a	2.11E-03	5.86E-01
NW1a_ND^2	6.11E-03	6.11E-01
NW1a_ND	5.92E-03	5.92E-01
NW1a_ND$^{0.67}$	5.61E-03	5.61E-01
NW1a_ND$^{0.5}$	5.85E-03	5.85E-01
NW1a_ND$^{0.33}$	5.70E-03	5.70E-01

Experiment	MSD* (m^2)	MSD*$/D^2$
HB1a	9.58E-04	2.66E-01
HB1a_ND^2	1.93E-03	1.93E-01
HB1a_ND	2.71E-03	2.71E-01
HB1a_ND$^{0.67}$	3.51E-03	3.51E-01
HB1a_ND$^{0.5}$	3.75E-03	3.75E-01
HB1a_ND$^{0.33}$	3.41E-03	3.41E-01

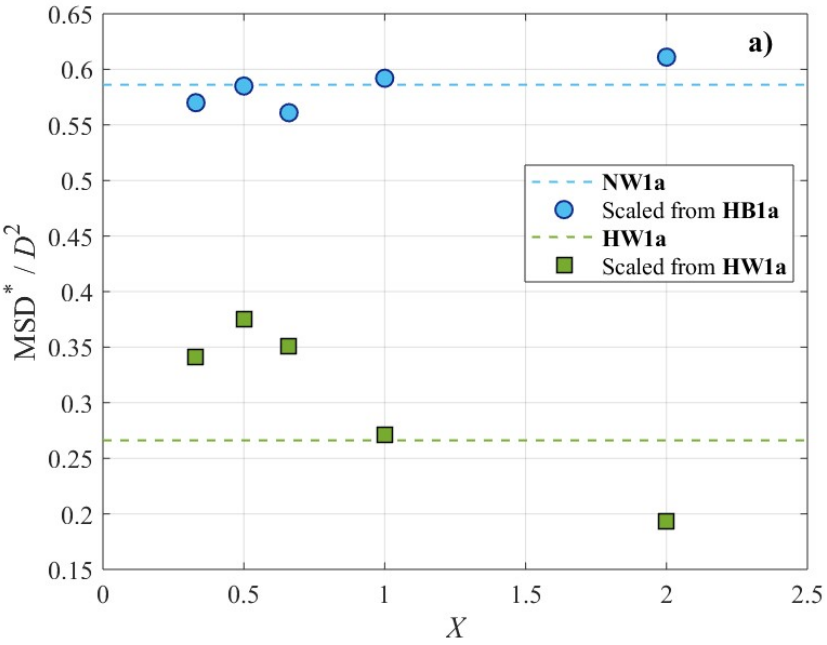

***Figure VI-5**: Plot of the normalised MSD^* against the scale-up index.*

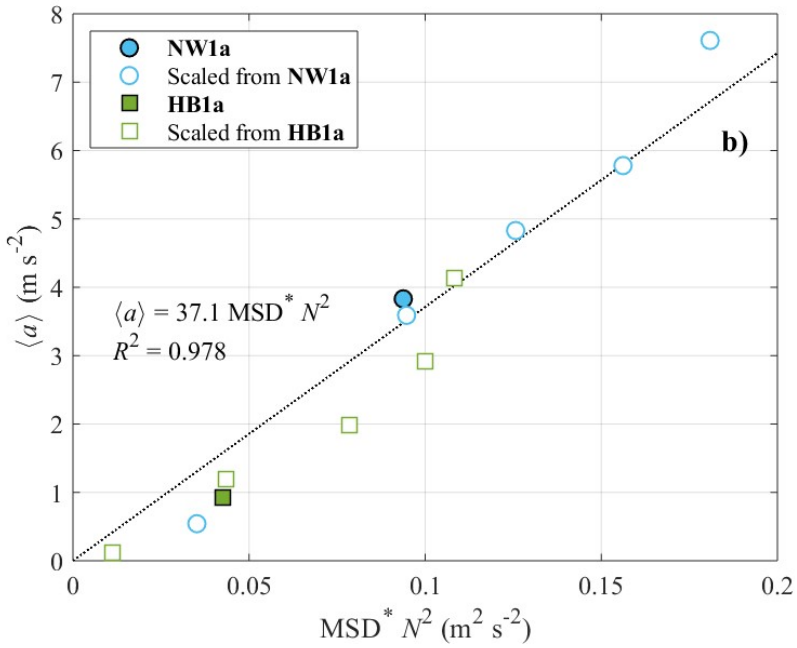

***Figure VI-6**: Plot of the average Lagrangian acceleration in the impeller region against MSD^* multiplied by N^2 at two vessel scales.*

VI.3.3. Scaling of the energy dissipation rate and turbulent kinetic energy

The turbulent quantities in the vessel have been obtained with the CFD simulations. The scale-up index X had considerable impact on the azimuthally averaged profiles of energy dissipation rate in the vertical plane of the vessel (***Figure VI-7***). The energy dissipation scaled differently depending on the position relative to the impeller. At $r = R/3$, along the height of the impeller blades ($0.30\ H \leq y \leq 0.37\ H$), ε was about three orders of magnitude higher than in the rest of the vessel, and the profile of the smaller scale lay between the profiles corresponding to $X = 0.5$ and $X = 0.66$. However, for larger radial and axial distances from the impeller, ε diminished significantly and X was between 0.67 and 1.

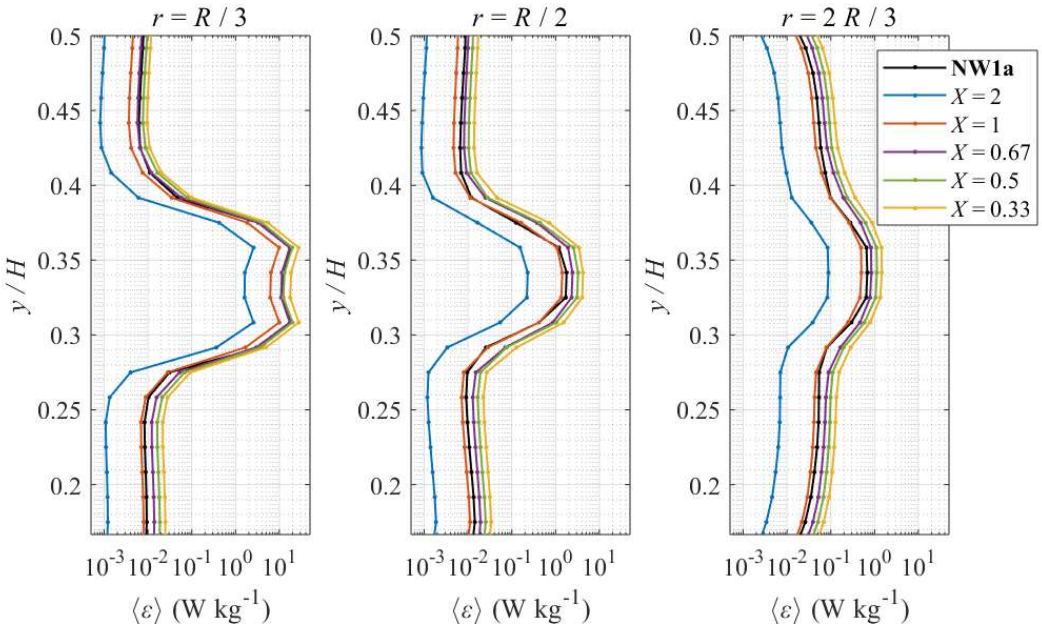

Figure VI-7*: Azimuthally averaged profiles of the energy dissipation rate at three radial coordinates, as predicted with CFD (Newtonian data), in log scale (top) and linear scale (bottom).**(Continues in the next page).*

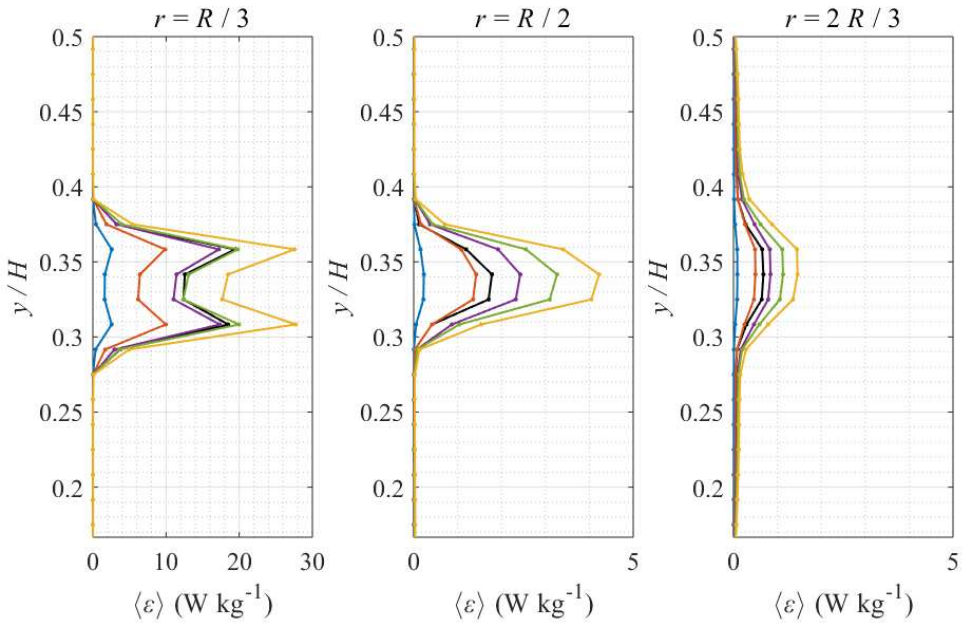

***Figure VI-7** (continues).*

Figure VI-8 shows how ε and k in two sample cells varied with X. Close to the edge of the impeller blade, the energy dissipation rate of the smaller scale was very similar with the one predicted at $X = 0.33$. Instead, in the jet flow, the scale-up index that would keep the same ε was between 0.66 and 1.

The results of the multivariate regressions of energy dissipation rate data are given in ***Table VI-3***. The symbol '±' indicates the 95% confidence intervals around the calculated parameters. The value of X that keeps the same ε of the smaller scale is simply $X = \beta/\gamma$.

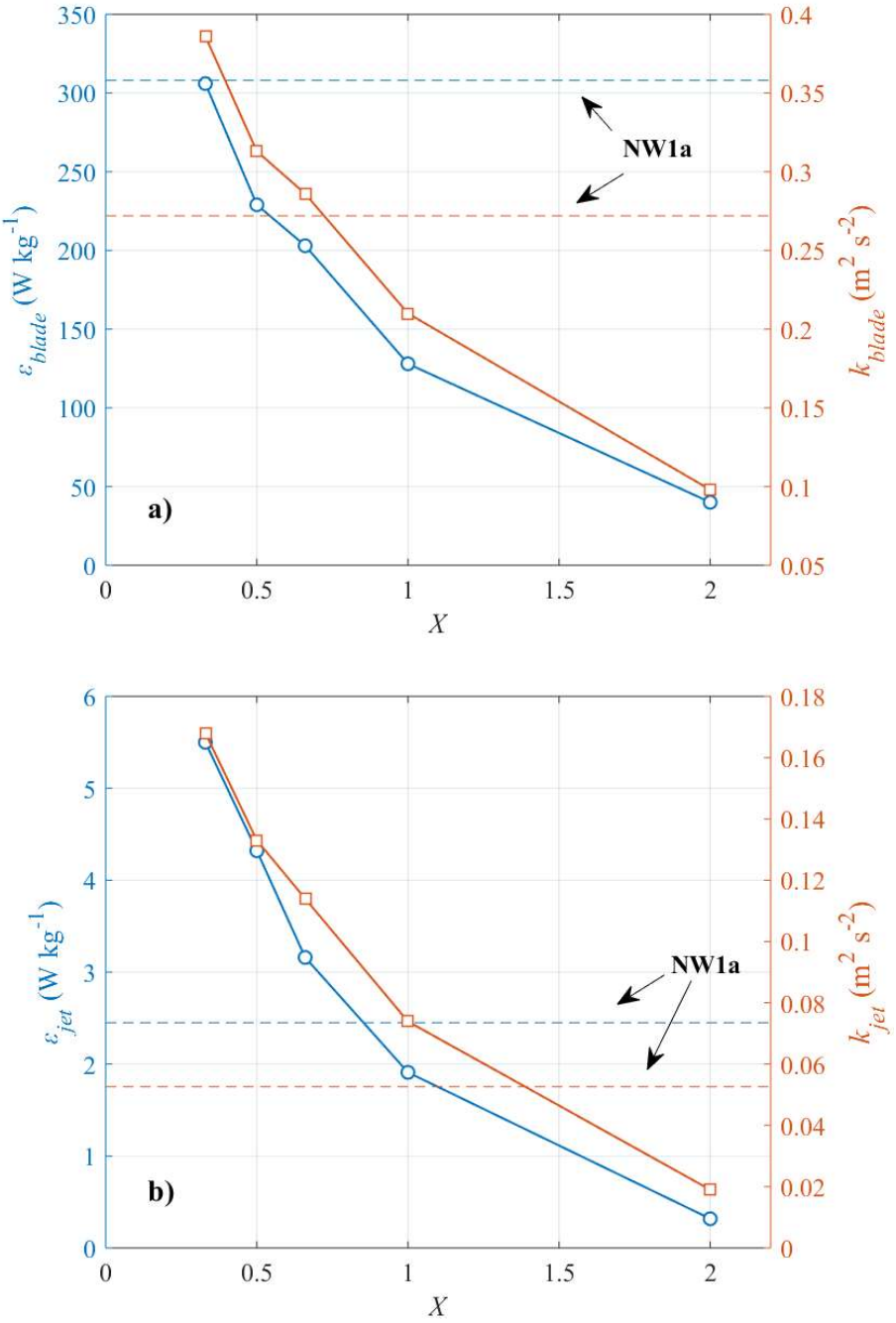

***Figure VI-8**: Plots of the local energy dissipation rate and turbulent kinetic energy close to the impeller blade (a) and in the impeller jet (b) against the scale-up index (Newtonian data).*

***Table VI-3**: Parameters to be used in the models for the local energy dissipation rate.*

Sample cell	$\mathrm{Log}_{10}(\alpha)$	β	γ	δ	ϵ	X
Only fluid NW1a (Eq. VI-2)						
blade	1.40 ± 0.32	0.69 ± 0.36	2.35 ± 0.21	-	-	0.29
jet	1.00 ± 0.30	2.76 ± 0.33	3.36 ± 0.19	-	-	0.82

Only Newtonian fluids, NW1a and NW1b (Eq. VI-3)						
blade	5.21 ± 0.43	0.71 ± 0.13	2.34 ± 0.06	0.86 ± 0.08	-	0.30
jet	-14.8 ± 0.6	2.62 ± 0.16	3.27 ± 0.08	-3.56 ± 0.11	-	0.80
Newtonian and non-Newtonian fluids (Eq. VI-4)						
blade	5.52 ± 0.81	0.79 ± 0.22	2.33 ± 0.13	0.91 ± 0.16	-0.96 ± 0.12	0.34

By using the data from the Newtonian case study only, the local energy dissipation rate scaled as $\varepsilon_{blade} \sim D^{0.69}N^{2.35}$ close to the impeller blade and as $\varepsilon_{jet} \sim D^{2.76}N^{3.36}$ in the discharge flow. Note that, at the blade, γ was between the theoretical values of 2 and 3, valid in the laminar and fully turbulent regimes, respectively. The resulting scale-up index was 0.29, between 0 and 0.67. Interestingly, in the impeller jet, $X = 0.82$, which is even higher than the value expected in the turbulent regime. The two models fitted well the validation dataset (***Figure VI-9***).

When the Newtonian fluid viscosity was added as a predictor into the models, the exponents β and γ, and thus X, remained basically unchanged. The scaling rules became $\varepsilon_{blade} \sim D^{0.71}N^{2.34}\mu^{0.86}$ and $\varepsilon_{jet} \sim D^{2.62}N^{3.27}\mu^{-3.56}$, valid in the range $86 \leq Re \leq 2{,}214$. These results highlight the critical importance of fluid viscosity on energy dissipation. Close to the impeller blade, where most of the energy is dissipated, $X = 0.30$ and ε increases with the fluid viscosity. The exponent $\delta = 0.86$ is slightly smaller than the value of 1 expected in the laminar regime, but definitely larger than the value of 0 characteristic of fully turbulent conditions. Very interestingly, away from the impeller ε decreases rapidly with the Newtonian viscosity. That means that the fraction of vessel volume where most energy dissipation occurs becomes smaller and smaller as the fluid viscosity increases. The two models fitted the energy dissipation rate of the Newtonian fluids very well ($R^2 > 0.99$). However, the data from non-

Newtonian simulations did not align to the Newtonian ones (***Figure VI-10*** shows ε_{blade}), indicating that Newtonian and non-Newtonian fluids behave very differently.

In light of the above, an attempt to generate a general model has been made by adding the dummy variable M to the equation, as explained in **§VI.2.3.2**. The multivariate regression using both Newtonian and non-Newtonian data gave $\varepsilon_{blade} \sim D^{0.79} N^{2.33} {\mu_e}^{0.91} M^{-0.96}$, with a scale-up index $X = 0.34$. The parity plot of the model against the dataset is given in ***Figure VI-11***. Despite the coefficient of determination of the fitting being very high ($R^2 > 0.994$), non-Newtonian data from the validation dataset did not align to the parity line. This highlights how scale-up fittings with high R^2 are not always meaningful, and validation against new data is always necessary. It has been concluded that *Eq. VI-4* did not fit the scaling of the energy dissipation rate in the case of non-Newtonian fluids. As a recommendation for future research, more CFD simulations should be conducted for different values of D, N and μ_e in order to test more complex models.

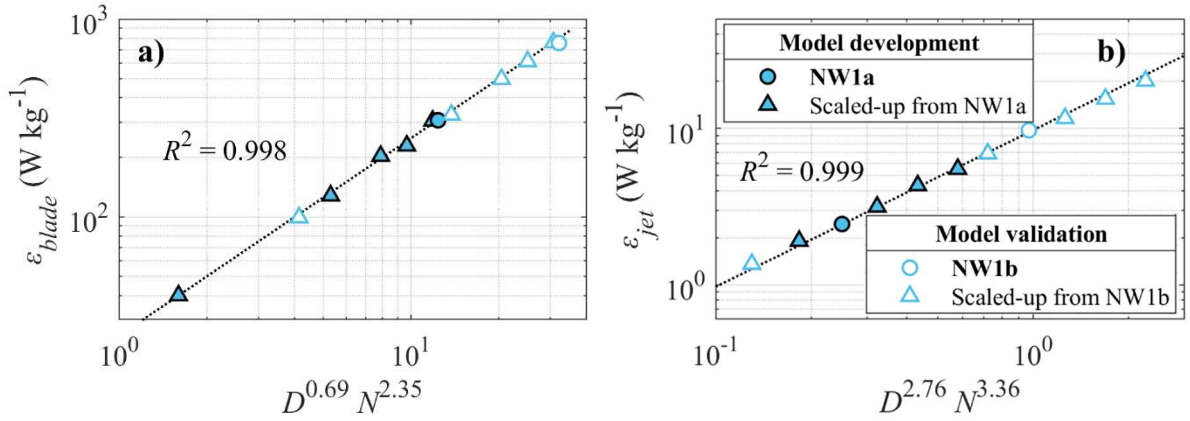

Figure VI-9*: Fittings of the local energy dissipation rate data with Newtonian fluid NW1.*

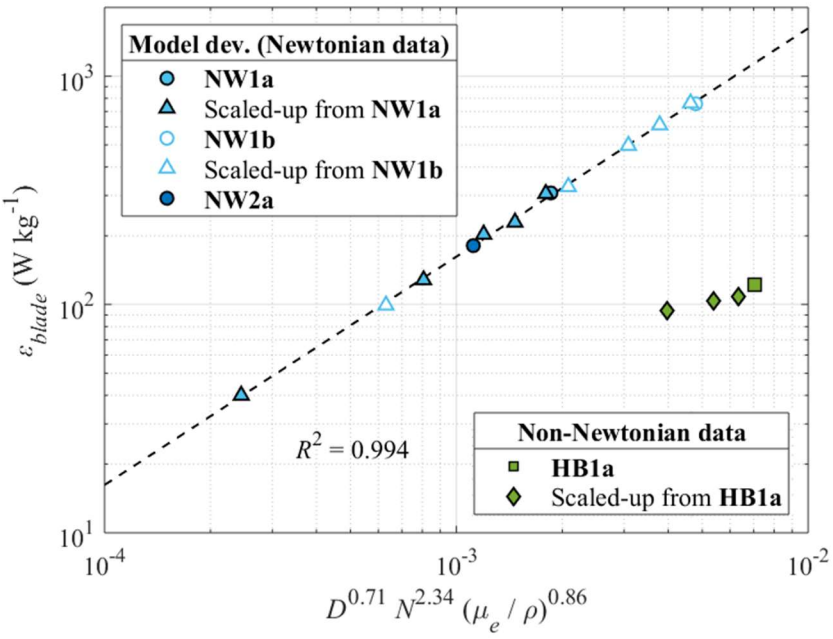

***Figure VI-10**: Fitting of the local energy dissipation rate data with Newtonian fluids NW1 and NW2.*

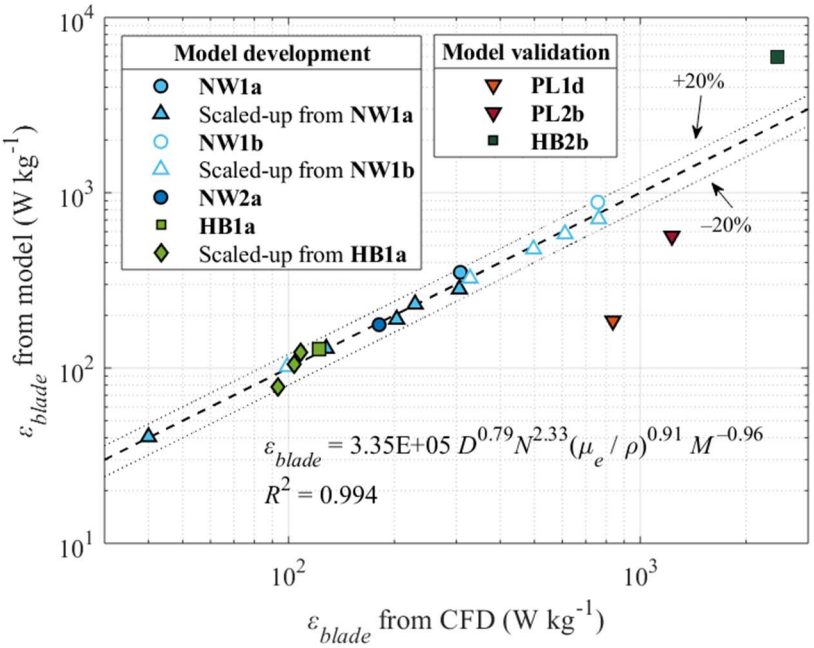

***Figure VI-11**: Fitting of the local energy dissipation rate data with Newtonian and non-Newtonian fluids.*

VI.3.1. Cavern extension with non-Newtonian fluids

As explained in the previous chapters, the cavern boundary is commonly determined as the isoline where the fluid velocity equals 1% of the U_{tip}. Both experimental and numerical results showed that, with the non-Newtonian fluid HB1, the scale-up at equal impeller speed ($X = 1$) kept the same cavern extension (***Figure VI-12***). This is not surprising. The balance equation between the torque transmitted by the impeller ($\propto \rho\, Po\, D^5\, N^2$) and the torque acting on the cavern surface ($\propto \tau_0\, {D_c}^3$) would lead to

$$\left(\frac{D_c}{D}\right)^3 \propto \frac{\rho\, Po\, (D\, N)^2}{\tau_0}. \qquad \textit{Eq. VI-5}$$

This approach has been used by Wilkens et al. (2005) to develop a cavern model for Bingham plastic fluids. The predictions were in good agreement with the experimental observations. For $X = 2$, thus lower impeller speed, the cavern was significantly smaller. At higher impeller speeds, the cavern dimensions increased slightly until they became almost constant. Based on the definition used to determine the cavern boundary, the following conclusions can be drawn. At low impeller speeds, the local fluid velocity increases more than proportionally with the impeller tip speed; as a result, the cavern boundary expands as the impeller speed is increased. At higher impeller speeds, the local fluid velocity becomes almost proportional to the impeller tip speed, so the cavern boundary remains in the same position.

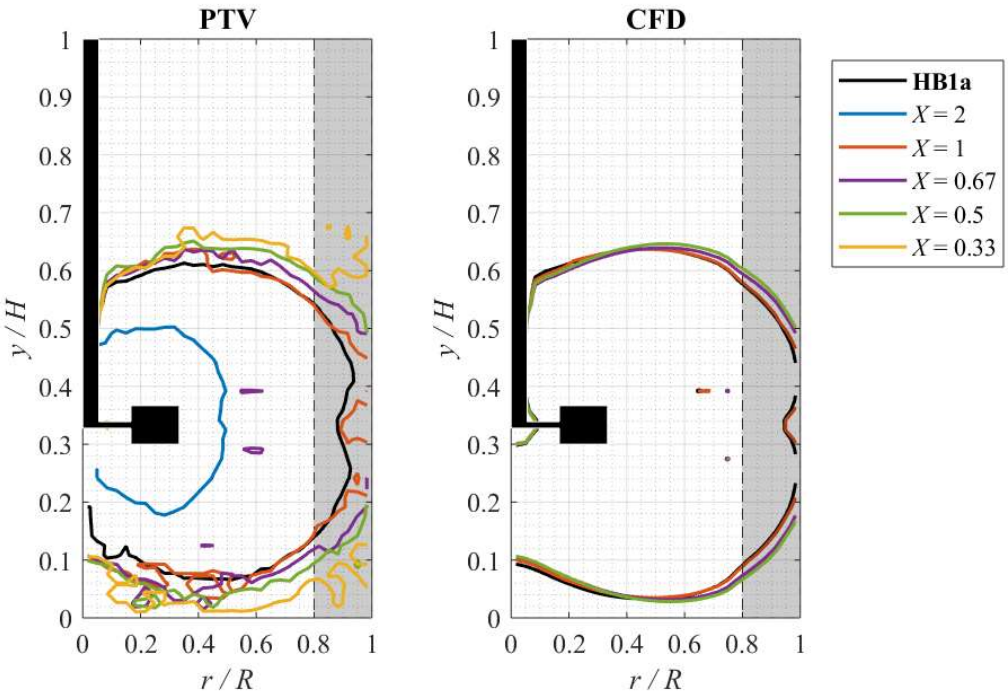

***Figure VI-12**: Boundaries of the caverns formed by the yield stress fluid HB1 for different values of scale-up index, as measured with PTV and simulated with CFD.*

VI.4. Summary and conclusions

The scale-up effects on the flows of Newtonian and non-Newtonian fluids in geometrically similar vessels stirred with Rushton turbines have been addressed. The flow regime was transitional ($71 \leq Re \leq 2{,}214$).

The PTV measurements have enabled the analysis of the Lagrangian acceleration distributions in a control region surrounding the impeller. The average acceleration at the smaller scale has been replicated in the larger vessel by scaling up the flows at approximately constant tip speed ($X = 1$). Higher values of accelerations have been obtained for $X < 1$. Also, the square distance travelled by a tracer in a time span $1/N$ was found to be proportional to $\langle a \rangle / N^2$.

The energy dissipation rate and turbulent kinetic energy in the vessel have been investigated by means of RANS. Two models for predicting ε close to the impeller blade and in the impeller jet flow have been proposed. Newtonian data have been fitted through power-law equations and the models have been validated successfully against new data. Close to the impeller blade, ε is kept constant by scaling up the flows with $X \sim 0.3$. Also, ε increases with the Newtonian viscosity to the power of 0.86. In the jet flow, ε is kept constant with $X \sim 0.8$ and it decreases rapidly with the Newtonian viscosity to the power of -3.6. It can be concluded that, as the fluid viscosity increases, most of the energy dissipation is concentrated in a smaller and smaller region around the impeller. The attempt to produce a generalised model for Newtonian and non-Newtonian data was unsuccessful. Despite a very high R^2 of the fitting, the model did not agree with validation data. This demonstrates the importance of validation against new data even when seemingly excellent statistics of the fittings are obtained.

Finally, both PTV experimental data and CFD simulations showed that the cavern extension in the case of the yield stress fluids was replicated at equal tip speed ($X \sim 1$). This seems in line with a simple balance between the torque transmitted by the impeller and the torque acting on the cavern surface.

Chapter VII

OVERALL CONCLUSIONS

VII.1. Overview

The use of stirred tanks is ubiquitous throughout the process industries (Nienow, 2014). Formulated products usually exhibit complex rheology and possess high apparent viscosity (Dickey, 2015). Thus, mixing operations of such fluids are often conducted in the transitional flow regime (Mendoza et al., 2018). Transitional flows in stirred vessels show intermediate overall behaviour between laminar and fully turbulent flows. Local flow quantities can vary greatly within the vessel volume and also change with the fluid properties. This poses considerable difficulties in developing general scaling rules. Practitioners must be careful not to design and scale-up transitional mixing operations by improperly using correlations outside of their range of applicability, as this may lead to product yield reduction, process corrections and lost opportunities (Paul et al., 2003). Flow measurement techniques and CFD are complementary tools for obtaining case-specific raw data and gaining access to valuable information on the flow hydrodynamics occurring in the vessel. This is paramount for a reliable and robust process development.

In Johnson Matthey, the agitation of non-Newtonian fluids under transitional conditions is an important intermediate step in the manufacturing process of catalytic converters and fuel cell electrode assemblies. These complex mixing operations involve many process tasks, such as solid powder drawdown and dispersion, homogenisation and liquid blending. The research in this thesis had two main industry-driven aims: to improve know-how and capabilities in flow

visualisation, measurement and simulation within JM and to study fluid mixing in agitated vessels operating in the transitional flow regime. The work undertaken has led to journal publications and conference presentations, which demonstrate the impact achieved by the research.

In **Chapter I**, the industrial background and business case on which the EngD project was funded have been described in detail. The scope and specific objectives of the thesis have been discussed.

Chapter II was a survey of the existing literature in the fields of fluid mixing in agitated vessels, experimental flow measurement techniques and computational fluid dynamics applied to mixing research. The gaps in current knowledge have been highlighted. Although the agitation of non-Newtonian fluids under transitional flow conditions is very common in industry, most of the published works concerning stirred tanks focus on fully turbulent or fully laminar flow conditions and are limited to Newtonian fluid rheology. More studies are needed to determine how the flow quantities scale in the transitional regime. There are various flow measurement techniques that allow stirred tanks to be studied at the laboratory and pilot scale. Due to technological aspects, most widespread techniques provide a Eulerian description of the flow. 3D-PTV is a Lagrangian technique which has never before been applied to stirred tank flows, with the exception of a single group of authors (Alberini et al., 2017). Their preliminary findings showed that this application was worth exploring and led to the launch of this EngD project. CFD is an increasingly important research tool and can provide useful information that would be difficult to obtain experimentally. Today, the RANS approach is the most common method of turbulence modelling. For the time being, they remain the only practical approach for modelling stirred tanks, as LES and DNS are too expensive (Lane, 2017). However,

common RANS models were developed for fully turbulent conditions. More studies are needed to identify the best practices for simulating transitional mixing in agitated vessels.

Subsequent chapters showed the experimental and numerical work undertaken to help fill the knowledge gaps summarised above. **Chapter III** discussed the methodology development aimed at identifying best practices for PTV measurements in lab-scale vessels. In **Chapter IV**, the agitation of Newtonian and non-Newtonian fluids in a lab-scale tank has been investigated by means of PTV. The effects of fluid rheology and Reynolds number on the mean flow patterns have been assessed and the distributions of shear rate and Lagrangian acceleration have been analysed. In **Chapter V**, PTV and CFD data at the lab scale have been cross validated. The effects of the RANS closure model, numerical discretisation scheme and mesh size have been discussed. Finally, **Chapter VI** presented a scale-up study of a 4.6 L vessel to a geometrically similar 21.2 L vessel. Scaling laws of Lagrangian acceleration and energy dissipation rate valid under transitional flow conditions have been identified.

In the remainder of this chapter, the research findings are thoroughly discussed in relation to the thesis objectives and recommendations for future work are given.

VII.2. Reflection on thesis objectives

I. The methodology for 3D-PTV experiments in agitated vessels at the laboratory scale has been developed and tested.

    a. The effects of tracer concentration and camera frame rate on the experimental errors, tracking efficiency and computational cost have been assessed. The guidelines for setting these variables as a function of the flow conditions and

measurement error have been expressed through *Eq. III-1* and *Eq. III-5*. To the author's knowledge, similar recommendations for PTV experiments in stirred tanks have not been published in any previous work. The frame rate should be low enough so that the distance travelled by low-speed tracers between consecutive frames is greater than the error on the reconstructed coordinates. The tracer concentration should be low enough so that the typical nearest neighbour distance is greater than the distance travelled by high-speed tracers. In this case, a high frame rate is desirable. Thus, *Eq. III-1* and *Eq. III-5* represent conflicting requirements for optimising PTV tracking efficiency, and the ratio between maximum and minimum velocity in the flow is a measure of tracking difficulty. Tracking efficiency has been shown to decrease substantially if these requirements are not met. *Eq. III-1* and *Eq. III-5* can be generalised to other flow applications at the laboratory scale. The flow visualisation capabilities within JM have been improved through documentation and dissemination of these findings.

b. It has been demonstrated that the application of a Savitzky-Golay filter to the experimental Lagrangian data enhances significantly their signal-to-noise ratio. The filter parameters have been optimised based on the definition of goodness of fit. The difference between filtered and unfiltered coordinates should be of the same order of magnitude of the typical experimental error in the coordinates. In fact, the optimal filter reduces most of the noise while minimising distortion of the information contained in the original signal. Noise reduction enables precise calculation of the Lagrangian derivatives of the coordinates, i.e. velocity and acceleration, and provides access to meaningful information on the flow dynamics. A second order polynomial filter has been found to perform better

than first order filters and comparably with higher order filters. This means that, at the experimental conditions investigated, the motion of the flow tracers can be described locally as uniformly accelerated, as previously reported by Malik et al. (1993) for turbulent flows. It also highlights the importance of Lagrangian acceleration as a descriptor of local flow dynamics.

c. The limitations of the current hardware have been addressed. Multi-camera PTV setups can substantially reduce stereoscopic ambiguities, 3D reconstruction errors and tracking ambiguities, compared to a single camera (split view) setup. This is particularly important for turbulence research in small measurement volumes and for Lagrangian analysis that requires very long trajectories. However, one of the main purposes of this research project was to develop a cost-effective method for flow measurement and visualisation to be used within JM, as a complementary method to, for example, PIV and PEPT available at the University of Birmingham. Therefore, the possibility of upgrading the PTV rig to a multi-camera setup has not been explored. Nevertheless, other rooms for improvement have been identified. The typical experimental errors obtained with the current setup have been measured. A camera with higher digital resolution could reduce these errors. Also, a larger memory of the camera would allow more frames to be recorded, with many beneficial consequences. In particular, binning of the Lagrangian data on a Eulerian grid requires a large amount of data per grid node.

II. The flow fields of Newtonian and non-Newtonian fluids in a lab scale agitated vessel operated in the transitional regime have been measured by means of 3D-PTV.

a. It has been shown that fluid rheology greatly impacts the overall hydrodynamics occurring in the vessel. The differences between Newtonian and non-Newtonian fluid flows have been highlighted. For the Newtonian fluids, the overall flow patterns were independent of the Reynolds number in the investigated range, and fluid turnover was achieved in the entire vessel. With the non-Newtonian fluids, the flow patterns changed dramatically with the Reynolds number. Caverns and pseudo-caverns of moving fluid were formed around the impeller, while the fluid outside was stagnant. The (pseudo-) cavern size increased with the Reynolds number and depended on the fluid rheology. Compared to Newtonian fluids, non-Newtonian fluids showed smaller flow numbers and lower shear rate levels at comparable Reynolds number.

b. The validity of the Metzner-Otto model for predicting the average shear rate in a region surrounding the impeller outside of fully laminar conditions has been assessed. The original linear model has been refined to account for the effects of fluid rheology and Reynolds number in the transitional flow regime. A power-law correlation between average shear rate and average Lagrangian acceleration in the impeller region has been found, indicating that these two quantities scaled consistently over many combinations of fluid rheology and flow conditions.

III. CFD simulations of transitional flows in stirred tanks have been compared against PTV measurements.

a. The effects of the turbulence model and discretisation scheme on the predicted flows have been assessed. The standard k-ε model has been found to provide slightly better predictions of the power required for mixing, compared to the

SST and RNG models. The second order upwind scheme enabled about 80% of the total energy dissipation rate to be resolved, in line with other numerical studies in the literature. Instead, the first order upwind scheme was found to be severely inaccurate.

b. Experimental and numerical velocity data have been compared with fluids of different rheology. The differences between PTV and CFD data have been highlighted and discussed. While for Newtonian fluids a good agreement in the velocity profiles was observed, non-Newtonian rheology was found to exacerbate the difficulties associated with RANS simulations of transitional flows in stirred tanks. In general, CFD predicted higher velocities than PTV measurements, and this influenced the resulting mean flow patterns. In particular, with the shear thinning fluids, the two main recirculation loops were quite different. With the yield-stress fluids, the cavern boundaries differed slightly, but the agreement was better than that usually reported in the literature.

c. The spatial distribution of the onset of turbulence has been investigated. Large differences were found between different zones of the vessel. Validation of the simulated data against experimental measurements of k or ε was not possible. However, the power number obtained from integration of the stresses acting on the moving elements and from integration of ε in the vessel volume were closed to the expected values. This supported the accuracy of the predictions. A power-law correlation between local shear rate and local Lagrangian acceleration has been demonstrated. This observation suggests that Lagrangian acceleration, measured directly through PTV, can provide information about local mixing and should be taken into account in the development of scale-up strategies.

IV. The viability of 3D-PTV experiments in agitated vessels at the pilot scale (21 L) has been explored. *Eq. III-1* and *Eq. III-5* represent conflicting requirements and could not be met in practice in the larger vessel. However, PTV was still able to provide useful information on the velocity and acceleration in the investigated flows.

V. The scaling of Lagrangian acceleration, energy dissipation rate, turbulent kinetic energy and cavern size in the transitional regime has been investigated by comparing experimental and numerical data at the 4.6 L and 21 L scales.

   a. Energy dissipation rate and turbulent kinetic energy have been shown to scale differently depending on the position in which they are monitored. That is due to the heterogenous nature of transitional flows. Scale-up strategies should take this into consideration. Two models have been proposed to predict the energy dissipation rate of Newtonian fluids at two different locations (*Eq. VI-3*, ***Table VI-2***). Close to the impeller blade, the energy dissipation was found to increase with fluid viscosity; in the discharge jet, it decreased rapidly with viscosity, due to the viscous damping of turbulence away from the impeller.

   b. Non-Newtonian fluid rheology was found to influence the scaling of the flow quantities. At the macroscopic flow scales, for both Newtonian and non-Newtonian fluids, the distributions of Lagrangian acceleration in the impeller region have been replicated successfully by scaling-up the vessel at equal tip speed. However, non-Newtonian fluids did not follow the same scaling of energy dissipation rate as Newtonian fluids. This might indicate that most of the differences between Newtonian and non-Newtonian fluid mixing occur at microscales that could not be resolved experimentally. In order to test more complex models, more data are necessary.

c. With yield stress fluids, cavern size in relation to the tank diameter was replicated by working at equal tip speed.

VII.3. Recommendations for future work

I. JM is devoting great efforts in the digitisation of its manufacturing processes to drive a change towards Industrie 4.0. This requires a multidisciplinary approach, from empowering of IT capabilities to engineering understanding of both processes and diagnostic tools. One important outcome of this EngD is the increased know-how in flow measurement and simulation within the company. The work presented in this thesis has laid the foundations for a further EngD project funded by JM that will use 3D-PTV measurements and CFD simulations to develop simplified models for design and real-time control of fluid mixing processes.

II. In this thesis, fluid mixing in stirred tanks has been studied for many combinations of flow conditions and fluid rheological properties. This limited the research to the Rushton turbine only. This impeller was chosen because it is one of the most common mixing geometries and its hydrodynamic properties have been studied extensively, allowing comparison and validation of the research findings against current knowledge. It would be interesting and of commercial value to extend the work undertaken to other geometries which are also encountered in JM mixing processes, many of which use proprietary impellers and/or non-standard configurations for which there are few if any data in the public domain.

III. This work has shown that fluid mixing in agitated vessels at the bench and pilot scale can be studied by means 3D-PTV. Steady state RANS simulations have also

been conducted to identify good practices for modelling this flow application. The two techniques have been cross-validated in **Chapter V**, through binning of the PTV Lagrangian velocity data on a Eulerian grid. While for Newtonian fluids, the experimental and numerical data matched well, non-Newtonian rheology exacerbated the difficulties associated to RANS simulations of transitional flows in stirred tanks. The key differences were localised in the impeller discharge jet and in the recirculation loops, thus in the flow regions with highest velocity and turbulence offset. This might indicate an influence of turbulence modelling. PIV and PEPT experiments might help clarify the observed differences. For example, PIV can be used to estimate the turbulent kinetic energy in the vessel, and this can be compared against CFD predictions. LES would constitute a very accurate numerical method for such a study, but, for the time being, they remain excessively expensive (Lane, 2017). On the other hand, flow patterns and Lagrangian acceleration data measured with PEPT and 3D-PTV could be compared directly, without the need for data binning.

IV. In **Chapter VI**, non-Newtonian fluids have been shown not to obey the same scaling rules of Newtonian fluids in the transitional regime. A power-law model for predicting the local energy dissipation rate at the impeller blade as a function of impeller speed, diameter and fluid viscosity has been developed, based on 17 data points. However, despite a very high coefficient of determination ($R^2 > 0.99$), the model failed to pass cross-validation against new (unseen) data. Probably, more sophisticated models should be tested (i.e. by separating the effect of yield stress and apparent viscosity). These, however, would require larger datasets for accurate evaluation of the model parameters and for validation. As numerical simulations allow changing of each input variable as desired, it would make an interesting study

to vary the flow conditions and fluid properties with a design of experiments (simulations) (DoE) approach. Bayesian adaptive DoE methods have been demonstrated in JM for non-linear model parameterisation and these could be usefully exploited in this work to minimise the number of simulations.

V. The application of the discrete Fourier transform (DFT) to individual 3D-PTV trajectories can potentially give quantitative information regarding the frequency spectra of acceleration. This might, for instance, provide new insight on the flow macro-instabilities, a frequent phenomenon in transitional flows in agitated vessels that is still not fully understood and cannot be investigated through steady state RANS. However, this type of data analysis requires very long trajectories because the frequency resolution of the DFT (the width of the frequency bins) is determined by the total number of samples of the signal. With the current setup, the PTV trajectories were relatively short, so it was impossible to resolve the frequency peaks (see an example in **§A.5**). For this reason, the frequency analysis of the acceleration signals has not been carried out in this thesis. Nevertheless, future hardware and software enhancements might open this research opportunity. As explained earlier, a camera with higher digital resolution may help reduce the experimental error in the tracer coordinates, allowing higher frame rates to be used and facilitating particle tracking. The development of new algorithms for centroid determination in digital images is an active research topic, as target positioning and tracking is a very common task in many scientific disciplines, such as observational astronomy, microbiology, aerospace and automotive engineering (Sun et al., 2022).

VI. Recently, the OpenPTV Consortium © has released an open-source 3D-PTV software (https://openptv.net/). The original algorithm developed at the ETH

Zurich, which has been used in this thesis, remains the core of the software. Many updates have been developed by the Turbulence Structure Laboratory at Tel Aviv University and the Turbulence and Vortex Dynamics research group at Eindhoven University of Technology. Most importantly, the code has been translated into Python language. Python allows parallel computing on multiple CPUs, resulting in much quicker experimental data processing. Future work with PTV should use this new version of the software.

REFERENCES

Adamczyk, A.A. and Rimai, L. (1988a) 2-Dimensional particle tracking velocimetry (PTV): Technique and image processing algorithms. *Experiments in Fluids*, 6 (6): 373–380. doi:10.1007/BF00196482.

Adamczyk, A.A. and Rimai, L. (1988b) Reconstruction of a 3-dimensional flow field from orthogonal views of seed track video images. *Experiments in Fluids*, 6 (6): 380–386. doi:10.1007/BF00196483.

Adams, L.W. (2009) *Experimental and computational study of non-turbulent flow regimes and cavern formation of non-Newtonian fluids in a stirred tank*. PhD Thesis, University of Birmingham. Available at: https://etheses.bham.ac.uk//id/eprint/394/ (Accessed: 31 March 2020).

Adams, L.W. and Barigou, M. (2007) CFD Analysis of Caverns and Pseudo-Caverns Developed During Mixing of Non-Newtonian Fluids. *Chemical Engineering Research and Design*, 85 (5): 598–604. doi:10.1205/cherd06170.

Adegbite, S. (2010) *Coating of catalyst supports: Links between slurry characteristics, coating process and final coating quality*. PhD Thesis, University of Birmingham.

Adrian, L., Adrian, R.J. and Westerweel, J. (2011) *Particle Image Velocimetry*. Cambridge, UK: Cambridge University Press.

Adrian, R.J. (1984) Scattering particle characteristics and their effect on pulsed laser measurements of fluid flow: speckle velocimetry vs particle image velocimetry. *Applied Optics*, 23 (11): 1690–1691. doi:10.1364/AO.23.001690.

Adrian, R.J. (1991) Particle-Imaging Techniques for Experimental Fluid Mechanics. *Annual Review of Fluid Mechanics*, 23 (1): 261–304. doi:10.1146/annurev.fl.23.010191.001401.

Adrian, R.J. (1997) Dynamic ranges of velocity and spatial resolution of particle image velocimetry. *Measurement Science and Technology*, 8 (12): 1393–1398. doi:10.1088/0957-0233/8/12/003.

Agrafiotis, C., Tsetsekou, A. and Ekonomakou, A. (1999) The effect of particle size on the adhesion properties of oxide washcoats on cordierite honeycombs. *Journal of Materials Science Letters*, 18 (17): 1421–1424. doi:10.1023/A:1006675524692.

Aguirre-Pablo, A.A., Aljedaani, A.B., Xiong, J., et al. (2019) Single-camera 3D PTV using particle intensities and structured light. *Experiments in Fluids*, 60 (2): 25. doi:10.1007/s00348-018-2660-7.

Akizuki, S., Joo, H., Koyama, M., et al. (2021) Mechanism of cell proliferation during starvation in a continuous stirred tank anaerobic reactor treating food waste. *Bioprocess and Biosystems Engineering*, 44 (8): 1659–1669. doi:10.1007/s00449-021-02548-0.

Alberini, F., Liu, L., Stitt, E.H., et al. (2017) Comparison between 3-D-PTV and 2-D-PIV for determination of hydrodynamics of complex fluids in a stirred vessel. *Chemical Engineering Science*, 171: 189–203. doi:10.1016/j.ces.2017.05.034.

Alberini, F., Simmons, M.J.H., Ingram, A., et al. (2014b) Assessment of different methods of analysis to characterise the mixing of shear-thinning fluids in a Kenics KM static mixer using PLIF. *Chemical Engineering Science*, 112: 152–169. doi:10.1016/j.ces.2014.03.022.

Alberini, F., Simmons, M.J.H., Ingram, A., et al. (2014a) Use of an areal distribution of mixing intensity to describe blending of non-newtonian fluids in a kenics KM static mixer using PLIF. *AIChE Journal*, 60 (1): 332–342. doi:https://doi.org/10.1002/aic.14237.

Alcamo, R., Micale, G., Grisafi, F., et al. (2005) Large-eddy simulation of turbulent flow in an unbaffled stirred tank driven by a Rushton turbine. *Chemical Engineering Science*, 60 (8): 2303–2316. doi:10.1016/j.ces.2004.11.017.

Alexopoulos, A.H., Maggioris, D. and Kiparissides, C. (2002) CFD analysis of turbulence non-homogeneity in mixing vessels: A two-compartment model. *Chemical Engineering Science*, 57 (10): 1735–1752. doi:10.1016/S0009-2509(02)00053-2.

Amanullah, A., Hjorth, S.A. and Nienow, A.W. (1998) A new mathematical model to predict cavern diameters in highly shear thinning, power law liquids using axial flow impellers. *Chemical Engineering Science*, 53 (3): 455–469. doi:10.1016/S0009-2509(97)00200-5.

Ameur, H. and Bouzit, M. (2012) Mixing in shear thinning fluids. *Brazilian Journal of Chemical Engineering*, 29 (2): 349–358. doi:10.1590/S0104-66322012000200015.

Ammar, M., Driss, Z., Chtourou, W., et al. (2011) Effects of baffle length on turbulent flows generated in stirred vessels. *Central European Journal of Engineering*, 1 (4): 401–412. doi:10.2478/s13531-011-0040-7.

Anne-Archard, D., Marouche, M. and Boisson, H.-C. (2006) Hydrodynamics and Metzner-Otto correlation in stirred vessels for yield stress fluids. *Chemical Engineering Journal*, 125 (1): 15–24. doi:10.1016/j.cej.2006.08.002.

Antognoli, M., Galletti, C., Capaci, R.B.D., et al. (2019) Numerical Investigation of the Mixing of Highly Viscous Liquids with Cowles Impellers. *Chemical Engineering Transactions*, 74: 973–978. doi:10.3303/CET1974163.

Arratia, P.E., Kukura, J., Lacombe, J., et al. (2006) Mixing of shear-thinning fluids with yield stress in stirred tanks. *AIChE Journal*, 52 (7): 2310–2322. doi:10.1002/aic.10847.

Aubin, J., Fletcher, D.F. and Xuereb, C. (2004) Modeling turbulent flow in stirred tanks with CFD: the influence of the modeling approach, turbulence model and numerical scheme. *Experimental Thermal and Fluid Science*, 28 (5): 431–445. doi:10.1016/j.expthermflusci.2003.04.001.

Aubin, J., Kresta, S.M., Bertrand, J., et al. (2006) Alternate Operating Methods for Improving the Performance of Continuous Stirred Tank Reactors. *Chemical Engineering Research and Design*, 84 (7): 569–582. doi:10.1205/cherd.05216.

Baek, S.J. and Lee, S.J. (1996) A new two-frame particle tracking algorithm using match probability. *Experiments in Fluids*, 22 (1): 23–32. doi:10.1007/BF01893303.

Baghli, H., Benyettou, M., Tchouar, N., et al. (2018) Energy efficiency in industrial mixing and cooling of non-Newtonian fluid in a stirred tank reactor. *AIP Conference Proceedings*, 1968 (1): 030073. doi:10.1063/1.5039260.

Bakhtiari, F., Atashi, H., Zivdar, M., et al. (2008) Continuous copper recovery from a smelter's dust in stirred tank reactors. *International Journal of Mineral Processing*, 86 (1): 50–57. doi:10.1016/j.minpro.2007.10.003.

Bakker, A. and Van den Akker, H.E.A. (1994) Gas-liquid contacting with axial flow impellers. *Transactions of the Institution of Chemical Engineers*, 72 (A4): 573–582.

Baldi, S. and Yianneskis, M. (2003) On the Direct Measurement of Turbulence Energy Dissipation in Stirred Vessels with PIV. *Industrial & Engineering Chemistry Research*, 42 (26): 7006–7016. doi:10.1021/ie0208265.

Baldi, S. and Yianneskis, M. (2004) On the quantification of energy dissipation in the impeller stream of a stirred vessel from fluctuating velocity gradient measurements. *Chemical Engineering Science*, 59 (13): 2659–2671. doi:10.1016/j.ces.2004.03.021.

Bao, Y., Lu, Y., Liang, Q., et al. (2015) Power demand and mixing performance of coaxial mixers in a stirred tank with CMC solution. *Chinese Journal of Chemical Engineering*, 23 (4): 623–632. doi:10.1016/j.cjche.2015.01.002.

Bartels, C., Breuer, M. and Durst, F. (2000) *Comparison between Direct Numerical simulation and k-e Prediction of the Flow in a Vessel Stirred by a Rushton Turbine*. In Delft, The Netherlands, 2000. pp. 239–243. doi:10.1016/B978-044450476-0/50031-5.

Bartels, C., Breuer, M., Wechsler, K., et al. (2002) Computational fluid dynamics applications on parallel-vector computers: computations of stirred vessel flows. *Computers & Fluids*, 31 (1): 69–97. doi:10.1016/S0045-7930(01)00016-0.

Başbuğ, S., Papadakis, G. and Vassilicos, J.C. (2017) DNS investigation of the dynamical behaviour of trailing vortices in unbaffled stirred vessels at transitional Reynolds numbers. *Physics of Fluids*, 29 (6): 064101. doi:10.1063/1.4983494.

Bashiri, H., Alizadeh, E., Bertrand, F., et al. (2016a) Investigation of turbulent fluid flows in stirred tanks using a non-intrusive particle tracking technique. *Chemical Engineering Science*, 140: 233–251. doi:10.1016/j.ces.2015.10.005.

Bashiri, H., Bertrand, F. and Chaouki, J. (2016b) Development of a multiscale model for the design and scale-up of gas/liquid stirred tank reactors. *Chemical Engineering Journal*, 297: 277–294. doi:10.1016/j.cej.2016.03.102.

Beckner, J.L. and Smith, J.M. (1966) Anchor-Agitated Systems: PowerInput With Newtonian and Pseudo-Plastic Fluids. *Transactions of the Institution of Chemical Engineers*, 44: 224–236.

Benchabane, A. and Bekkour, K. (2008) Rheological properties of carboxymethyl cellulose (CMC) solutions. *Colloid and Polymer Science*, 286 (10): 1173–1180. doi:10.1007/s00396-008-1882-2.

Bendicks, C., Tarlet, D., Roloff, C., et al. (2011) Improved 3-D Particle Tracking Velocimetry with Colored Particles. *Journal of Signal and Information Processing*, 2 (2): 59–71. doi:10.4236/jsip.2011.22009.

Bertrand, F., Tanguy, P.A. and Fuente, E.B.-D.L. (1996) A New Perspective for the Mixing of Yield Stress Fluids with Anchor Impellers. *Journal of Chemical Engineering of Japan*, 29 (1): 51–58. doi:10.1252/jcej.29.51.

Böhme, G. and Stenger, M. (1988) Consistent scale-up procedure for the power consumption in agitated non-newtonian fluids. *Chemical Engineering & Technology*, 11 (1): 199–205. doi:10.1002/ceat.270110127.

Bonvillani, P., Ferrari, M.P., Ducrós, E.M., et al. (2006) Theoretical and experimental study of the effects of scale-up on mixing time for a stirred-tank bioreactor. *Brazilian Journal of Chemical Engineering*, 23 (1): 1–7. doi:10.1590/S0104-66322006000100001.

Brown, D.A.R., Jones, P.N., Middleton, J.C., et al. (2003) "Experimental Methods." In *Handbook of Industrial Mixing*. Hoboken, N.J., US: John Wiley & Sons, Ltd. pp. 145–256. doi:10.1002/0471451452.ch4.

Brucato, A., Ciofalo, M., Grisafi, F., et al. (1998) Numerical prediction of flow fields in baffled stirred vessels: A comparison of alternative modelling approaches. *Chemical Engineering Science*, 53 (21): 3653–3684. doi:10.1016/S0009-2509(98)00149-3.

Brůha, O., Brůha, T., Fořt, I., et al. (2007) Dynamics of the Flow Pattern in a Baffled Mixing Vessel with an Axial Impeller. *Acta Polytechnica*, 47 (6). doi:10.14311/996.

Brůha, O., Fořt, I., Smolka, P., et al. (1996) Experimental Study of Turbulent Macroinstabilities in an Agitated System with Axial High-Speed Impeller and with Radial Baffles. *Collection of Czechoslovak Chemical Communications*, 61 (6): 856–867. doi:10.1135/cccc19960856.

Bulnes-Abundis, D., Carrillo-Cocom, L.M., Aráiz-Hernández, D., et al. (2013) A simple eccentric stirred tank mini-bioreactor: Mixing characterization and mammalian cell culture experiments. *Biotechnology and Bioengineering*, 110 (4): 1106–1118. doi:10.1002/bit.24780.

Cabaret, F., Fradette, L. and Tanguy, P.A. (2008) New Turbine Impellers for Viscous Mixing. *Chemical Engineering & Technology*, 31 (12): 1806–1815. doi:10.1002/ceat.200800385.

Calderbank, P.H. and Moo-Young, M.B. (1959) The prediction of power consumption in the agitation of non-Newtonian fluids. *Transactions of the Institution of Chemical Engineers*, 37: 26–33.

Calderbank, P.H. and Moo-Young, M.B. (1961) The Power Characteristics of Agitators for the Mixing of Newtonian and Non-Newtonian Fluids. *Transactions of the Institution of Chemical Engineers*, 39: 337–347.

Campolo, M., Sbrizzai, F. and Soldati, A. (2003) Time-dependent flow structures and Lagrangian mixing in Rushton-impeller baffled-tank reactor. *Chemical Engineering Science*, 58 (8): 1615–1629.

Candelier, F., Angilella, J.R. and Souhar, M. (2004) On the effect of the Boussinesq–Basset force on the radial migration of a Stokes particle in a vortex. *Physics of Fluids*, 16 (5): 1765–1776. doi:10.1063/1.1689970.

Castillo-Hernández, A., Mar-Alvarez, I. and Moreno-Andrade, I. (2015) Start-up and operation of continuous stirred-tank reactor for biohydrogen production from restaurant organic solid waste. *International Journal of Hydrogen Energy*, 40 (48): 17239–17245. doi:10.1016/j.ijhydene.2015.04.046.

Cavadas, A.S. and Pinho, F.T. (2004) Some Characteristics of Stirred Vessel Flows of Dilute Polymer Solutions Powered by a Hyperboloid Impeller. *The Canadian Journal of Chemical Engineering*, 82 (2): 289–302. doi:10.1002/cjce.5450820210.

Celani, A., Blackburn, S., Simmons, M.J.H., et al. (2018) Effect of mixing conditions on the wet preparation of ceramic foams. *Chemical Engineering Research and Design*, 134: 1–14. doi:10.1016/j.cherd.2018.03.044.

Chapman, C.M., Nienow, A.W., Cooke, M., et al. (1983a) Particle—gas—liquid mixing in stirred vessels. Part I. *Chemical Engineering Research and Design*, 61: 71–81.

Chapman, C.M., Nienow, A.W., Cooke, M., et al. (1983b) Particle-gas-liquid mixing in stirred vessels. Part II. *Chemical Engineering Research and Design*, 61: 82–95.

Chapman, C.M., Nienow, A.W., Cooke, M., et al. (1983c) Particle-gas-liquid mixing in stirred vessels. Part III. *Chemical Engineering Research and Design*, 61: 167–181.

Chapman, C.M., Nienow, A.W., Cooke, M., et al. (1983d) Particle-gas-liquid mixing in stirred vessels. Part IV. *Chemical Engineering Research and Design*, 61: 182–185.

Chara, Z., Kysela, B., Konfrst, J., et al. (2016) Study of fluid flow in baffled vessels stirred by a Rushton standard impeller. *Applied Mathematics and Computation*, 272: 614–628. doi:10.1016/j.amc.2015.06.044.

Chiti, F., Bakalis, S., Bujalski, W., et al. (2011) Using positron emission particle tracking (PEPT) to study the turbulent flow in a baffled vessel agitated by a Rushton turbine: Improving data treatment and validation. *Chemical Engineering Research and Design*, 89: 1947–1960. doi:10.1016/j.cherd.2011.01.015.

Chtourou, W., Ammar, M., Driss, Z., et al. (2011) Effect of the turbulence models on Rushton turbine generated flow in a stirred vessel. *Central European Journal of Engineering*, 1 (4): 380. doi:10.2478/s13531-011-0039-0.

Chung, K.H.K., Barigou, M. and Simmons, M.J.H. (2007) Reconstruction of 3-D Flow Field Inside Miniature Stirred Vessels Using a 2-D PIV Technique. *Chemical Engineering Research and Design*, 85 (5): 560–567. doi:10.1205/cherd06165.

Chung, K.H.K., Simmons, M.J.H. and Barigou, M. (2009) Angle-Resolved Particle Image Velocimetry Measurements of Flow and Turbulence Fields in Small-Scale Stirred Vessels of Different Mixer Configurations. *Industrial & Engineering Chemistry Research*, 48 (2): 1008–1018. doi:10.1021/ie8008204.

Cierpka, C., Lütke, B. and Kähler, C.J. (2013) Higher order multi-frame particle tracking velocimetry. *Experiments in Fluids*, 54 (5): 1533. doi:10.1007/s00348-013-1533-3.

Ciofalo, M., Brucato, A., Grisafi, F., et al. (1996) Turbulent Flow in Closed and Free-Surface Unbaffled Tanks Stirred by Radial Impeller. *Chemical Engineering Science*, 51 (14): 3557–3573. doi:10.1016/0009-2509(96)00004-8.

CORDIS (2022) *Flow Visualization Based Pressure*. Available at: https://cordis.europa.eu/project/id/665477/results (Accessed: 27 August 2022).

Coroneo, M., Montante, G., Paglianti, A., et al. (2011) CFD prediction of fluid flow and mixing in stirred tanks: Numerical issues about the RANS simulations. *Computers & Chemical Engineering*, 35 (10): 1959–1968. doi:10.1016/j.compchemeng.2010.12.007.

Cortada-Garcia, M., Dore, V., Mazzei, L., et al. (2017) Experimental and CFD studies of power consumption in the agitation of highly viscous shear thinning fluids. *Chemical Engineering Research and Design*, 119: 171–182. doi:10.1016/j.cherd.2017.01.018.

Cybulski, A. and Moulijn, J.A. (eds.) (2005) *Structured Catalysts and Reactors*. 2nd ed. Boca Raton, FL, US: CRC Press. doi:10.1201/9781420028003.

Deglon, D.A. and Meyer, C.J. (2006) CFD modelling of stirred tanks: Numerical considerations. *Minerals Engineering*, 19 (10): 1059–1068. doi:10.1016/j.mineng.2006.04.001.

Delafosse, A., Collignon, M.-L., Crine, M., et al. (2011) Estimation of the turbulent kinetic energy dissipation rate from 2D-PIV measurements in a vessel stirred by an axial Mixel TTP impeller. *Chemical Engineering Science*, 66 (8): 1728–1737. doi:10.1016/j.ces.2011.01.011.

Delafosse, A., Liné, A., Morchain, J., et al. (2008) LES and URANS simulations of hydrodynamics in mixing tank: Comparison to PIV experiments. *Chemical Engineering Research and Design*, 86 (12): 1322–1330. doi:10.1016/j.cherd.2008.07.008.

Delafosse, A., Morchain, J., Guiraud, P., et al. (2009) Trailing vortices generated by a Rushton turbine: Assessment of URANS and large Eddy simulations. *Chemical Engineering Research and Design*, 87 (4): 401–411. doi:10.1016/j.cherd.2008.12.018.

Derksen, J.J., Doelman, M.S. and Van den Akker, H.E.A. (1999) Three-dimensional LDA measurements in the impeller region of a turbulently stirred tank. *Experiments in Fluids*, 27 (6): 522–532. doi:10.1007/s003480050376.

Derksen, J.J. and Van den Akker, H.E.A. (1999) Large eddy simulations on the flow driven by a rushton turbine. *AIChE Journal*, 45 (2): 209–221. doi:10.1002/aic.690450202.

Dickey, D.S. (2015) Tackling Difficult Mixing Problems. *Chemical Engineering Progress*, 111 (8): 35–42.

Distelhoff, M.F.W., Laker, J., Marquis, A.J., et al. (1995) The application of a strain gauge technique to the measurement of the power characteristics of five impellers. *Experiments in Fluids*, 20 (1): 56–58. doi:10.1007/BF00190598.

Doran, P.M. (2013) “Chapter 8 - Mixing.” In Doran, P.M. (ed.) *Bioprocess Engineering Principles (Second Edition)*. London, UK: Academic Press. pp. 255–332. doi:10.1016/B978-0-12-220851-5.00008-3.

Driss, Z., Kaffel, A., Amira, B.B., et al. (2014) PIV Measurements to Study the Effect of the Reynolds Number on the Hydrodynamic Structure in a Baffled Vessel Stirred by a Rushton Turbine. *American Journal of Energy Research*, 2 (3): 67–73. doi:10.12691/ajer-2-3-4.

Ducci, A., Doulgerakis, Z. and Yianneskis, M. (2008) Decomposition of Flow Structures in Stirred Reactors and Implications for Mixing Enhancement. *Industrial & Engineering Chemistry Research*, 47 (10): 3664–3676. doi:10.1021/ie070905m.

Ducci, A. and Yianneskis, M. (2005) Direct determination of energy dissipation in stirred vessels with two-point LDA. *AIChE Journal*, 51 (8): 2133–2149. doi:10.1002/aic.10468.

Ducci, A. and Yianneskis, M. (2007) Vortex tracking and mixing enhancement in stirred processes. *AIChE Journal*, 53 (2): 305–315. doi:10.1002/aic.11076.

Dusting, J., Sheridan, J. and Hourigan, K. (2006) A fluid dynamics approach to bioreactor design for cell and tissue culture. *Biotechnology and Bioengineering*, 94 (6): 1196–1208. doi:10.1002/bit.20960.

Dyster, K.N., Koutsakos, E., Jaworski, Z., et al. (1993) An LDA study of the radialdischarge velocities generated by a Rushton turbine: Newtonian Fluids, Re>=5. *Transactions of the Institution of Chemical Engineers*, 71: 11–23.

Eckert, M. (2017) Ludwig Prandtl and the growth of fluid mechanics in Germany. *Comptes Rendus Mécanique*, 345 (7): 467–476. doi:10.1016/j.crme.2017.05.005.

Elson, T.P., Cheesman, D.J. and Nienow, A.W. (1986) X-ray studies of cavern sizes and mixing performance with fluids possessing a yield stress. *Chemical Engineering Science*, 41 (10): 2555–2562. doi:10.1016/0009-2509(86)80041-0.

Escudié, R., Bouyer, D. and Liné, A. (2004) Characterization of trailing vortices generated by a Rushton turbine. *AIChE Journal*, 50 (1): 75–86. doi:10.1002/aic.10007.

Escudié, R. and Liné, A. (2006) Analysis of turbulence anisotropy in a mixing tank. *Chemical Engineering Science*, 61 (9): 2771–2779. doi:10.1016/j.ces.2005.09.022.

Euler, L. (1757) Principes généraux du mouvement des fluides. *Mémoires de l’académie des sciences de Berlin*, 11: 274–315.

Fan, J., Wang, Y., Rao, Q., et al. (2004) A Study on Intermittency Phenomena in the Impeller Stream Via Digital Particle Image Velocimetry (DPIV). *Chemical Engineering Journal*, 102: 25–33. doi:10.1016/j.cej.2004.02.002.

Fangary, Y.S., Barigou, M., Seville, J.P.K., et al. (2000) Fluid trajectories in a stirred vessel of non-newtonian liquid using positron emission particle tracking. *Chemical Engineering Science*, 55 (24): 5969–5979. doi:10.1016/S0009-2509(00)00176-7.

Fangary, Y.S., Barigou, M., Seville, J.P.K., et al. (2002) A Langrangian Study of Solids Suspension in a Stirred Vessel by Positron Emission Particle Tracking (PEPT). *Chemical*

Engineering & Technology, 25 (5): 521–528. doi:10.1002/1521-4125(200205)25:5<521::AID-CEAT521>3.0.CO;2-C.

Fradette, L., Thomé, G., Tanguy, P.A., et al. (2007) Power and Mixing Time Study Involving a Maxblend® Impeller with Viscous Newtonian and Non-Newtonian Fluids. *Chemical Engineering Research and Design*, 85 (11): 1514–1523. doi:10.1205/cherd07051.

Gabelle, J.-C., Morchain, J., Anne-Archard, D., et al. (2013) Experimental determination of the shear rate in a stirred tank with a non-newtonian fluid: Carbopol. *AIChE Journal*, 59 (6): 2251–2266. doi:10.1002/aic.13973.

Gabriele, A., Nienow, A.W. and Simmons, M.J.H. (2009) Use of angle resolved PIV to estimate local specific energy dissipation rates for up- and down-pumping pitched blade agitators in a stirred tank. *Chemical Engineering Science*, 64 (1): 126–143. doi:10.1016/j.ces.2008.09.018.

Gabriele, A., Tsoligkas, A.N., Kings, I.N., et al. (2011) Use of PIV to measure turbulence modulation in a high throughput stirred vessel with the addition of high Stokes number particles for both up- and down-pumping configurations. *Chemical Engineering Science*, 66 (23): 5862–5874. doi:10.1016/j.ces.2011.08.007.

Galletti, C., Brunazzi, E., Pintus, S., et al. (2004b) A Study of Reynolds Stresses, Triple Products and Turbulence States in a Radially Stirred Tank with 3-D Laser Anemometry. *Chemical Engineering Research and Design*, 82 (9): 1214–1228. doi:10.1205/cerd.82.9.1214.44151.

Galletti, C., Brunazzi, E., Yianneskis, M., et al. (2003) Spectral and wavelet analysis of the flow pattern transition with impeller clearance variations in a stirred vessel. *Chemical Engineering Science*, 58 (17): 3859–3875. doi:10.1016/S0009-2509(03)00230-6.

Galletti, C., Paglianti, A., Lee, K.C., et al. (2004a) Reynolds number and impeller diameter effects on instabilities in stirred vessels. *AIChE Journal*, 50 (9): 2050–2063. doi:10.1002/aic.10236.

Gallo, D., Gülan, U., Di Stefano, A., et al. (2014) Analysis of thoracic aorta hemodynamics using 3D particle tracking velocimetry and computational fluid dynamics. *Journal of Biomechanics*, 47 (12): 3149–3155. doi:10.1016/j.jbiomech.2014.06.017.

Gao, X., Du, Z., Ding, H., et al. (2010) Kinetics of NOx Absorption into (NH4)2SO3 Solution in an Ammonia-Based Wet Flue Gas Desulfurization Process. *Energy & Fuels*, 24 (11): 5876–5882. doi:10.1021/ef101137k.

Gargouri, B., Karray, F., Mhiri, N., et al. (2011) Application of a continuously stirred tank bioreactor (CSTR) for bioremediation of hydrocarbon-rich industrial wastewater effluents. *Journal of Hazardous Materials*, 189 (1): 427–434. doi:10.1016/j.jhazmat.2011.02.057.

van Gent, P.L., Michaelis, D., van Oudheusden, B.W., et al. (2017) Comparative assessment of pressure field reconstructions from particle image velocimetry measurements and Lagrangian particle tracking. *Experiments in Fluids*, 58 (4): 33. doi:10.1007/s00348-017-2324-z.

Ghannam, M.T. and Esmail, M.N. (1997) Rheological properties of carboxymethyl cellulose. *Journal of Applied Polymer Science*, 64 (2): 289–301. doi:10.1002/(SICI)1097-4628(19970411)64:2<289::AID-APP9>3.0.CO;2-N.

Gillissen, J.J.J. and Van den Akker, H.E.A. (2012) Direct numerical simulation of the turbulent flow in a baffled tank driven by a Rushton turbine. *AIChE Journal*, 58 (12): 3878–3890. doi:https://doi.org/10.1002/aic.13762.

Gimbun, J., Rielly, C.D., Nagy, Z.K., et al. (2012) Detached eddy simulation on the turbulent flow in a stirred tank. *AIChE Journal*, 58 (10): 3224–3241. doi:https://doi.org/10.1002/aic.12807.

Govender, I., Mangesana, N., Mainza, A.N., et al. (2011) Measurement of shear rates in a laboratory tumbling mill. *Minerals Engineering*, 24 (3): 225–229. doi:10.1016/j.mineng.2010.08.009.

Graftieaux, L., Michard, M. and Grosjean, N. (2001) Combining PIV, POD and vortex identification algorithms for the study of unsteady turbulent swirling flows. *Measurement Science and Technology*, 12 (9): 1422–1429. doi:10.1088/0957-0233/12/9/307.

Grand View Research (2020) *Catalyst Market Size, Share & Trends Analysis Report By Raw Material (Chemical Compounds, Zeolites, Metals), By Product (Heterogeneous, Homogeneous), By Application, By Region, And Segment Forecasts, 2020 - 2027*.

Greenville, R.K. (1992) *Blending of Viscous Newtonian and Pseudo-Plastic FLuids*. PhD Thesis, Cranfield Institute of Technology.

Guala, M., Lüthi, B., Liberzon, A., et al. (2005) On the evolution of material lines and vorticity in homogeneous turbulence. *Journal of Fluid Mechanics*, 533: 339–359. doi:10.1017/S0022112005004362.

Gülan, U., Lüthi, B., Holzner, M., et al. (2012) Experimental study of aortic flow in the ascending aorta via Particle Tracking Velocimetry. *Experiments in Fluids*, 53 (5): 1469–1485. doi:10.1007/s00348-012-1371-8.

van der Gulik, G.-J.S., Wijers, J.G. and Keurentjes, J.T.F. (2001) Hydrodynamics in a Horizontal Stirred Tank Reactor. *Industrial & Engineering Chemistry Research*, 40 (3): 785–794. doi:10.1021/ie000054h.

Guoqiang, D., Kaul, R. and Mattiasson, B. (1992) Immobilization of Lactobacillus casei cells to ceramic material pretreated with polyethylenimine. *Applied Microbiology and Biotechnology*, 37 (3): 305–310. doi:10.1007/BF00210983.

Haam, S., Brodkey, R.S. and Fasano, J.B. (1992) Local Heat Transfer in a Mixing Vessel Using Heat Flux Sensors. *Industrial and Engineering Chemistry Research*, 31 (5): 1384–1391. doi:10.1021/ie00005a020.

Hadad, T. and Gurka, R. (2013) Effects of particle size, concentration and surface coating on turbulent flow properties obtained using PIV/PTV. *Experimental Thermal and Fluid Science*, 45: 203–212. doi:10.1016/j.expthermflusci.2012.11.006.

Haddadi, B., Jordan, C. and Harasek, M. (2017) Cost efficient CFD simulations: Proper selection of domain partitioning strategies. *Computer Physics Communications*, 219: 121–134. doi:10.1016/j.cpc.2017.05.014.

Hanjalić, K. and Launder, B.E. (1972) A Reynolds stress model of turbulence and its application to thin shear flows. *Journal of Fluid Mechanics*, 52 (4): 609–638. doi:10.1017/S002211207200268X.

Haque, J.N., Mahmud, T., Roberts, K.J., et al. (2011) Free-surface turbulent flow induced by a Rushton turbine in an unbaffled dish-bottom stirred tank reactor: LDV measurements and CFD simulations. *The Canadian Journal of Chemical Engineering*, 89 (4): 745–753. doi:https://doi.org/10.1002/cjce.20599.

Harrison, S.T.L., Kotsiopoulos, A., Stevenson, R., et al. (2020) Mixing indices allow scale-up of stirred tank slurry reactor conditions for equivalent homogeneity. *Chemical Engineering Research and Design*, 153: 865–874. doi:10.1016/j.cherd.2019.10.049.

Hartmann, H., Derksen, J.J. and van den Akker, H.E.A. (2006) Mixing times in a turbulent stirred tank by means of LES. *AIChE Journal*, 52 (11): 3696–3706. doi:10.1002/aic.10997.

Hasal, P., Fořt, I. and Kratěna, J. (2003) The Tangential Force Affecting the Radial Baffles in a Stirred Vessel: Analysis of the Macro-instability Related Component. *Acta Polytechnica*, 43 (4). doi:10.14311/450.

Hasal, P., Fort, I. and Kratena, J. (2004) Force Effects of the Macro-Instability of Flow Pattern on Radial Baffles in a Stirred Vessel With Pitched-Blade and Rushton Turbine Impellers. *Chemical Engineering Research and Design*, 82 (9): 1268–1281. doi:10.1205/cerd.82.9.1268.44169.

Hasal, P., Kratěna, J. and Fořt, I. (2002) Frequency and Magnitude Analysis of Macro-Instability Related Component of Tangential Force Affecting Radial Baffles in a Stirred Vessel. *Acta Polytechnica*, 42: 59–69.

Hasal, P., Montes, J.-L., Boisson, H.-C., et al. (2000) Macro-instabilities of velocity field in stirred vessel: detection and analysis. *Chemical Engineering Science*, 55 (2): 391–401. doi:10.1016/S0009-2509(99)00334-6.

Heidari, A. and Karim Nejadian, S. (2022) Design of Industrial Water-based Polymerization Agitated Vessel by CFD Simulation. *Iranian Journal of Chemistry and Chemical Engineering*. doi:10.30492/ijcce.2022.527497.4660.

Hemrajani, R.R. and Tatterson, G.B. (2003) "Mechanically Stirred Vessels." In *Handbook of Industrial Mixing*. Hoboken, N.J., US: John Wiley & Sons, Ltd. pp. 345–390. doi:10.1002/0471451452.ch6.

Holzner, M., Liberzon, A., Nikitin, N., et al. (2008) A Lagrangian investigation of the small-scale features of turbulent entrainment through particle tracking and direct numerical simulation. *Journal of Fluid Mechanics*, 598: 465–475. doi:10.1017/S0022112008000141.

Hörmann, T., Suzzi, D., Adam, S., et al. (2012) DOE-Based CFD Optimization of Pharmaceutical Mixing Processes. *Journal of Pharmaceutical Innovation*, 7 (3): 181–194. doi:10.1007/s12247-012-9142-x.

Hörmann, T., Suzzi, D. and Khinast, J.G. (2011) Mixing and Dissolution Processes of Pharmaceutical Bulk Materials in Stirred Tanks: Experimental and Numerical Investigations. *Industrial & Engineering Chemistry Research*, 50 (21): 12011–12025. doi:10.1021/ie2002523.

Hoyer, K., Holzner, M., Lüthi, B., et al. (2005) 3D scanning particle tracking velocimetry. *Experiments in Fluids*, 39 (5): 923–934. doi:10.1007/s00348-005-0031-7.

Hu, Y., Liu, Z., Yang, J., et al. (2010) Study on the reactive mixing process in an unbaffled stirred tank using planar laser-induced fluorescence (PLIF) technique. *Chemical Engineering Science*, 65 (15): 4511–4518. doi:10.1016/j.ces.2010.04.033.

Hu, Y., Wang, W., Shao, T., et al. (2012) Visualization of reactive and non-reactive mixing processes in a stirred tank using planar laser induced fluorescence (PLIF) technique. *Chemical Engineering Research and Design*, 90 (4): 524–533. doi:10.1016/j.cherd.2011.08.021.

Huang, W. and Li, K. (2013) "CFD Simulation of Flows in Stirred Tank Reactors Through Prediction of Momentum Source." In Guillen, D.P. (ed.) *Nuclear Reactor Thermal Hydraulics and Other Applications*. London, UK: IntechOpen.

Hubbard, D.W. (1987) Scaleup Strategies for Bioreactors Containing Non-Newtonian Broths. *Annals of the New York Academy of Sciences*, 506 (1): 600–606. doi:https://doi.org/10.1111/j.1749-6632.1987.tb23854.x.

Hui, L.K., Bennington, C.P.J. and Dumont, G.A. (2009) Cavern formation in pulp suspensions using side-entering axial-flow impellers. *Chemical Engineering Science*, 64 (3): 509–519. doi:10.1016/j.ces.2008.09.021.

Hwang, T.G., Doh, D.H., Jo, H.J., et al. (2007) Analysis of fluid–elastic-structure interactions in an impinging jet with a dynamic 3D-PTV and non-contact 6D-motion tracking system. *Chemical Engineering Journal*, 130 (2): 153–164. doi:10.1016/j.cej.2006.06.018.

Ismail, M.M., Essam, T.M., Ragab, Y.M., et al. (2017) Remediation of a mixture of analgesics in a stirred-tank photobioreactor using microalgal-bacterial consortium coupled with attempt to valorise the harvested biomass. *Bioresource Technology*, 232: 364–371. doi:10.1016/j.biortech.2017.02.062.

Israel, R. and Rosner, D.E. (1982) Use of a Generalized Stokes Number to Determine the Aerodynamic Capture Efficiency of Non-Stokesian Particles from a Compressible Gas Flow. *Aerosol Science and Technology*, 2 (1): 45–51. doi:10.1080/02786828308958612.

Issa, R.I. (1986) Solution of the implicitly discretised fluid flow equations by operator-splitting. *Journal of Computational Physics*, 62 (1): 40–65. doi:10.1016/0021-9991(86)90099-9.

Jafari, R., Tanguy, P.A. and Chaouki, J. (2012) Experimental investigation on solid dispersion, power consumption and scale-up in moderate to dense solid–liquid suspensions. *Chemical Engineering Research and Design*, 90 (2): 201–212. doi:10.1016/j.cherd.2011.07.009.

Jahangiri, M., Golkar-Narenji, M.R., Montazerin, N., et al. (2001) Investigation of the viscoelastic effect on the Metzner and Otto coefficient through LDA velocity measurements. *Chinese Journal of Chemical Engineering*, 9 (1): 77–83.

Jaszczur, M., Młynarczykowska, A. and Demurtas, L. (2020) Effect of Impeller Design on Power Characteristics and Newtonian Fluids Mixing Efficiency in a Mechanically Agitated Vessel at Low Reynolds Numbers. *Energies*, 13 (3): 640. doi:10.3390/en13030640.

Johnson Matthey (2021) *2021 Annual Report and Accounts*. Available at: https://matthey.com/-/media/ara-21/files/jm-ar21-secured.pdf (Accessed: 19 July 2021).

Joshi, J.B., Nere, N.K., Rane, C.V., et al. (2011) CFD simulation of stirred tanks: Comparison of turbulence models. Part I: Radial flow impellers. *The Canadian Journal of Chemical Engineering*, 89 (1): 23–82. doi:https://doi.org/10.1002/cjce.20446.

Kähler, C.J., Scharnowski, S. and Cierpka, C. (2012a) On the resolution limit of digital particle image velocimetry. *Experiments in Fluids*, 52 (6): 1629–1639. doi:10.1007/s00348-012-1280-x.

Kähler, C.J., Scharnowski, S. and Cierpka, C. (2012b) On the uncertainty of digital PIV and PTV near walls. *Experiments in Fluids*, 52 (6): 1641–1656. doi:10.1007/s00348-012-1307-3.

Kaiser, S.C., Werner, S., Jossen, V., et al. (2017) Development of a method for reliable power input measurements in conventional and single-use stirred bioreactors at laboratory scale. *Engineering in Life Sciences*, 17 (5): 500–511. doi:10.1002/elsc.201600096.

Kapic, A. and Heindel, T.J. (2006) Correlating Gas-Liquid Mass Transfer in a Stirred-Tank Reactor. *Chemical Engineering Research and Design*, 84 (3): 239–245. doi:10.1205/cherd.05117.

Karthikeyan, O.P., Selvam, A. and Wong, J.W.C. (2016) Hydrolysis–acidogenesis of food waste in solid–liquid-separating continuous stirred tank reactor (SLS-CSTR) for volatile organic acid production. *Bioresource Technology*, 200: 366–373. doi:10.1016/j.biortech.2015.10.017.

Kelly, W. and Gigas, B. (2003) Using CFD to predict the behavior of power law fluids near axial-flow impellers operating in the transitional flow regime. *Chemical Engineering Science*, 58 (10): 2141–2152. doi:10.1016/S0009-2509(03)00060-5.

Kemp, M. (2019) Leonardo da Vinci's laboratory: studies in flow. *Nature*, 571 (7765): 322–323. doi:10.1038/d41586-019-02144-z.

Khan, F.R., Rielly, C.D. and Brown, D.A.R. (2006) Angle-resolved stereo-PIV measurements close to a down-pumping pitched-blade turbine. *Chemical Engineering Science*, 61 (9): 2799–2806. doi:10.1016/j.ces.2005.10.067.

Khan, F.R., Rielly, C.D. and Hargrave, G.K. (2004) A Multi-Block Approach to Obtain Angle-Resolved PIV Measurements of the Mean Flow and Turbulence Fields in a Stirred Vessel. *Chemical Engineering & Technology*, 27 (3): 264–269. doi:10.1002/ceat.200401998.

Kieft, R., Schreel, K., van der Plas, G., et al. (2002) The application of a 3D PTV algorithm to a mixed convection flow. *Experiments in Fluids*, 33 (4): 603–611. doi:10.1007/s00348-002-0513-9.

Kolmogorov, A.N. (1941b) Dissipation of energy in locally isotropic turbulence. *Proceedings of the USSR Academy of Sciences*, 32: 16–18. doi:10.1098/rspa.1991.0076.

Kolmogorov, A.N. (1941a) The local structure of turbulence in incompressible viscous fluid for very large Reynolds numbers. *Proceedings of the USSR Academy of Sciences*, 30: 301–305. doi:10.1098/rspa.1991.0075.

Kompenhans, J. and Hinsch, K. (2009) *25 Years of Particle Image Velocimetry in Aerodynamics: Program and Abstracts*. In Göttingen, Germany, 23 September 2009. p. 76. Available at: https://elib.dlr.de/60201/1/program_abstracts_25y_red.pdf (Accessed: 6 November 2021).

Kouko, J., Prakash, B., Luukkainen, V.-M., et al. (2021) Generation of aqueous foams and fiber foams in a stirred tank. *Chemical Engineering Research and Design*, 167: 15–24. doi:10.1016/j.cherd.2020.12.013.

Koutsakos, E., Nienow, A.W. and Dyster, K.N. (1990) Laser Anemometry study of shear thinning fluids agitated by a Rushton turbine. *IChemE Sympsosium Series*, 121: 51–73.

Kreizer, M. and Liberzon, A. (2011) Three-dimensional particle tracking method using FPGA-based real-time image processing and four-view image splitter. *Experiments in Fluids*, 50 (3): 613–620. doi:10.1007/s00348-010-0964-3.

Kreizer, M., Ratner, D. and Liberzon, A. (2010) Real-time image processing for particle tracking velocimetry. *Experiments in Fluids*, 48 (1): 105–110. doi:10.1007/s00348-009-0715-5.

Kresta, S.M. and Brodkey, R.S. (2003) "Turbulence in Mixing Applications." In *Handbook of Industrial Mixing*. Hoboken, N.J., US: John Wiley & Sons, Ltd. pp. 19–87. doi:10.1002/0471451452.ch2.

Kresta, S.M., Mao, D. and Roussinova, V. (2006) Batch blend time in square stirred tanks. *Chemical Engineering Science*, 61 (9): 2823–2825. doi:10.1016/j.ces.2005.10.069.

Kresta, S.M. and Wood, P.E. (1991) Prediction of the three-dimensional turbulent flow in stirred tanks. *AIChE Journal*, 37 (3): 448–460. doi:10.1002/aic.690370314.

Kresta, S.M. and Wood, P.E. (1993) The flow field produced by a pitched blade turbine: Characterization of the turbulence and estimation of the dissipation rate. *Chemical Engineering Science*, 48 (10): 1761–1774. doi:10.1016/0009-2509(93)80346-R.

Krug, D., Holzner, M., Lüthi, B., et al. (2014) A combined scanning PTV/LIF technique to simultaneously measure the full velocity gradient tensor and the 3D density field. *Measurement Science and Technology*, 25 (6): 065301. doi:10.1088/0957-0233/25/6/065301.

Krug, D., Lüthi, B., Seybold, H., et al. (2012) 3D-PTV measurements in a plane Couette flow. *Experiments in Fluids*, 52 (5): 1349–1360. doi:10.1007/s00348-011-1256-2.

Kukukova, A., Aubin, J. and Kresta, S.M. (2011) Measuring the scale of segregation in mixing data. *The Canadian Journal of Chemical Engineering*, 89 (5): 1122–1138. doi:https://doi.org/10.1002/cjce.20532.

Kumaresan, T. and Joshi, J.B. (2006) Effect of impeller design on the flow pattern and mixing in stirred tanks. *Chemical Engineering Journal*, 115 (3): 173–193. doi:10.1016/j.cej.2005.10.002.

Kysela, B., Konfrst, J., Chara, Z., et al. (2017) Evaluation of the turbulent kinetic dissipation rate in an agitated vessel. *EPJ Web of Conferences*, 143: 02062. doi:10.1051/epjconf/201714302062.

La Forgia, G.L., Cavaliere, D., Espa, S., et al. (2022) Numerical and experimental analysis of Lagrangian dispersion in two-dimensional chaotic flows. *Scientific Reports*, 12 (1): 7461. doi:10.1038/s41598-022-11350-1.

Labonté, G. (1999) A new neural network for particle-tracking velocimetry. *Experiments in Fluids*, 26 (4): 340–346. doi:10.1007/s003480050297.

Labonté, G. (2000) On a Neural Network that Performs an Enhanced Nearest-Neighbour Matching. *Pattern Analysis & Applications*, 3 (3): 267–278. doi:10.1007/s100440070011.

Lamberto, D.J., Alvarez, M.M. and Muzzio, F.J. (1999) Experimental and computational investigation of the laminar flow structure in a stirred tank. *Chemical Engineering Science*, 54 (7): 919–942. doi:10.1016/S0009-2509(98)00275-9.

Lane, G.L. (2017) Improving the accuracy of CFD predictions of turbulence in a tank stirred by a hydrofoil impeller. *Chemical Engineering Science*, 169: 188–211. doi:10.1016/j.ces.2017.03.061.

Launder, B.E. and Spalding, D.B. (1974) The numerical computation of turbulent flows. *Computer Methods in Applied Mechanics and Engineering*, 3 (2): 269–289. doi:10.1016/0045-7825(74)90029-2.

Lei, Y.-C., Tien, W.-H., Duncan, J., et al. (2012) A vision-based hybrid particle tracking velocimetry (PTV) technique using a modified cascade correlation peak-finding method. *Experiments in Fluids*, 53 (5): 1251–1268. doi:10.1007/s00348-012-1357-6.

Letellier, B., Xuereb, C., Swaels, P., et al. (2002) Scale-up in laminar and transient regimes of a multi-stage stirrer, a CFD approach. *Chemical Engineering Science*, 57 (21): 4617–4632. doi:10.1016/S0009-2509(02)00371-8.

Li, G., Gao, Z., Li, Z., et al. (2018a) Particle-resolved PIV experiments of solid-liquid mixing in a turbulent stirred tank. *AIChE Journal*, 64 (1): 389–402. doi:10.1002/aic.15924.

Li, G., Li, Z., Gao, Z., et al. (2018b) Particle image velocimetry experiments and direct numerical simulations of solids suspension in transitional stirred tank flow. *Chemical Engineering Science*, 191: 288–299. doi:10.1016/j.ces.2018.06.073.

Li, L., Bao, Y., Yang, B., et al. (2012) Power Demand and Mixing Performance of Helical Ribbon Coaxial Mixers with Newtonian Fluids. *International Journal of Chemical Reactor Engineering*, 10 (1). doi:10.1515/1542-6580.3033.

Li, M., White, G., Wilkinson, D., et al. (2004) LDA measurements and CFD modeling of a stirred vessel with a retreat curve impeller. *Industrial & Engineering Chemistry Research*, 43 (20): 6534–6547. doi:10.1021/ie034222s.

Li, M., White, G., Wilkinson, D., et al. (2005) Scale up study of retreat curve impeller stirred tanks using LDA measurements and CFD simulation. *Chemical Engineering Journal*, 108 (1): 81–90. doi:10.1016/j.cej.2005.01.005.

Liberzon, A., Lüthi, B., Holzner, M., et al. (2012) On the structure of acceleration in turbulence. *Physica D: Nonlinear Phenomena*, 241 (3): 208–215. doi:10.1016/j.physd.2011.07.008.

Lin, Y., Wang, D., Li, Q., et al. (2011) Kinetic study of mesophilic anaerobic digestion of pulp & paper sludge. *Biomass and Bioenergy*, 35 (12): 4862–4867. doi:10.1016/j.biombioe.2011.10.001.

Luo, J.Y., Gosman, A.D., Issa, R.I., et al. (1993) Full flow field computation of mixing in baffled stirred vessels. *Transactions of the Institution of Chemical Engineers*, 71: 342–344.

Luo, J.Y., Issa, R.I. and Gosman, A.D. (1994) Prediction of impeller-induced flows in mixing vessels usin multiple frames of references. *IChemE Sympsosium Series*, 136: 549–556.

Lüthi, B., Holzner, M. and Tsinober, A. (2009) Expanding the Q–R space to three dimensions. *Journal of Fluid Mechanics*, 641: 497–507. doi:10.1017/S0022112009991947.

Lüthi, B., Tsinober, A. and Kinzelbach, W. (2005) Lagrangian measurement of vorticity dynamics in turbulent flow. *Journal of Fluid Mechanics*, 528: 87–118. doi:10.1017/S0022112004003283.

Maas, H.G. (1992) *Digitale Photogrammetrie in der dreidimensionalen Strömungsmesstechnik*. Doctoral Thesis, ETH Zurich. doi:10.3929/ethz-a-000627387.

Maas, H.G., Gruen, A. and Papantoniou, D. (1993) Particle tracking velocimetry in three-dimensional flows. *Experiments in Fluids*, 15 (2): 133–146. doi:10.1007/BF00190953.

Machado, M.B., Bittorf, K.J., Roussinova, V.T., et al. (2013) Transition from turbulent to transitional flow in the top half of a stirred tank. *Chemical Engineering Science*, 98 (7): 218–230. doi:10.1016/j.ces.2013.04.039.

Maingonnat, J.F., Doublier, J.L., Lefebvre, J., et al. (2008) Power consumption of a double ribbon impeller with newtonian and shear thinning fluids and during the gelation of a iota-carrageenan solution. *Journal of Food Engineering*, 87 (1): 82–90. doi:10.1016/j.jfoodeng.2007.11.015.

Malcata, F.X. (1991) Modelling of a series of continuously stirred tank reactors for thermal processing of liquid foods. *International Journal of Food Science & Technology*, 26 (5): 535–546. doi:10.1111/j.1365-2621.1991.tb01998.x.

Malik, N.A., Dracos, Th. and Papantoniou, D.A. (1993) Particle tracking velocimetry in three-dimensional flows. *Experiments in Fluids*, 15 (4): 279–294. doi:10.1007/BF00223406.

Márquez-Baños, V.E., De La Concha-Gómez, A.D., Valencia-López, J.J., et al. (2019) Shear rate and direct numerical calculation of the Metzner-Otto constant for a pitched blade turbine. *Journal of Food Engineering*, 257: 10–18. doi:10.1016/j.jfoodeng.2019.03.021.

Martinetz, M.C., Kaiser, F., Kellner, M., et al. (2021) Hybrid Approach for Mixing Time Characterization and Scale-Up in Geometrical Nonsimilar Stirred Vessels Equipped with Eccentric Multi-Impeller Systems—An Industrial Perspective. *Processes*, 9 (5): 880. doi:10.3390/pr9050880.

McKeon, B., Comte-Bellot, G., Foss, J., et al. (2007) "Velocity, Vorticity, and Mach Number." In Tropea, C., Yarin, A.L. and Foss, J.F. (eds.) *Springer Handbook of Experimental Fluid Mechanics*. Springer Handbooks. Berlin, Heidelberg, Germany: Springer. pp. 215–471. doi:10.1007/978-3-540-30299-5_5.

Mehauden, K., Cox, P.W., Bakalis, S., et al. (2009) The flow of liquid foods in an agitated vessel using PEPT: Implications for the use of TTI to assess thermal treatment. *Innovative Food Science & Emerging Technologies*, 10 (4): 643–654. doi:10.1016/j.ifset.2009.06.004.

Melling, A. (1997) Tracer particles and seeding for particle image velocimetry. *Measurement Science and Technology*, 8 (12): 1406–1416. doi:10.1088/0957-0233/8/12/005.

Mendoza, F., Bañales, A.L., Cid, E., et al. (2018) Hydrodynamics in a stirred tank in the transitional flow regime. *Chemical Engineering Research and Design*, 132: 865–880. doi:10.1016/j.cherd.2017.12.011.

Menter, F.R. (1994) Two-equation eddy-viscosity turbulence models for engineering applications. *AIAA Journal*, 32 (8): 1598–1605. doi:10.2514/3.12149.

Menter, F.R. (2009) Review of the shear-stress transport turbulence model experience from an industrial perspective. *International Journal of Computational Fluid Dynamics*, 23 (4): 305–316. doi:10.1080/10618560902773387.

Menter, F.R. and Egorov, Y. (2005) "A Scale Adaptive Simulation Model using Two-Equation Models." In *43rd AIAA Aerospace Sciences Meeting and Exhibit*. Aerospace Sciences Meetings. American Institute of Aeronautics and Astronautics. pp. 271–283. doi:10.2514/6.2005-1095.

Metzner, A.B. and Otto, R.E. (1957) Agitation of non-Newtonian fluids. *AIChE Journal*, 3 (1): 3–10. doi:10.1002/aic.690030103.

Micheletti, M., Baldi, S., Yeoh, S.L., et al. (2004) On Spatial and Temporal Variations and Estimates of Energy Dissipation in Stirred Reactors. *Chemical Engineering Research and Design*, 82 (9): 1188–1198. doi:10.1205/cerd.82.9.1188.44172.

Monica, M., Cushman, J.H. and Cenedese, A. (2009) Application of Photogrammetric 3D-PTV Technique to Track Particles in Porous Media. *Transport in Porous Media*, 79 (1): 43–65. doi:10.1007/s11242-008-9270-4.

Montante, G., Bourne, J.R. and Magelli, F. (2008) Scale-Up of Solids Distribution in Slurry, Stirred Vessels Based on Turbulence Intermittency. *Industrial & Engineering Chemistry Research*, 47 (10): 3438–3443. doi:10.1021/ie070339v.

Montante, G., Pinelli, D. and Magelli, F. (2003a) Scale-up criteria for the solids distribution in slurry reactors stirred with multiple impellers. *Chemical Engineering Science*, 58 (23): 5363–5372. doi:10.1016/j.ces.2003.09.021.

Montante, G., Pinelli, D. and Magelli, F. (2003b) Scale-up criteria for the solids distribution in slurry reactors stirred with multiple impellers. *Chemical Engineering Science*, 58 (23): 5363–5372. doi:10.1016/j.ces.2003.09.021.

Montes, J.L., Boisson, H.C., Fořt, I., et al. (1997) Velocity field macro-instabilities in an axially agitated mixing vessel. *Chemical Engineering Journal*, 67 (2): 139–145. doi:10.1016/S1385-8947(97)00042-9.

Murasiewicz, H. and Esteban, J. (2019) Assessment of the Dispersion of Glycerol in Dimethyl Carbonate in a Stirred Tank. *Industrial & Engineering Chemistry Research*, 58 (16): 6933–6947. doi:10.1021/acs.iecr.9b01061.

Murthy, B.N. and Joshi, J.B. (2008) Assessment of standard k–ε, RSM and LES turbulence models in a baffled stirred vessel agitated by various impeller designs. *Chemical Engineering Science*, 63 (22): 5468–5495. doi:10.1016/j.ces.2008.06.019.

Nagata, S., Nishikawa, M., Tada, H., et al. (1971) Power Consumption of Mixing Impellers in Pseudoplastic Liquids. *Journal of Chemical Engineering of Japan*, 4 (1): 72–76. doi:10.1252/jcej.4.72.

NAMF (2011) *21 most influential contributions to mixing research*. Available at: https://mixing.net/21-most-influential-contributions-to-mixing-research/ (Accessed: 4 June 2021).

Navier, C.L. (1821) Sur les lois des mouvements des fluides, en ayant égard à l'adhésion des molécules. *Annales de Chimie et de Physique*, 19: 244–260.

Ng, K. and Yianneskis, M. (2000) Observations on the Distribution of Energy Dissipation in Stirred Vessels. *Chemical Engineering Research and Design*, 78 (3): 334–341. doi:10.1205/026387600527446.

Nienow, A.W. (2014) Stirring and Stirred-Tank Reactors. *Chemie Ingenieur Technik*, 86 (12): 2063–2074. doi:10.1002/cite.201400087.

Nienow, A.W., Kendall, A., Moore, I.P.T., et al. (1995) The characteristics of aerated 12- and 18-blade Rushton turbines at transitional Reynolds numbers. *Chemical Engineering Science*, 50 (4): 593–599. doi:10.1016/0009-2509(94)00250-U.

Nienow, A.W. and Wisdom, D.J. (1974) Flow over disc turbine blades. *Chemical Engineering Science*, 29 (9): 1994–1997. doi:10.1016/0009-2509(74)85019-0.

Nikiforaki, L., Yu, J., Baldi, S., et al. (2004) On the variation of precessional flow instabilities with operational parameters in stirred vessels. *Chemical Engineering Journal*, 102 (3): 217–231. doi:10.1016/j.cej.2004.05.002.

Nobach, H., Damaschke, N. and Tropea, C. (2005) High-precision sub-pixel interpolation in particle image velocimetry image processing. *Experiments in Fluids*, 39 (2): 299–304. doi:10.1007/s00348-005-0999-z.

Norwood, K.W. and Metzner, A.B. (1960) Flow patterns and mixing rates in agitated vessels. *AIChE Journal*, 6 (3): 432–437. doi:10.1002/aic.690060317.

Okibe, N., Gericke, M., Hallberg, K.B., et al. (2003) Enumeration and Characterization of Acidophilic Microorganisms Isolated from a Pilot Plant Stirred-Tank Bioleaching Operation. *Applied and Environmental Microbiology*, 69 (4): 1936–1943. doi:10.1128/AEM.69.4.1936-1943.2003.

Oliveira, J.L.G., Geld, C.W.M. van der and Kuerten, J.G.M. (2015) Lagrangian velocity and acceleration statistics of fluid and inertial particles measured in pipe flow with 3D particle tracking velocimetry. *International journal of multiphase flow*, 73: 97–107. doi:10.1016/j.ijmultiphaseflow.2015.03.017.

Olivieri, S., Picano, F., Sardina, G., et al. (2014) The effect of the Basset history force on particle clustering in homogeneous and isotropic turbulence. *Physics of Fluids*, 26 (4): 041704. doi:10.1063/1.4871480.

Özcan-Taşkin, G. (2006) Effect of scale on the draw down of floating solids. *Chemical Engineering Science*, 61 (9): 2871–2879. doi:10.1016/j.ces.2005.10.061.

Paglianti, A., Liu, Z., Montante, G., et al. (2008) Effect of Macroinstabilities in Single- and Multiple-Impeller Stirred Tanks | Industrial & Engineering Chemistry Research. *Industrial & Engineering Chemistry Research*, 47: 4944–4952. doi:10.1021/ie800253u.

Parker, D.J. (2017) Positron emission particle tracking and its application to granular media. *Review of Scientific Instruments*, 88 (5): 051803. doi:10.1063/1.4983046.

Patankar, S.V. and Spalding, D.B. (1972) A calculation procedure for heat, mass and momentum transfer in three-dimensional parabolic flows. *International Journal of Heat and Mass Transfer*, 15 (10): 1787–1806. doi:10.1016/0017-9310(72)90054-3.

Patel, D., Ein-Mozaffari, F. and Mehrvar, M. (2015a) Effect of rheological parameters on non-ideal flows in the continuous-flow mixing of biopolymer solutions. *Chemical Engineering Research and Design*, 100: 126–134. doi:10.1016/j.cherd.2015.05.010.

Patel, D., Ein-Mozaffari, F. and Mehrvar, M. (2015b) Effect of rheological parameters on non-ideal flows in the continuous-flow mixing of biopolymer solutions. *Chemical Engineering Research and Design*, 100: 126–134. doi:10.1016/j.cherd.2015.05.010.

Paul, E.L., Atiemo-Obeng, V.A. and Kresta, S.M. (2003) “Introduction.” In *Handbook of Industrial Mixing*. Hoboken, N.J., US: John Wiley & Sons, Ltd. pp. xxxiii–lxi.

Peralta-Reyes, E., Vizarretea-Vásquez, D., Natividad, R., et al. (2022) Electrochemical reforming of glycerol into hydrogen in a batch-stirred electrochemical tank reactor equipped with stainless steel electrodes: Parametric optimization, total operating cost, and life cycle assessment. *Journal of Environmental Chemical Engineering*, 10 (4): 108108. doi:10.1016/j.jece.2022.108108.

Pereira, F., Stüer, H., Graff, E.C., et al. (2006) Two-frame 3D particle tracking. *Measurement Science and Technology*, 17 (7): 1680–1692. doi:10.1088/0957-0233/17/7/006.

Pérez-Mohedano, R., Letzelter, N., Amador, C., et al. (2015) Positron Emission Particle Tracking (PEPT) for the analysis of water motion in a domestic dishwasher. *Chemical Engineering Journal*, 259: 724–736. doi:10.1016/j.cej.2014.08.033.

Piirto, M., Eloranta, H. and Saarenrinne, P. (2000) *Interactive Software for Turbulence Analysis from PIV Vector Data*. In Lisbon, Portugal, 2000. p. 12.

Poernomo, H., Kundari, N.A., and Nafiah (2022) The effect of stirring speed and reactant residence time in the bench scales CSTR on the reaction conversion of ZBS. *Alexandria Engineering Journal*, 61 (2): 1309–1317. doi:10.1016/j.aej.2021.06.012.

Pope, S.B. (2000) *Turbulent Flows*. Cambridge, UK: Cambridge University Press.

Prasad, A.K. (2000) Stereoscopic particle image velocimetry. *Experiments in Fluids*, 29 (2): 103–116. doi:10.1007/s003480000143.

Qiu, N., Wang, P., Si, Q., et al. (2021) Scale process effect on the power consumption characteristics of a novel curved Rushton turbine within a reactor vessel. *Chemical Engineering Research and Design*, 166: 109–120. doi:10.1016/j.cherd.2020.11.029.

Ramírez-Muñoz, J., Guadarrama-Pérez, R. and Márquez-Baños, V.E. (2017) A direct calculation method of the Metzner-Otto constant by using computational fluid dynamics. *Chemical Engineering Science*, 174: 347–353. doi:10.1016/j.ces.2017.09.023.

Rammohan, A.R., Duduković, M.P. and Ranade, V.V. (2003) Eulerian Flow Field Estimation from Particle Trajectories: Numerical Experiments for Stirred Tank Type Flows. *Industrial & Engineering Chemistry Research*, 42 (12): 2589–2601. doi:10.1021/ie020552l.

Rammohan, A.R., Kemoun, A., Al-Dahhan, M.H., et al. (2001) A Lagrangian description of flows in stirred tanks via computer-automated radioactive particle tracking (CARPT). *Chemical Engineering Science*, 56 (8): 2629–2639. doi:10.1016/S0009-2509(00)00537-6.

Ranade, V.V., Perrard, M., Le Sauze, N., et al. (2001) Trailing Vortices of Rushton Turbine: PIV Measurements and CFD Simulations with Snapshot Approach. *Chemical Engineering Research and Design*, 79 (1): 3–12. doi:10.1205/026387601528471.

Reynolds, A.M., Mordant, N., Crawford, A.M., et al. (2005) On the distribution of Lagrangian accelerations in turbulent flows. *New Journal of Physics*, 7: 58–58. doi:10.1088/1367-2630/7/1/058.

Reynolds, O. (1883) An experimental investigation of the circumstances which determine whether the motion of water shall be direct or sinuous, and of the law of resistance in parallel channels. *Philosophical Transactions of the Royal Society of London*, 174: 935–982. doi:10.1098/rstl.1883.0029.

Reynolds, O. (1895) On the dynamical theory of incompressible viscous fluids and the determination of the criterion. *Philosophical Transactions of the Royal Society of London*, 186: 123–164. doi:10.1098/rsta.1895.0004.

Rice, M., Hall, J., Papadakis, G., et al. (2006) Investigation of laminar flow in a stirred vessel at low Reynolds numbers. *Chemical Engineering Science*, 61 (9): 2762–2770. doi:10.1016/j.ces.2005.10.074.

Rieger, F. and Novak, V. (1973) Power Consumption of Agitators in Highly Viscous Non-Newtonian Liquids. *Transactions of the Institution of Chemical Engineers*, 51: 105–111.

Robinson, G. and Robinson, I. (2018) Model trajectories for a spinning tennis ball: I. The service stroke. *Physica Scripta*, 93 (12): 123002. doi:10.1088/1402-4896/aae733.

Rosato, A. and Windows-Yule, K. (2020) “Chapter 3 - Investigative approaches I: experimental imaging techniques.” In Rosato, A. and Windows-Yule, K. (eds.) *Segregation in Vibrated Granular Systems*. London, UK: Academic Press. pp. 37–74. doi:10.1016/B978-0-12-814199-1.00009-3.

Roser, M. and Ritchie, H. (2013) Technological Progress. *Our World in Data*. Available at: https://ourworldindata.org/technological-progress (Accessed: 7 March 2022).

Roussinova, V., Kresta, S.M. and Weetman, R. (2003) Low frequency macroinstabilities in a stirred tank: scale-up and prediction based on large eddy simulations. *Chemical Engineering Science*, 58 (11): 2297–2311. doi:10.1016/S0009-2509(03)00097-6.

Roussinova, V.T., Grgic, B. and Kresta, S.M. (2000) Study of Macro-Instabilities in Stirred Tanks Using a Velocity Decomposition Technique. *Chemical Engineering Research and Design*, 78 (7): 1040–1052. doi:10.1205/026387600528157.

Roy, S., Larachi, F., Al-Dahhan, M.H., et al. (2002) Optimal design of radioactive particle tracking experiments for flow mapping in opaque multiphase reactors. *Applied Radiation and Isotopes*, 56 (3): 485–503. doi:10.1016/S0969-8043(01)00142-7.

Saarenrinne, P. and Piirto, M. (2000) Turbulent kinetic energy dissipation rate estimation from PIV velocity vector fields. *Experiments in Fluids*, 29 (1): S300–S307. doi:10.1007/s003480070032.

Saarenrinne, P., Piirto, M. and Eloranta, H. (2001) Experiences of turbulence measurement with PIV*. *Measurement Science and Technology*, 12 (11): 1904–1910. doi:10.1088/0957-0233/12/11/320.

Sánchez Pérez, J.A., Rodríguez Porcel, E.M., Casas López, J.L., et al. (2006) Shear rate in stirred tank and bubble column bioreactors. *Chemical Engineering Journal*, 124 (1): 1–5. doi:10.1016/j.cej.2006.07.002.

Savitzky, A. and Golay, M.J.E. (1964) Smoothing and Differentiation of Data by Simplified Least Squares Procedures. *Analytical Chemistry*, 36 (8): 1627–1639. doi:10.1021/ac60214a047.

Sbrizzai, F., Lavezzo, V., Verzicco, R., et al. (2006) Direct numerical simulation of turbulent particle dispersion in an unbaffled stirred-tank reactor. *Chemical Engineering Science*, 61 (9): 2843–2851. doi:10.1016/j.ces.2005.10.073.

Scargiali, F., Busciglio, A., Grisafi, F., et al. (2013) Power Consumption in Uncovered Unbaffled Stirred Tanks: Influence of the Viscosity and Flow Regime. *Industrial & Engineering Chemistry Research*, 52 (42): 14998–15005. doi:10.1021/ie402466w.

Schröder, A., Agocs, J., Geisler, R., et al. (2009) *Developments for Industrial PIV*. In Göttingen, Germany, 2009. Available at: http://25-years-PIV.dlr.de (Accessed: 27 August 2022).

Serra, A., Campolo, M. and Soldati, A. (2001) Time-dependent finite-volume simulation of the turbulent flow in a free-surface CSTR. *Chemical Engineering Science*, 56 (8): 2715–2720. doi:10.1016/S0009-2509(00)00519-4.

Shaffer, F., Ibarra, E. and Savaş, Ö. (2021) Visualization of submerged turbulent jets using particle tracking velocimetry. *Journal of Visualization*, 24 (4): 699–710. doi:10.1007/s12650-021-00744-4.

Shah, Y.T. and Kakar, N. (1972) Settling of Iron Pigment in Water. *Industrial & Engineering Chemistry Process Design and Development*, 11 (2): 308–312. doi:10.1021/i260042a027.

Sharp, K.V. and Adrian, R.J. (2001) PIV study of small-scale flow structure around a Rushton turbine. *AIChE Journal*, 47 (4): 766–778. doi:10.1002/aic.690470403.

Shih, T.-H., Liou, W.W., Shabbir, A., et al. (1995) A new k-ϵ eddy viscosity model for high reynolds number turbulent flows. *Computers & Fluids*, 24 (3): 227–238. doi:10.1016/0045-7930(94)00032-T.

Siddique, Md.N.I., Sakinah Abd Munaim, M. and Zularisam, A.W. (2014) Mesophilic and thermophilic biomethane production by co-digesting pretreated petrochemical wastewater with beef and dairy cattle manure. *Journal of Industrial and Engineering Chemistry*, 20 (1): 331–337. doi:10.1016/j.jiec.2013.03.030.

Simmons, M.J.H., Zhu, H., Bujalski, W., et al. (2007) Mixing in a Model Bioreactor Using Agitators with a High Solidity Ratio and Deep Blades. *Chemical Engineering Research and Design*, 85 (5): 551–559. doi:10.1205/cherd06157.

Singh, H., Fletcher, D.F. and Nijdam, J.J. (2011) An assessment of different turbulence models for predicting flow in a baffled tank stirred with a Rushton turbine. *Chemical Engineering Science*, 66 (23): 5976–5988. doi:10.1016/j.ces.2011.08.018.

Smagorinsky, J. (1963) General circulation experiments with the primitive equations: I. The basic experiment. *Monthly Weather Review*, 91 (3): 99–164. doi:10.1175/1520-0493(1963)091<0099:GCEWTP>2.3.CO;2.

Smirnov, P.E. and Menter, F.R. (2009) Sensitization of the SST Turbulence Model to Rotation and Curvature by Applying the Spalart–Shur Correction Term. *Journal of Turbomachinery*, 131 (041010). doi:10.1115/1.3070573.

Smith, N. (1978) Roman Hydraulic Technology. *Scientific American*, 238 (5): 154–161.

Solomon, J., Elson, T.P., Nienow, A.W., et al. (1981) Cavern Sizes in Agitated Fluids with a Yield Stress. *Chemical Engineering Communications*, 11 (1–3): 143–164. doi:10.1080/00986448108910992.

Soos, M., Kaufmann, R., Winteler, R., et al. (2013) Determination of maximum turbulent energy dissipation rate generated by a rushton impeller through large eddy simulation. *AIChE Journal*, 59 (10): 3642–3658. doi:10.1002/aic.14206.

Sossa-Echeverria, J. and Taghipour, F. (2012) Mixing of Newtonian and Non-Newtonian Fluids in a Cylindrical Mixer Equipped with a Side-Entry Impeller. *Industrial & Engineering Chemistry Research*, 51 (46): 15258–15267. doi:10.1021/ie300979y.

Stamatopoulos, K., Alberini, F., Batchelor, H., et al. (2016) Use of PLIF to assess the mixing performance of small volume USP 2 apparatus in shear thinning media. *Chemical Engineering Science*, 145: 1–9. doi:10.1016/j.ces.2016.01.032.

Stitt, E.H. (2002) Alternative multiphase reactors for fine chemicals: A world beyond stirred tanks? *Chemical Engineering Journal*, 90 (1): 47–60. doi:10.1016/S1385-8947(02)00067-0.

Story, A., Jaworski, Z., Simmons, M.J., et al. (2018) Comparative PIV and LDA studies of Newtonian and non-Newtonian flows in an agitated tank. *Chemical Papers*, 72 (3): 593–602. doi:10.1007/s11696-017-0307-4.

Sun, T., Xing, F., Bao, J., et al. (2022) Centroid determination based on energy flow information for moving dim point targets. *Acta Astronautica*, 192: 424–433. doi:10.1016/j.actaastro.2021.12.046.

Szewc, K., Mangold, J., Bauinger, C., et al. (2018) "GPU-Accelerated Meshless CFD methods for Solving Engineering Problems in the Automotive Industry." In *SAE Technical Paper Series*. 2018. doi:10.4271/2018-01-0492.

Taghavi, M. and Moghaddas, J. (2019) Using PLIF/PIV techniques to investigate the reactive mixing in stirred tank reactors with Rushton and pitched blade turbines. *Chemical Engineering Research and Design*, 151: 190–206. doi:10.1016/j.cherd.2019.08.016.

Tamburini, A., Brucato, A., Ciofalo, M., et al. (2021) CFD simulations of early- to fully-turbulent conditions in unbaffled and baffled vessels stirred by a Rushton turbine. *Chemical Engineering Research and Design*, 171: 36–47. doi:10.1016/j.cherd.2021.04.021.

Tamburini, A., Gagliano, G., Micale, G., et al. (2018) Direct numerical simulations of creeping to early turbulent flow in unbaffled and baffled stirred tanks. *Chemical Engineering Science*, 192: 161–175. doi:10.1016/j.ces.2018.07.023.

Tanaka, T. and Eaton, J.K. (2007) A correction method for measuring turbulence kinetic energy dissipation rate by PIV. *Experiments in Fluids*, 42 (6): 893–902. doi:10.1007/s00348-007-0298-y.

Torotwa, I. and Ji, C. (2018) A Study of the Mixing Performance of Different Impeller Designs in Stirred Vessels Using Computational Fluid Dynamics. *Designs*, 2 (1): 10. doi:10.3390/designs2010010.

Torrez, C. and André, C. (1998) Power Consumption of a Rushton Turbine Mixing Viscous Newtonian and Shear-thinning Fluids: Comparison between Experimental and Numerical Results. *Chemical Engineering & Technology*, 21 (7): 599–604. doi:https://doi.org/10.1002/(SICI)1521-4125(199807)21:7<599::AID-CEAT599>3.0.CO;2-6.

Twigg, M.V. (2011) Catalytic control of emissions from cars. *Catalysis Today*, 163 (1): 33–41. doi:10.1016/j.cattod.2010.12.044.

Twigg, M.V. (2015) Urea-SCR Technology for deNOx After Treatment of Diesel Exhausts. *Johnson Matthey Technology Review*, 59 (3). doi:10.1595/205651315x688280.

Venneker, B.C.H., Derksen, J.J. and Van den Akker, H.E.A. (2010) Turbulent flow of shear-thinning liquids in stirred tanks—The effects of Reynolds number and flow index. *Chemical Engineering Research and Design*, 88 (7): 827–843. doi:10.1016/j.cherd.2010.01.002.

Verschuren, I.L.M., Wijers, J.G. and Keurentjes, J.T.F. (2001) Effect of mixing on product quality in semibatch stirred tank reactors. *AIChE Journal*, 47 (8): 1731–1739. doi:10.1002/aic.690470805.

Verzicco, R., Fatica, M., Iaccarino, G., et al. (2004) Flow in an impeller-stirred tank using an immersed-boundary method. *AIChE Journal*, 50 (6): 1109–1118. doi:10.1002/aic.10117.

Wessel, R.A. and Righi, J. (1988) Generalized Correlations for Inertial Impaction of Particles on a Circular Cylinder. *Aerosol Science and Technology*, 9 (1): 29–60. doi:10.1080/02786828808959193.

Wilcox, D.C. (1988) Reassessment of the scale-determining equation for advanced turbulence models. *AIAA Journal*. doi:10.2514/3.10041.

Wilcox, D.C. (2008) Formulation of the k-w Turbulence Model Revisited. *AIAA Journal*, 46 (11): 2823–2838. doi:10.2514/1.36541.

Wildman, R.D., Huntley, J.M. and Hansen, J.-P. (1999) Self-diffusion of grains in a two-dimensional vibrofluidized bed. *Physical Review E*, 60 (6): 7066–7075. doi:10.1103/PhysRevE.60.7066.

Wilkens, R.J., Miller, J.D., Plummer, J.R., et al. (2005a) New techniques for measuring and modeling cavern dimensions in a Bingham plastic fluid. *Chemical Engineering Science*, 60 (19): 5269–5275. doi:10.1016/j.ces.2005.04.058.

Wilkens, R.J., Miller, J.D., Plummer, J.R., et al. (2005b) New techniques for measuring and modeling cavern dimensions in a Bingham plastic fluid. *Chemical Engineering Science*, 60 (19): 5269–5275. doi:10.1016/j.ces.2005.04.058.

Willneff, J. (2003) *A Spatio-Temporal Matching Algorithm for 3D Particle Tracking Velocimetry*. Doctoral Thesis, Swiss Federal Institute of Technology Zurich.

Willneff, J. and Gruen, A. (2002) *A new spatio-temporal matching algorithm for 3D-Particle Tracking Velocimetry*. In Honolulu, Hawaii, USA, 2002.

Windows-Yule, C., Seville, J.P.K., Ingram, A., et al. (2020b) Positron Emission Particle Tracking of Granular Flows. *Annual Review of Chemical and Biomolecular Engineering*, 11. doi:10.1146/annurev-chembioeng-011620-120633.

Windows-Yule, C.R.K., Hart-villamil, R., Ridout, T., et al. (2020a) Positron Emission Particle Tracking for Liquid-Solid Mixing in Stirred Tanks. *Chemical Engineering and Technology*, 43 (10): 1939–1950. doi:10.1002/ceat.v43.10.

Windows-Yule, C.R.K., Herald, M.T., Nicuşan, A.L., et al. (2022) Recent advances in positron emission particle tracking: a comparative review. *Reports on Progress in Physics*, 85 (1): 016101. doi:10.1088/1361-6633/ac3c4c.

Windows-Yule, C.R.K. and Parker, D.J. (2014) Self-diffusion, local clustering and global segregation in binary granular systems: The role of system geometry. *Powder Technology*, 261: 133–142. doi:10.1016/j.powtec.2014.04.009.

Wood, T., Simmons, M.J.H., Greenwood, R.W., et al. (2018a) Concentrated slurry formation via drawdown and incorporation of wettable solids in a mechanically agitated vessel. *AIChE Journal*, 64 (5): 1885–1895. doi:10.1002/aic.16121.

Wood, T., Simmons, M.J.H. and Stitt, E.H. (2018b) Optimisation of stirred vessel geometry for the drawdown and incorporation of floating solids to prepare concentrated slurries. *Chemical Engineering Research and Design*, 133: 70–78. doi:10.1016/j.cherd.2018.03.002.

Xiang, Y., Yu, B., Yuan, Q., et al. (2017) GPU Acceleration of CFD Algorithm: HSMAC and SIMPLE. *Procedia Computer Science*, 108: 1982–1989. doi:10.1016/j.procs.2017.05.124.

Xiao, Q., Yang, N., Zhu, J., et al. (2014) Modeling of cavern formation in yield stress fluids in stirred tanks. *AIChE Journal*, 60 (8): 3057–3070. doi:https://doi.org/10.1002/aic.14470.

Yakhot, V. and Orszag, S.A. (1986) Renormalization group analysis of turbulence. I. Basic theory. *Journal of Scientific Computing*, 1 (1): 3–51. doi:10.1007/BF01061452.

Yavuz, N. and Sandeep, K.P. (2019) Scale-Up of Shear Thinning Fluid Mixing in an Unbaffled Stirred Vessel with Eccentrically Located and Modified Impellers. *International Journal of Chemical Reactor Engineering*, 17 (4). doi:10.1515/ijcre-2018-0205.

Yeh, Y. and Cummins, H.Z. (1964) Localized fluid flow measurements with an He–Ne Laser Spectrometer. *Applied Physics Letters*, 4 (10): 176–178. doi:10.1063/1.1753925.

Yeoh, S.L., Papadakis, G. and Yianneskis, M. (2004) Numerical Simulation of Turbulent Flow Characteristics in a Stirred Vessel Using the LES and RANS Approaches with the Sliding/Deforming Mesh Methodology. *Chemical Engineering Research and Design*, 82 (7): 834–848. doi:10.1205/0263876041596751.

Yianneskis, M., Popiolek, Z. and Whitelaw, J.H. (1987) An experimental study of the steady and unsteady flow characteristics of stirred reactors. *Journal of Fluid Mechanics*, 175: 537–555. doi:10.1017/S002211208700051X.

Yoon, H.S., Hill, D.F., Balachandar, S., et al. (2005) Reynolds number scaling of flow in a Rushton turbine stirred tank. Part I - Mean flow, circular jet and tip vortex scaling. *Chemical Engineering Science*, 60 (12): 3169–3183. doi:10.1016/j.ces.2004.12.039.

Zadghaffari, R., Moghaddas, J.S. and Revstedt, J. (2010) Large-eddy simulation of turbulent flow in a stirred tank driven by a Rushton turbine. *Computers & Fluids*, 39 (7): 1183–1190. doi:10.1016/j.compfluid.2010.03.001.

Zalc, J.M., Alvarez, M.M., Muzzio, F.J., et al. (2001) Extensive validation of computed laminar flow in a stirred tank with three Rushton turbines. *AIChE Journal*, 47 (10): 2144–2154. doi:10.1002/aic.690471003.

Zamiri, A. and Chung, J.T. (2018) Numerical evaluation of turbulent flow structures in a stirred tank with a Rushton turbine based on scale-adaptive simulation. *Computers and Fluids*, 170: 236–248. doi:10.1016/j.compfluid.2018.05.007.

Zeff, B.W., Lanterman, D.D., McAllister, R., et al. (2003) Measuring intense rotation and dissipation in turbulent flows. *Nature*, 421 (6919): 146–149. doi:10.1038/nature01334.

Zhang, M., Karjala, T.W. and Kolthammer, B.W.S. (2007) Delayed Dynamics of Polymer Properties in Continuous Stirred Tank Polymerization Reactors. *Industrial & Engineering Chemistry Research*, 46 (18): 5922–5935. doi:10.1021/ie0614935.

Zhang, Y., Gao, Z., Li, Z., et al. (2017) Transitional flow in a Rushton turbine stirred tank. *AIChE Journal*, 63 (8): 3610–3623. doi:10.1002/aic.15809.

Zhao, H., Zhao, X., Zhang, L., et al. (2017) Experimental Study on Scale-Up of Solid–Liquid Stirred Tank with an Intermig Impeller. *JOM*, 69 (2): 301–306. doi:10.1007/s11837-016-2163-z.

Zhao, J., Gao, Z. and Bao, Y. (2011) Effects of the Blade Shape on the Trailing Vortices in Liquid Flow Generated by Disc Turbines. *Chinese Journal of Chemical Engineering*, 19 (2): 232–242. doi:10.1016/S1004-9541(11)60160-2.

Zhou, G. and Kresta, S.M. (1996) Impact of tank geometry on the maximum turbulence energy dissipation rate for impellers. *AIChE Journal*, 42 (9): 2476–2490. doi:10.1002/aic.690420908.

Zou, X.-Y., Cheng, H., Zhang, C.-L., et al. (2007) Effects of the Magnus and Saffman forces on the saltation trajectories of sand grain. *Geomorphology*, 90 (1): 11–22. doi:10.1016/j.geomorph.2007.01.006.

APPENDIX

A.1. Elements of camera imaging and stereoscopic reconstruction

A.1.1. Image formation

The imaging process of a camera can be modelled by means of projective transformations. These preserve only a few geometrical properties, such as

(i) type, i.e. points remain points and lines remain lines;

(ii) incidence, that is whether or not a point lies on a line (this is equivalent to say whether or not two lines cross);

(iii) cross ratio, that is a ratio of ratios of lengths.

The simplest mathematical description of image formation is the *pinhole camera* model, in which the camera lens is totally represented by its focal point. Consider a coordinate system $E \equiv \{O, \mathbf{e}_x, \mathbf{e}_y, \mathbf{e}_z\}$ in 3D space and a point P at position $\mathbf{p}$ from O (***Figure A-1***). The coordinates of the vector $\mathbf{p}$ are $[\mathbf{p}] \equiv [x, y, z]$. Now consider a camera somewhere in 3D space. The coordinate system of the camera is $E' \equiv \{O', \mathbf{e}'_x, \mathbf{e}'_y, \mathbf{e}'_z\}$, where O' is the *focal point* and $\mathbf{e}'_z$ defines the direction of the *focal axis*. Real devices form the image upside-down on the *focal plane*, which is perpendicular to the focal axis and behind the focal point, at a position $-f\mathbf{e}'_z$. The distance f between the focal point and the image plane and is called the *focal length*. For the sake of simplicity, it is more convenient to consider the plane π'', placed symmetrically at the front of the camera at $+f\boldsymbol{e}'_z$. The orthonormal coordinate system of the virtual image plane is $E'' \equiv \{O'', \mathbf{e}''_x, \mathbf{e}''_y\}$. Its origin, O'', lays on the focal axis and is called the *focal centre*. The

position of the point P from O' is the vector $\mathbf{p}'$, which has coordinates $[\mathbf{p}'] \equiv [x', y', z']$ in E'. P is projected onto the point P'' on π''. The position of P'' from O'' is the vector $\mathbf{p}''$ with coordinates $[\mathbf{p}''] \equiv [x'', y'']$ in E''.

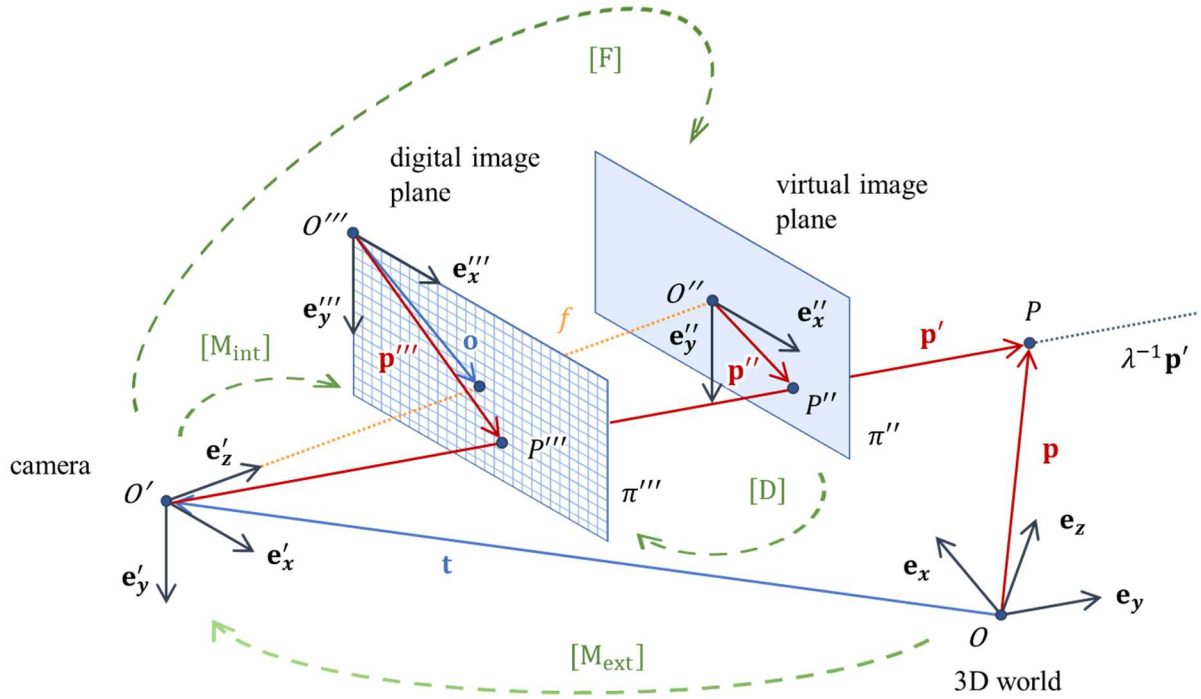

***Figure A-1**: Geometrical elements in a pinhole camera model.*

The relationship between $[\mathbf{p}']$ and $[\mathbf{p}'']$ can be expressed by

$$\begin{cases} x'' = f\dfrac{x'}{z'} \\ y'' = f\dfrac{y'}{z'}. \end{cases} \qquad \textit{Eq. A-1}$$

These equations are not linear, as there is no matrix [A] such that $[\mathbf{p}''] = [\mathrm{A}][\mathbf{p}']$. However, homogeneous coordinates can be used to obtain a linear expression. Let us define $[\mathbf{p}''_{\mathbf{h}}] \equiv [x'', y'', 1]$. Then

$$\lambda[\mathbf{p}''_{\mathbf{h}}] = \lambda\begin{bmatrix} x'' \\ y'' \\ 1 \end{bmatrix} = [\mathrm{F}][\mathbf{p}'] = \begin{bmatrix} f & 0 & 0 \\ 0 & f & 0 \\ 0 & 0 & 1 \end{bmatrix}\begin{bmatrix} x' \\ y' \\ z' \end{bmatrix}. \qquad \textit{Eq. A-2}$$

The scalar $\lambda = z'$ is the *depth* of the point P, that is its distance from the focal point of the camera. If f is known, this relationship allows $[\mathbf{p}''_{\mathbf{h}}]$ to be calculated from $[\mathbf{p}']$, but not the opposite to be done. In other words:

i. given a point in the 3D space, it is always possible to determine its projection on the image plane;

ii. given a point on the image plane, it is impossible to determine its back-projection in the 3D space, as the depth remains unknown (only its *sight line*, $\lambda^{-1}\mathbf{p}'$, can be determined).

This explains why the reconstruction of a 3D scene requires a stereoscopic imaging system.

The relationship between $[\mathbf{p}]$ and $[\mathbf{p}']$ involves a translation [t] and a rotation [R]:

$$[\mathbf{p}'] = [\mathrm{R}]([\mathbf{p}] - [\mathrm{t}]). \qquad \textit{Eq. A-3}$$

Let us define $[\mathbf{p_h}] \equiv [x, y, z, 1]$. r_{ij} indicates the element in the i-th row and j-th column of the rotation matrix. $[\mathrm{R}_k]$ represents the k-th row of the rotation matrix. Then

$$[\mathbf{p}'] \equiv \begin{bmatrix} x' \\ y' \\ z' \end{bmatrix} = [\mathrm{M_{ext}}][\mathbf{p_h}] = \begin{bmatrix} r_{11} & r_{12} & r_{13} & -[\mathrm{R}_1][\mathrm{t}] \\ r_{21} & r_{22} & r_{23} & -[\mathrm{R}_2][\mathrm{t}] \\ r_{31} & r_{32} & r_{33} & -[\mathrm{R}_3][\mathrm{t}] \end{bmatrix} \begin{bmatrix} x \\ y \\ z \\ 1 \end{bmatrix}. \qquad \textit{Eq. A-4}$$

The matrix $[\mathrm{M_{ext}}]$ contains the *extrinsic parameters* of the camera.

In digital images, the coordinates are expressed in pixels, starting from the top-left corner. The coordinate system of the digital image plane π''' is $E''' = \{O''', \mathbf{e}'''_x, \mathbf{e}'''_y\}$ and the projection of the point P on π''' is P''' at a position $\mathbf{p}'''$ from O'''. $\mathbf{p}'''$ has coordinates $[\mathbf{p}'''] \equiv [x''', y''']$ in E'''. Let us indicate the linear pixel dimensions with d_x and d_y (px) and the position of the focal centre with the vector $\mathbf{o}$. Let us define $[\mathbf{p}'''_{\mathbf{h}}] \equiv [x''', y''', 1]$. Then

$$[\mathbf{p}_\mathbf{h}'''] \equiv \begin{bmatrix} x''' \\ y''' \\ 1 \end{bmatrix} = [\mathrm{D}][\mathbf{p}_\mathbf{h}''] = \begin{bmatrix} \frac{1}{d_x} & 0 & \frac{o_x}{d_x} \\ 0 & \frac{1}{d_y} & \frac{o_y}{d_y} \\ 0 & 0 & 1 \end{bmatrix} \begin{bmatrix} x'' \\ y'' \\ 1 \end{bmatrix}. \qquad \textit{Eq. A-5}$$

The matrix $[\mathrm{M}_{\mathrm{int}}] = [\mathrm{D}][\mathrm{F}]$ contains the *intrinsic parameters* of the camera.

Combining all the relationships above, the following expression is obtained:

$$\lambda[\mathbf{p}_\mathbf{h}'''] = \lambda \begin{bmatrix} x''' \\ y''' \\ 1 \end{bmatrix} = [\mathrm{M}][\mathbf{p}_\mathbf{h}] = [\mathrm{D}][\mathrm{F}][\mathrm{M}_{\mathrm{ext}}] \begin{bmatrix} x \\ y \\ z \\ 1 \end{bmatrix}. \qquad \textit{Eq. A-6}$$

The matrix [M] is called the *projection matrix* of the camera and transforms the coordinates of a point in 3D world into the coordinates of its projection on the digital image plane. The elements of [M] are generally unknown, but they can be determined if some 2D-3D point correspondences are provided. This process is called *calibration*. The *inverse* of the projection matrix associates each point in the image to its sight line. With a stereoscopic image acquisition system, the full 3D reconstruction of the point becomes possible.

A.1.2. Image calibration

The projection matrix contains $3 \times 4 = 12$ elements. The degrees of freedom are 11, corresponding to $\{[R_1], [R_2], [R_3], t_1, t_2, t_3, f, d_x, d_y, o_x, o_y\}$. The elements m_{ij} can be determined by providing at least six correspondences between 2D image points and 3D points. The k-th correspondence can be written as

$$\begin{cases} x'''^{(k)} = \dfrac{m_{11}x^{(k)} + m_{12}y^{(k)} + m_{13}z^{(k)} + m_{14}}{m_{31}x^{(k)} + m_{32}y^{(k)} + m_{33}z^{(k)} + m_{34}} \\ y'''^{(k)} = \dfrac{m_{21}x^{(k)} + m_{22}y^{(k)} + m_{23}z^{(k)} + m_{24}}{m_{31}x^{(k)} + m_{32}y^{(k)} + m_{33}z^{(k)} + m_{34}} \end{cases}. \qquad \textit{Eq. A-7}$$

It is convenient to define the array of unknowns $[\mathrm{m}] \equiv [m_{11}, m_{12}, m_{13}, m_{21}, \dots, m_{34}]$. The set of all correspondences can be rearranged in matrix form as

$$[\mathrm{A}][\mathrm{m}] = 0, \qquad \textit{Eq. A-8}$$

with

$$[\mathrm{A}] = \begin{bmatrix} x^{(1)} & y^{(1)} & z^{(1)} & 1 & 0 & 0 & 0 & 0 & -x'''^{(1)}x^{(1)} & -x'''^{(1)}y^{(1)} & -x'''^{(1)}z^{(1)} & -x'''^{(1)} \\ 0 & 0 & 0 & 0 & x^{(1)} & y^{(1)} & z^{(1)} & 1 & -y'''^{(1)}x^{(1)} & -y'''^{(1)}y^{(1)} & -y'''^{(1)}z^{(1)} & -y'''^{(1)} \\ \vdots & \vdots & \vdots & \vdots & \vdots & \vdots & \vdots & \vdots & \vdots & \vdots & \vdots & \vdots \\ x^{(6)} & y^{(6)} & z^{(6)} & 1 & 0 & 0 & 0 & 0 & -x'''^{(6)}x^{(6)} & -x'''^{(6)}y^{(6)} & -x'''^{(6)}z^{(6)} & -x'''^{(6)} \\ 0 & 0 & 0 & 0 & x^{(6)} & y^{(6)} & z^{(6)} & 1 & -y'''^{(6)}x^{(6)} & -y'''^{(6)}y^{(6)} & -y'''^{(6)}z^{(6)} & -y'''^{(6)} \\ \vdots & \vdots & \vdots & \vdots & \vdots & \vdots & \vdots & \vdots & \vdots & \vdots & \vdots & \vdots \end{bmatrix}. \qquad \textit{Eq. A-9}$$

Ideally, $\mathrm{rank}[\mathrm{A}] = \mathrm{DoF}[\mathrm{m}] = 11$, but numerical and experimental errors cause $\mathrm{rank}[\mathrm{A}] = 12$. This means that a unique solution can be determined by providing six correspondences. However, it is better to use more than six correspondences, in order to calculate a least squares solution and reduce the effects of errors. The experiments described in this thesis have been calibrated based on 147 correspondences.

A.1.3. Method of the epipolar lines for 3D reconstruction and correspondence establishment

Given a point P that is projected on (at least) two separate image planes (***Figure A-2***), the reconstruction of its 3D coordinates requires the establishment of the stereoscopic correspondences between its projections. The segment $\overline{O'_A\, P'''_A}$ relative to camera A is seen by camera B as a line, called *epipolar line*. The points O'_A, O'_B and P define what is called the *epipolar plane*. Given the projection P'''_A, all possible stereoscopic matches lie on the epipolar plane and are projected on the epipolar line on π'''_B. In the PTV experiments described in this thesis, the tracking algorithm developed by Willneff (2003) was used. This combines the establishment of stereoscopic and temporal correspondences for two-view PTV systems. Given

a tracer image in view A, a list of all candidates within a tolerance distance from the epipolar line in view B is defined, and vice versa. The tolerance is set based on the typical experimental error. For each candidate, its 3D position is reconstructed through triangulation, and temporal tracking at the next frames is attempted until no more temporal candidates are found. Generally, most stereoscopic candidates are discarded immediately, because their current 3D position is not compatible with the previous ones. However, a number of stereoscopic candidates may be tracked for several time steps. In that case, the trajectory with the smallest average change in Lagrangian acceleration is taken. Since 3D reconstruction is performed for each stereoscopic candidate and each temporal candidate at each time step, the number of possibilities increases exponentially with the tracer concentration. PTV setups with three or four views eliminate most stereoscopic ambiguities because the candidates must be at the intersection of three or four epipolar lines.

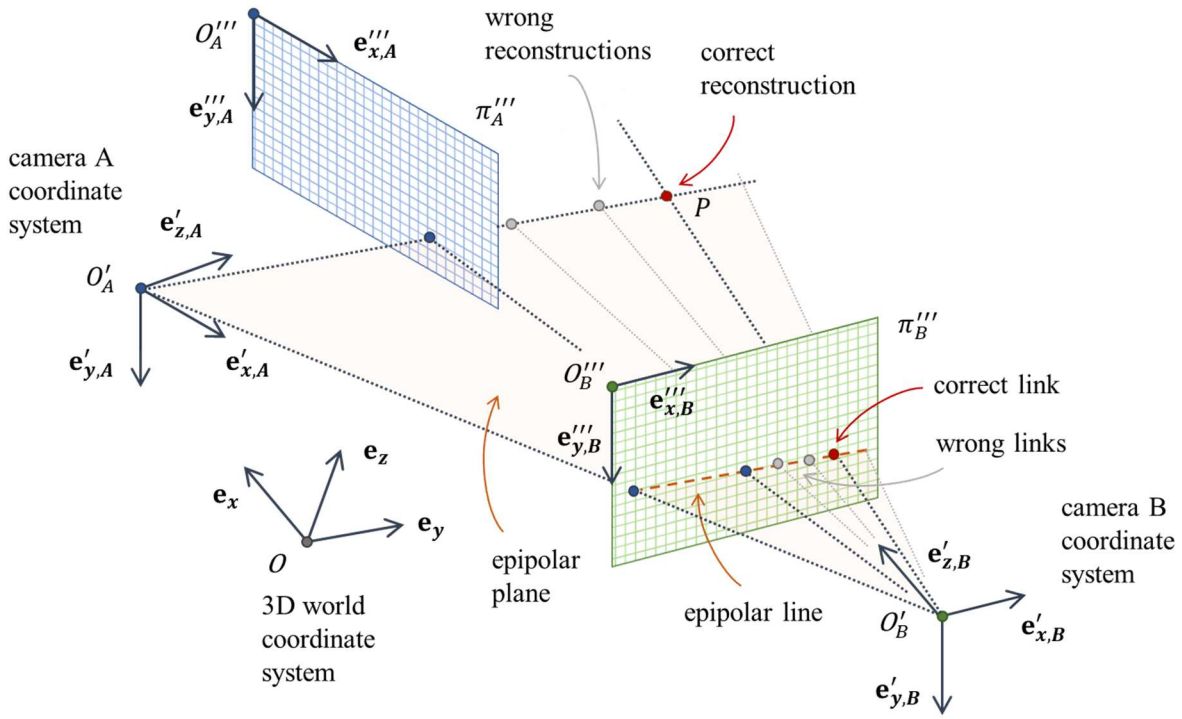

***Figure A-2**: Principles of epipolar geometry and stereoscopic ambiguities in a two-camera image acquisition system.*

A.1.4. Error and uncertainty in 3D reconstruction

Real data inevitably contain experimental errors. Understanding how these affect the measurements is extremely important. The main output of a 3D-PTV experiment consists of three velocity components, resolved in time. The input, that is the physical quantity that is measured, is the luminance of each pixel of the camera sensor. The data flow that transforms the input into the output involves many processing steps. Experimental errors are amplified throughout this process.

During image acquisition, vibrations and inconstant illumination are two inevitable sources of random error. Even small perturbations in the setup geometry and a low level of randomness in the pixel grey levels can appreciably affect the determination of the particle centroids. This error propagates through the stereo-matching process and is amplified with the velocity calculation. It is impossible to measure all the errors involved. However, the level of uncertainty in the centroids is measurable through controlled experiments. It can be assumed that the error in the centroids explains all the random error sources upstream (***Figure A-3***).

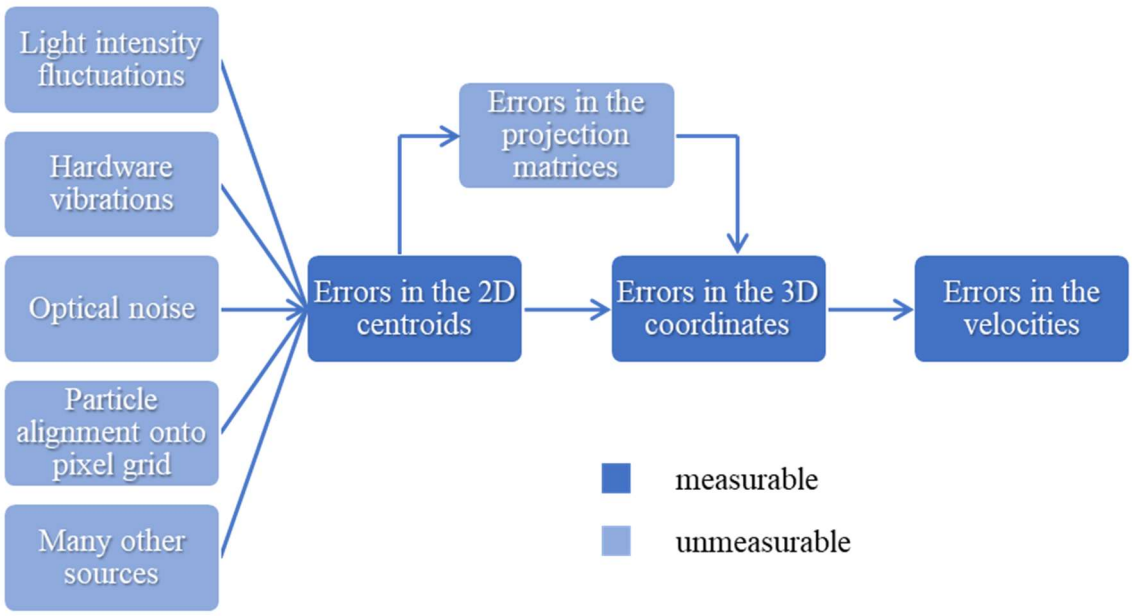

Figure A-3*: A simplified model for error propagation in PTV.*

3D-PTV measurements are also affected by systematic errors. Image sensors usually have non-linear sensitivity. Lenses have a limited depth of field and cause distortion in the images (straight lines become curves). If the focus of the images is carried out manually, its quality depends on the operator sensibility. The presence of multi-media interfaces causes diffraction effects. Image calibration accounts for these effects only partially. Finally, the calibration itself is based on a least square method using a finite set of real observations.

Consider a two-view setup in the 2D x- z space, as in ***Figure A-4***. The two cameras are at a distance X from each other along the x direction and at a distance Z from the 3D scene along z. A point P in the scene is projected on both the image planes. If the 3D scene is relatively small, the angle of view, $\alpha(P)$, changes only slightly in function of P and is almost equal to the angle between the two focal axes of the cameras. Therefore, it can be assumed that α is a geometric property of the setup, and $Z/X \approx 1/2\cot(\alpha/2)$ for any P.

Assume that the left camera (A) is perfectly accurate, while the right camera (B) has finite accuracy along x''. Also, assume that the two cameras are perfectly calibrated. If the projection on the second camera is affected by a small error $\delta x''$, there will be an error δx along x at the true depth of the 3D point. The error along the depth will be δz. The error along x at the biased depth will be $\delta x°$. Since $Z \gg \delta z$, then $\delta x° \approx \delta x$. Geometrical considerations lead to the following relationships:

$$\delta x \approx d_x \left(\frac{Z}{f_A}\right) \delta x''; \qquad \textit{Eq. A-10}$$

$$\delta x \approx \left(\frac{X}{Z}\right) \delta z; \qquad \textit{Eq. A-11}$$

The experimental error on x is proportional to the error in the centroid $(\delta x'')$ and to the ratio between the depth of the scene and the focal length (Z/f_A). By combining the two expressions,

$$\delta z \approx d_x \left(\frac{Z}{X}\right)\left(\frac{Z}{f_A}\right)\delta x''. \qquad \textit{Eq. A-12}$$

The error on z is proportional to the error in the centroid, $\delta x''$, the ratio between the distance of the scene and the focal length, Z/f_A, and the ratio of the distance of the scene over the distance between the cameras Z/X. In practical applications, while a large angle of view is desirable for better depth accuracy, a small angle of view may be needed to reduce blind spots caused by view occlusion. In that case, a suitable compromise should be sought. In the PTV experiments described in this thesis, the maximum angle allowed by the hardware was used. That was $\alpha \approx 16$ deg, with $Z/X \approx 3.6$.

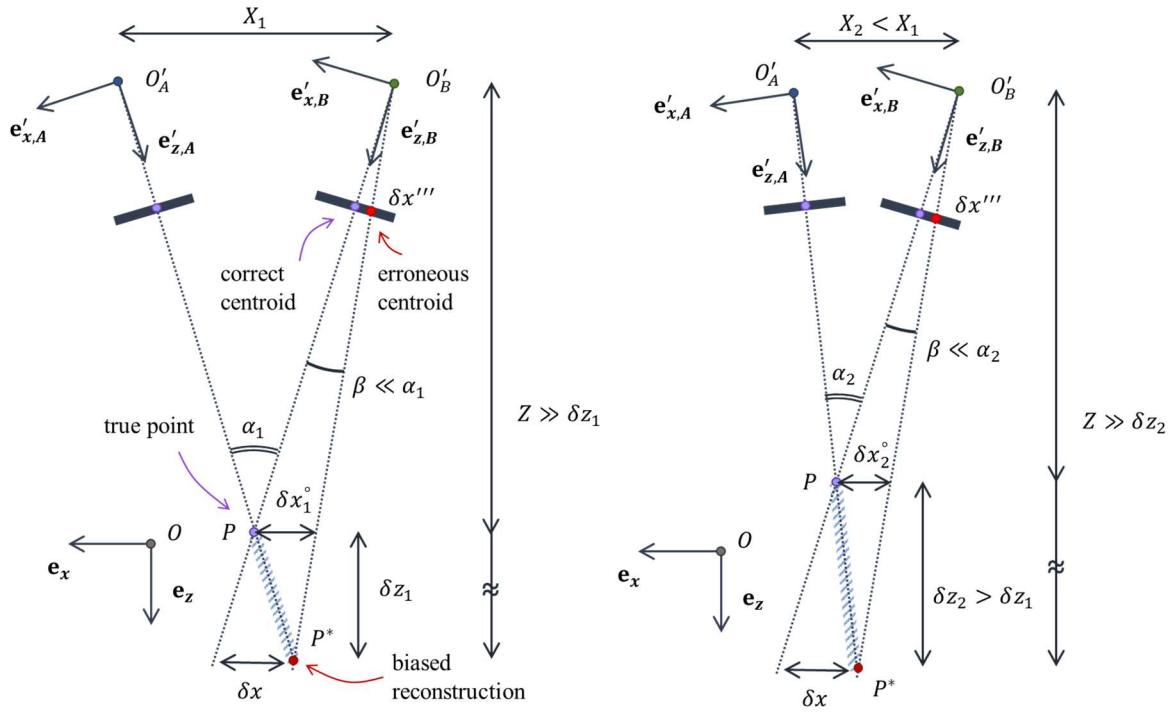

Figure A-4*: Errors in the 3D reconstruction of a point as a result of the errors in its projection on one image. Left: large angle of view. Right: small angle of view.*

A real 3D case is significantly more complex (***Figure A-5***), since (a) both the cameras have a finite accuracy on both x'' and y''; (b) both the cameras are not perfectly calibrated, so the sight lines are biased; (c) lines in 3D space are generally skew.

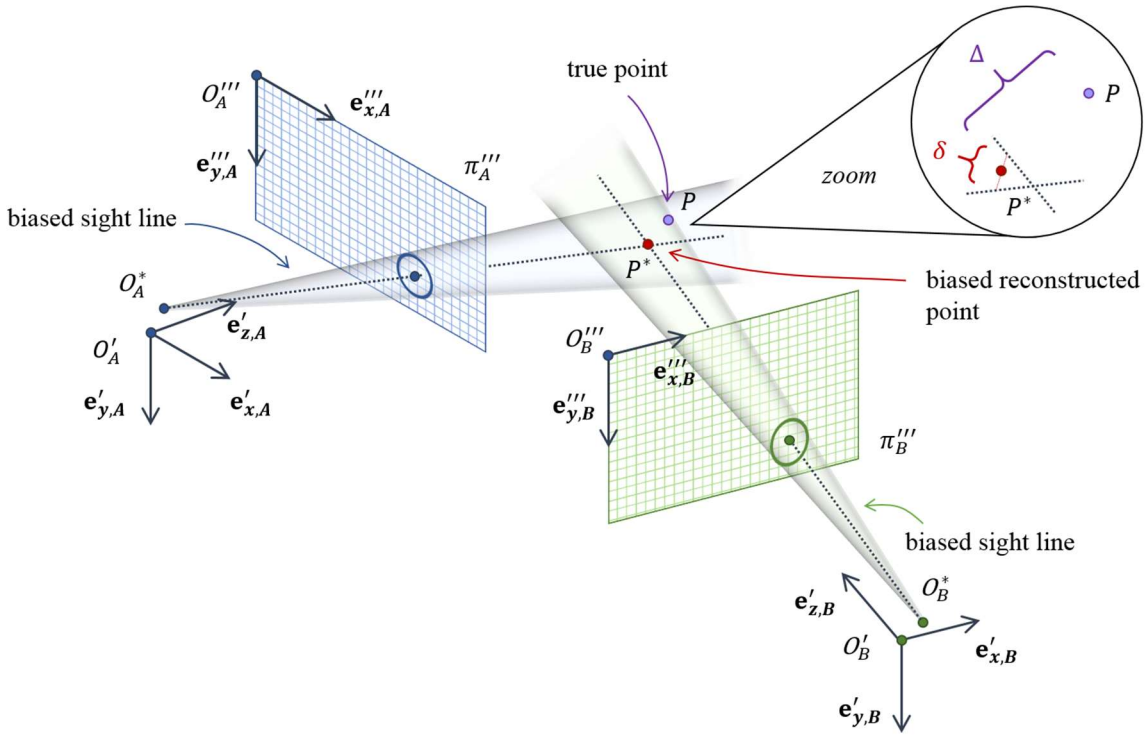

***Figure A-5**: 3D reconstruction with real data.*

Since the sight lines of real data do not cross, the point in the 3D space is placed at the midpoint of the distance between the two lines. This distance is indicated with δ. The distance between the reconstructed 3D point and the true point is indicated as Δ. Typically, the reconstruction errors along the depth are much larger than the errors along the other two dimensions of space.

An effective way to reduce the uncertainty in the 3D position of the reconstructed point is to create a measurement redundancy by using more than two imaging views. This has also another significant advantage. A particle can only be located in the 3D space if it is detected in at least two synchronous views. In real experiments, particles may be obscured by other particles or setup elements (e.g. by the impeller, in agitated vessels), and light reflections can produce bright areas in the images, where particles are not detectable. In these cases, the particles affected are lost at the stereo-matching step. If more cameras are used, the chances for a particle being visible in at least two views are higher and the stereo-matching efficiency increases

significantly. Most of 3D-PTV setups used in the literature use three or four cameras. However, multi-camera facilities have high installations costs.

A.1.5. Error in the 2D centroid coordinates with JM's PTV rig

The precision of JM's PTV rig in the determination of the 2D centroids has been assessed by taking 15 pictures of the calibration target, conducting the image processing and comparing the centroid coordinates of 8 points distributed in space (***Figure A-6***).

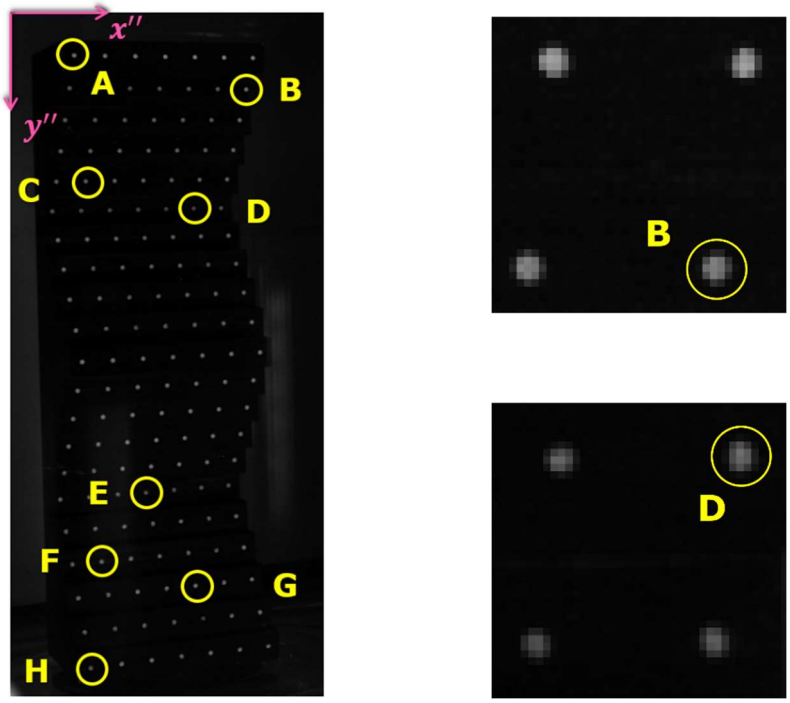

Figure A-6*. Left: one of the images of the calibration target to assess the variability in the determination of the centroids. Used dots within the yellow circles. Right: zoom around point B (top) and point D (bottom).*

The calibration target was placed within a 4.6 L cylindrical vessel filled with water, which in turn was inside a larger square vessel filled with the same liquid. This was to mimic real experiment conditions, as the presence of multiple media through the optic path has a significant impact on the centroid precision (Maas et al., 1993). The overall brightness of the images and the field of view (hence the pixel size) were also adjusted similarly to mixing

experiments. Since the calibration dots and the tracers used in PTV experiments have different physical size, it was impossible to obtain the same blur dimension while maintaining the same field of view. In real experiments, tracers appear slightly smaller (3-4 px) than the target dots here (4-5 px). However, this analysis remains representative, because the precision of the pixel interpolation scheme becomes independent of the blur size if this is 2 px or more (Nobach et al., 2005). The calibration target, the camera and the mirrors were kept in the same position while capturing the pictures, in order to obtain ideally identical images. Any variability in the centroid coordinates would be completely random. On average, the standard deviation was almost identical between the two image coordinates, 0.0141 px for x''' and 0.0144 px for y''' (***Table A-1***). A rough estimate of the pixel size is given by

$$d_{px} \approx \frac{0.18\ \mathrm{m}}{512\ \mathrm{px}} \approx 350\ \mu\mathrm{m\ px^{-1}}. \qquad \textit{Eq. A-13}$$

Therefore, $\langle \sigma_x''' \rangle \approx \langle \sigma_y''' \rangle \approx 5$ µm, meaning that ~95% of the measurements would lie within ± 10 µm from the true value. By generalising *Eq. A-9*, $\langle \sigma_z''' \rangle \approx 2\,(Z/X)(Z/f)\,\sqrt{2}\langle \sigma_x''' \rangle = 51$ µm, which is very close to the $\langle \Delta_z \rangle = 49$ µm measured in **§III.2.3**.

Table A-1*: 3D coordinates, average pixel level and standard deviation of the centroid coordinated of eight calibration dots, as measured with JM's PTV rig.*

Dot	x (mm)	y (mm)	z (mm)	$\langle I \rangle$ ($\pm\sigma_I$)	σ_x''' (px)	σ_y''' (px)
A	−30	+100	+27.5	103.00 (±2.07)	0.0081	0.0107
B	+30	+90	+16.5	108.53 (±2.80)	0.0143	0.0163
C	−20	+60	−16.5	93.33 (±1.45)	0.0085	0.0106
D	+20	+50	−27.5	69.80 (±1.26)	0.0288	0.0276
E	0	−50	−27.5	73.87 (±1.25)	0.0248	0.0092

F	−20	−70	−5.5	93.67 (±1.59)	0.0131	0.0208
G	+10	−80	+5.5	105.07 (±2.15)	0.0060	0.0087
H	−30	−100	+27.5	87.73 (±2.34)	0.0095	0.0111
				Average ($\pm\sigma$):	0.0141 ($\pm$0.0083)	0.0144 ($\pm$0.0067)

Figure A-7 shows a negative correlation between σ_x''' and σ_y''' with the depth in the 3D space, z. There was also a negative correlation with the average grey level of the pixel containing the centroid, $\langle I \rangle$ (***Figure A-8***). This means that that the precision in the image coordinates is worse for dots more distant from the camera and for darker dots. The correlation coefficients are reported in ***Table A-2***. The vertical image coordinate was less sensitive to both the depth and the pixel brightness, but this was probably due to the outlier behaviour of point E. The contrast of the bright dots with respect to the surrounding background may seem more relevant than the absolute brightness, therefore the effect of the difference in grey level between the pixel containing the centroid and a pixel nearby (at 5 px distance along both x''' and y'''), $\langle \Delta I \rangle$, have been also assessed. The results were almost identical to those for $\langle I \rangle$.

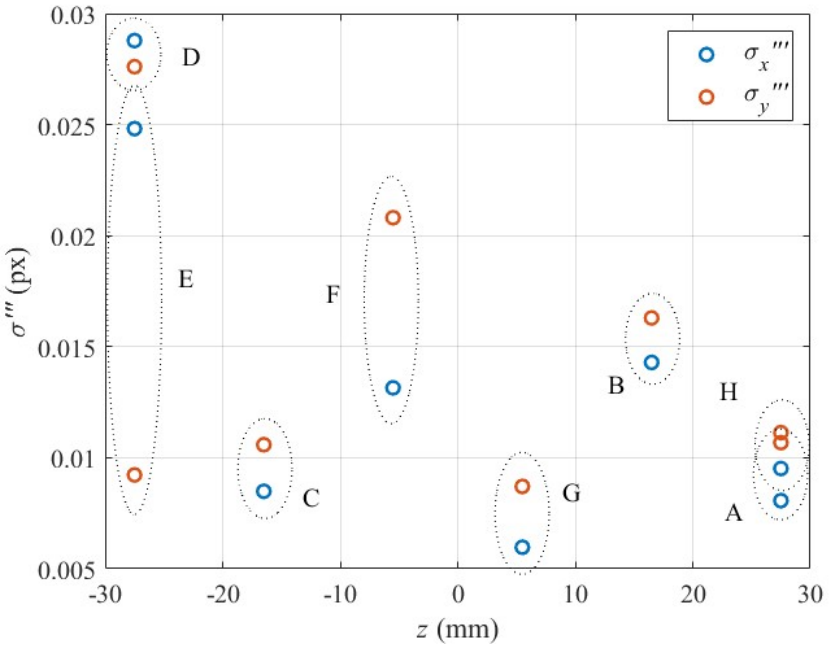

***Figure A-7**: Scatter plot of the standard deviation of the centroid coordinates against the depth in 3D space.*

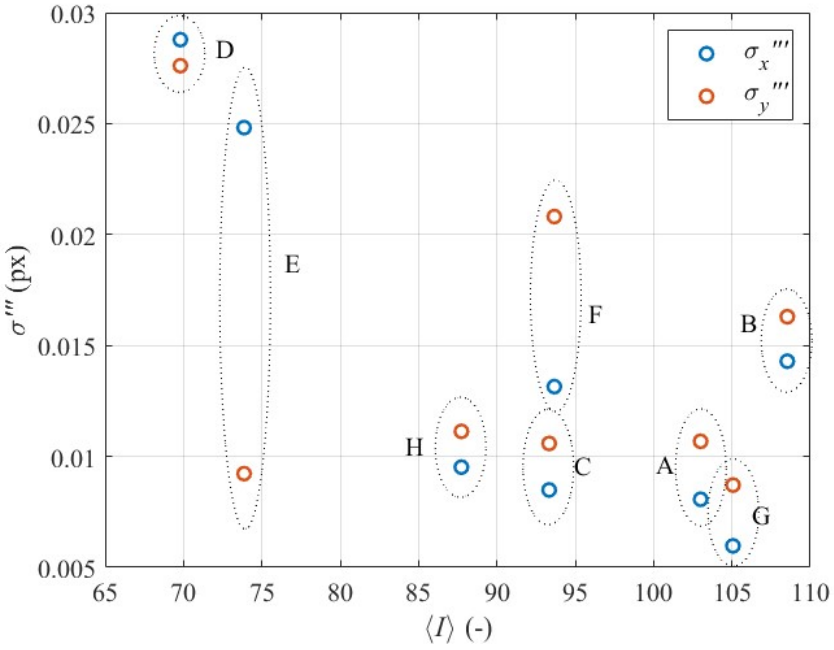

***Figure A-8**: Scatter plot of the standard deviation of the centroid coordinates against the average level of the pixel containing the centroid.*

***Table A-2**: Correlation coefficients between the relevant quantities involved in the centroid determination.*

PCC	z	$\langle I \rangle$	$\langle \Delta I \rangle$
σ_x'''	-0.7031	-0.8204	-0.8312
σ_y'''(without point E)	-0.3591 (-0.615)	-0.3944 (-0.678)	-0.4149 (-0.736)

In the 300 mm tank used in **chapter VI**, $d_{px} \approx 590$ μm px^{-1}. The errors in the centroids and in the reconstructed 3D points were about 4 times larger than in the 180 mm vessel.

A.2. Reliability of the PTV measurements

A.2.1. Tracer occupancy

In the experimental chapters, azimuthally averaged data have been obtained by binning the individual observations on a Eulerian grid of 30×60 voxels in the r-y plane. The tracer occupancy, i.e. the number of data within each voxel, has been calculated to verify that the statistics of the quantities under study have been determined based on a sufficiently large number of events. In ***Figure A-9*** and ***Figure A-10***, the occupancy is represented in terms of tracking efficiency, Φ, according to

$$\Phi_{i,j} = \frac{1}{5{,}400} \frac{m_{i,j} \,/\, V_{i,j}}{n_p \,/\, V}. \qquad \textit{Eq. A-14}$$

Here, 5,400 is the number of frames of each experiment, $m_{i,j}$ is the number of data within the voxel identified by the indices i and j, $V_{i,j}$ is the voxel volume and $n_p \,/\, V$ is the volumetric tracer concentration (m^{-3}). This normalisation was necessary to account for the increase in the

voxel volume along the radial coordinate. Ideally, a uniform tracking efficiency close to unity is desirable. Unfortunately, not all the tracers present in the vessel could be tracked in every time step. In particular, Φ was lower close to the impeller, due to the light attenuation through the liquid medium and the higher velocities.

Figure A-9 shows that, with the same fluid, the tracking efficiency maps in the different PTV experiments (at different impeller speed) were qualitatively similar. Given the large number of PTV experiments undertaken, only one tracking efficiency map per fluid is shown in ***Figure A-10***.

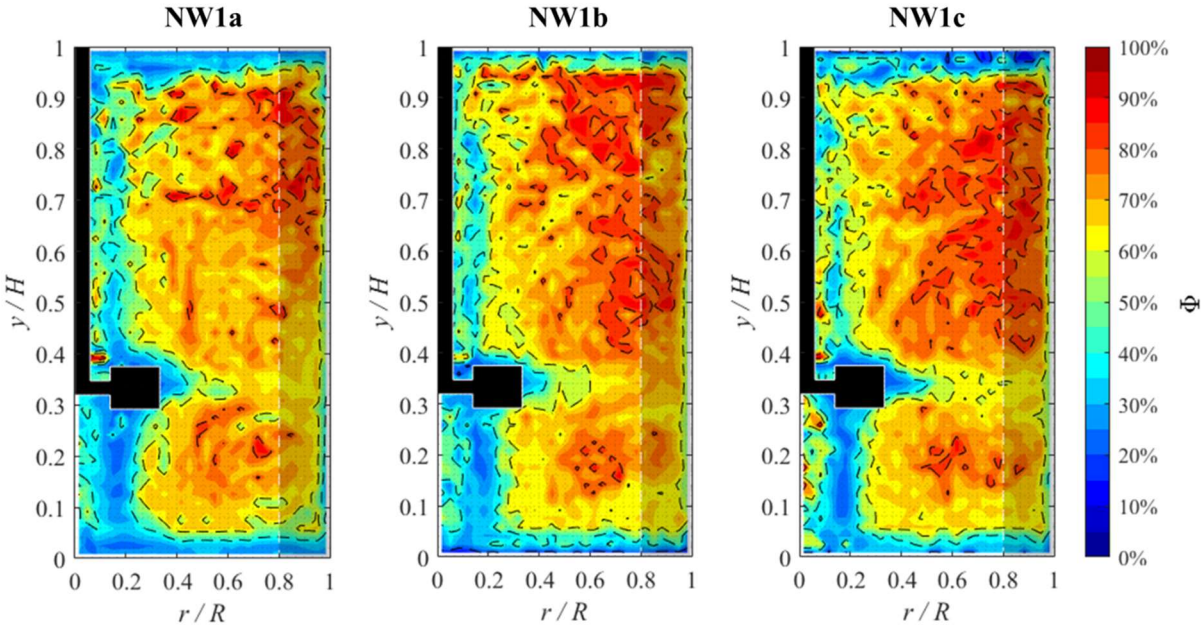

Figure A-9: *Tracking efficiency maps for the 75% glycerol solution at different impeller speeds.*

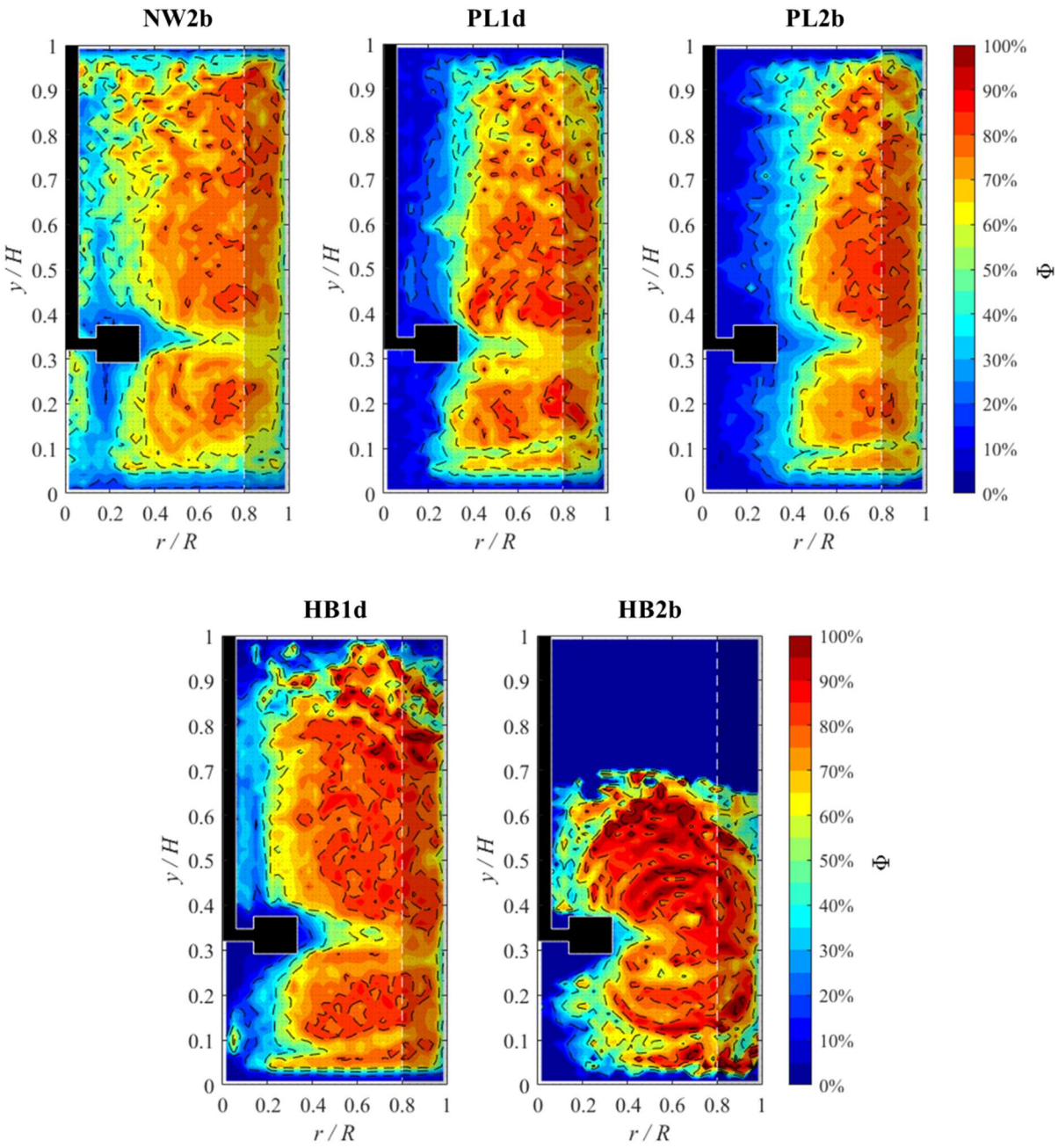

Figure A-10: *Some tracking efficiency maps for the remaining fluids.*

A.2.2. Statistical convergence of the velocity measurements

As mentioned in **§IV.2.3.3**, the statistical convergence of the PTV velocity measurements has been demonstrated in three sample volumes, which are illustrated in **Figure A-11**. The sample volumes were semi-annular voxels and corresponded to 0.1% of the measurement volume (half vessel). The first was placed in the impeller discharge region at $r = T/4 \pm 2$ mm, $y = C \pm 2$

mm. The second was close to the wall, at $r = (T - B)/2 \pm 1.5$ mm, $y = H/2 \pm 1.5$ mm. The third was in the bulk of the flow, at $r = T/3 \pm 1.75$ mm, $y = 2H/3 \pm 1.75$ mm. With the Herschel-Bulkley fluids, the bulk sample volume was positioned at $y = 3H/5 \pm 1.75$ mm to make sure it was within the cavern boundary.

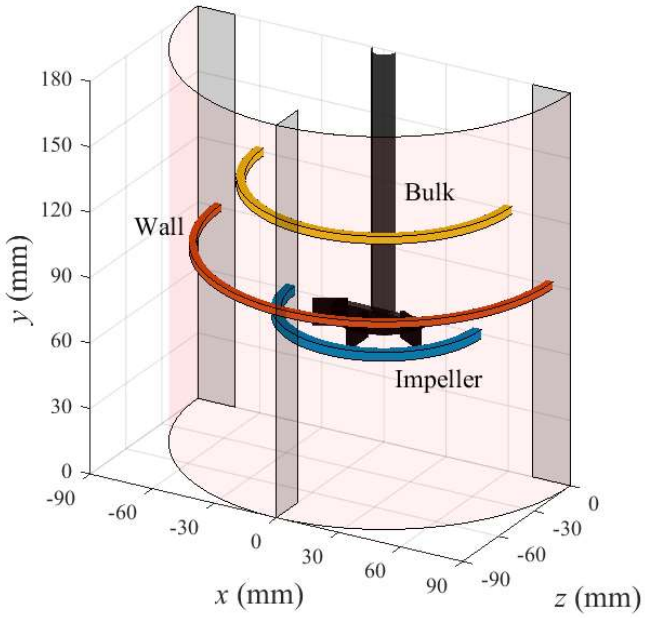

***Figure A-11**: Position of the sample volumes in the vessel for the velocity convergence analysis.*

The average velocity was calculated as

$$\langle U \rangle_m = \frac{1}{m} \sum_{i=1}^{m} U_i. \qquad \textit{Eq. A-15}$$

and the standard deviation as

$$\sigma_m = \sqrt{\frac{1}{m-1} \sum_{i=1}^{m} (U_i - \langle U \rangle_m)^2}\,. \qquad \textit{Eq. A-16}$$

Here i indicates the individual observation and m is the number of events.

Some plots of $\langle U \rangle_m$ and σ_m against m are given in ***Figure A-12***. Again, only one convergence plot per fluid is shown. Condensed data are summarised in ***Table A-3***. It can be seen that approximately $\sim 10^2$ observations are enough to guarantee the statistical convergence of the velocity.

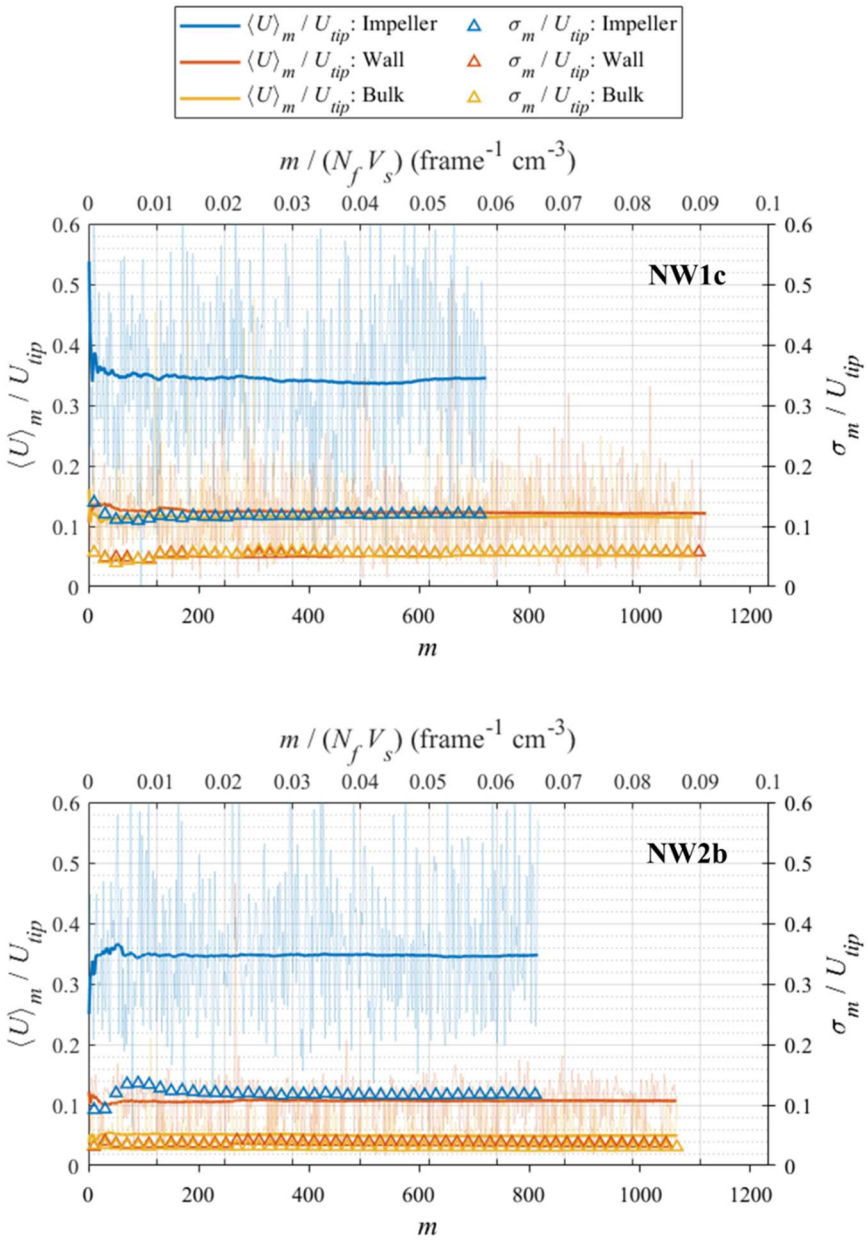

Figure A-12*: Convergence plots of the ensemble average and standard deviation of the velocity in three sample volumes against the number of events. (Continues in the next pages).*

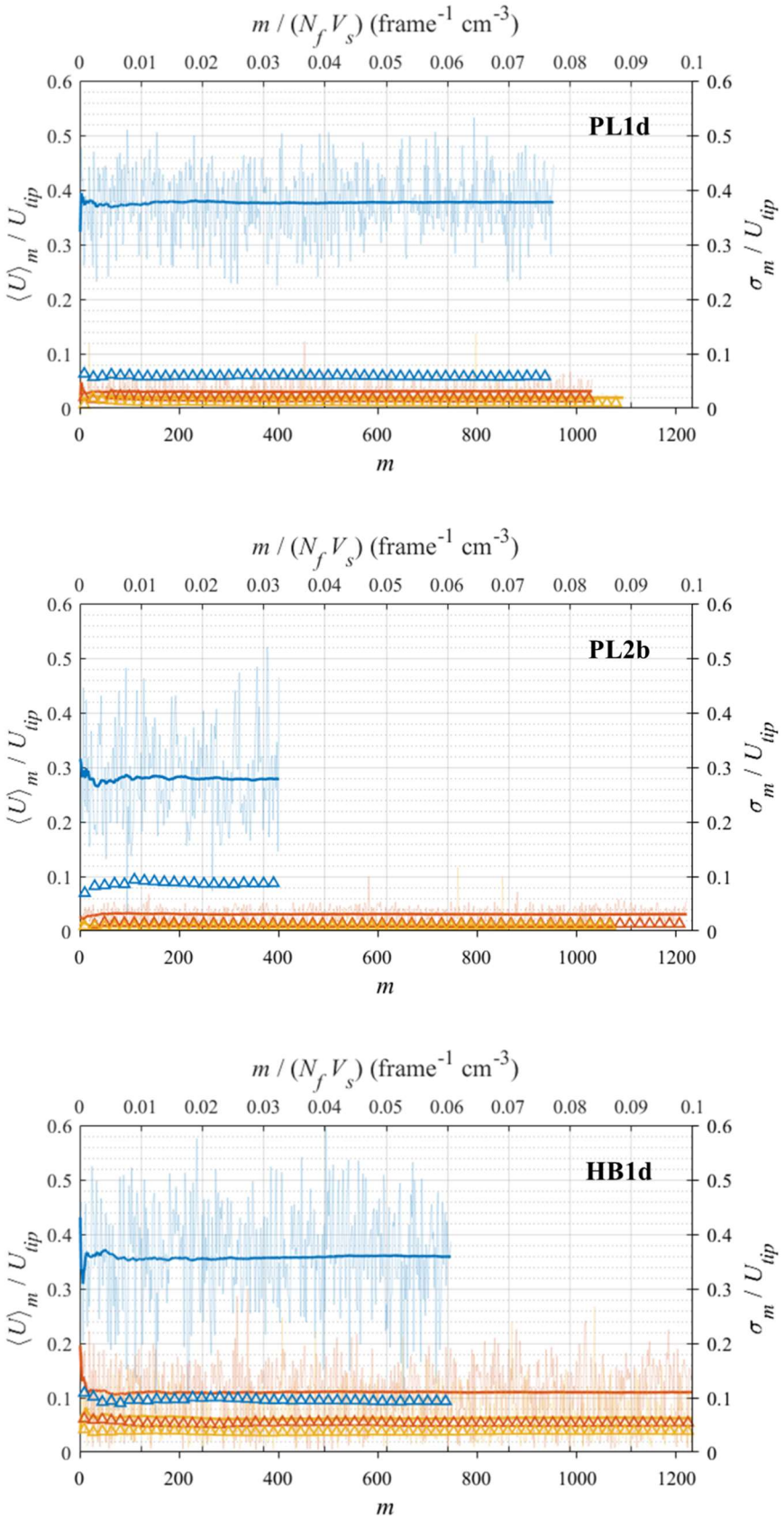

***Figure A-12** (continues).*

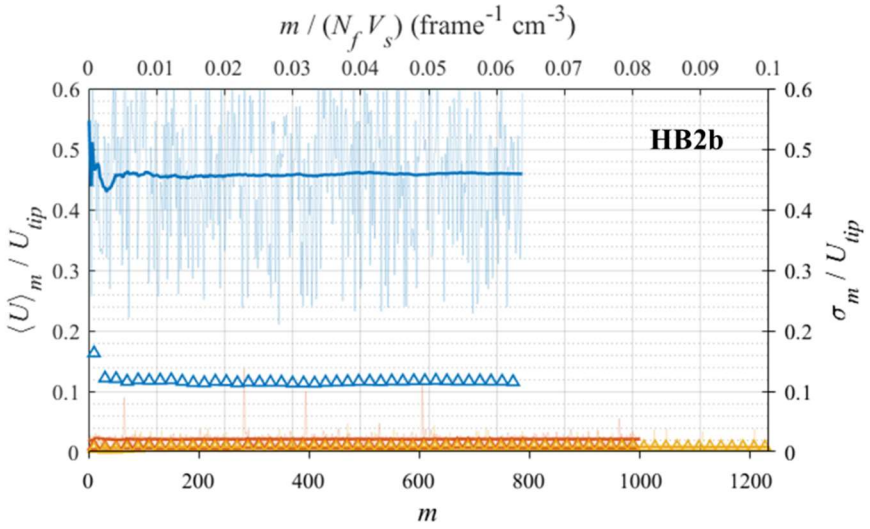

Figure A-12 *(continues).*

Table A-3*: Condensed data from the convergence plots of the PTV velocity measurements.*

Exp	Impeller sample volume			Bulk sample volume			Wall sample volume		
	m	$\frac{\langle U \rangle_m}{U_{tip}}$	$\frac{\sigma_m}{U_{tip}}$	m	$\frac{\langle U \rangle_m}{U_{tip}}$	$\frac{\sigma_m}{U_{tip}}$	m	$\frac{\langle U \rangle_m}{U_{tip}}$	$\frac{\sigma_m}{U_{tip}}$
NW1a	872	0.37	0.15	1,097	0.11	0.05	1,210	0.09	0.05
NW1b	858	0.40	0.11	1,266	0.12	0.06	1,252	0.12	0.05
NW1c	717	0.34	0.12	1,097	0.12	0.05	1,125	0.12	0.06
NW2a	858	0.38	0.07	1,195	0.04	0.02	914	0.08	0.03
NW2b	816	0.35	0.12	1,069	0.05	0.03	1,069	0.10	0.04
PL1a	802	0.32	0.04	1,083	0.03	0.02	1,224	0.02	0.02
PL1b	900	0.35	0.06	1,041	0.03	0.02	1,097	0.04	0.02
PL1c	942	0.38	0.06	1,055	0.02	0.01	1,041	0.03	0.02
PL1d	774	0.40	0.07	886	0.06	0.02	1,013	0.08	0.03
PL2a	422	0.29	0.08	1,111	0.01	0.01	1,167	0.01	0.01
PL2b	408	0.28	0.09	1,083	0.02	0.01	1,224	0.04	0.01
HB1a	605	0.30	0.09	1,097	0.01	0.01	1,266	0.02	0.02

HB1b	577	0.32	0.12	1,139	0.02	0.02	1,055	0.04	0.02
HB1c	506	0.34	0.13	1,139	0.02	0.03	1,125	0.04	0.04
HB1d	731	0.36	0.09	1,238	0.06	0.04	1,224	0.11	0.05
HB2a	450	0.37	0.07	1,224	<0.01	<0.01	1,153	<0.01	0.02
HB2b	788	0.46	0.12	1,688	0.01	0.01	999	0.02	0.01

A.3. About the bias in PTV velocity binning on a Eulerian grid

Two methods for binning the PTV velocity data on a Eulerian grid have been compared. The first one consists of a simple ensemble average over all m velocity events, thus

$$\langle U \rangle_{i,j} = \frac{1}{m} \sum_{l=1}^{m} U_{i,j,l}. \qquad \textit{Eq. A-17}$$

Indices i and j identify the voxel position in the r-y space, while l indicates the velocity observation. This method is biased in favour of lower values of velocity for two reasons:

i. Detectability and traceability of the flow tracers are negatively correlated with their velocity, hence low velocity values are measured more easily than high ones. It is possible to show that a negative correlation exists between the trajectory length and the average velocity along that trajectory. For instance, data from experiment NW1c are scattered in ***Figure A-13***. This dataset consists of 15,645 trajectories. The higher density of observations in the low-velocity region reflects the velocity distribution in the vessel. Clearly, long trajectories were only reconstructed if the velocity was sufficiently low. The PCC between the trajectory length and the average velocity was -0.225, which indicates a moderate correlation, given the large size of the dataset. In addition, trajectory terminations tended to occur when the instantaneous

velocity was higher than the average velocity. The condition $U_{end} > \langle U \rangle$ was true in 71% of the cases.

ii. The residence time of a particle in a given voxel is inversely proportional to its velocity. Consequently, low-velocity particles are observed many times in the voxel, while high-velocity particles are seen comparatively few times. Therefore, low values of velocity will have a larger weight in the arithmetic mean.

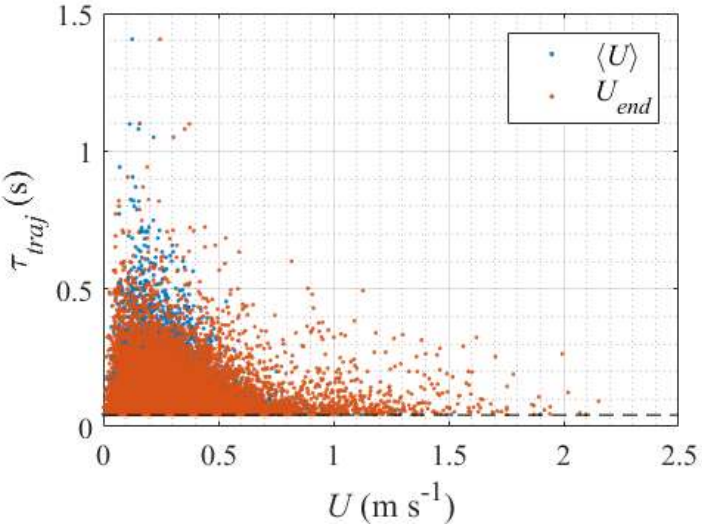

***Figure A-13**: Scatter of the trajectory duration against the average and terminating velocity (data from experiment NW1c).*

A second method, which mitigates the effects of point ii, has been proposed. In each voxel, the velocity events were grouped in individual trajectories and a first mean was calculated for each trajectory (*Eq. A-18*). Then, the final value was determined by averaging over all the trajectories entering that voxel (*Eq. A-19*). By doing so, the velocity events were weighted based on the trajectory residence time in the voxel. In the equations below, k identifies a specific trajectory. The number $m_k(i,j,k)$ is the number of events for a given trajectory in that voxel, while $n_t(i,j)$ is the number of trajectories entering the voxel (both m_k and n_t are random integers).

$$\langle U \rangle_{i,j,k} = \frac{1}{m_k} \sum_{l=1}^{m_k} U_{i,j,k,l}. \qquad \textit{Eq. A-18}$$

$$\langle U \rangle_{i,j} = \frac{1}{n_t} \sum_{k=1}^{n_t} \langle U \rangle_{i,j,k}. \qquad \textit{Eq. A-19}$$

In the following, the "weighted average" method is compared to the "ensemble average" method for the case of experiments NW1c (glycerol 75% at $Re = 1{,}257$) and PL1a (CMC 0.5% at $Re = 73$). These are the experiments that have been conducted at the highest and lowest Reynolds numbers, respectively. The velocity data have been binned on a 30×60 grid (1,800 voxels).

Figure A-14 shows the velocity maps obtained with the two algorithms in the case of NW1c. In most of the vessel, the ensemble average underestimated the velocity magnitude for less than 10%, compared to the weighted average (***Figure A-15b***). The largest relative differences were found in the upper part of the vessel, where the velocity magnitude was small. The absolute differences were actually significant only in the impeller jet (up to ~0.18 m s^{-1}, that equals ~25% of the velocity magnitude and ~7% of the tip speed) and in the two recirculation loops, close to the tank wall (***Figure A-15a***). The velocity profiles at specific radial coordinates in the vessel are illustrated in ***Figure A-16***. The differences in terms of velocity components were within a few percent.

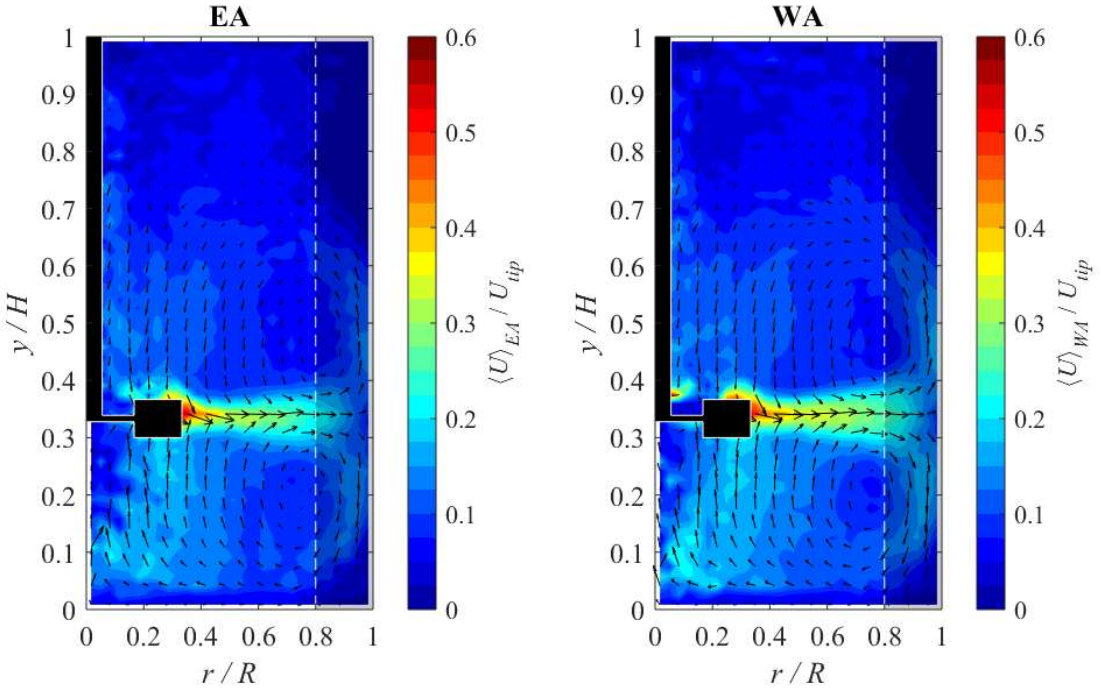

***Figure A-14**: Velocity fields as obtained with the ensemble average (EA) and the weighted average (WA) methods. Data from experiment NW1c.*

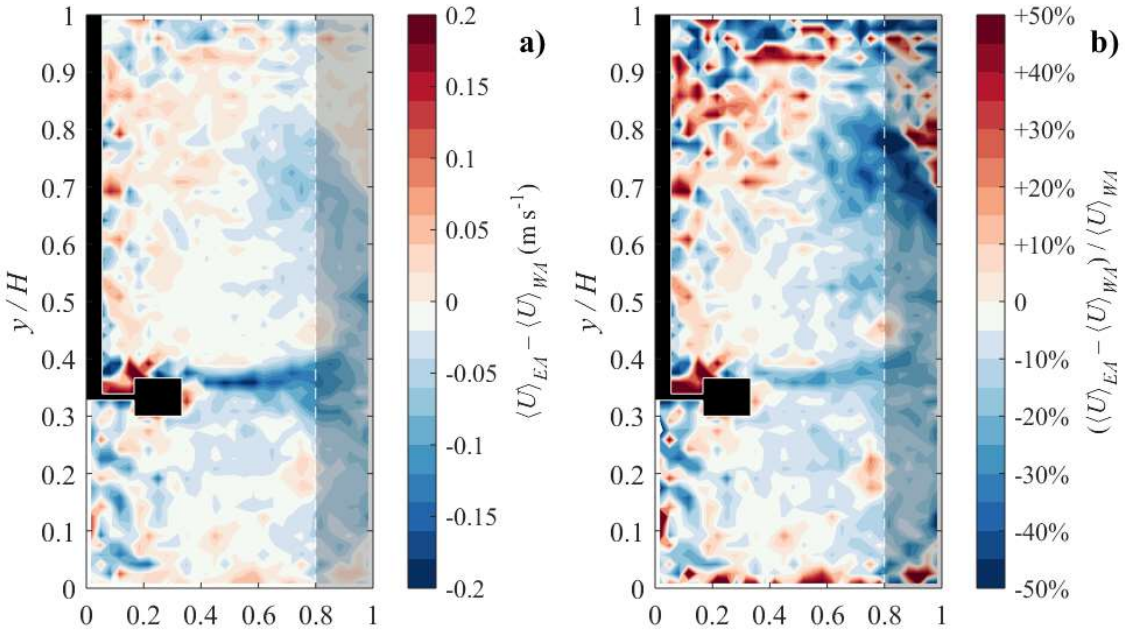

***Figure A-15**: Absolute (a) and relative (b) difference in the velocity, as calculated with the ensemble average (EA) and the weighted average (WA) methods. Data from experiment NW1c.*

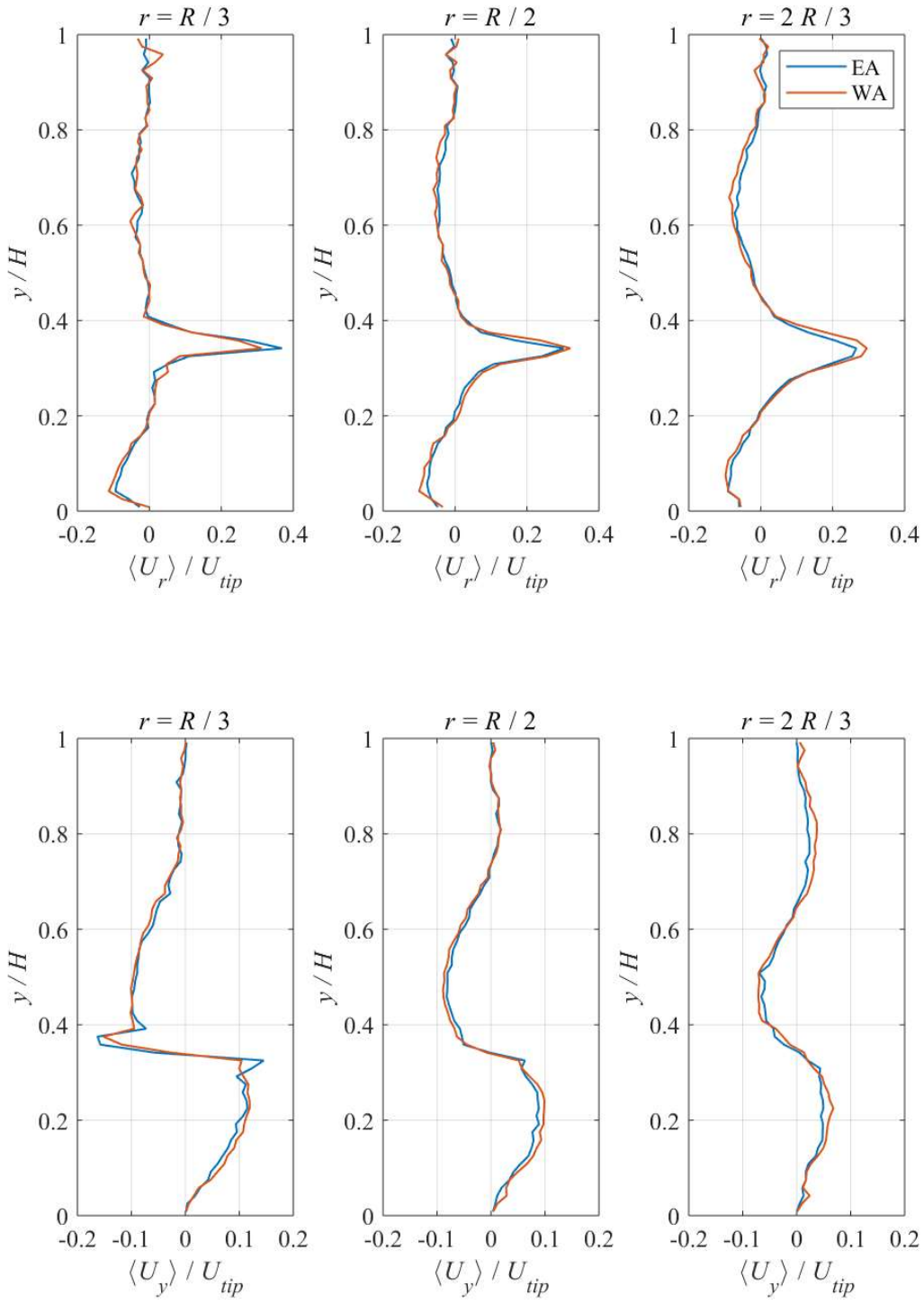

***Figure A-16**: Azimuthally averaged profiles of the velocity components, as obtained with the ensemble average (EA) and weighted average methods (WA). Data from experiment NW1c.*
(Continues in the next page).

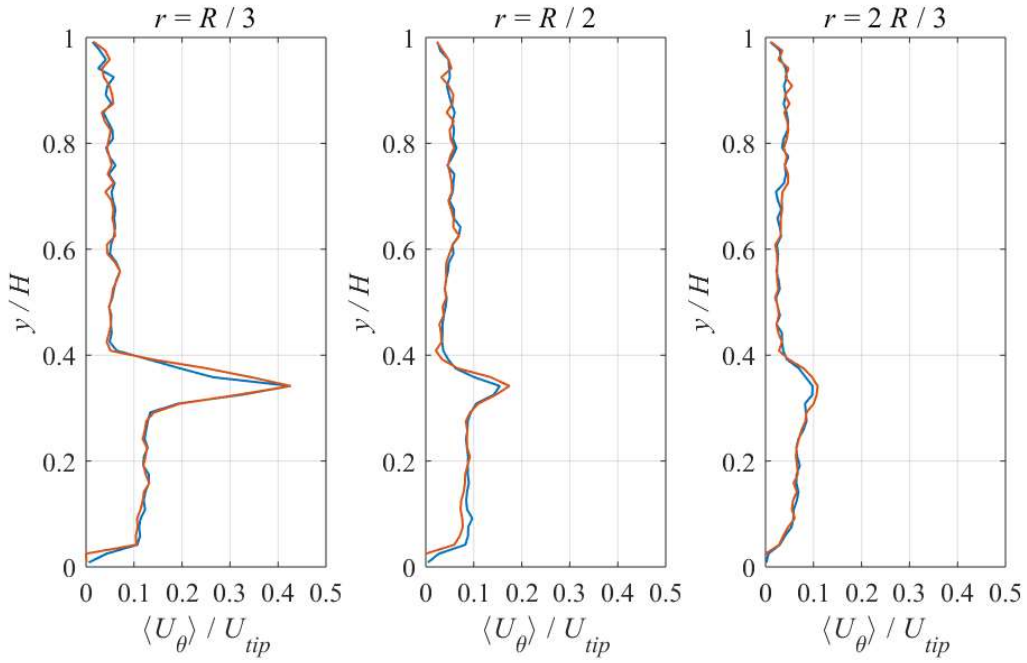

Figure A-16 *(continues).*

In the case of PL1a, which is representative of low Reynolds numbers and low absolute velocities, the absolute differences between the two methods were negligible everywhere in the tank (***Figure A-17***). The relative differences look large only because the velocity magnitude is nearly zero. Other experiments showed intermediate bias effects between experiments NW1c and PL1a.

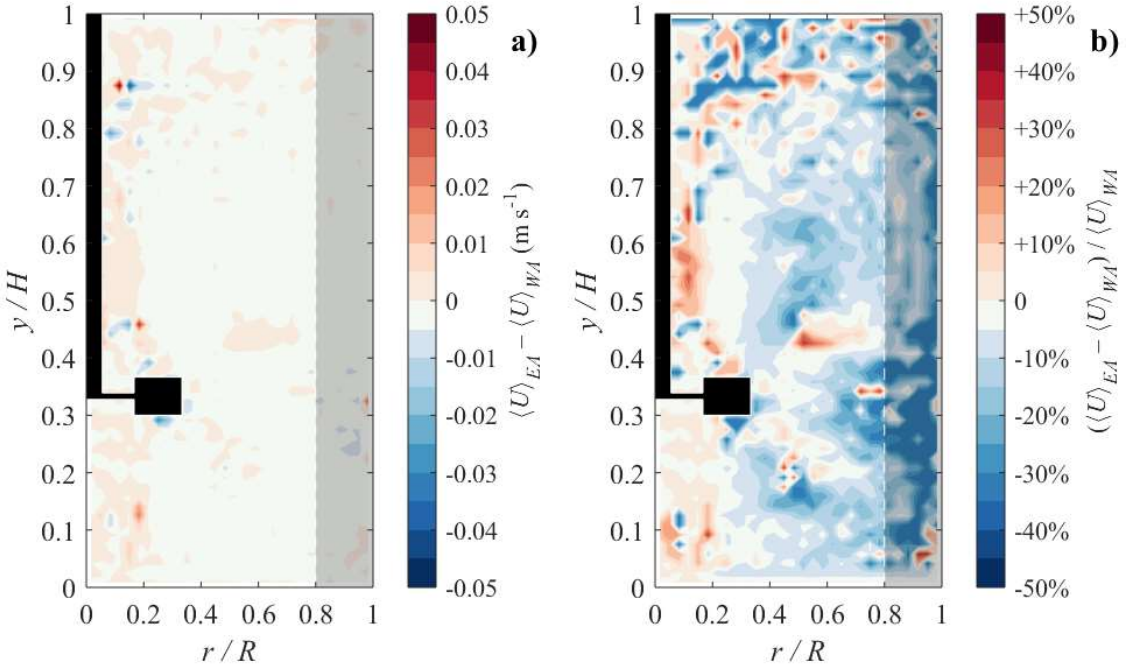

***Figure A-17**: Absolute (a) and normalised (b) difference in the planar velocity, as calculated with the ensemble average (EA) and the weighted average (WA) methods. Data from experiment PL1a.*

A.4. Stokes numbers and tracer dynamics in PTV experiments

A number of forces acting on the PTV tracers may cause their trajectories to deviate from the instantaneous fluid flow. It is important that such forces are small compared to the drag force, which makes the tracers follow the fluid faithfully and limits the particle-fluid relative velocity. The expression of the drag force depends on the particle Reynolds number,

$$Re_p \equiv \frac{\rho \, d_p \, U_{rel}}{\mu}. \qquad \textit{Eq. A-20}$$

For $Re_p \ll 1$, the drag force is given by the Stokes' law. For a sphere,

$$\mathbf{F}_d = -3\pi\,\mu\,d_p\,\mathbf{u}_{rel}. \qquad \textit{Eq. A-21}$$

For higher Re_p, the drag force is

$$\mathbf{F}_d = -\frac{\pi}{8}\rho\,{d_p}^2 c_d\,{\mathbf{u}_{rel}}^2. \qquad \textit{Eq. A-22}$$

The coefficient c_d is typically in the order of 1. A good indicator of the tracing properties of a particle is the Stokes number, defined as the ratio between the relaxation time of a tracer, t_P, and a characteristic time scale of the flow, t_F. Small values ($St < \sim 10^{-1}$) indicate that the tracer can rapidly and faithfully respond to the variations of the flow, down to length scales comparable to the tracer size. In the Stokesian regime ($Re_p \ll 1$), the particle time is conventionally calculated applying the Stokes drag law to a particle moving in the fluid, i.e.

$$t_P = \frac{\rho_P\,{d_P}^2}{18\,\mu}. \qquad \textit{Eq. A-23}$$

The time scale of the flow depends on what is being investigated in the tracking experiment. Turbulent phenomena are characterised by the Kolmogorov time scale, $t_F = \tau_\eta \sim (\nu/\varepsilon)^{1/2}$. For the mean flow in a stirred tank, some authors have used $t_F = D/U_{tip} = 1/\pi N$ (Fangary et al., 2000; Chiti et al., 2011; Alberini et al., 2017). A more conservative value is given by the time between consecutive passages of the impeller blades, i.e. $t_F = 1/6N$. In this case, the Stokes number is

$$St_L = \frac{\rho_P\,{d_P}^2\,N}{3\,\mu}. \qquad \textit{Eq. A-24}$$

As Re_p increases, the Stokes' law underestimates the drag force on the particle and overpredicts the relaxation time. Israel and Rosner (1982) generalized the Stokes number in non-Stokesian flow regimes introducing a correction factor $\psi < 1$:

$$St = \psi \, St_L. \qquad \textit{Eq. A-25}$$

Wessel and Righi (1988) provided an analytical correlation for ψ for $Re_p < 10^3$:

$$\psi = \frac{3\left(\sqrt{c}{Re_p}^{1/3} - \operatorname{atan}\left(\sqrt{c}{Re_p}^{1/3}\right)\right)}{c^{3/2}Re_p}. \qquad \textit{Eq. A-26}$$

with $c = 0.158$. The Stokes number in the PTV experiments are listed in ***Table A-4***. All quantities discussed in this section have been calculated based on $d_P = 785 \cdot 10^{-6}$ m and assuming $U_{rel} = 1\% \, U_{tip}$. The apparent viscosity of non-Newtonian fluids has been evaluated at a shear rate ten times higher than Metzner-Otto's prediction, i.e. $\dot{\gamma} = 10 \, k_s N = 115 \, N$. This is highly conservative, as values of shear $\dot{\gamma} < \sim 40 \, N$ were actually observed in the impeller region. With Re_p ranging between 10^{-2} and 10^0, the flows around the tracers were intermediate between Stokesian and turbulent.

Table A-4*: Stokes number in the PTV experiments. Maxima in bold.*

Exp.	U_{rel} (m s^{-1})	Re_p	St_L	ψ	St
Water **(§III)**	6.28E-03	1.07E-01	1.49E-02	0.981	1.46E-02
NW1a	1.26E-02	2.36E-01	3.27E-02	0.967	3.17E-02
NW1b	1.88E-02	3.54E-01	4.91E-02	0.956	4.70E-02
NW1c	2.51E-02	4.72E-01	6.55E-02	0.947	6.20E-02
NW2a	6.28E-03	3.19E-02	4.43E-03	0.994	4.40E-03
NW2b	1.88E-02	9.57E-02	1.33E-02	0.983	1.31E-02
PL1a	3.14E-03	5.97E-02	8.28E-03	0.989	8.19E-03
PL1b	6.28E-03	1.47E-01	2.04E-02	0.976	1.99E-02
PL1c	1.26E-02	3.62E-01	5.02E-02	0.955	4.80E-02
PL1d	2.51E-02	**8.91E-01**	**1.24E-01**	0.921	**1.14E-01**
PL2a	1.26E-02	1.03E-01	1.43E-02	0.982	1.41E-02
PL2b	2.51E-02	2.55E-01	3.53E-02	0.965	3.41E-02
HB1a	1.26E-02	2.18E-01	3.03E-02	0.968	2.93E-02
HB1b	1.88E-02	4.10E-01	5.69E-02	0.952	5.42E-02
HB1c	2.51E-02	6.40E-01	8.88E-02	0.935	8.31E-02

HB1d	3.14E-02	2.01E-01	2.78E-02	0.970	2.70E-02
HB2a	3.77E-02	2.68E-01	3.72E-02	0.964	3.58E-02
HB2b	**4.71E-02**	3.81E-01	5.29E-02	0.954	5.05E-02

The Magnus force is caused by the spinning of the tracer. Rotation causes an asymmetry in velocity on opposite sides of the tracer. According to Bernoulli's principle, this results in a difference in pressure, thus in a lift force which deflects the particle trajectory perpendicularly to its velocity. At $Re_p \ll 1$, the Magnus force is given by

$$\mathbf{F}_M = \frac{\pi}{8}\rho\, {d_p}^3\, \boldsymbol{\omega} \times \mathbf{u}_{rel}\,, \qquad \textit{Eq. A-27}$$

where $\boldsymbol{\omega}$ is the spin pseudo-vector (rad s^{-1}). The ratio to the drag force is

$$\frac{F_M}{F_d} = \frac{1}{24\,\nu}\,{d_p}^2\,\omega\,, \qquad \textit{Eq. A-28}$$

which is independent of U_{rel}. At higher Re_p, the Magnus force becomes

$$\mathbf{F}_M = \frac{\pi}{8}\rho\, {d_p}^2\, c_l\, U_{rel}\, \frac{\boldsymbol{\omega} \times \mathbf{U}_{rel}}{\omega}, \qquad \textit{Eq. A-29}$$

and is proportional to ω because $c_l = \alpha \cdot \omega$. For new tennis balls (rough surface) at $15 - 65$ m s^{-1}, α is between 10^{-4} and 10^{-3} rad^{-1} s (Robinson and Robinson, 2018). The coefficient is much lower for smooth spheres (Robinson and Robinson, 2018), so $c_l = 10^{-2}\ \mathrm{rad}^{-1}\ \mathrm{s} \cdot \omega$ is very conservative. The ratio to the drag force is simply

$$\frac{F_M}{F_d} = \frac{c_l}{c_d} \sim 10^{-2}\ \mathrm{rad}^{-1}\ \mathrm{s} \cdot \omega. \qquad \textit{Eq. A-30}$$

Zou et al. (2007) measured the effects of Magnus and Saffman forces on saltating sand grains in air. These particles (250 microns) were subject to shear velocities of ~0.9 m s^{-1} (air velocity up to 40 m s^{-1}) and the maximum observed spin was 800 rpm. They reported that the maximum

increase in saltation height due to Magnus and Saffman forces was $\sim 10\%$ and $< 5\%$ respectively. The conservation of angular momentum states that $\omega = M/I$, where M is the moment of the force and $I = \pi/60\ \rho_p\ {d_p}^5$ is the moment of inertia of a sphere. The spinning of PTV tracers can be estimated by assuming that the moment initiating spin is $M \sim mUr \sim \rho_p\ {d_p}^4\ U$. Thus, spin scales as $\omega \sim U/d_p$ and, by proportionality against the values reported by Zou et al. (2007),

$$\omega = \frac{\left(U_{tip}\ /\ 40\ \mathrm{m\ s^{-1}}\right)}{(800\ /\ 250)} \cdot 800\ \mathrm{rpm}. \qquad \textit{Eq. A-31}$$

For $U_{tip} = 2\ \mathrm{m\ s^{-1}}$, $\omega = 12.5\ \mathrm{rpm} = 1.3\ \mathrm{rad\ s^{-1}}$. Depending on Re_p, the ratios of the Magnus force to the drag force for the PTV experiments are reported in ***Table A-5***. These estimates are highly conservative for different reasons:

i. Spinning in sand saltation is initiated by frequent particle-particle collisions, which happen rarely in PTV experiments due to low particle density. When PTV tracers hit the wall or the impeller, the rapid change in velocity typically leads to the interruption of the trajectory. Provided that Magnus effects are significant immediately after these events, they are not measured.

ii. Particle spin decays due to the friction with the fluid, and this happens more quickly as fluid viscosity increases. The fluids used in PTV experiments are more than 10^3 times more viscous than air.

iii. Added mass is a fictitious increase in the mass (and volume) of the tracers, due to the fact that when the particle moves, so does the fluid around it. The particle motion influences the entire flow, but the effects are only appreciable in a very small volume around it. The added mass of a sphere in a fluid is $\pi/12\ \rho\ {d_p}^3$ (half of its mass). The

equivalent diameter is 1.14 d_p. Therefore, for a given value of the Magnus force acting on a tracer, the resulting acceleration will be 33% lower because of the added mass. As Magnus force is typically studied with solid particles in air (small fluid-to-solid density ratio), virtual mass is neglected. In PTV, the density ratio was ~1. For an 800 μm sphere in water or similar liquids, $m_a = 1.3 \cdot 10^{-10}$ kg. The added radius is $\pm 0.07\ d_p/2 = \pm 28$ μm. These were not considered in the calculations. On the other end, the effects of the tracers' inertia on the fluid can be quantified in terms of mass ratio. For a particle concentration of 114 L^{-1} and a fluid volume of 4.6 L, the total mass of particles per mass of fluid was 6.6×10^{-6}, thus negligible.

iv. Non-Newtonian apparent viscosity was evaluated at $\dot{\gamma} = 10\ k_s N$.

Basset force arises from the lag in the boundary layer development when the particle accelerates with respect to the fluid. The force after a time t of relative acceleration is given by

$$\mathbf{F}_B(t) = \frac{3}{2} {d_p}^2 \sqrt{\pi\, \rho\, \mu} \int_0^t \frac{\mathbf{u} \cdot \nabla \mathbf{u} + \left(\frac{\partial \mathbf{u}}{\partial t'} - \frac{d\mathbf{v}_p}{dt'}\right)}{\sqrt{t - t'}} dt' \,. \qquad \textit{Eq. A-32}$$

The computation is extremely complex, as all the particle history must be available. Note that the relative acceleration term vanishes if the particle follows the instantaneous velocity field. Candelier et al. (2004) have measured the effect of Basset force on particles ($\rho_p = 1410$ kg m^{-3}, $d_p = 3$ mm) in swirling water (fluid within rotating cylinder). The ratio between the Basset and the centrifugal force was ~10% and the authors provided the following formula

$$\frac{F_B}{F_{centr}} \sim 3 \frac{|\rho_p/\rho - 1|}{\rho_p/\rho} \sqrt{St} \,. \qquad \textit{Eq. A-33}$$

The force ratio scales more quickly with the density ratio than with the Stokes number. In their case, with $\rho_p/\rho = 1.4$, the ratio was ~10%. Olivieri et al. (2014) and references therein also

reported similar values. In the PTV experiments described in this thesis, the particle-to-fluid density ratio was close to unity and particles were not subject to gravity or centripetal relative acceleration. PTV particle density is provided by the manufacturer with a precision below 1%. The density of CMC and Carbopol solutions is essentially equal to the density of water. Tracers having $\rho_p = 1000\ \mathrm{kg\,m^{-3}}$ were used in those cases, thus $\rho_p/\rho \sim 0.98$ is a conservative estimation. For the glycerol solutions, density was $\rho \sim 1200\ \mathrm{kg\,m^{-3}}$, while $\rho_p = 1100\ \mathrm{kg\,m^{-3}}$ was used, thus $\rho_p/\rho \sim 0.90$. The effects of Basset force on the tracers were negligible (***Table A-5***).

The Saffman force is due to the gradient of the velocity along the physical length of an object immersed in the fluid and directed perpendicularly to the relative velocity. For small Re_p and Newtonian fluids,

$$F_S = \frac{1.6}{4}\sqrt{\rho\,\mu}\,{d_p}^2\,U_{rel}\sqrt{\nabla_\perp U_{rel}}. \qquad \textit{Eq. A-34}$$

The force tends to 0 as the relative velocity approaches 0. The velocity gradient term is related to the stresses acting on the particle surface, and, for non-Newtonian rheology, the exponent should change according to $n < 1$. Note that acceleration decreases with d_p. Rammohan et al., 2003 have shown that the Saffman effects on velocity data obtained through CARPT were negligible for the case of a neutrally buoyant tracer of 250 μm. This adds to the aforementioned observations by Zou et al. (2007). If it is assumed that $\nabla_\perp U_{rel} \sim U_{rel}/d_p$, then the ratio of the Saffman force over the drag force is

$$\frac{F_S}{F_d} = 4.24 \cdot 10^{-2}\sqrt{\frac{\rho\,d_p\,U_{rel}}{\mu}} = 4.24 \cdot 10^{-2}\sqrt{Re_p}. \qquad \textit{Eq. A-35}$$

It is shown in ***Table A-5*** that this ratio was small in all PTV experiments. Such estimates are conservative, because it was assumed a perfect directionality of the velocity gradient over

length scales comparable to the particle size, thus smaller than the Taylor scales. Shear rates at even smaller scales would tend towards isotropy and thus (a) the integration of the resulting stresses over the tracer surface would vanish, and (b) the integration of the cumulative effects over time would vanish.

***Table A-5**: Effects of the forces affecting the dynamics of PTV tracers. Maxima in bold.*

Exp.	ω (rad s^{-1})	$\frac{F_M}{F_d}$ (small Re_p)	$\frac{F_M}{F_d}$ (large Re_p)	$\frac{F_B}{F_d}$	$\frac{F_S}{F_d}$ (small Re_p)
Water **(§III)**	4.11E-01	2.30E-04	4.11E-03	8.94E-03	9.99E-02
NW1a	8.22E-01	5.05E-04	8.22E-03	9.06E-03	2.06E-02
NW1b	1.23E+00	7.57E-04	1.23E-02	1.34E-02	2.52E-02
NW1c	1.64E+00	1.01E-03	1.64E-02	**1.78E-02**	2.92E-02
NW2a	4.11E-01	6.83E-05	4.11E-03	1.44E-03	7.58E-03
NW2b	1.23E+00	2.05E-04	1.23E-02	4.28E-03	1.31E-02
PL1a	2.06E-01	1.28E-04	2.06E-03	5.01E-04	1.04E-02
PL1b	4.11E-01	3.15E-04	4.11E-03	1.22E-03	1.63E-02
PL1c	8.22E-01	7.74E-04	8.22E-03	2.94E-03	2.55E-02
PL1d	1.64E+00	**1.91E-03**	1.64E-02	6.97E-03	**4.01E-02**
PL2a	8.22E-01	2.21E-04	8.22E-03	8.63E-04	1.36E-02
PL2b	1.64E+00	5.45E-04	1.64E-02	2.09E-03	2.14E-02
HB1a	8.22E-01	4.67E-04	8.22E-03	1.80E-03	1.98E-02
HB1b	1.23E+00	8.78E-04	1.23E-02	3.32E-03	2.72E-02
HB1c	1.64E+00	1.37E-03	1.64E-02	5.09E-03	3.40E-02
HB1d	2.06E+00	4.29E-04	2.06E-02	1.65E-03	1.90E-02
HB2a	2.47E+00	5.74E-04	2.47E-02	2.19E-03	2.20E-02
HB2b	**3.08E+00**	8.16E-04	**3.08E-02**	3.09E-03	2.62E-02

A.5. Example of application of the DFT to a PTV trajectory

Figure A-18 shows a selection of trajectories sampled from experiment NW2b and located in the lower circulation loop. The trajectories are coloured according to the acceleration component parallel to the instantaneous velocity, $a_{//} = \mathbf{a} \cdot \mathbf{u} \,/\, (\mathbf{u} \cdot \mathbf{u})^{1/2}$. Positive values indicate increasing velocity magnitude, while negative values indicate a decrease. For experiment NW2b, $a_{tip} = 118.4$ m s^{-2}. As the fluid elements rotated around the axis of the circulation loop, they were not only subject to changes in the velocity direction, but also to fluctuations of the velocity magnitude. An attempt has been made to apply the discrete Fourier transform (DFT) to these trajectories, in order to study the frequency properties of the acceleration events.

In ***Figure A-19a***, the instantaneous 3D acceleration vectors along a single trajectory in the bottom circulation loop are represented by arrows. The time signals of the vertical and parallel components of the acceleration and their corresponding frequency spectra are given in ***Figure A-19b*** and ***Figure A-19c***, respectively. While a_y had a strong sinusoidal behaviour due to the rotation around the vortex axis, $a_{//}$ had a more chaotic evolution. In both cases, however, the spectra indicated a strong contribution of the low frequencies, well below the frequency of the blade passage ($f = 6\ N$). Unfortunately, the low spectral resolution would not allow to identify frequency peaks clearly.

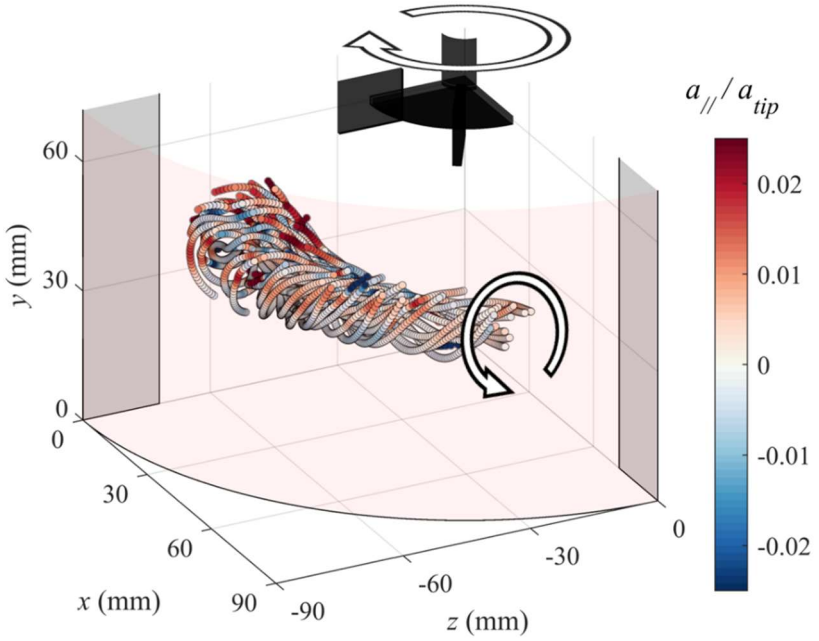

***Figure A-18**: Component of the acceleration parallel to the instantaneous velocity, along a selection of trajectories in the lower circulation loop sampled from experiment NW2b at Re = 258.*

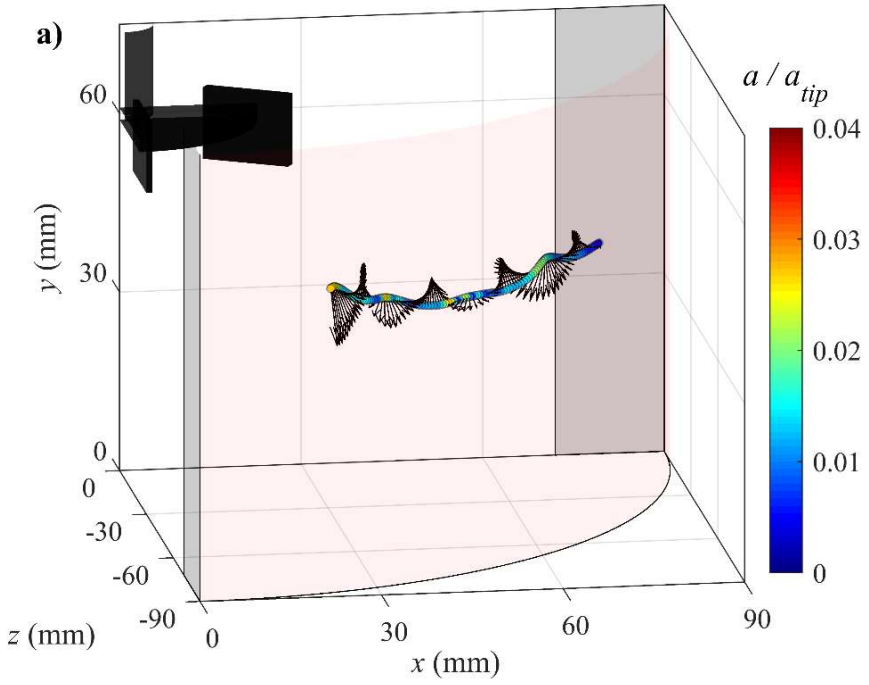

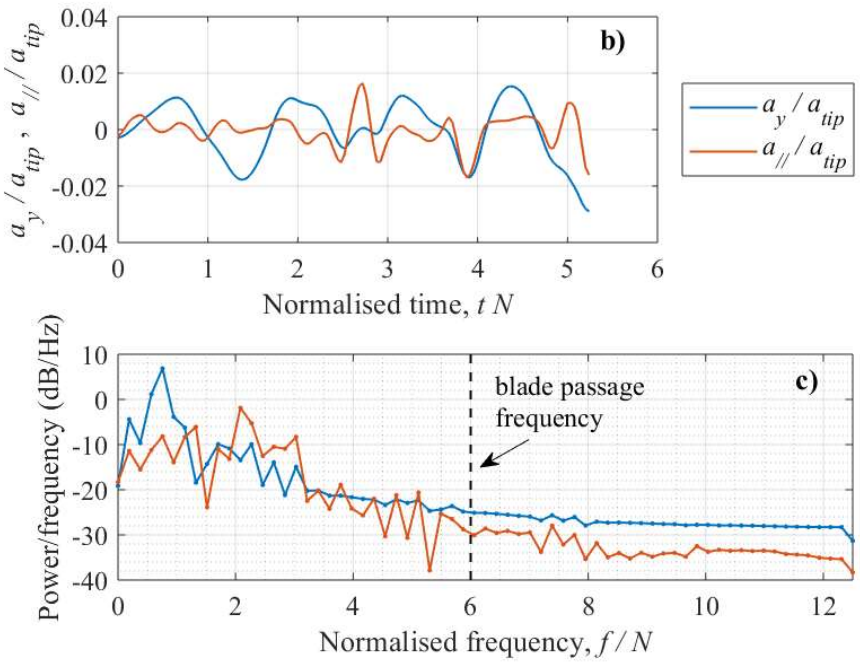

***Figure A-19**: Acceleration 3D vectors along a single trajectory sampled from experiment NW2b (a), vertical and parallel components of the acceleration (b) and resulting frequency spectra (c).*

A.6. Rheological measurements

A.6.1. Small vessel (Chapter IV and Chapter V)

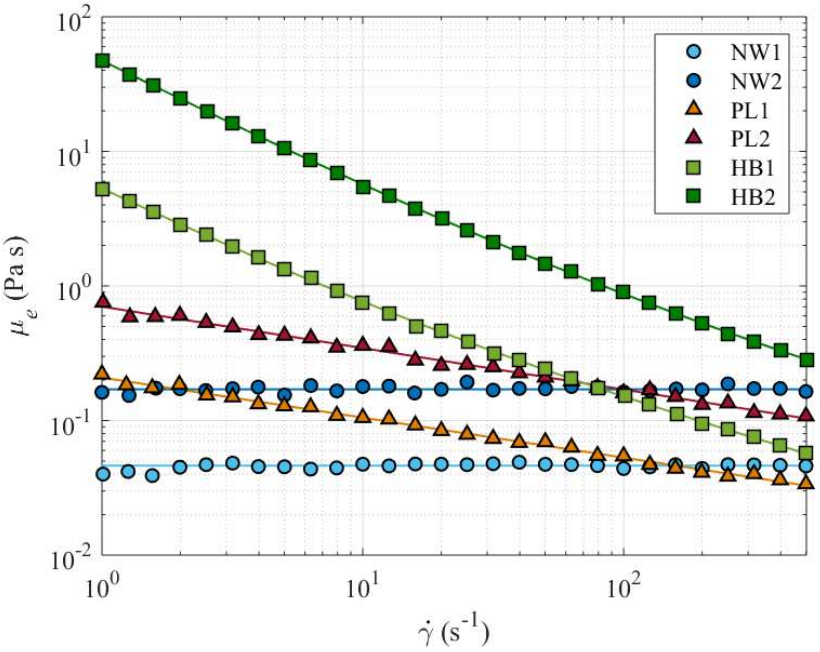

***Figure A-20**: Flow sweep data of the fluids used in the small vessel.*

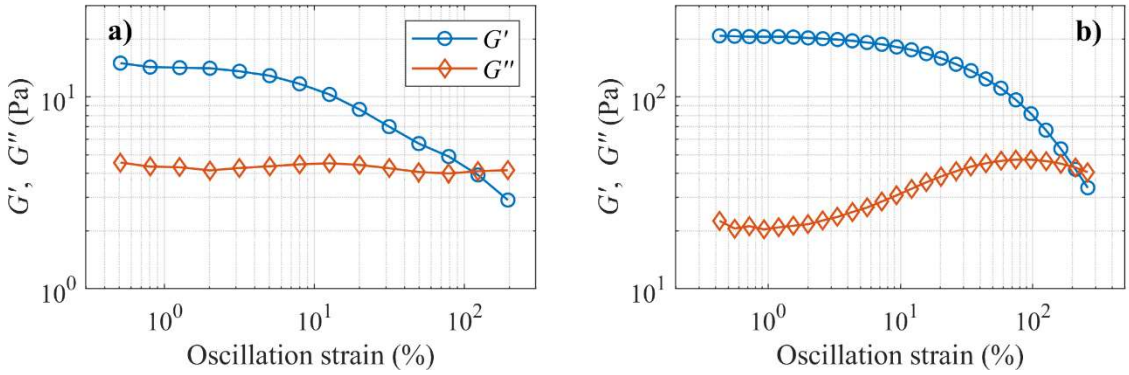

***Figure A-21**: Amplitude sweep data of fluids HB1 (a) and HB2 (b) used in the small vessel.*

A.6.2. Large vessel (Chapter VI)

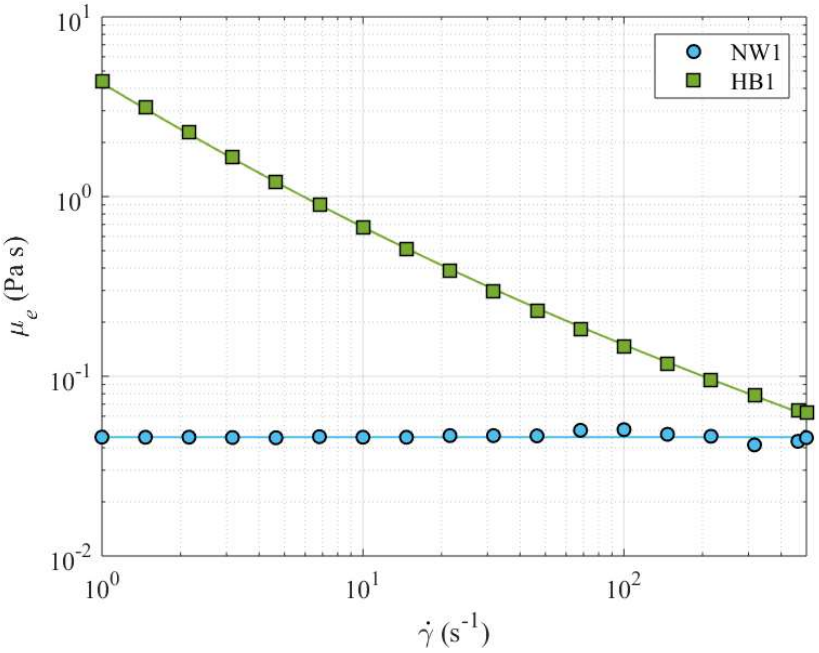

***Figure A-22**: Flow sweep data of the fluids used in the large vessel.*

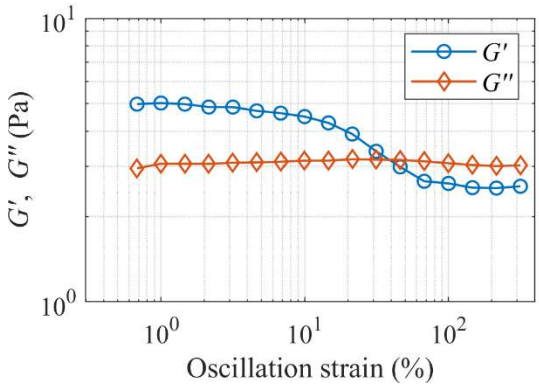

***Figure A-23**: Amplitude sweep data of fluid HB1 used in the large vessel.*

A.7. MATLAB in-house scripts

A.7.1. Trajectory identification and length distribution

```
t = data(:,1);                      % time step vector
tl = length(t);
d = t(2:tl)-t(1:tl-1);
d = [d(1);d];
be = find(d~=1);                    % start index vector
en = be-1;                          % termination index vector
be = [1;be];
en = [en;tl];
le = en-be+1;                       % length vector (size of be)
lele = zeros(tl,1);                 % length vector (size of t)
vmtraj = zeros(tl,1);               % avg velocity vector (size of t)

for j = 1:length(be)-1
     lele(be(j):be(j+1)-1) = le(j);
     vmtraj(be(j):be(j+1)-1) = mean(vm(be(j):be(j+1)-1));
end
lele(be(end):end) = le(end);
vmtraj(be(end):end) = mean(vm((be(j):be(j+1)-1)));

%% lele can be used for trajectory categorization, e.g.

maxle = find(lele==max(lele);
datamax = data(maxle,:);            % longest trajectory
long = find(lele>L);
datalong = data(long,:);            % only trajectories longer than L
short = find(lele<L);
datashort = data(long,:);           % only trajectories shorter than L

%% le can be used for trajectory length distribution, e.g.

fps = 125;                          % frame rate
tau = (le-1)/fps;                   % trajectory duration [s]
```

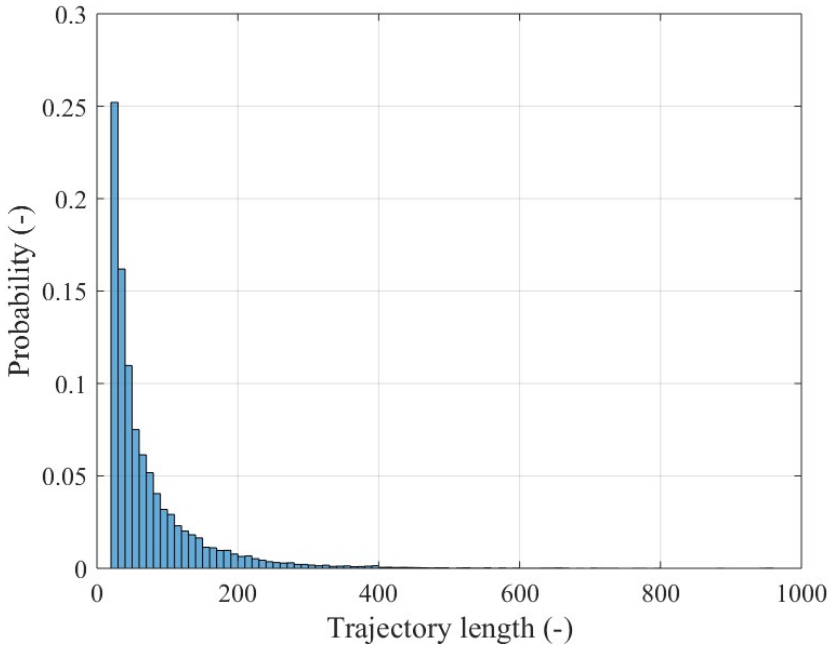

***Figure A-24**: Example of trajectory length distribution (PTV data from experiment NW1a).*

A.7.2. Savitzky-Golay filter and reduced Chi-squared

```
function [smooth_vec,chi2] = sgf(noised_vec,width,order,sigma)

l = length(noised_vec);
w = round(width/2)-1;

smooth_vec = zeros(l,1);
chi2 = zeros(l,1);

%% Main calculations


for i = 1:l

    be = i-w;
    en = i+w;
    if  be < 1
        be = 1;                          % dealing with first points
    end
    if  en > l
        en = l;                          % dealing with last points
    end
    if  en-be < 10 && order > 2
        order = 2;              % order reduction for short sequences
    end
    if  en-be < 5 && order > 1
        order = 1;
    end
    if  en-be < 3 && order > 0
```

```
        order = 0;
    end

    y = zeros(en-be+1,1);
    A = zeros(en-be+1,order+1);
    for j = 1:en-be+1
        y(j,1) = noised_vec(be+j-1);   % sequence
        h = (be+j-1-i);
        for o = 0:order
            A(j,o+1) = h^o;            % convolution matrix
        end
    end

    c = (A'*A)\A'*y;                   % least square solution
    yy = A*c;                          % filtered sequence
    res = y-yy;                        % fitting residuals

    smooth_vec(i) = c(1);
    chi2(i) = (norm(res)^2/sigma^2)/(en-be+1-(order+1));

end
```

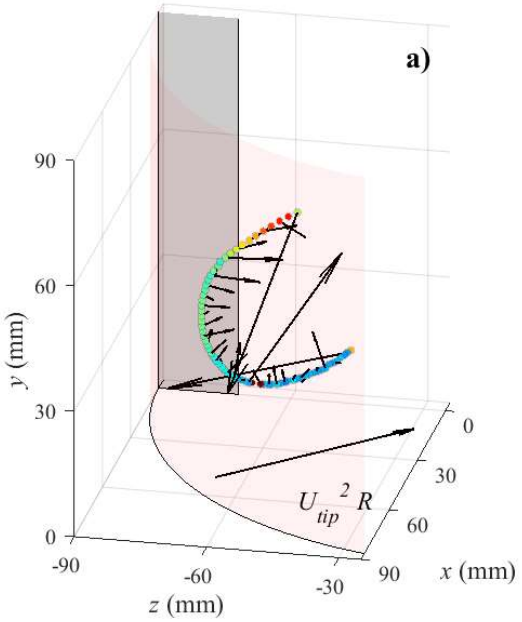

***Figure A-25**: Effect of the Savitzky-Goley filter on the acceleration vectors along a single PTV trajectory (data from experiment NW1a). Unfiltered data, derivatives calculated through central finite differences (a); Filtered data (b). (Continues in the next page).*

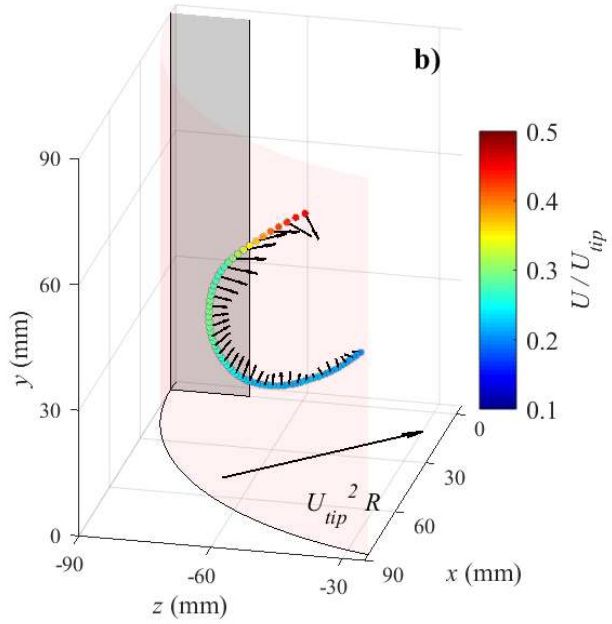

Figure A-25 *(continues).*

A.7.3. Autocorrelation coefficients of a 3D vector

```
function [ac,band] = acf3D(y,l)

%% Input checks

[n1,n2] = size(y);
if  n2 ~= 3
    if  n1 == 3
        y = y';
    else
        error('The signal must be a vector (3 x n) or (n x 3)')
    end
end

n1 = length(y);
[a1, a2] = size(l);
if ~((a1==1 && a2==1) && (l<n1))
    error('The maximum number of lags must be an integer smaller
than the length of the signal')
end

%% Main calculations

global N
N = max(size(y));
global ybar
ybar = mean(y);
ac = zeros(l,1);
band = zeros(l,1);
```

```
for i = 1:l
   ac(i) = acf_k(y,i);
end

band(1) = 1/sqrt(N);
for i = 2:l
    r = ac(1:i-1);
    band(i) = 1.96*sqrt((1+2*(r'*r))/N);
end

%% Sub function
function ack = acf_k(y,k)
global ybar
global N
cross_sum = zeros(N-k,1);
yvar = zeros(N,1);

for i = 1:N-k
    cross_sum(i) = (y(i,:)-ybar)*(y(i+k,:)-ybar)';
end

for i = 1:N
    yvar(i) = (y(i,:)-ybar)*(y(i,:)-ybar)';
end

ack = sum(cross_sum) / sum(yvar);
```